Universidad de Concepción
Facultad de Ingeniería
Departamento de Ingeniería Química

INFLUENCIA DE LAS PROPIEDADES ÁCIDAS Y REDOX EN EL MECANISMO DE LA OXIDACIÓN SELECTIVA DE METANOL A FORMIATO DE METILO

INFLUENCE OF ACID AND REDOX PROPERTIES ON THE MECHANISM OF SELECTIVE METHANOL OXIDATION TO METHYL FORMATE

Tesis presentada a la Facultad de Ingeniería de
la Universidad de Concepción para optar al
grado de Doctor en Ciencias de la Ingeniería
con Mención en Ingeniería Química

Por: Gabriel Alexander Galdames Oliva

Profesor Guía: Alejandro Iván Karelovic Burotto

Profesor Co-guía: Romel Mario Jiménez Concepción

Marzo 2025

Concepción, Chile

ORCID ID:

Gabriel Galdames O.: 0009-0008-3321-2217

Alejandro Karelovic B.: 0000-0001-5189-0902

Romel Jiménez C.: 0000-0003-0839-4393

Acknowledgements

First and foremost, I would like to express my deepest gratitude to my advisors, Dr. Alejandro Karelovic and Dr. Romel Jiménez, for their invaluable guidance, support, and encouragement throughout the course of my PhD. I am especially grateful for the collaborative and supportive research group they lead, whose warmth and camaraderie were instrumental in the successful completion of this thesis. This environment made this challenging journey a profoundly rewarding experience.

I am also deeply thankful to the other members of the Carbocat laboratory, where I had the privilege to conduct my research. My sincere thanks go to the laboratory staff—Karen, Veronica and Ignacia—for all their help during my PhD. I also thank my co-workers—Bastián, Daviel, Francisco, Tomás, among others— with whom I engaged in scientific discussions (and coffee breaks), which greatly contributed to my learning and personal growth.

I would like to thank Dr. Patricia Concepción, who welcomed me to the Instituto de Tecnología Química in Valencia, allowing me to experience cutting-edge science and to learn that I am more than capable of competing in their environment.

To my family, for always believing in me and for fostering my curiosity and love for math since childhood. I owe them my passion for science.

Paulina, thank you for your understanding, support, patience and motivation, especially during the most challenging moments in this journey. You were the foundation that allowed me to successfully overcome these obstacles.

Finally, I would like to acknowledge the institutions that made this work possible: ANID scholarship n° 21201192 and Dirección de Postgrado, Facultad de Ingeniería and Departamento de Ingeniería Química of Universidad de Concepción, for providing me with the opportunity and resources to pursue this PhD.

Table of contents

General introduction

Emission of greenhouse gases and its connection to climate change [1], fossil fuel depletion due to their unsustainable use [2], increase of energy prices due to global phenomena like pandemics or armed conflicts [3], are some of the reasons that require the active search of efficient and renewable energy sources. Hydrogen produced by water electrolysis induced by sustainable energy sources (hydro, wind or solar power) has emerged as an attractive energy carrier alternative due to its versatility as raw chemical material, high heating energy and minimal greenhouse gasses emissions [4,5]. Nevertheless, the renewable hydrogen industry faces many challenges [6]. Hydrogen has a low energy density at room temperature, which has motivated the proposal of its transformation and subsequent storage in fuel carriers [7,8].

In this context, methanol has arisen as an attractive candidate due to its possible applications, simple handling, and its potential to make use of infrastructure already available [9–14], surfacing as the ideal hydrogen carrier [15–19]. When combining green hydrogen produced by the above-mentioned methods, and CO_2 obtained by direct air capture (DAC) or by capture of exhausts of the chemical industries, it is possible to produce renewable electricity-based methanol (e-methanol). This technology, which has already been successfully deployed [20–23], introduces the concept of green methanol or liquid sunshine [24], which serves as a hydrogen carrier and motivates the so-called methanol economy, as it can produce high value chemicals with carbon neutral/carbon net zero emissions [9,15,25,26]. In this context, methanol could be essential to accomplish the goals established by the Paris agreements to restrict the increase in global temperature to below 2 °C [27–29], as methanol fulfills two purposes: it acts as a storage medium for renewable energy in a chemical state, a concept recently labeled as power-to-fuel (PtF) [3,30–36], and can be directly used as an entirely renewable clean fuel, that could potentially replace the fossil-based ones.

Methanol contributes to the formation of about 30% of industrial raw materials, being one of the most important C1 chemical building blocks as it is used in the chemical, petrochemical and pharmaceutical industry to produce multitude of value-added chemicals [37–40]. This way, the methanol economy can introduce renewable carbon to existing chemical processes. Therefore, it is interesting to study novel ways of transforming the e-methanol to chemical intermediates in processes yet to be developed at industrial scale.

Methanol oxidative dehydrogenation (ODH), also known as methanol partial oxidation, stands out because its primary products: formaldehyde (FA), methyl formate (MF) and dimethoxymethane (DMM), have a wide array of direct applications or uses as feedstock in various chemical processes. FA is utilized in the production of resins such as urea formaldehyde, phenol formaldehyde and melamine formaldehyde [41]. MF is primarily used to produce formamide, dimethylformamide, and formic acid. DMM is mainly used as a solvent and in the production of perfumes, resins, adhesives, paint strippers, and protective coatings [42]. Furthermore, by oxidizing methanol with O_2, this reaction allows to obtain

value-added chemical using a simple, cheap, and abundant benign molecule, contributing to the search of sustainable processes [43,44].

Methanol ODH produces FA, MF and DMM by parallel pathways. Nevertheless, these chemical compounds are commercially mass-produced through substantially distinct processes. The production of FA involves the methanol ODH reaction using either silver or combined iron oxide-molybdenum oxide catalysts [45]. MF is industrially produced through methanol carbonylation using carbon monoxide over sodium methoxide catalysts, in liquid phase. DMM is produced via a two-stage process that begins with the oxidation of methanol to FA followed by condensation reactions in a mixture of methanol and formaldehyde using either sulfuric acid or solid acidic catalysts [42]. In this context, the heterogeneous catalysis surges as an attractive prospect for methanol ODH reaction because it could selectively produce each of the reaction products by finely tuning the structural or physicochemical properties of the reactive surfaces used for this reaction.

Mixed oxides have been extensively studied for partial oxidation reactions, thanks to its abundance and affordability [45–82]. Independent of the material, it is known that the methanol partial oxidation follows a Mars-van Krevelen redox mechanism, with the dehydrogenation of a methanol molecule on a lattice oxygen active site to produce adsorbed formaldehyde as the rate-determining step (rds) [69,72,83–85]. The adsorbed FA can desorb or keep reacting to form MF and/or DMM.

Despite extensive research, there is no consensus regarding the reaction mechanism or intermediates involved in the formation of methanol ODH products. Various intermediates and mechanisms have been proposed, including the hemiacetal intermediate, which can yield MF or DMM through dehydrogenation or dehydration reactions, respectively [86–92] ; the dioxymethylene and formate intermediates, where the former leads to DMM and the latter to MF [42,50,93]; and the Tishchenko reaction, which involves the condensation of FA to form MF [48,94,95]. Each of these intermediates requires specific active sites, with acid sites generally associated with DMM formation and redox sites essential for FA and MF formation. The role of the catalyst support has also been extensively studied, as it is widely accepted that the support influences and participates in the reaction in various ways. However, critical questions remain unresolved, such as the precise nature of the intermediate species, the specific types of active sites involved, and the detailed reaction mechanisms.

Objectives

General objective

Study the formation of formaldehyde, methyl formate and dimethoxymethane from the partial oxidation of methanol over molybdenum and vanadium catalysts supported on titania and silica-alumina.

Specific objectives

i) Investigate the nature and role of redox sites in the formation of formaldehyde, methyl formate and dimethoxymethane from the partial oxidation of methanol.
ii) Examine the effect of total acidity and the Brønsted or Lewis nature of acid sites on the activity and selectivity of the partial oxidation of methanol.
iii) Propose a reaction mechanism based on the study of reaction intermediates and develop a kinetic model for the formation of formaldehyde, methyl formate and dimethoxymethane from the partial oxidation of methanol.

General outline

In an effort to understand the complex parallel and sequential pathways of the methanol ODH reaction, as well as the corresponding kinetics parameters that govern the reactivity and requirements of active sites, this study was carried out along four main axes:

i) Molybdenum supported on titania catalysts were synthetized with varying metal content, and they were rigorously characterized using techniques such as X-ray diffraction (XRD), BET surface area analysis, H_2-temperature programmed reduction (H_2-TPR), Low-temperature FTIR CO adsorption, X-ray photoelectron spectroscopy, NH_3-temperature programmed desorption (NH_3-TPD), FTIR pyridine adsorption and UV-vis spectroscopy.
ii) Operando-FTIR studies were carried out to investigate the adsorbed species on MoO_3/TiO_2 catalysts surface under reaction conditions, correlating their behavior with the transient response of reaction products as the system feed was changed, as to elucidate the reaction mechanism and identify the key intermediates in the methanol ODH, and its link with the catalyst characterizations.
iii) A kinetic model was developed which accurately describes the complex kinetic pathways for the formation of the main ODH reaction products (FA, MF and DMM), with hemiacetal (HA) (CH_3OCH_2OH) as the sole MF and DMM reaction intermediate, under integral reaction conditions using V_2O_5/TiO_2 catalysts,
iv) Molybdenum catalyst supported on aluminosilicates with varying alumina fraction were synthetized as to modify the Brønsted/Lewis (B/L) acid site ratio, and the impact of this property on the selectivity to the different reaction products was studied.

Chapter I: Characterization of MoO_3/TiO_2 catalysts: structural, redox and acid properties

Summary

Supported MoO_3/TiO_2 catalysts with varying molybdenum surface densities (0.5, 2.5, 8, 15, and 25 at. Mo nm^{-2}) were synthesized and characterized to investigate the structural and chemical properties as a function of molybdenum content and its corresponding structure. XRD and in-situ Raman spectroscopy revealed a transition in the oxide structure from sub-monolayer oligomeric molybdenum species to crystalline molybdenum oxide phases as the molybdenum content surpassed the oxide monolayer coverage threshold (4.6 at. Mo nm^{-2}). The molybdenum oxidation state, studied by XPS and low-temperature FTIR CO adsorption, transformed from coordinatively unsaturated Mo^{5+} sites in defect-rich structures to the Mo^{6+} state characteristic of ordered bulk MoO_3 as the molybdenum content increased. H_2-TPR measurements showed that octahedral molybdenum structures with larger domain size reduced at lower temperatures than dispersed tetrahedral phases, while all catalysts reduced at lower temperatures compared to bulk MoO_3 due to enhanced reducibility attributed to their interaction with the titanium support. NH_3-TPD and pyridine FTIR adsorption revealed that total acid site density decreased with increasing molybdenum content, primarily due to the loss of titania Lewis acid sites, while the Brønsted/Lewis acid site ratio increased with molybdenum loading, driven by titania Lewis site loss rather than by a significant increase in Brønsted acidity. These results highlight the structural transformation of molybdenum oxide phases supported on TiO_2 and the corresponding changes in their chemical properties, providing the detailed framework for the future exploration of the relationship between structure and catalytic behavior in methanol oxidative dehydrogenation.

1. Introduction

The commercial production of MF is predominantly achieved through the liquid-phase carbonylation of methanol at 80 °C and 40 bar, using sodium methoxide as a homogeneous catalyst [96]. This reaction exhibits high selectivity and has been widely employed since 1980 [97], with global production exceeding 6 million tons in 2016 [98].

However, this method is not without challenges. It has a maximum conversion of only 30%, and the use of sodium methoxide presents significant disadvantages, such as equipment corrosion due to its strong basicity, the requirement for highly pure reactants because of the catalyst's sensitivity to water, high capital investment due to the high-pressure requirements, and complex, costly separation processes associated with homogeneous catalysis [98].

These challenges have prompted interest in exploring more efficient and sustainable alternatives for MF production from methanol, such as the use of heterogeneous catalysts. Heterogeneous catalysis offers several advantages, including continuous operation, simpler separation of products and catalysts, and the potential for catalyst regeneration [99].

The methanol partial oxidation reaction holds significant industrial potential because it avoids the intrinsic limitations of earlier approaches. For instance, it is not thermodynamically constrained like direct methanol dehydrogenation [100–109] and does not require the high pressures (160–300 bar) associated with exploratory works on CO_2 hydrogenation in the presence of methanol [110–115].

However, while metal oxide-based catalysts are promising, they are not yet sufficiently active or selective. Meanwhile, noble metal-based catalysts, although highly active, face practical limitations due to their high cost. Consequently, the search for efficient catalysts for the oxidative dehydrogenation of methanol remains critical.

Mixed oxides have been extensively studied for partial oxidation reactions, thanks to its abundance and affordability [45–61]. Among metal oxides, examples include V_2O_5/ZrO_2–Al_2O_3 [116], MoO_3/TiO_2 [117], ReO_x/CeO_2 [118], RuO_2 supported on SnO_2, ZrO_2, TiO_2, Al_2O_3 y SiO_2 [119], MoO_3 supported on Al_2O_3, TiO_2, ZrO_2, SiO_2, MnO, NiO, Nb_2O_5 and Cr_2O_3 [120], Sn-Mo-O [121], MoO_3/SnO_2 [122], V_2O_5/TiO_2 [123]. Noble metal catalysts have also being studied for this reaction, like Au-Pd/SiO_2 [124], Pt/TiO_2 [125], Pt-Bi [126], Pd/TiO_2 [127], np-Au [128] and Pd/Al_2O_3 [129].

The selectivity toward different reaction products is influenced by factors such as temperature, conversion, residence time, reactant partial pressures, active metal coverage, and the redox and acidic properties of the catalyst [116,123,126,130–135]. A strong dependence on the structural characteristics and physicochemical properties of the metal oxide and the support has been observed. This has led many researchers to use methanol oxidation as a probe reaction, complementing catalyst characterization by linking product selectivity to specific active sites. Literature primarily highlights the effects of redox, acid-base, and structural properties of the active phase on reaction behavior.

As previously discussed, rigorous catalyst characterization is essential for conducting in-depth studies and enabling meaningful comparisons between catalytic activity and structural properties. In this chapter, synthesized TiO_2-supported molybdenum catalysts were thoroughly characterized. Surface structure was analyzed using X-ray diffraction (XRD), BET surface area measurements, low-temperature FTIR CO adsorption, X-ray photoelectron spectroscopy, and in-situ Raman spectroscopy. Acidic properties were assessed using NH_3-temperature programmed desorption (NH_3-TPD) and FTIR pyridine adsorption, while redox properties were evaluated through H_2-temperature programmed reduction (H_2-TPR).

2. Experimental

2.1 Catalysts preparation

MoO_3/TiO_2 supported catalysts were prepared by wet impregnation varying the molybdenum surface density (0.5, 2.5, 8, 15 and 25 atom Mo nm^{-2}). Ammonium heptamolybdate tetrahydrate (HMoA, $(NH_4)_6Mo_7O_{24} \cdot 4\ H_2O$, 81.0-83.0% MoO_3, CAS No.:12054-85-2) was used as the molybdenum source supported on titania (Evonik P-25). The desired surface concentration was determined by the corresponding number of molybdenum atoms per square nanometer of the catalyst, which was calculated based on the equivalent MoO_3 nominal weight content and the BET surface area of the TiO_2 support (50 $m^2\ g^{-1}$). The samples were labelled χ MoTi where χ stands for the nominal Mo concentration expressed as Mo atoms nm^{-2}. A representative preparation of the 2.5 MoTi catalyst is described as follows. First, a solution of oxalic acid ($C_2H_2O_4$, ReagentPlus®, ≥99%, CAS No.:144-62-7) was prepared, dissolving 0.053 g of oxalic acid in 250 ml of distilled water heated at 60 °C under stirring at 200 rpm. Afterwards, 0.172 g de HMoA were added (in a 3:1 molar ratio), and after the dissolution, the solution was cooled down to room temperature and the pH was measured (ca. pH = 5). Afterwards, the TiO_2 support was added to the solution under stirring at 400 rpm, at room temperature for 1 h. Next, the water of the solution was evaporated under vacuum at 80 °C for 15 min in a rotary evaporator (Laborota 4002, Heidolph). Afterwards, the resulting solids were dried overnight at 105 °C and then calcined in static air in a box furnace (Lindberg/Blue M Moldatherm, Thermo Scientific) at 500 °C for 3 h, after raising the temperature with a heating rate of 10 °C min^{-1}. Bulk MoO_3 was also prepared in an analogous procedure, without the addition of TiO_2 support.

2.2 Catalysts characterization

X-ray diffraction (XRD) patterns were obtained in a X-ray diffractometer Bruker D4 Endeavor (Billerica, USA) equipped with a solid-state detector (LynxEye) using Cu Kα radiation (λ = 0.154 nm) in the range of 2θ = 5-90°, with a scan rate of 0.4 °/min and a step time of 20 s.

BET surface area, pore volumes and pore size distributions were determined in a Gemini VII Surface Area Analyzer Micromeritics (Georgia, USA) by N_2 adsorption-desorption isotherms at -195.8 °C. Prior to the experiments, the samples were degassed at 200 °C during

4 h under N_2 flow (Airliquide 99.999%) to remove from the surface potential adsorbed species in the porous structure that could impact N_2 adsorption. Surface area was calculated from the BET equation while the pore size distribution was obtained from the desorption branch of the nitrogen isotherms using the Barrett-Joyner-Halenda (BJH) method.

H_2 Temperature programed reduction (H_2-TPR) was performed in a ChemBet Pulsar TPR/TPD (Quantachrome). The samples were pretreated in 30 ml min^{-1} of Ar (Air Liquide 99.999%) heating from room temperature to 150 °C. After the samples cooled down to room temperature, to remove from the surface potential adsorbed species. Subsequently, the samples were reduced in a mixture of 10% vol H_2/Ar and a total flow of 30 ml min^{-1} heating until 700 °C with a heating rate of 5 °C min^{-1}.

Low temperature CO pulse adsorption was performed using a Nicolet iS50 FTIR spectrometer equipped with a DTGS detector using home-made IR cell with KRS-5 (Thallium-iodide bromide) windows. Before the experiment, the samples were pressed down into wafers and in-situ pretreated in the IR cell at 300 °C for 30 min under dry air flow (30 ml min^{-1}, 21% vol O_2/ N_2) to completely oxidize the catalysts, with mass flow controllers Bronkhorst El-Flow F201 CV. Afterwards, the samples were degassed under vacuum (10-4 mbar) for 30 min. Finally, the cell was cooled down under vacuum to -130 °C and CO pulses were injected stepwise until CO physisorption was observed (3 mbar). CO desorption was achieved by stepwise outgassing the cell under vacuum. Infrared spectra were recorded in the range of 1500 – 2500 cm^{-1} with a resolution of 4 cm^{-1}.

X-ray photoelectron spectroscopy (XPS) was performed using a PHOIBOS 150 MCD 9 analyzer from SPECS and a monochromatic Alka α X-ray energy of 1486.60 eV, under vacuum (10^{-9} mbar) and 25 °C. Binding energies were corrected using the C 1s component at 284.6 eV. The data was analyzed using CasaXPS (Casa Software Ltd) software with the NIST library (NIST X-ray Photoelectron Spectroscopy (XPS) Database, version 3.5).

NH_3 temperature-programmed desorption (TPD) was performed using a 3FLEX (Micromeritics) equipped with a TCD combined with a mass spectrometer (Pfeiffer Vacuum OmniStar GSD 320). Approximately 100 mg of sample was pretreated under helium flow at 350 °C (20 °C min^{-1}) for 30 min and then cooled to 100 °C for NH_3 adsorption, to remove from the surface potential adsorbed species. NH_3 was fed by pulses at 10 min intervals (loop of 0.5 cm^3), and then the weakly adsorbed NH_3 was desorbed at 100 °C for 30 min under He flow (100 ml min^{-1}). The temperature was subsequently increased to 800 °C (10 °C min^{-1}) to induce NH_3 desorption under He flow.

The pyridine adsorption test (C_5H_5N, J.T. Baker, >99.9%) was carried out by FTIR analysis on a Nicolet iS50 instrument (ThermoScientific). For each experiment, materials were pelletized using 2 metric tons of pressure for 1 min. Pellets of 13 mm diameter and ~10 mg were obtained. The pellets were transferred to a vacuum system composed of a cell with ZnSe windows and a Pfeiffer Hicube Eco Turbo Pumping Station that reaches a pressure of $1x10^{-4}$ Pa. The Infrared Pyridine adsorption study (IR-Pyr) was carried out by pretreating the

sample disk at 400 °C for 12 h under vacuum conditions, to remove from the surface potential adsorbed species. The sample was then cooled to 150 °C and the reference spectrum was taken. Subsequently, the pyridine was brought into contact with the sample for 10 minutes. The measurements were carried out (and the spectra collected) at three different temperatures (150, 250 and 350 °C). At each temperature, spectra were collected after 30 minutes to monitor pyridine desorption and ensure its removal from the system.

Raman spectroscopy studies were conducted using a Renishaw "in Via" spectrometer coupled with an Olympus microscope. The system includes a He-Ne green laser (514 nm, 25 mW), along with a CCD detector, with spectral acquisition times of 10 s. In situ Raman measurements were carried out at 1 bar using a Linkam THMS600 cell, which operates within a temperature range of -195 to 600 °C with a precision of 0.01 °C. For in situ studies, the samples were pretreated in air (20 ml min^{-1}) at 300 °C for 30 min before being exposed to reaction conditions (CH_3OH/O_2 = 2, 20 ml min^{-1}) within a temperature range of 100–200 °C. Raman spectra were collected simultaneously at multiple points on the sample.

3. Results

3.1 Characterization

Table I-1 shows the structural properties of the synthetized MoO_3/TiO_2 catalysts, with their corresponding MoO_3 loading (%) and Mo surface density (at. Mo nm^{-2}), as well as the calculated BET surface area and the pore volume and pore size determined by the BJH method. Values for TiO_2 and bulk MoO_3 are also presented. The surface area does not vary significantly with the deposition of metal on the support, staying similar to the bare TiO_2 support area. A small effect of molybdenum loading on the pore volume and size is observed in the supported catalysts. BET area, pore volume and pore size are independent of metal content presenting similar values for all supported catalysts, so molybdenum agglomerations or pore filling as the metal content increases are discarded. Also, the molybdenum phase was satisfactorily dispersed on TiO_2, as the properties of the supported catalysts have a significant difference with bulk MoO_3. N_2 adsorption-desorption isotherms can be found on Figure A-I.2 (Appendix: Chapter II)

Table I-1. Molybdenum surface density, surface BET area, mean pore volume and pore size of the supported MoO_3/TiO_2 catalysts, TiO_2 and MoO_3.

Sample	Loading (MoO_3 wt. %)	Surface density (at. Mo nm^{-2})	BET Area ($m^2\ g^{-1}$)	Pore volume ($cm^3\ g^{-1}$)	Pore size (nm)
TiO_2	0	0	50	0.15	15
0.5 MoTi	0.6	0.5	48	0.07	7
2.5 MoTi	2.7	2.5	49	0.08	8
8 MoTi	8.2	8	46	0.08	8
15 MoTi	14.4	15	44	0.08	8

25 MoTi	21.9	25	42	0.07	8
MoO_3	-	-	10	0.01	6

Figure I-1 shows the XRD diffractogram of the molybdenum supported catalysts. MoO_3 and TiO_2 diffraction patterns are also presented. The identification of the species was done using VESTA software to calculate the powder diffraction patterns. All supported catalysts show typical TiO_2 diffraction peaks attributed to anatase (COD-1010942) and rutile phases (COD-1532819), characteristic of TiO_2 P25. At low metal content there is a clear absence of diffraction peaks due to the molybdenum phases, indicating small crystallite size and/or amorphous phases. At surface densities higher than 2.5 at. Mo nm^{-2}, peaks corresponding to the thermodynamically stable orthorhombic α-MoO_3 (COD- 9009669) structure [136] start to appear. These results align with the molybdenum monolayer coverage reported by Wachs at 4.6 at. Mo nm^{-2} [137], corresponding to the point where surface hydroxyls of the oxide support are consumed by oxide deposition. This value agrees with the theoretical monolayer coverage of 4.9 at. Mo nm^{-2}, threshold at which the crystalline MoO_3 phase begins to form. At lower metal densities, monomeric and polymeric molybdenum phases should dominate the surface, but cannot be detected by XRD. This was also reported by Oyama et al. [138] who only observed peaks associated to MoO_3 on supported P25 titania at loadings higher or equal to 9.0 wt.%.

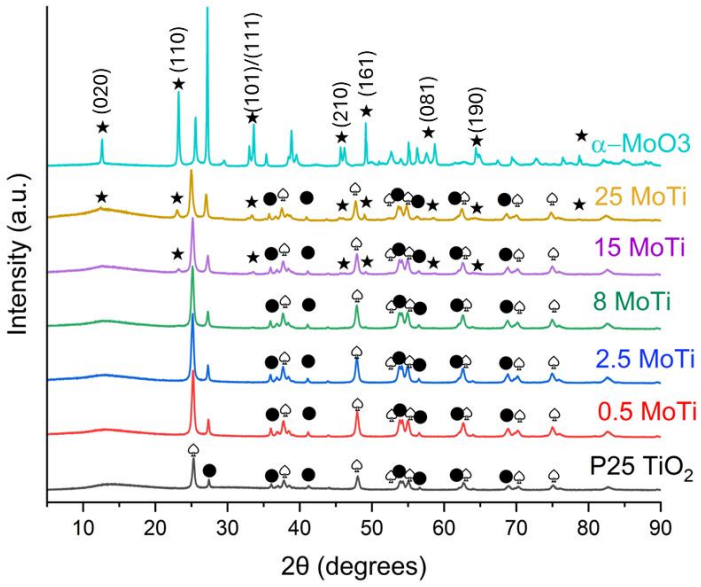

Figure I-1. X-ray diffraction patterns and MoO_3 crystalline planes for all Mo supported catalysts, titania P25 and bulk MoO_3. ★: α-MoO_3, ♤: anatase, ●: rutile.

The specific molybdenum structure depends on the support characteristics. On titania, there is agreement that at monolayer coverage, the molybdenum surface species are arranged mostly as polymolibdates resembling mono-oxo two dimensional oligomeric chains of

distorted MoO_6 octahedral species, coexisting with a small fraction of MoO_4 tetrahedral monomolybdate species [66,138–140]. Only at very low loadings (≤ 1 wt.%), the monomolybdates as highly distorted isolated mono-oxo tetrahedral species dominate the surface [141]. The latter diminish as the metal content increases. It has been reported that even at loadings of 2 wt.% there are already mostly octahedral species [142]. Recently, it has been reported that on titania P25 and at monolayer coverage, the molybdena species are primarily oligomeric mono-oxo $O=Mo(–O–Ti)_{4/5}$ [140]. Excess of monolayer capacity results in bulk crystalline α-MoO_3.

Table I-2 shows the crystallite size of the crystalline MoO_3 in 15 MoTi and 25 MoTi samples calculated using the Scherrer equation [143]. A closer examination of the XRD diffraction pattern at the main crystalline plane (110) for the 8 MoTi sample revealed very small MoO_3 peaks, whose size could not be estimated with the Scherrer equation due to uncertainty attributed to its low intensity. The similar value of the crystallite size with no clear dependence of the metal content shows that the crystals in these samples have similar size, independent of the molybdenum loading, which has also been previously reported [144]. This indicates that the MoO_3 domain size remains constant at surface densities of 8 at. Mo nm^{-2} or higher, while smaller domains dominate the surface at lower Mo densities.

Table I-2. Calculated crystallite size using Scherrer equation of the crystalline MoO_3 on the supported catalysts for plane (111).

Sample	Size (nm)
8	-
15	18
25	21

Figure I-2 shows the H_2-TPR results of the supported MoO_3/TiO_2 catalysts. The profile for bulk MoO_3 is also presented for comparison. Molybdenum supported on titania catalysts present 2 to 4 reduction peaks [145–152], in line with our results. At low surface density (0.5 and 2.5 at. Mo nm^{-2}), two low-intensity peaks are observed at 350 °C and 550 °C, which have been assigned to the first reduction of octahedral and tetrahedral molybdenum structures, respectively [146,153,154]. The low intensity of the peaks is due to the low metal oxide content in these samples. Octahedral species are readily reduced at lower temperatures due to their weaker interaction with the support compared to the highly dispersed tetrahedral species [155]. At surface density of 8 at. Mo nm^{-2} the 550 °C peak disappears, in line with the transition from monomers of tetrahedral molybdenum to oligomers of octahedral species, as has been previously discussed. A third peak appears around 450 °C and the start of a fourth peak starts to appear at around 700 °C. These signals have been attributed to sequential reductions of crystalline MoO_3 or bulk MoO_3 [145]. At higher surface densities (15 and 25 at. Mo nm^{-2}) the octahedral MoO_3 species disappears completely, in line with the appearance

of crystalline MoO_3. The crystalline MoO_3 peak noticeably grows, becoming similar to the peak observed for bulk MoO_3. There is a clear distinction on the reduction peaks of supported catalysts starting at metal content higher than 2.5 at. Mo nm^{-2}, related to the emergence of crystalline MoO_3 as the Mo monolayer fills, evidenced by the disappearance of octahedral and tetrahedral species, in agreement with what was observed by XRD. When comparing with bulk MoO_3, the dispersion of MoO_3 on TiO_2 favors its reducibility, as the first peak of crystalline MoO_3 reduction shifts from 650 to 450-500 °C, demonstrating the effect of the titania support on the reducibility of the catalysts.

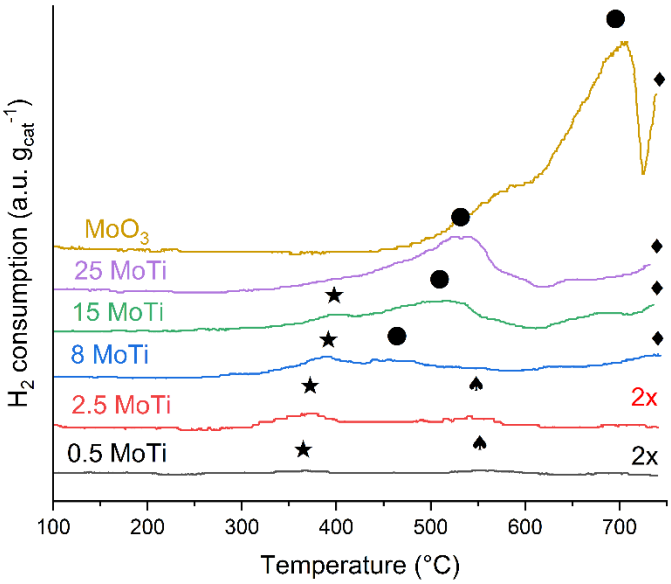

Figure I-2. H_2-temperature programmed reduction for all supported MoO_3/TiO_2 catalysts and bulk MoO_3. ●,♦: crystalline MoO_3, ♣: isolated tetrahedral MoO_3 species, ★: oligomeric octahedral MoO_3 species.

Table I-3 shows the H_2/Mo consumption ratio calculated from the H_2-TPR, as well as this ratio considering the total Mo reduction ($MoO_3 + 3H_2 \rightarrow Mo + 3H_2O$). It can be seen that as the MoO_3 content rises, the H_2/Mo ratio decreases. This indicates that crystalline MoO_3 is reduced in less proportion than the monomeric or polymeric MoO_3 phases at the evaluated temperature range, because H_2 access to the bulk Mo atoms is hindered at the well-ordered crystalline MoO_3 oxide structure. The total reduction of 0.5 MoTi was not quantified due to the low intensity of the reduction peaks caused by the low Mo content. Catalysts near the threshold of Mo monolayer formation (between 8 MoTi and 15 MoTi) present a H_2/3Mo ratio close to 1, as their Mo atoms are still accessible to the H_2 and can be fully reduced. At higher Mo surface density, the ratio starts to decrease, as the Mo atoms are not totally accessible to the H_2, and the catalysts behaves more similar to bulk MoO_3 at the studied experimental conditions.

Table I-3. Calculated H_2/Mo ratio and H_2/3Mo ratio for bulk and supported MoO_3 catalysts.

Sample	H_2/Mo	H_2/3Mo
0.5	-	-
2.5	3.7	1.2
8	3.6	1.2
15	2.4	0.8
25	2.0	0.7
Bulk	1.3	0.4

Figure I-3 shows the results of the XPS analysis, in particular the spectra of Mo 3d and O1s core level, respectively. It is observed that Mo $3d_{5/2}$ peak shifts from 231.7 to 232.4 as the Mo content increases. In literature, it has been reported that the peaks associated to Mo^{5+} and Mo^{6+} are presented at 230.8-231.6 eV and 232.2-232.8 eV, respectively [144,153,156–160]. Therefore, the observed shift is due to a change of the primary oxidation state of Mo from 5+ to 6+ as the molybdenum surface density increases. These observations are in line with reports from other authors, which indicated that the oxidation state of Mo supported on TiO_2 is usually a combination of Mo^{5+} and Mo^{6+} [153,158,161,162]. As the metal content increases and agglomeration state changes from tetrahedral/octahedral to crystalline MoO_3, surface defects and/or coordinatively unsaturated Mo^{5+} sites are transformed to the most ordered structure, as is the Mo^{6+} in MoO_3 bulk. O 1s spectra shows 3 different species of surface oxygen at 530 eV, 531.7 eV and 533.4 eV, which can be assigned to lattice oxygen in Mo-O bonds, adsorbed oxygen associated with surface defects and/or hydroxyls (O-H) or carbonyls (C=O) groups, and carbonates/chemisorbed water due to air exposition, respectively [144,161,163–165]. Contributions from Mo and Ti on the O1s spectra cannot be discerned, as they appear closely.

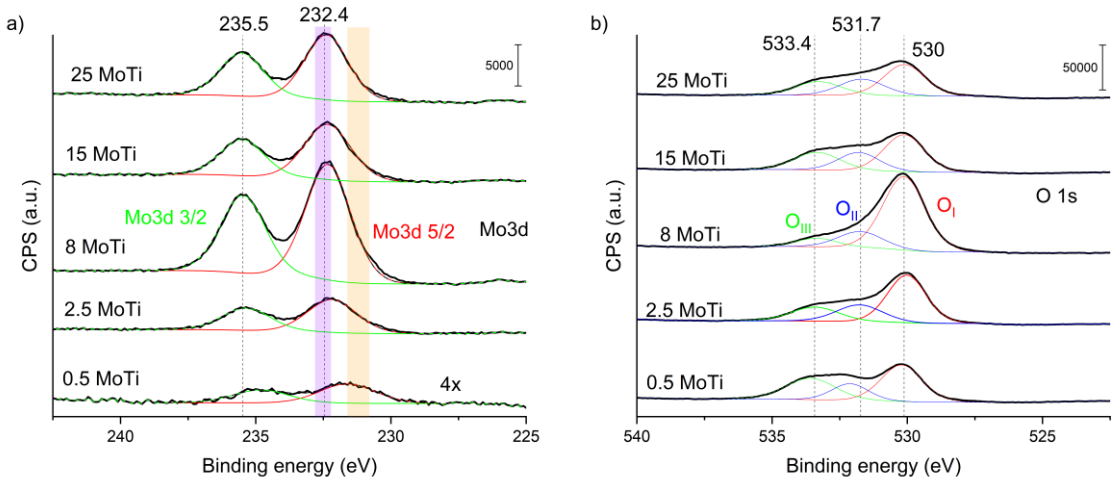

Figure I-3. X-ray photoelectron spectroscopy spectra of a) Mo 3d and b) O 1s core level of all supported MoTi samples.

Figure I-4 shows the Mo/Ti and (Mo+Ti)/O atomic surface ratio as a function of Mo surface density in the studied catalysts. It can be seen that the surface molybdenum/titanium fraction increases as the metal content rises, in line with the gradual coverage of titania surface with molybdenum deposition. Surface Mo atoms per surface titanium reaches a plateau at 8 at. Mo nm^{-2}, in line with the formation of crystalline MoO_3 as the metal oxide content rises. The surface (Mo+Ti)/O ratio remains mostly constant from the 2.5 MoTi sample onwards, due to the predominance of a well ordered crystalline MoO_3 structure, as observed Figure I-3.

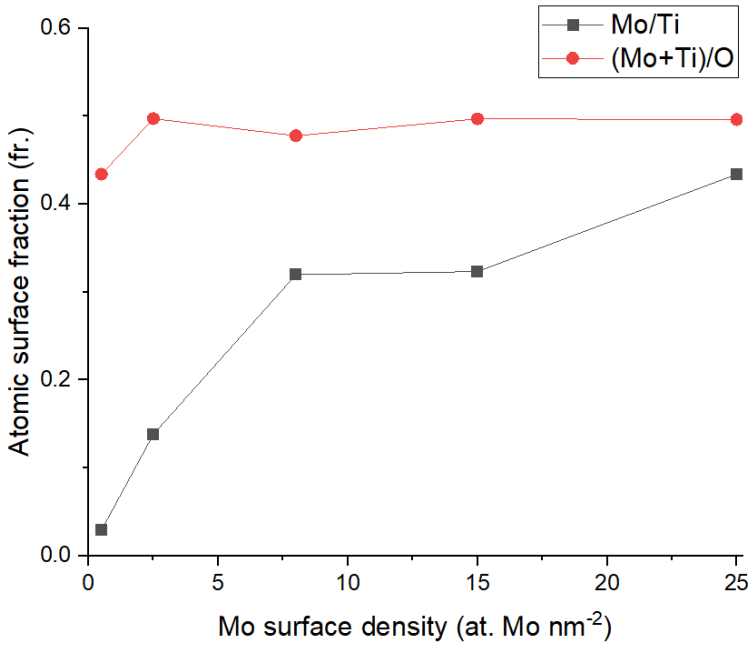

Figure I-4. Surface fraction atoms of Mo 3d and O 1s, measured by XPS, of all TiO_2-supported Mo samples.

Figure I-5 shows the low-temperature CO adsorption at a CO pressure of 0.4-0.7 mbar. The spectra were normalized by Mo content to ensure proper comparison between catalysts with varying Mo content, assuming that the IR signal intensity is proportional to the amount of adsorbed species. All the MoTi samples have the same band at 2191 cm^{-1}, attributed to the ν(C-O) stretching mode of carbonyls adsorbed on Mo^{5+} species [166]. At low pressure this band appears at 2196 cm^{-1} and gradually shifts to 2191 cm^{-1} as the CO pressure increases [166] (Figure I-6). The intensity of this band decreases as the metal oxide content increases, in line with the formation of crystalline MoO_3 and the predominance of Mo^{6+} species related to the bulk oxide, as previously observed by XPS. The presence of Mo^{6+} cannot be confirmed by low-temperature CO adsorption, as Mo^{6+} does not form carbonyls complexes when interacting with CO in oxidized MoO_3 bulk [167,168]. Nevertheless, the significant difference between 2.5 and the 8-15 MoTi samples evidences the sub-monolayer behavior of the lowest content sample, as the Mo^{5+} species are clearly identified.

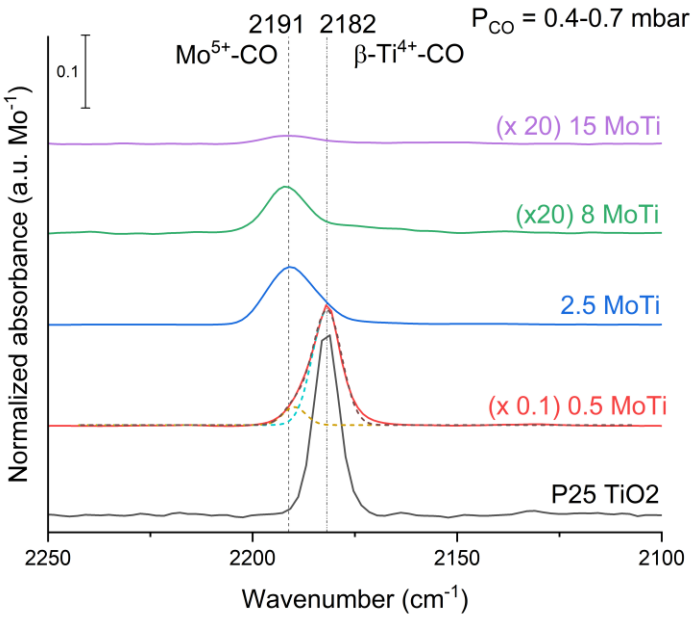

Figure I-5. IR spectra for low-temperature CO adsorption (0.4-0.7 mbar) on TiO_2 and supported 0.5, 2.5, 8 and 15 MoTi samples (normalized per Mo content).

The 0.5 MoTi sample presents an intense band at 2182 cm^{-1}, which could be assigned to CO adsorbed on Mo^{4+} or on Ti^{4+} of the TiO_2 support due to the low metal content of this sample [167,169]. The deconvolution of this band reveals a small contribution from Mo^{5+} band and alongside the band at 2182 cm^{-1}. This latter band is also observed on P25 TiO_2, which allows us to assign it to the coordinatively unsaturated β-Ti^{4+}-CO bond on a Lewis acid site [170] . Although the β-Ti^{4+}-CO band at 2182 cm^{-1} can be found both on anatase and rutile phases of TiO_2, [171], due to the P25 composition and previous characterizations, we attribute this band to anatase. The similarities between the titania and the 0.5 MoTi sample are also observed at higher CO pressures Figure I-6. Both samples have the same band at 2210 cm^{-1},

which belongs to α-Ti^{4+}-CO, further indicating that on the 0.5 MoTi catalyst CO is primarily interacting with the titania, due to the low Mo content on this sample.

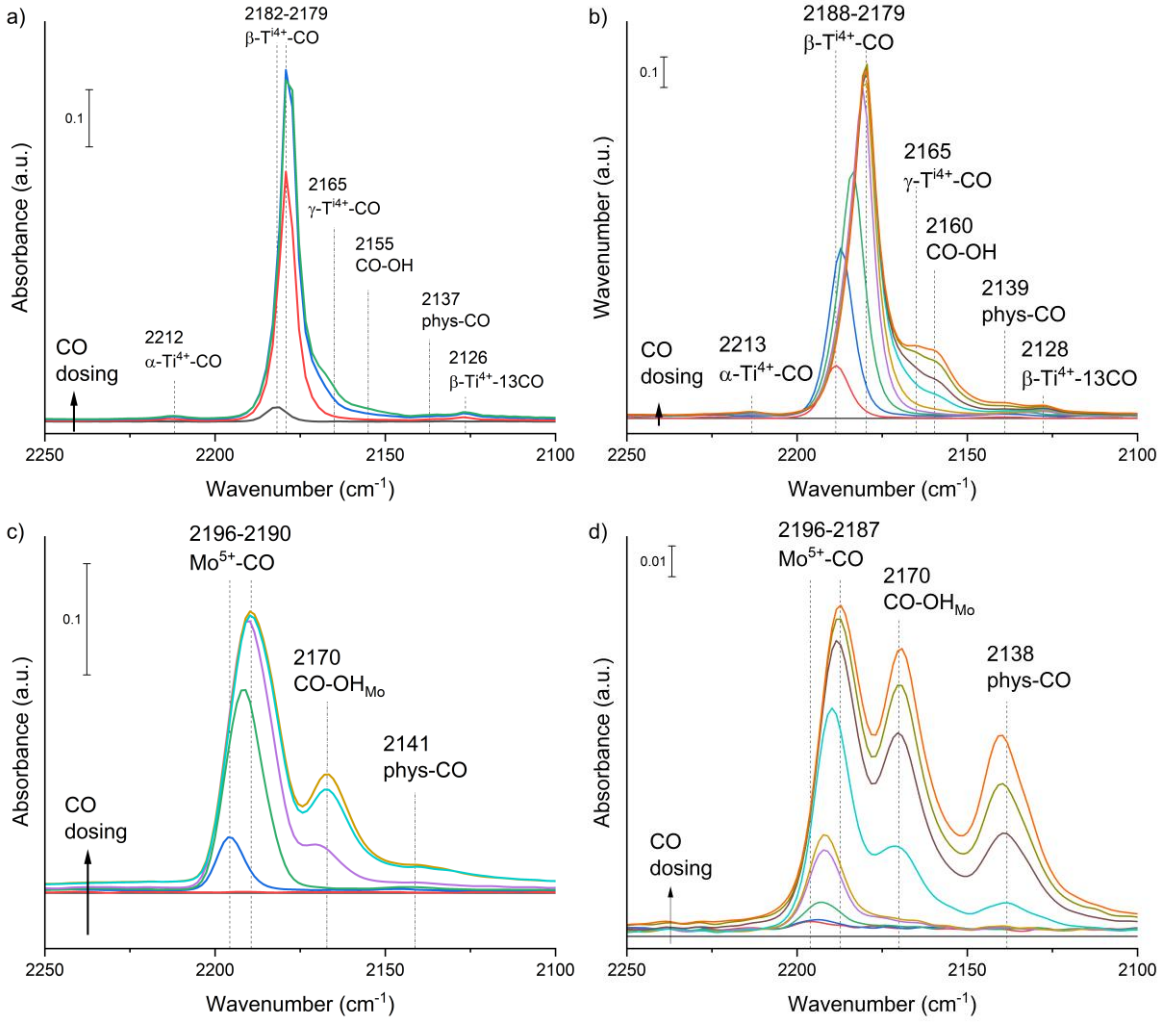

Figure I-6. FTIR spectra of CO adsorbed at low temperature at increasing CO dosing on a) P25 TiO_2, b) 0.5 MoTi, c) 2.5 MoTi and d) 8 MoTi.

Figure I-7 shows the IR spectra for low-temperature CO adsorption at low CO pressures (0-0.1 mbar) for the supported molybdenum catalysts. In accordance with Figure I-5, the decrease in the intensity of the Mo^{5+}-CO band as the molybdenum content rises from 0.5 to 15 at. Mo nm^{-2} is related with the increase in the concentration of Mo^{6+} oxidation state of the supported samples. This is consistent with the structural change from tetrahedral/octahedral dispersed species to crystalline MoO_3 as the molybdenum content increases and the monolayer coverage of the TiO_2 surface is achieved, as observed by XPS. Considering the H_2-TPR results, the 2.5 MoTi sample should be the superior redox catalyst due to the gradual absence of molybdenum oxide species with Mo^{5+} oxidation state in favor of readily reducible

Mo^{6+}, while still retaining interfacial Mo-O-Ti sites that enhance redox properties through the interaction with titania, thanks to its oligomeric sub-monolayer molybdenum structure.

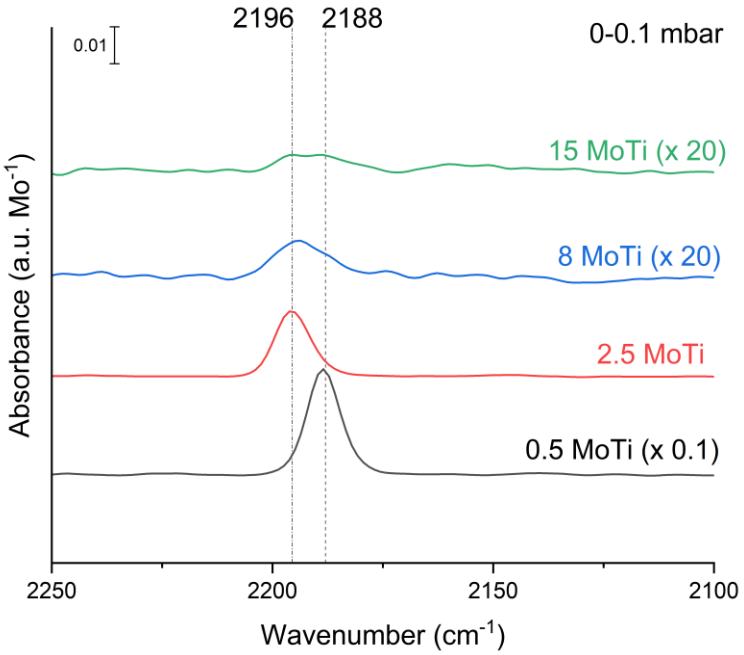

Figure I-7. FTIR spectra of CO adsorption at low temperature (0–0.1 mbar), normalized by Mo content, for 0.5, 2.5, 8, and 15 MoTi samples.

Figure I-8 shows the OH stretching region ν(OH) after low-temperature CO adsorption. The formation of hydrogen-bonded OH-CO species is evidenced by the red shift of the OH frequency, characteristic of surface hydroxyl groups. The 2.5 MoTi, 8 MoTi and 15 MoTi samples behave similarly, likely by the effect of Mo deposition, while 0.5 MoTi behaves differently, as it has a low Mo oxide dispersion. P25 TiO_2 presents two types of surface hydroxyl groups, which are characteristic of the stretching mode of anatase Ti^{4+}-OH [170]. The ν(OH) shift, due to the low temperature CO adsorption, gives information of protonic acid strength of the surface OH groups (Brønsted and/or Lewis sites), because CO is a weak base [167]. 0.5 MoTi has a shift of 140 cm^{-1}, while the higher content samples have a shift of 186 cm^{-1}. The latter has stronger acidic surface hydroxyl groups, due to the higher Mo loading. P25 TiO_2 presents higher acidity compared to supported molybdenum oxide OH groups, related to the Lewis characteristic of TiO_2 [167].

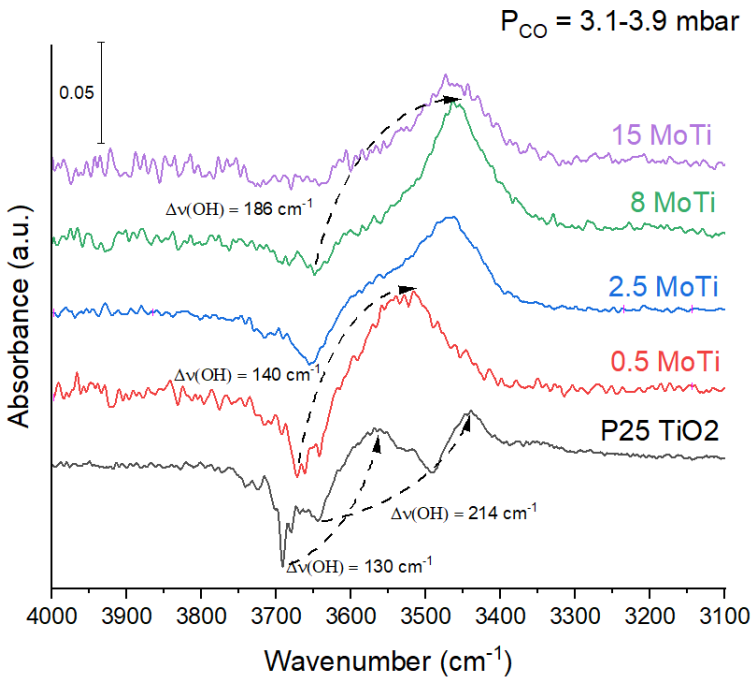

Figure I-8. Infrared signals shift in the OH stretching region for the low-temperature CO adsorption (3.1-3.9 CO mbar) on TiO_2 and supported 0.5, 2.5, 8 and 15 MoTi samples.

Figure I-9 a) and Figure I-9 b) show the results of the temperature programmed desorption of NH_3 for 0.5, 2.5, and 8 MoTi, as well as P25 TiO_2. The quantity of total acid sites, given by total ammonia uptake, diminishes as Mo content increases, in line with the coverage of the titania Lewis acid sites as the molybdenum monolayer is formed. Figure I-9 b) shows that the medium strength acid sites decrease with molybdenum oxide incorporation, while the number of weak sites also decreases. In general, total sites diminish after the monolayer formation of crystalline MoO_3 oxide between 2.5 and 8 at. Mo nm^{-2}. These results are in line with what has been previously reported for MoO_3/TiO_2 catalysts [172].

Figure I-9 c) and Figure I-9 d) show the results of FTIR of adsorbed pyridine at 150°C. The spectrum displays bands characteristic of pyridine adsorbed on Lewis acid sites (1445 cm^{-1}) and a broad band of pyridine adsorbed on Brønsted acid sites (1544 cm^{-1}). The P25 TiO_2, 2.5 and 15 MoTi samples present primarily Lewis acidity with a minimal contribution from MoO_3 Brønsted acidity. Figure I-9 d) shows that Lewis acidity diminishes as the metal content rises, in line with MoO_3 deposition and coverage of available titania. Our samples have a lower B/L ratio than those reported for MoO_3/TiO_2 catalysts [161]. We attribute this to our preparation method, which uses oxalic acid in the impregnation solution to obtain better MoO_3 oxide dispersion [173], as the Brønsted acidity of MoO_3 oxide is related to its crystalline phase.

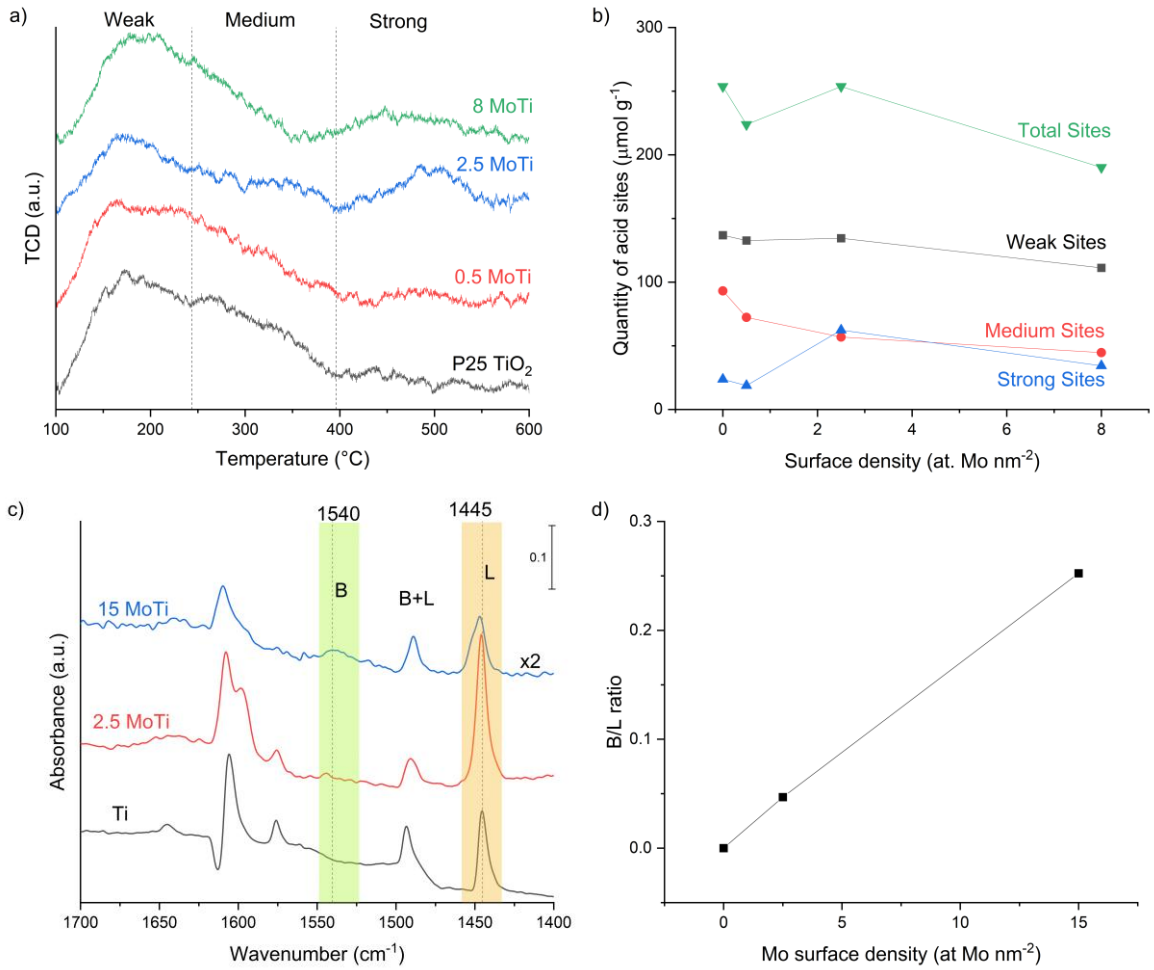

Figure I-9. a) NH_3 TPD for P25 TiO_2, and 0.5, 2.5 and 8 MoTi. b) Ammonium uptake as a function of molybdenum loading. c) Adsorbed pyridine FTIR spectra of P25 TiO_2, 2.5 MoTi and 15 MoTi (B: Brønsted, L: Lewis), d) B/L ratio as a function of Mo surface density.

Figure I-10 a) and Figure I-10 b) shows in-situ Raman spectra for samples 2.5 and 15 MoTi, respectively under ambient and reaction conditions. Only frequencies higher than 700 cm^{-1} are shown due to the strong Raman response of TiO_2 at lower wavenumbers. The Raman spectra were normalized by the anatase TiO_2 crystalline support bands at 640, 520 and 399 cm^{-1} [66]. The conformation of supported molybdates depends on the conditions at which the experiment is performed. On non-dehydrated samples, the structures formed behave like tetrahedral and isolated species (MoO_4^{2-}) and polymolybdate species ($Mo_7O_{24}^{6-}$), as the ones observed in aqueous solutions [141,174]. For the 2.5 MoTi sample, two broad peaks are observed at wavenumbers 796 cm^{-1} and 970 cm^{-1}. The 970 cm^{-1} Raman band corresponds to the stretching mode of the terminal Mo=O bond, characteristic of octahedral surface species, while the 796 cm^{-1} peak is assigned to the overtone of the 395 cm^{-1} band of anatase TiO_2, evidencing the sub-monolayer Mo coverage on this sample. The latter is further supported by the absence of sharp Raman bands at 817 and 994 cm^{-1}, characteristic of crystalline MoO_3 [65,80,141,175,176]. No bands attributed to tetrahedral species were detected (932, 883 cm^{-}

[1]) [141,177]. During in-situ Raman methanol oxidation on the 2.5 MoTi sample (Figure I-10 a)), the terminal Mo=O bond stretching mode band becomes slightly sharper and decreases in intensity, indicating a modest reduction of the surface molybdenum species during the reaction. No significant changes in the Raman spectra due to CH_3OH adsorption were observed. Additionally, the reaction temperature had a negligible effect on the structure of the surface molybdenum oxide. This suggests that, under the studied reaction conditions, neither CH_3OH adsorption nor the extent of Mo oxide reduction is significantly influenced by temperature on the sub-monolayer catalyst. As discussed before, the presence of crystalline MoO_3 is confirmed by the sharp bands at 817 and 994 cm^{-1} [138,140,158,177] in Figure I-10 b), consistent with the crystalline MoO_3 observed by XRD in this catalyst. The Raman band at 994 cm^{-1} corresponds to the terminal Mo-O bond of the crystalline MoO_3 oxide, while 820 cm^{-1} band is attributed to Mo-O-Mo bonds within the crystalline framework [178,179]. In the 15 MoTi sample, as was observed in the 2.5 MoTi sample, no significant changes in the crystalline bands were observed between ambient conditions and methanol oxidation reaction at 100°C, ruling out an effect of the CH_3OH adsorption on the crystalline structure of MoO_3. However, an increase in the intensity of the Raman bands attributed to crystalline MoO_3 was observed at 150 and 200 °C, suggesting agglomeration of surface oxide species into crystalline MoO_3 during reaction conditions at higher temperatures.

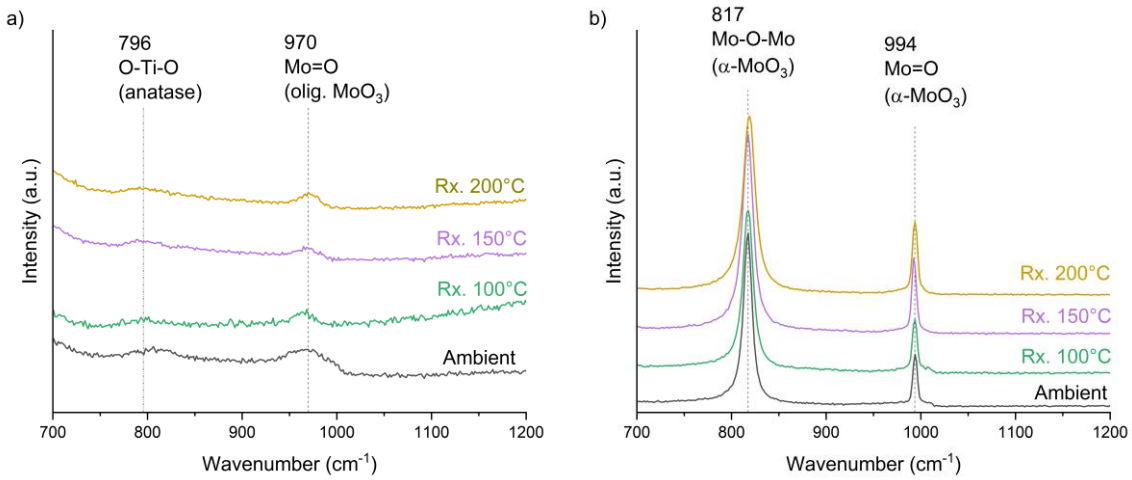

Figure I-10. In-situ Raman spectra at ambient and reaction conditions for a) 2.5 and b) 15 MoTi samples.

The lack of a strong effect of the reduction of the surface molybdenum oxide species under reaction conditions on the MoO_3 bands is consistent with the rapid reoxidation of the surface during a Mars-van Krevelen redox cycle. It is also noteworthy that in-situ measurements exhibit similar Raman spectra to those under ambient conditions, even when accounting for the high-temperature oxidation pretreatment to which the samples were subjected. It must be noted that Mo oxide species in the 8 MoTi and 15 MoTi sample are not entirely crystalline, as the presence of oligomeric species was also detected by Raman spectroscopy at certain points on the surface (Figure I-11). Therefore, the 15 MoTi sample should be a mostly

crystalline structure with a slight presence of octahedral structures yet to form crystalline MoO_3 above monolayer coverage. It is to be expected that at higher loadings, these octahedral species will fully disappear due to the formation of crystalline MoO_3. The in-situ Raman spectra of sample 8 MoTi is shown in Figure I-12.

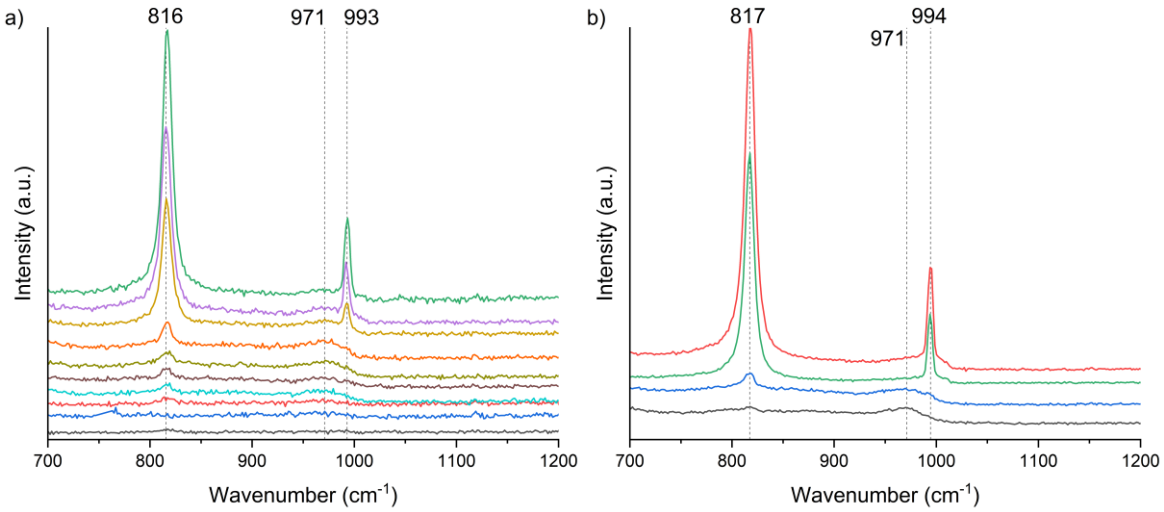

Figure I-11. In-situ Raman spectra at different spots on the catalyst surface at ambient conditions, for: a) 8 MoTi and b) 15 MoTi samples.

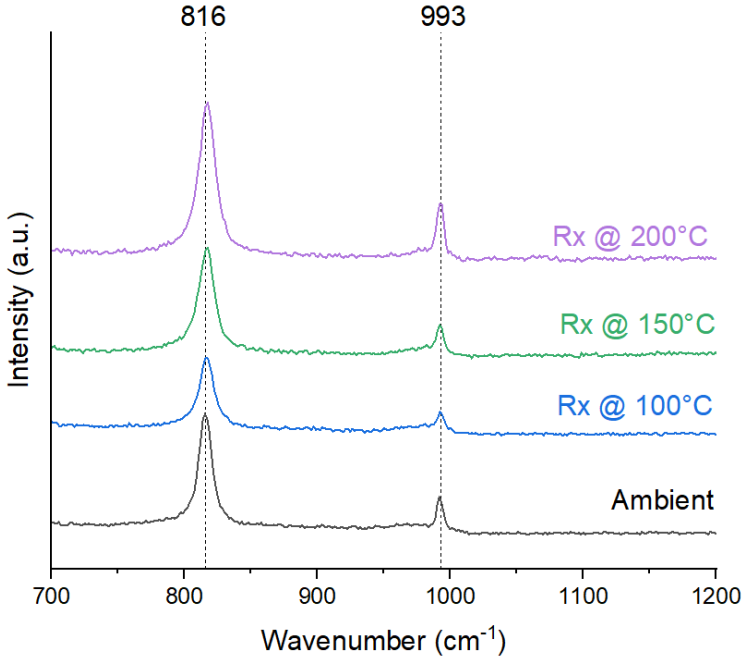

Figure I-12. In-situ Raman spectra at ambient and reaction conditions for 8 MoTi sample.

Figure I-13 a) and Figure I-13 b) show the evolutions of the normalized Raman spectra with increasing Mo surface density, under ambient conditions and during CH_3OH oxidation at 150

°C, respectively. The differences between the sub-monolayer and crystalline MoO_3 catalysts are evident. The 8 MoTi and 15 MoTi samples present the same sharp bands characteristic of crystalline MoO_3 structures, while the 2.5 MoTi sample has broad and weak bands related to oligomeric MoO_3 species. The extent of crystallization is also noticeable, with 8 MoTi sample presenting significantly lower intensity bands compared to the 15 MoTi sample. These results are consistent with the previously discussed characterizations (XRD, H_2-TPR, XPS, low temperature CO FTIR, pyridine FTIR, and NH_3-TPD) evidencing the structural changes occurring as the molybdenum surface density increases and exceeds monolayer coverage.

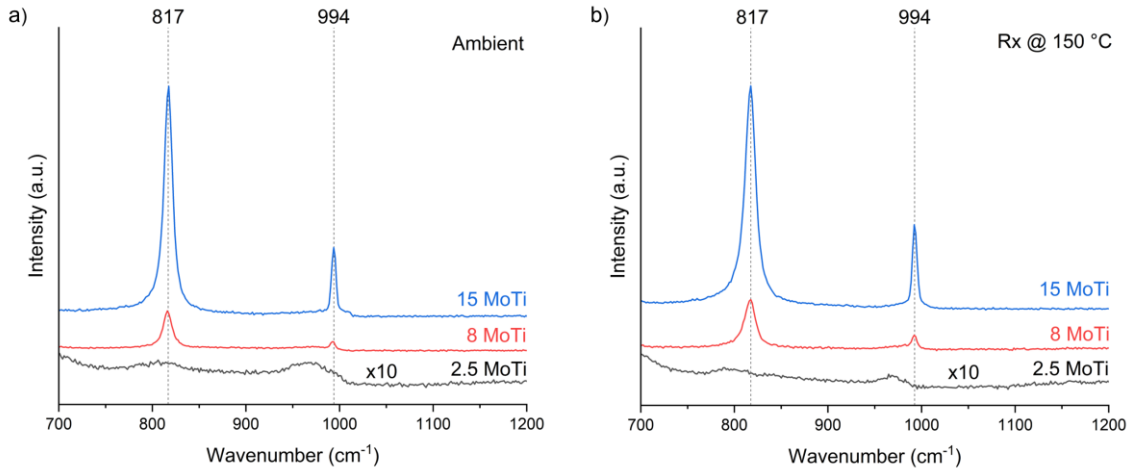

Figure I-13. In-situ Raman spectra as a function of metal content at a) ambient conditions and b) methanol ODH reaction at 150 °C.

Figure I-14 shows the in-situ full Raman spectra with increasing Mo content, normalized by the titania bands at lower frequencies. All catalysts present bands attributed to crystalline anatase TiO_2 at 144, 195, 394, 513, and 634 cm^{-1}. The bands at 144, 195 and 634 cm^{-1} corresponds to the symmetric stretching vibrations of O-Ti-O, while the 399 cm^{-1} band is attributed to the symmetric bending vibration of O-Ti-O, and the 515 cm^{-1} band to the anti-symmetric bending vibration of O-Ti-O. [180] It can be seen that under the same conditions these bands remain stable across all samples, not significantly altered and retaining intensity and full width at half maximum (FWHM) values. No clear Raman bands associated with the rutile phase of P25 (143, 235, 447 and 612 cm^{-1}) were observed, in accordance with the reported TiO_2 composition of approximately 85% of anatase. The rutile bands are likely occluded or superimposed by the intense anatase bands [180–182]

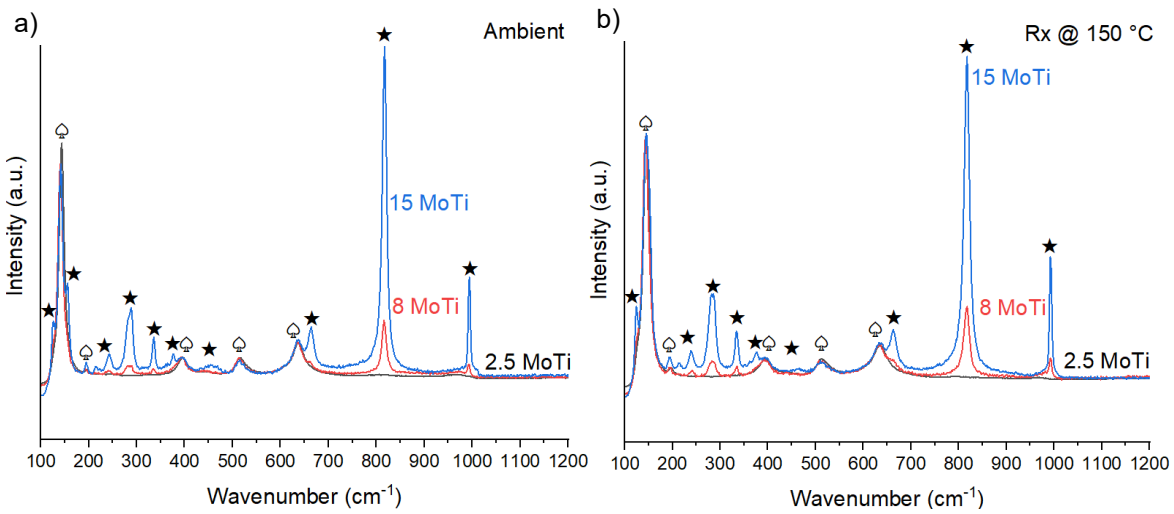

Figure I-14. Full-range in-situ Raman spectra as a function of metal content at a) ambient conditions and b) methanol ODH reaction at 150 °C. ★: α-MoO3, ♤: anatase TiO_2.

When increasing metal loading, some bands attributed to crystalline MoO_3 appear in the lower frequency zone. The 666 cm^{-1} band corresponds to the Mo-O-Mo bonds in the crystalline framework, while all bands at 400 and below belong to the angle-deformation vibrations of α-MoO_3 [178,179].

4. Conclusions

MoO_3/TiO_2 supported samples with increasing Mo content were synthetized and characterized, highlighting the structural evolution of the molybdenum oxide phase. At low Mo content, molybdenum exists as dispersed octahedral oligomeric Mo oxide species, in close interaction with the TiO_2 support. These dispersed species are associated with a sub-monolayer structure. As the Mo content increases beyond the monolayer threshold, the MoO_3 oxide structure transitions to crystalline domains. This structural change is accompanied by a shift from coordinatively unsaturated surface Mo^{5+} species in the dispersed phase to the Mo^{6+} of the fully oxidized crystalline phase, as the monolayer coverage of the TiO_2 surface is reached.

Characterization through in-situ Raman spectroscopy, XPS, low temperature CO FTIR and H_2-TPR revealed that this structural evolution directly impacts the redox properties of the catalysts. The near-monolayer oligomeric octahedral Mo oxide phase exhibits higher reducibility due to the influence of the TiO_2 support and the presence of reducible Mo^{6+}. Acidity of the supported MoO_3 samples, as observed by NH_3-TPD and pyridine adsorption, decreases due to the loss of titania Lewis acid sites caused by molybdenum deposition and the lack of strong Brønsted acidity in the molybdenum oxide.

This work highlights the structural evolution of molybdenum oxide from dispersed oligomeric species to crystalline MoO_3 and the implications of this transition for the redox and acid properties of the supported catalysts.

Chapter II: Operando-FTIR study of methanol partial oxidation over MoO_3/TiO_2 catalysts

Summary

Methanol oxidative dehydrogenation was studied on sub-monolayer and crystalline MoO_3/TiO_2-supported catalysts using operando-FTIR spectroscopy. Results revealed two distinct methyl formate (MF) formation pathways, determined by the molybdenum oxide structure. Quantitative and qualitative evidence indicated that MF and dimethoxymethane (DMM) formation occur via distinct reaction intermediates. MF formation is linked to surface formate consumption, supported by the similarity between steady-state MF formation rate measured in a fixed-bed reactor and transient initial formate consumption rate determined by operando-FTIR. Apparent activation energies for HCOO* consumption (90 and 88 kJ mol^{-1}) and MF formation (83 and 51 kJ mol^{-1}) for 2.5 and 15 at. Mo nm^{-2} samples, respectively, indicate that the formation pathway depends on the molybdenum oxide structure. Oligomeric, octahedral molybdenum oxide catalysts produce MF via adsorbed formate consumption, while crystalline MoO_3 catalysts enable a parallel pathway, likely involving hemiacetal intermediates. This change in reaction pathway correlates with the structural transition from oligomeric to crystalline molybdenum oxide, as characterized by XRD, in situ Raman spectroscopy, FTIR of low-temperature CO adsorption, and XPS, among other techniques. The increase of surface formate consumption is related to the enhancement of the redox properties of the catalyst, attributed to interactions of molybdenum oxide with titania support and the presence of readily reducible Mo^{6+} sites that influence adsorbed formaldehyde reaction pathways. The observed activity and selectivity are explained by a three-active-site mechanism: molybdenum oxide redox sites for methanol dehydrogenation, molybdenum oxide acid sites for hemiacetal and DMM formation, and molybdenum-titania interfacial sites for HCOO* and MF formation.

1. Introduction

Molybdenum-supported catalysts have been widely used for methanol ODH [62–82]. Independent of the material, it is known that the methanol oxidation follows a Mars-van Krevelen redox mechanism, with the dehydrogenation of a methanol molecule on a lattice oxygen active site to produce adsorbed formaldehyde as the rate-determining step (rds) [69,72,83–85]. The adsorbed FA can desorb or keep reacting to form MF and/or DMM. Nevertheless, there is little agreement about the reaction mechanism or the reaction intermediates of these latter reaction products, since multiple reaction intermediates and/or mechanisms have been proposed for this reaction.

In earlier works, Wachs and Madix proposed MF formation by dehydrogenation of a surface hemiacetal alcoholate intermediate (CH_3OCH_2O*), formed by FA acetalization with nucleophilic methoxides on Ag(110) single crystal, using temperature programmed reaction spectroscopy with isotopically labelled species. [86]. Later, Sambeth et al., studying the reaction on V_2O_5 samples by mass spectroscopy varying temperature and contact time,

proposed that the same hemimethylal (CH_3OCH_2OH) intermediate can be oxidized to form MF, but can also condense with another methanol molecule to form DMM [87]. Next, Tatibouët performed transient isotopic studies exchanging between CH_3OH and CD_3OD and observed that hemimethylal (CH_3OCH_2OH) intermediate participated in the DMM formation, on unsupported V_2O_5 catalysts [92]. Iglesia and Liu also proposed the hemiacetal intermediate for MF and DMM formation, now called methoxymethanol, on supported-RuO2 oxides samples by studying the effect of different supports, the kinetic effect of CH_3OH and O_2 feed concentration, and observed kinetic isotopic and residence time effects [88,89]. This mechanism has been confirmed by DFT calculations as the pathway with the lower energy barrier on V_2O_5/TiO_2 [90,91]. A schematic representation of the hemiacetal reaction pathway is shown on Figure II-1.

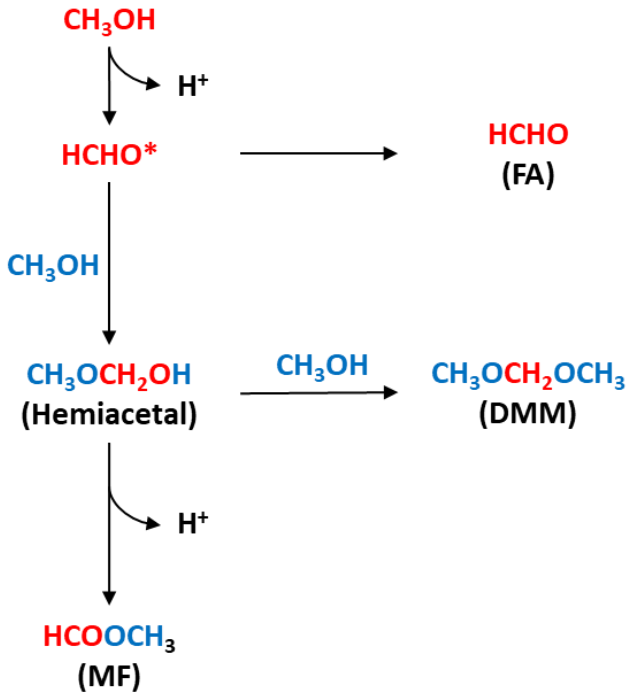

Figure II-1. Mechanism of methanol ODH reaction through the hemiacetal pathway.

Mamoru Ai (1982) proposed the Tishchenko reaction, or formaldehyde dimerization, for MF formation on SnO_2-MoO_3 catalysts [94] and on 60 mixed oxides [95], by studying the effect of reaction variables, reactant concentration and HCHO addition to the feed.

Cairati and Trifiro (1983) proposed MF formation by formic acid/surface formates on SiO_2 and Al_2O_3 catalysts [93]. Afterwards, Busca et al., by FT-IR spectroscopy and variation of temperature, contact time and feed ratios, proposed a complete mechanism on V_2O_5/TiO_2 samples involving a dioxymethylene (H_2COO) – formate (HCOO) pathway, where the first intermediate forms DMM in a reaction with methanol and the second one reacts with methanol to form MF [50]. More recently, Kaichev et al. clarified the above-mentioned mechanism on V_2O_5/TiO_2 catalysts using in-situ surface sensitive techniques like NAP XPS

and XANES, with FTIR, TPR, and kinetics measurements. The use of in-situ characterization techniques allowed them to introduce the chemical state of the vanadium in the reaction mechanism [42]. FTIR techniques have not been able to identify adsorbed hemiacetal as an intermediate species because of its unfavorable equilibrium and high reactivity [88]. A schematic representation of the formate/dioxymethylene reaction pathway is shown on Figure II-2.

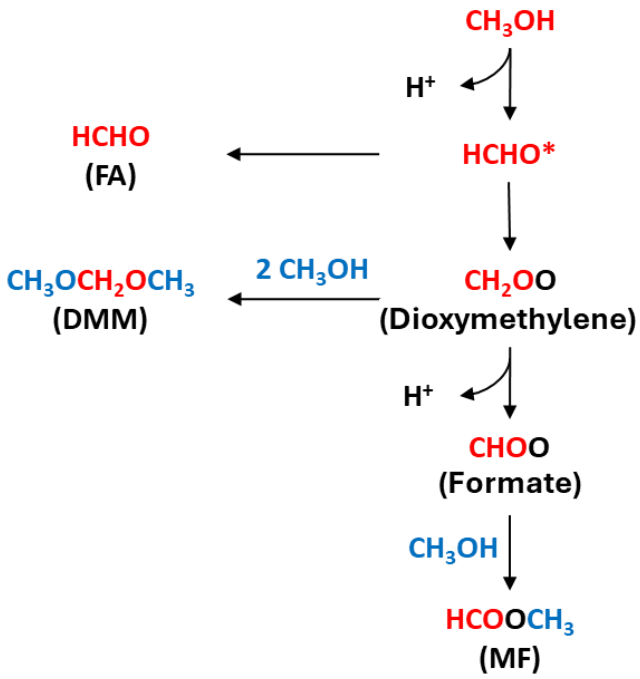

Figure II-2. Mechanism of methanol ODH reaction through the formate/dioxymethylene pathway.

More recently, Chin et al. [48] studied the methanol ODH reaction on V_2O_5/TiO_2, by analyzing different reaction conditions and addition of products to the feed, isotopic HCHO-DCDO exchange, and spectroscopic UV-vis studies.. They suggested that the DMM forms via methanol and hemiformal/hemiacetal, meanwhile, the MF forms via Tishchenko reaction from FA molecules on exposed titania.These different pathways for the MF and DMM formation is a consequence of the VO_x domain size: on highly dispersed, monomeric VO_x, as in the study by Chin et al., MF would follow the Tishchenko reaction on the Lewis sites of the titania, while on crystalline VO_x catalysts, MF would be formed by the hemiacetal route, as the titania active sites are fully covered by VO_x.

It is clear to see that even for the same active metal-support pairs, three mechanisms for MF and DMM formation have been proposed for the methanol ODH reaction: hemiacetal/hemiformal/hemimethylal intermediate, formate-dioximethylene mechanism and Tishchenko reaction. There is a current wave of moving from ex-situ characterizations or techniques to in-situ or operando studies in catalytic reactions [183–187]. In-situ and

operando characterizations allow us to study the catalyst during the reaction, as it may undergo structural changes by the reactants and/or products atmosphere. By using this approach, we can identify the real active sites and explore in real time how the materials and the intermediates behave, aiming to elucidate the catalytic reaction mechanism. Nevertheless, there is still a lack of proper operando studies for the methanol ODH reaction, a methodology that, to the best of our knowledge, has not been applied to this reaction before.

In light of the above presented arguments, this work focuses on operando-FTIR studies aimed to study the nature and dynamic behavior of the reactive adsorbed species during the methanol ODH reaction on MoO_3/TiO_2 catalyst. The study highlights clear differences in molybdenum oxide structure, as revealed by the extensive characterization to which the catalysts were subjected. Focusing on samples with octahedral and crystalline molybdenum oxide structure, the correlation of the adsorbed species with the reaction products was studied, in order to elucidate the reaction mechanism to form FA, MF and DMM. It was found that sub-monolayer, octahedral oligomeric Mo catalysts produce MF via a redox HCOO* pathway involving interfacial Mo-O-Ti sites, while on high loading, crystalline MoO_3 catalysts, MF formation proceeds through a hemiacetal pathway on redox metal sites besides the interfacial surface formate pathway. Our findings indicate that ODH activity is regulated by three active sites—redox metal sites, acid metal sites, and redox interfacial sites—whose proportions vary with Mo content and oxide structure; their surface distribution changes with catalyst composition and controls the selectivity between MF, FA, and DMM.

2. Experimental

2.1 Catalytic activity measurements

The kinetic tests of the MoO_3/TiO_2 catalysts were performed in a stainless-steel tubular fixed-bed reactor (length 60 cm, internal diameter 0.78 cm). A catalyst bed composed of catalyst sample (0.2 g, 150–380 μm particle size) and mixed-in quartz sand (2 g, 150–380 μm particle size) was prepared to avoid hot spots in the reactor. About 0.76 cm of the resulting bed was placed in the center of the reactor held down by quartz wool, while the reactor was placed inside an electric oven with the catalytic bed well inside the isothermal section of the oven.

Before the reaction, the catalyst was pretreated in air flow (21 % vol O_2/N_2, 20 ml min^{-1}) at 300 °C for 30 min at a heating rate of 10 °C min^{-1} to completely oxidize the surface. In a typical experiment, the temperature was adjusted to the desired value, the O_2/CH_3OH molar ratio was set to 9:4 (P_{CH3OH} = 4 kPa, P_{O2} = 9 kPa, P_{N2} = 87 kPa) and a total flow of 50 ml min^{-1} of the gas mixture was conducted through the catalytic bed. CH_3OH (Merck-Millipore) was fed to the reactor using a PTFE saturator submerged in a thermostatic bath at 25 °C, using N_2 (13 ml min^{-1}) as the bubbling gas. The N_2 (Airliquide 99.999%) and dry air (Airliquide 99.999%) flows were controlled by mass flow controllers (Kofloc 8500). The concentration of reagents and reaction products were monitored in real-time using a SRI 8610C gas chromatograph, equipped with a packed precolumn (SRI Hayesep D 18'', 5 m) and three separation columns: a packed column (Hayesep D 6'', 2 m) and two capillary columns

(MS5A, 1 m; MXT-WAX, 30 m). The GC is also equipped with an on-stream methanizer with Ni catalyst, a flame ionization detector (FID) and a thermal conductivity detector (TCD). Besides the fed CH_3OH y O_2, Only HCHO, MF, DMM, CO y CO_2 were detected. Methanol and reaction product lines were held at 100 °C to prevent condensation. To obtain steady state kinetic data, each reaction condition was maintained for 3 h, with 7-8 measurements per condition. The mean concentration of each reactant and reaction product at steady stated was calculated. An example of methanol concentration versus time on stream is shown in Figure A-II.1 of Appendix: Chapter II.

The effect of the temperature (100-300 °C) and residence time, by varying total flow rate (21-85 ml min^{-1}, constant length/mass of catalyst bed) was studied. Integral reactor conditions was used to achieve the conversion values (> 10 %) necessary to accurately measure the concentration of the 3 reaction products (FA, MF and DMM). Deactivation of the catalyst was discarded by repeating the first reaction condition at the end of the experiments, observing the same activity.

CH_3OH conversion (X_{CH3OH}) and FA, MF and DMM yields (Y_i) were calculated according to equations 1 to 4.

$$X_{CH3OH} = \frac{CH_3OH_{IN} - CH_3OH_{OUT}}{CH_3OH_{IN}} \times 100 \quad (1)$$

$$Y_{FA} = \frac{FA_{OUT}}{CH_3OH_{IN}} \times 100 \quad (2)$$

$$Y_{MF} = \frac{2\ MF_{OUT}}{CH_3OH_{IN}} \times 100 \quad (3)$$

$$Y_{DMM} = \frac{3\ DMM_{OUT}}{CH_3OH_{IN}} \times 100 \quad (4)$$

Where IN and OUT subscripts denote the inlet and outlet molar flow rate for each reactant and product, respectively.

2.2 Operando-FTIR measurements

FTIR measurements were performed on a Nicolet iS-10 spectrometer (Thermo Scientific), equipped with KBr windows, high temperature, reactor-cell (Harrick). MoTi catalysts and TiO_2 wafers (0.04 g) were placed into the IR cell, in-situ pretreated in air flow (30 ml/min, 300 °C) and then cooled down to reaction temperature (100, 150, 175, 200 and 250 °C). The cell and wafer temperature were measured and controlled with a temperature controller (Omega Instruments) equipped with two K-type thermocouples. Gases were fed to the reactor using mass flow controllers (Kofloc 8500, Kojima Instruments). Argon was used as internal standard for quantification. Infrared spectra were continuously recorded in absorbance mode, at a resolution of 4 cm^{-1} and 32 scans per spectrum, in the 3500-1200 cm^{-1} range. The respective background spectrum at the corresponding temperature and reactant atmosphere was subtracted.

The relative concentration of chemical compounds at the cell reactor outlet was monitored with a quadrupole mass spectrometer (Omnistar GSD 320), analyzing the evolution of m/z signals 60 (MF), 75 (DMM) and 40 (Ar). CH_3OH (31) and FA (30) were mathematically quantified by subtracting the contributions of MF and DMM to the m/z = 30 and m/z = 31 fragments, due to their significant contributions.

In a typical experiment, after pretreatment, 50 ml min^{-1} of a gaseous mixture of Ar, O_2, CH_3OH and N_2 (P_{CH3OH} = 1 kPa, P_{O2} = 10 kPa, P_{Ar} = 10, P_{N2} = 79 kPa) was fed to the reactor, as standard reaction condition. After the steady state was reached as observed in the MS, CH_3OH was removed from the feed maintaining the same total flow (P_{O2} = 10 kPa, P_{Ar} = 10, P_{N2} = 80 kPa). Then, O_2 was replaced by N_2 and CH_3OH was added back to the feed, to saturate the surface with methoxy species (P_{CH3OH} = 1 kPa, P_{Ar} = 10, P_{N2} = 89 kPa). At the end, CH_3OH was once again removed from the feed and, after a N_2 purge, replaced by O_2 to oxidize the surface species (P_{O2} = 10 kPa, P_{Ar} = 10, P_{N2} = 80 kPa). Each reaction condition was maintained for 30 min, to reach the new steady state. All transfer lines were held at 100 °C to prevent condensation of reactants and products.

3. Results

3.1 Catalytic activity

To study the effect of the molybdenum structure on the methanol ODH reaction and its corresponding surface intermediate species, catalysts with surface density 2.5 at. Mo nm^{-2} and 15 at. Mo nm^{-2} were employed. The samples were selected due to their clear differences in structure and redox and acid properties, which arise from the sub-monolayer (oligomeric octahedral MoO_x) and crystalline MoO_3 oxide species.

Figure II-3 a) shows the FA, MF and DMM yield as function of temperature for the 2.5 at. Mo nm^{-2} catalyst on the fixed-bed reactor experiments. The 2.5 MoTi sample has a higher selectivity to the DMM formation at lower temperatures, with increasing MF yield as the temperature rises. FA is not the main reaction product at any temperature. At higher temperatures methanol fully oxidizes to CO and CO_2. Figure II-3 b) shows the FA, MF and DMM yield as function of residence time for the 2.5 at. Mo nm^{-2} catalyst on the fixed-bed reactor experiments. An increase in the contact time favors the yield of all products. At higher residence time values, residence time increases the MF formation at the expense of DMM formation. FA formation is mostly unaffected by residence time.

The same behavior regarding the effect of residence time on FA formation was previously observed in a recent publication, where the methanol ODH reaction over V_2O_5 supported on TiO_2 catalysts under non-differential reactor conversion values was studied [188]. It was proposed that FA desorption was irreversible, and once it desorbs no longer participates in the reaction. Instead, adsorbed FA, without desorbing, could still react and participate in the methanol ODH, using neighboring active sites to continue reacting to form the reaction intermediates for MF and/or DMM formation. Additionally, DMM formation was found to

be in equilibrium with its intermediate, as to influence the MF formation observed for the MoO_3/TiO_2 catalyst.

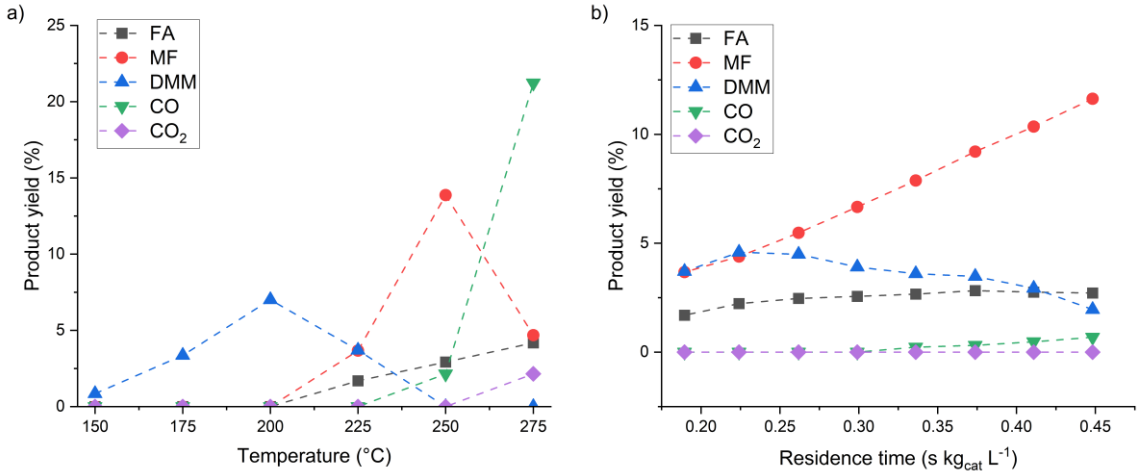

Figure II-3. Yield of FA, MF and DMM for the 2.5 MoTi sample as a function of: a) temperature (GHSV = 19 L h^{-1} g_{cat}^{-1}, $CH_3OH/O_2/N_2$ (feed) = 4/9/87 %v/v) and b) residence time (T = 225 °C, $CH_3OH/O_2/N_2$ (feed) = 4/9/87 %v/v).

Figure II-4 a) shows the FA, MF and DMM yields as function of temperature on the 15 MoTi catalyst. In this sample, FA is the main reaction product at most of the temperature range. DMM is the main product at lower temperatures, but as temperature increases, MF and FA formation becomes more significant. CO is the main reaction product at higher temperatures. This behavior is in line with previously reported findings, which suggest that the FA formation is favored on crystalline MoO_3 supported catalysts. This could be attributed to the requirement of adjacent Mo sites for FA desorption [189], the favored FA formation by adjacent Mo sites[75,190], the reduced availability of support sites which favor the other parallel reactions [191], or the influence of the redox properties which enhance methanol ODH to FA. Figure II-4 b) shows FA, MF and DMM yield as function of residence time on the 15 MoTi. FA formation significantly increases with residence time, while DMM formation reduces and MF increases. The effect of residence time on DMM and MF formation is similar to what was observed for the 2.5 MoTi catalyst, where DMM would be in equilibrium with its intermediate while FA desorption is irreversible. Since FA is the main reaction product over this sample, an increase in residence time leads to higher FA yields as the methanol conversion increases accordingly.

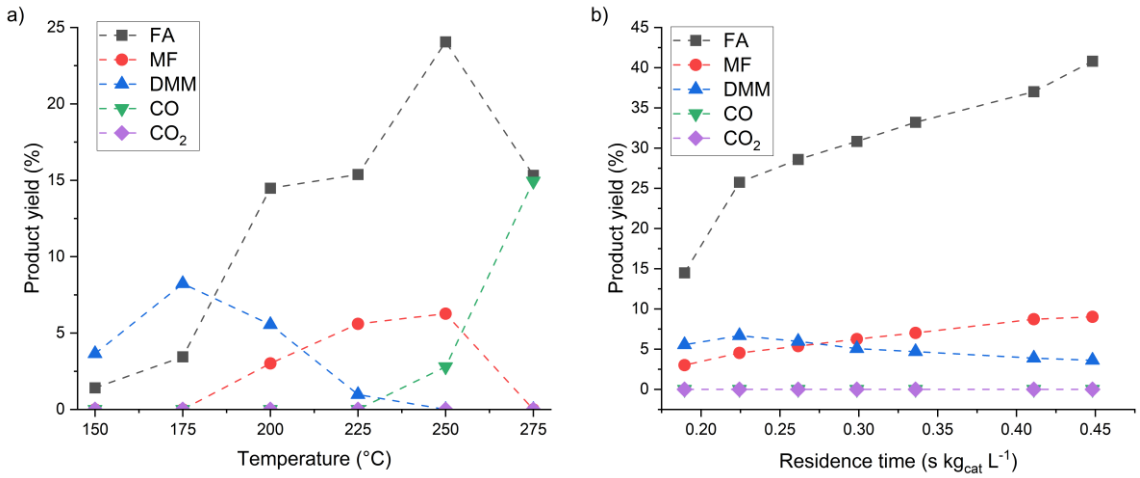

Figure II-4. Yield of FA, MF and DMM for the 15 MoTi sample as a function of: c) temperature (GHSV = 19 L h^{-1} g_{cat}^{-1}, $CH_3OH/O_2/N_2$ (feed) = 4/9/87 %v/v) and d) residence time (T = 225 °C, $CH_3OH/O_2/N_2$ (feed) = 4/9/87 %v/v).

Conversion and yields as a function of temperature for the rest of the samples (0.5, 8, 25 MoTi and bulk MoO_3) can be found in Figure II-5.

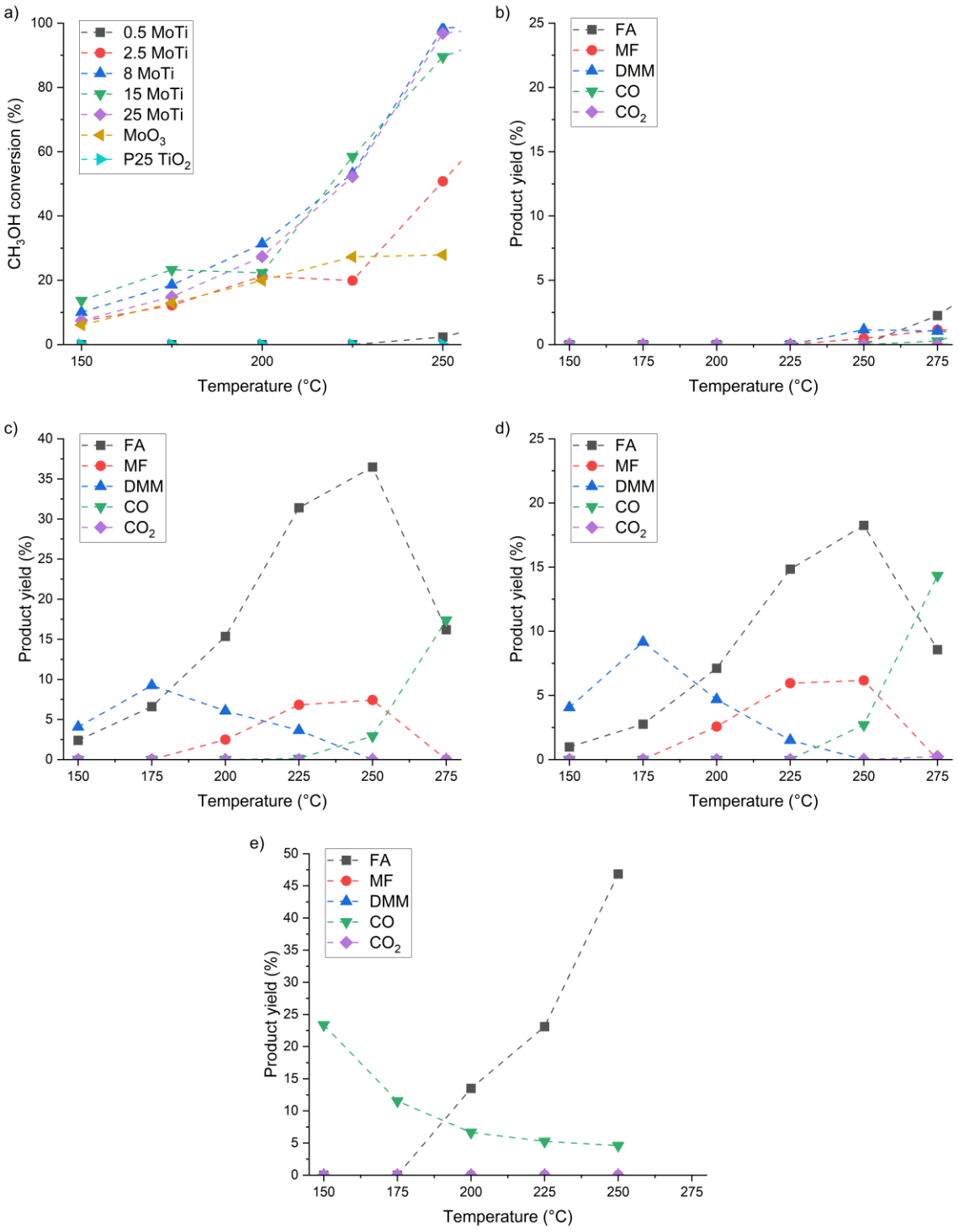

Figure II-5. a) Conversion as a function of temperature for MoTi samples, P25 TiO_2 and synthetized bulk MoO_3; Yields as a function of temperature for b) 0.5 MoTi, c) 8 MoTi, d) 25 MoTi and e) Bulk MoO_3.

3.2 Operando-FTIR results

Figure II-6 shows the evolution of the infrared bands when switching the feed mixture from $CH_3OH/O_2/N_2/Ar$ to $O_2/N_2/Ar$ at 200 °C, over the 2.5 MoTi sample. In general, the intensity of some bands diminishes under these oxidative conditions, due to the consumption of the respective surface species in an oxidation reaction, while the rest of the bands intensify, corresponding to the formation of surface species from the oxidation process. The bands at 2953/2863 cm^{-1} have been previously assigned to molecular CH_3OH adsorbed on Lewis acid sites, whereas the bands at 2938/2928/2832/2842 cm^{-1} have been assigned to surface methoxylated species, together with the 1455/1445 cm^{-1} bands in the lower wavenumber zone [192–194]. As these bands are associated with adsorbed methanol, their intensity decreases under oxidation conditions due to their consumption. 2897, 1360 and 1560 cm^{-1} bands are attributed to adsorbed formates, while the 1610 cm^{-1} band has been assigned to displaced water by molecular methanol adsorbed in Lewis acid sites. Other authors have assigned the 2924 cm^{-1} band to dioximethylene [195] and the 1650-1657 cm^{-1} band to adsorbed methyl formate [42,196]. Hemiacetal intermediary cannot be identified and/or followed by FTIR, as it is a highly reactive molecule with an unfavorable chemical equilibrium [89].

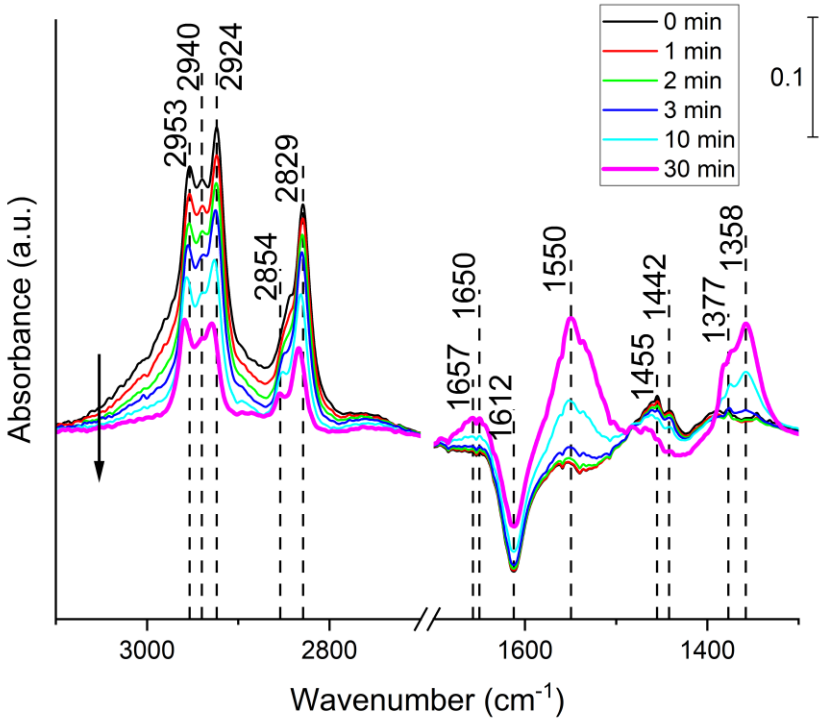

Figure II-6. FTIR spectra of 2.5 MoTi at 200°C after switching from N_2/Ar to $O_2/N_2/Ar$ on 2.5 MoTi at 200°C, on a surface covered with formates.

The FTIR spectra for the 15 MoTi and P25 TiO_2 at 200°C, switch from N_2/Ar to O_2/N_2/Ar, can be found on the Figure II-7. In general, the adsorbed species and observed behavior is the same as for 2.5 MoTi sample.

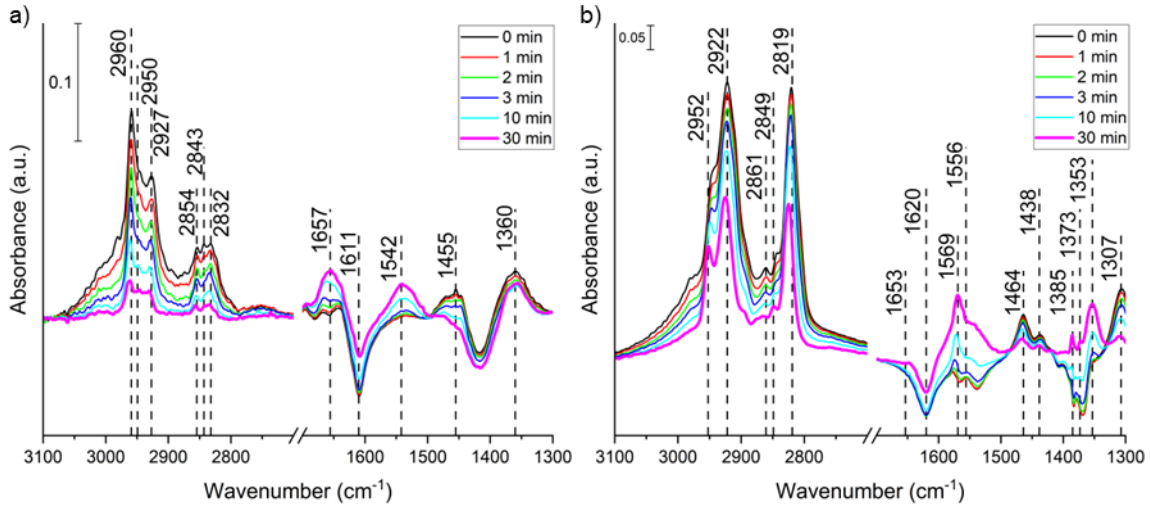

Figure II-7. FTIR spectra at 200°C after switching from N_2/Ar to O_2/N_2/Ar on 2.5 MoTi at 200°C of a) 15 MoTi and b) P25 TiO_2.

The vibrational frequencies are summarized in Table II-1.

Table II-2. IR bands of the surface species formed during the methanol ODH on MoTi catalysts.

Frequency	Surface Specie	Vibration	Reference
2953	Molecular methanol	Symmetric stretching ν_s (CH3)	[42] [192]
2940	Methoxy	Symmetric stretching ν_s (CH3)	[42,169,197,198]
	Formate	ν_{as} (CO2) + δ(C-H)	[192]
2924	Methoxy	ν_{as} (CH3)	[192]
	Dioxymethylene	asymmetric stretching ν_{as} (CH2)	[195]
2854	Molecular methanol	Fermi resonance of 2 δ_s (CH3)	[42,169,192]
2829	Methoxy	Fermi resonance of 2 δ_s (CH3)	[42,169,192,197,198]
1657	Methyl formate	Stretching ν (C=O)	[42,169,197,198]
1612	Water	δ(HOH)	[192,199]
1550	Formate	asymmetric stretching ν_{as} (O-C-O)	[42,169,192,197,198]

1455	Methoxy	asymmetric deformation δ_{as} (CH3)	[42,169,192]
1442	Methoxy	symmetric deformation δ_{s} (CH3)	[42,169,192]
1377	Formate	ν_{as} (O-C-O)	[192]
1358	Formate	Symmetric stretching ν_{s} (O-C-O)	[42,169,197,198] [192]
	Methanol	δ_{s}(OH)	[192]

Figure II-8 shows the bands intensities at steady state conditions for the P25 TiO_2, 2.5 MoTi and 15 MoTi catalysts and the corresponding shift in the consolidated signals. It was found that the same adsorbed species had a slight position shift as the metal loading increased in the different samples. In literature there are multiple explanations for observed shifts in band positions during FTIR spectra. These shifts can be the result of the overlapping of closely located bands, a surface coverage effect, adsorption center nature or an electrostatic effect due to the interaction of the adsorbed molecule and the metal cations and the oxygen anions in the metal oxide [200–204]. Due to the clear differences demonstrated in metal oxide structure between the oligomeric octahedral molybdenum surface phases and crystalline molybdenum oxide, an electrostatic effect is expected.

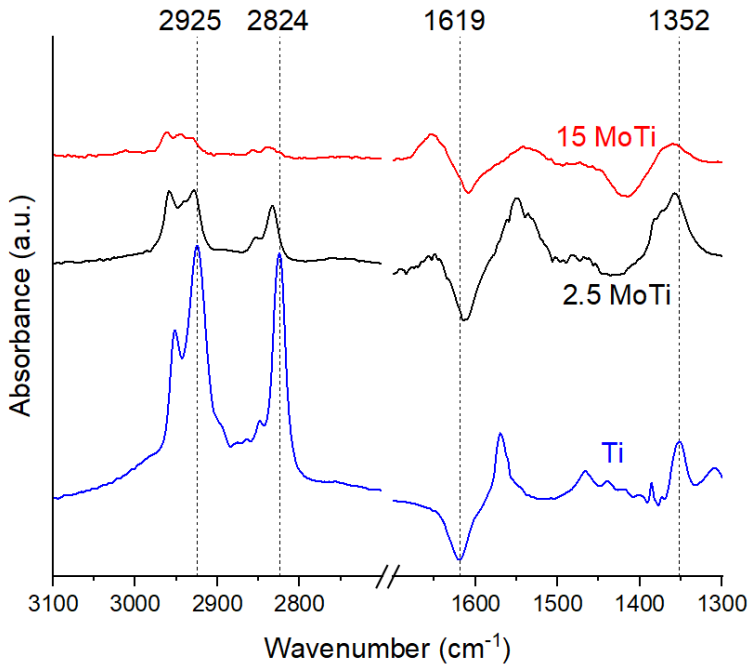

Figure II-8. FTIR spectra at 200 °C with a $CH_3OH/O_2/N_2$ feed composition for P25 TiO_2, 2.5 MoTi, and 15 MoTi samples.

Figure II-9 a) shows the evolution of the intensity of the infrared signals for the most relevant surface species when switching the feed of the cell reactor from $CH_3OH/O_2/Ar/N_2$ to $O_2/Ar/N_2$ and from $CH_3OH/Ar/N_2$ to $O_2/Ar/N_2$, over the 2.5 MoTi sample at 200 °C. The band 2924 cm^{-1} behaves extremely similar to the surface methoxy species, suggesting an overlapping between methoxy and dioxymethylene species, which does not allow to confirm the presence of the latter on the catalyst surface. Surface methoxy species increase in the presence of CH_3OH on the reactor feed, while surface formate species clearly increase when extracting CH_3OH from the feed of the reactor cell. This is in line with the reduction of intensity of adsorbed molecular CH_3OH and methoxy bands, suggesting that the methanol oxidation is producing adsorbed formates in these oxidative reaction conditions. At the end of the $O_2/Ar/N_2$ feed condition, the catalyst surface has a high concentration of formates. It is interesting to note that during the N_2 purge, the surface concentration of formate kept increasing, while methanol/methoxy species continued to decrease, as shown by the surface concentration of these species before and after the N_2 purge in Figure II-9 b). This behavior is characteristic of the Mars-van Krevelen mechanism, where oxidation occurs via lattice oxygen, as was observed, and the role of gaseous oxygen is solely to reoxidize the surface.

Figure II-9 b) shows the evolution of the MS intensity signals for MeOH, FA, MF and DMM formation when changing the feed of the cell reactor from $CH_3OH/O_2/Ar/N_2$ to $O_2/Ar/N_2$ and from $CH_3OH/Ar/N_2$ to $O_2/Ar/N_2$, over the 2.5 MoTi sample at 200 °C. MF is the main reaction product at the studied reaction conditions. When the cell feed is switched from $O_2/Ar/N_2$ to $CH_3OH/Ar/N_2$, thereby introducing CH_3OH onto a surface with high formate coverage, MF formation presents a behavior distinctly different from that of the DMM formation. The MF m/z signal presents a maximum, while the DMM m/z signal has a more gradual response, similar to its formation after the first switch from inert to the regular reaction conditions ($CH_3OH/O_2/Ar/N_2$). This stark difference suggests that these products are formed by different reaction intermediates. The MF reaction intermediate is rapidly consumed in absence of O_2 and in the presence of CH_3OH, while the DMM intermediate has a similar behavior regardless of the absence of O_2. The MF formation from DMM is discarded, as the MF is the only reaction product at 250 °C with the same MF m/z behavior.

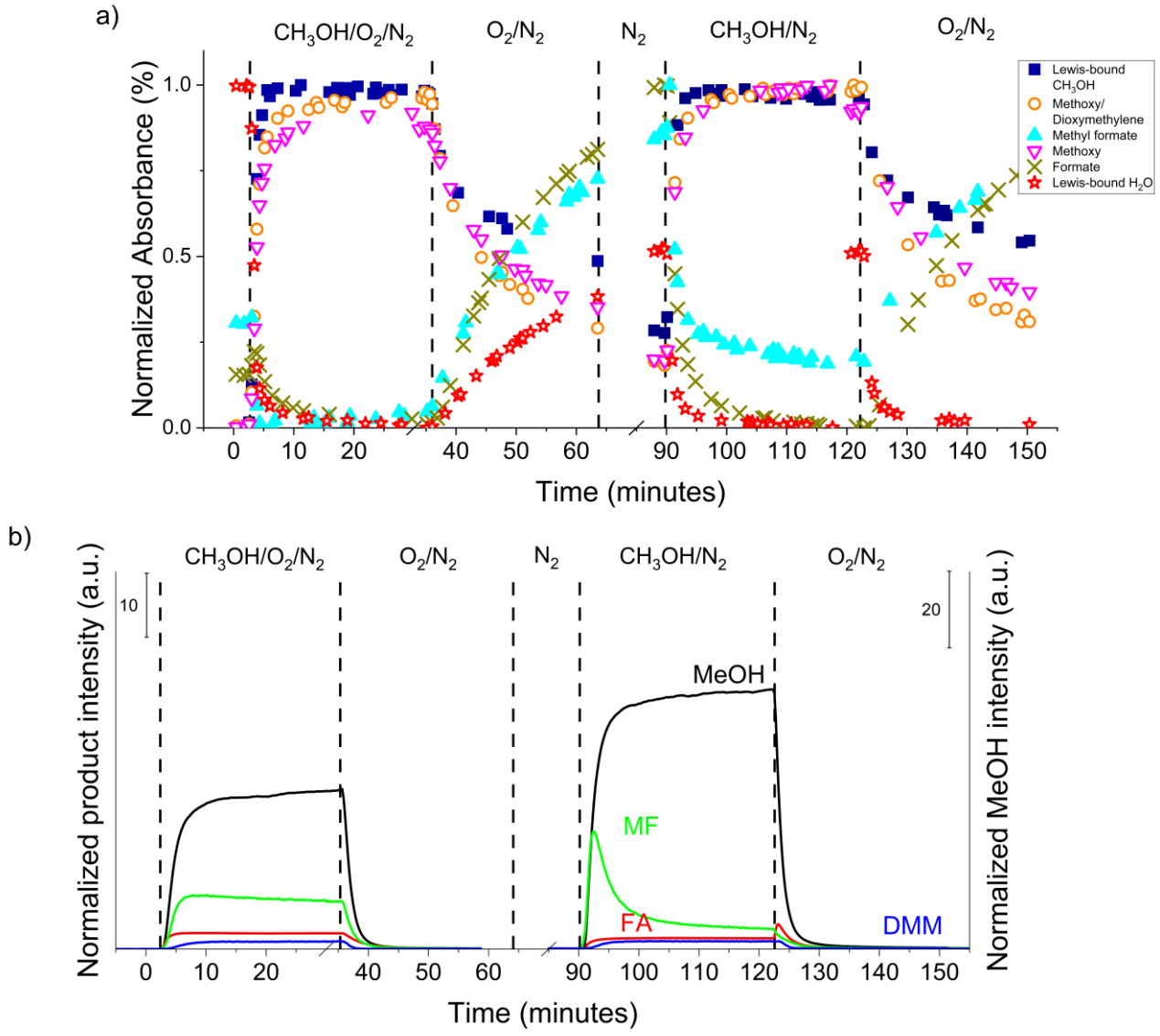

Figure II-9. Operando-FTIR measurements when switching from $CH_3OH/O_2/Ar/N_2$ to $O_2/Ar/N_2$, purging with N_2, and switching from $CH_3OH/Ar/N_2$ to $O_2/Ar/N_2$ on 2.5 MoTi at 200 °C. a) Surface detected species (FTIR) and b) dynamic behavior (MS) of CH_3OH (m/z = 31, corrected), FA (m/z = 30, corrected), MF (m/z = 60) and DMM (m/z = 75).

When comparing Figure II-9 a) and b), a correlation can be observed between surface formate consumption and the rapid increase in MF formation, suggesting that adsorbed formates are the intermediate of MF formation. Moreover, the sharp maximum in MF formation suggests that, before the addition of CH_3OH to the cell feed, an intermediate capable of forming MF was already present on the catalyst surface, which was only missing CH_3OH to form MF. Hemiacetal intermediate, proposed in previous works, can be ruled out as it could not have sufficiently high surface coverage to produce the MF peak, given its previously discussed reactivity and instability. Moreover, if hemiacetal was the MF formation intermediate, and it had a high coverage on the surface as to form the observed sharp maximum in MF formation,

it would have instead reacted with CH_3OH (due to the lack of available redox sites to dehydrogenate the hemiacetal) in a condensation/acid dehydration reaction, leading to a maximum in the DMM m/z signal, which was not the case. The observed behavior was also evidenced at all studied temperatures (Figure II-10).

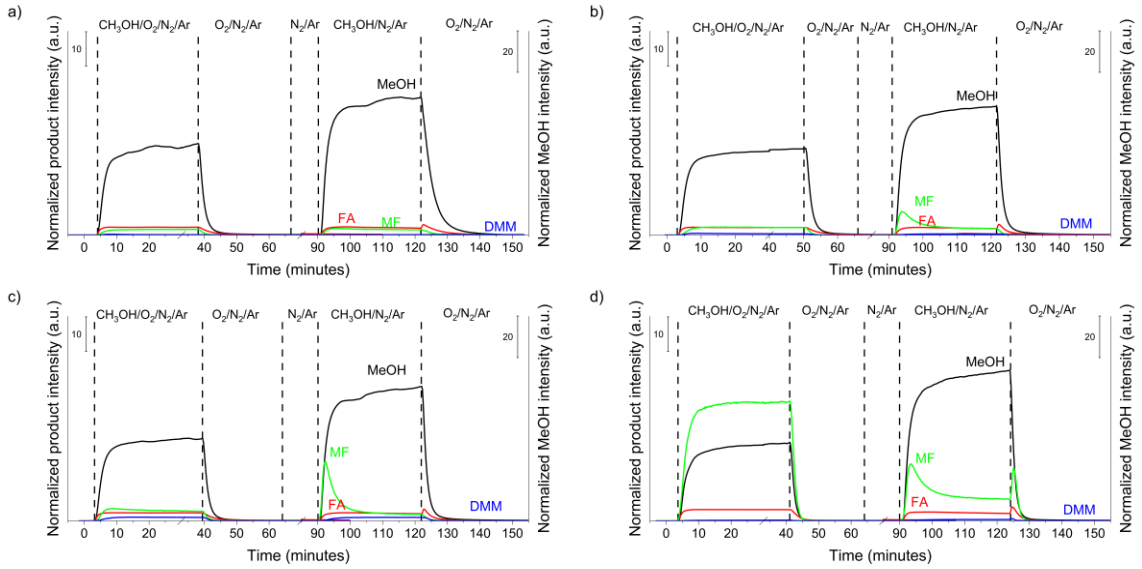

Figure II-10. Dynamic CH_3OH, FA, MF and DMM behavior (MS) during operando-FTIR measurements when switching from $CH_3OH/O_2/Ar/N_2$ to $O_2/Ar/N_2$ and from $CH_3OH/Ar/N_2$ to $O_2/Ar/N_2$ on 2.5 MoTi at a) 100 °C, b) 150 °C, c) 175 °C and d) 250 °C.

Figure II-11 shows the results from the same experiment but for 15 MoTi. A clear difference in the MF formation is observed between the 2.5 and 15 MoTi catalysts, particularly at the feed conditions that these samples present their higher MF formation. The catalyst with oligomeric MoO_x structure as per its lower MoO_3 content presents a higher steady state MF concentration when the reactor feed is switched to $CH_3OH/Ar/N_2$, therefore when the surface has a higher coverage of formates, as shown on Figure II-11 a). On the contrary, the 15MoTi catalyst presents its higher MF concentration during the first feed switch (from Ar/N_2 to $CH_3OH/O_2/Ar/N_2$), when the reactants encounter a clean surface. This suggests that, in the latter sample, the high coverage of formates inhibits overall MF formation, but it does not negate it completely. These results indicate that MF formation would occur by two different pathways in the 15 MoTi sample, the more active one being the one that does take place when reacting in presence of both CH_3OH and O_2. Therefore, on the 15 MoTi catalyst, MF would not be exclusively formed through the surface formate intermediate, but rather by two parallel intermediate pathways. Adsorbed formate would be the intermediate of one of those pathways, while the other may involve the proposed hemiacetal intermediate [48,89]. The absence of this behavior on the 2.5 MoTi sample suggests that the occurrence of this parallel pathway is subject to the metal oxide structure on the sample, evidencing an indirect effect of the metal content on the mechanism of MF formation, which was also proposed recently by Chin et. al [48].

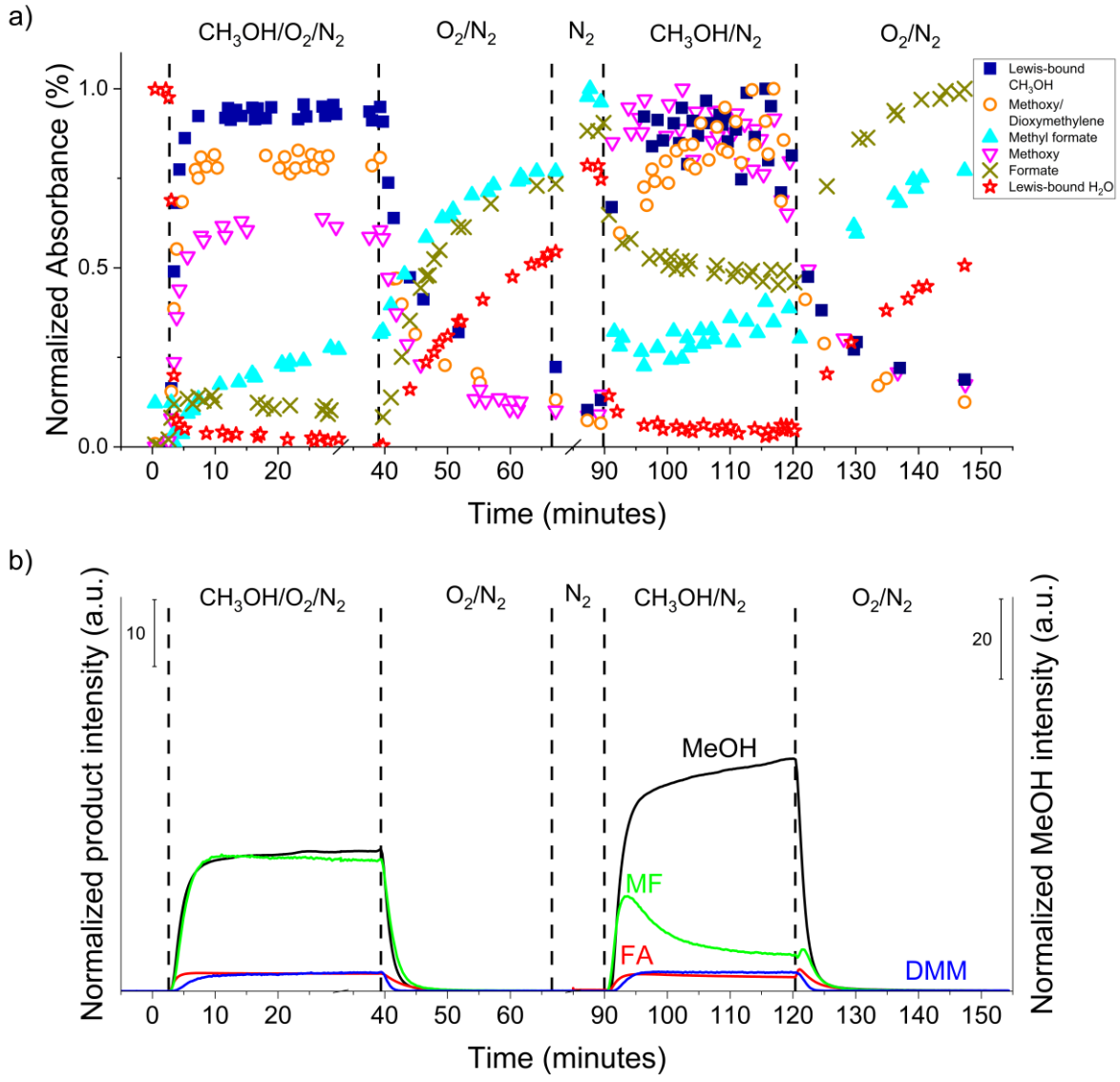

Figure II-11. Operando-FTIR measurements when switching from $CH_3OH/O_2/Ar/N_2$ to $O_2/Ar/N_2$, purging with N_2, and switching from $CH_3OH/Ar/N_2$ to $O_2/Ar/N_2$ on 15 MoTi at 200 °C. a) Surface detected species (FTIR) and b) dynamic behavior (MS) of CH_3OH (m/z = 31, corrected), FA (m/z = 30, corrected), MF (m/z = 60) and DMM (m/z = 75).

The observation of the same surface formate band on TiO_2 support and 15 MoTi (Figure II-7) and 2.5 MoTi sample (Figure II-6) suggests that HCOO* consumption likely occurs on Ti support sites. The absence of CH_3OH conversion on P25 TiO_2 (Figure II-5 a)) indicates that Mo metal sites are essential for CH_3OH ODH. Thus, MF formation through HCOO* consumption is likely taking place at interfacial Mo-O-Ti sites, with contributions from both the redox support sites and the Mo metal sites.

Figure II-12 a) and b) shows a zoom of the first transient response for 2.5 MoTi catalyst when changing reactor feeds from $CH_3OH/O_2/Ar/N_2$ to $O_2/Ar/N_2$ and from $CH_3OH/Ar/N_2$ to $O_2/Ar/N_2$, respectively. Is interesting to note that, when adding CH_3OH to a surface with

HCOO*, MF is formed before FA, which allows us to discard its formation by Tishchenko reaction, instead suggesting a formation consuming the formates already on the surface.

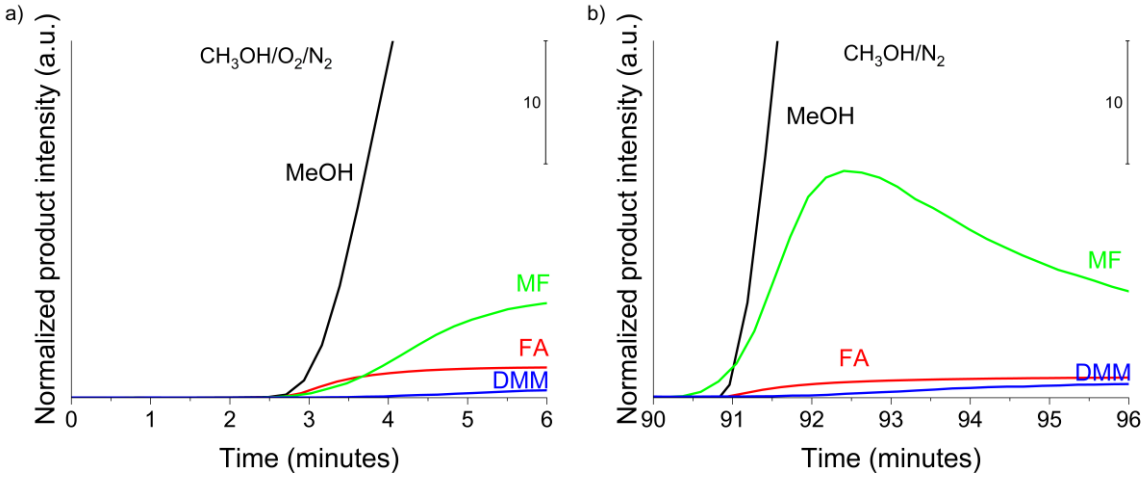

Figure II-12. Zoomed view of the initial transient response on 2.5 MoTi at 200 °C when a) switching from inert gas to $CH_3OH/O_2/Ar/N_2$ and b) when switching from N_2/Ar to CH_3OH/N_2/Ar on a surface with high formate coverage.

This behavior is also observed for all samples (Figure II-13). It is also interesting to note that DMM formation requires FA formation at both conditions, and is indifferent to the presence of surface formates, indicating that the DMM formation via dioxymethylene pathway is not favored. Since no intermediate is able to form DMM before introducing CH_3OH at the formate-covered surface, a formation via another pathway is suggested, which could be the proposed hemiacetal intermediate, resulting in a much slower DMM formation rate.

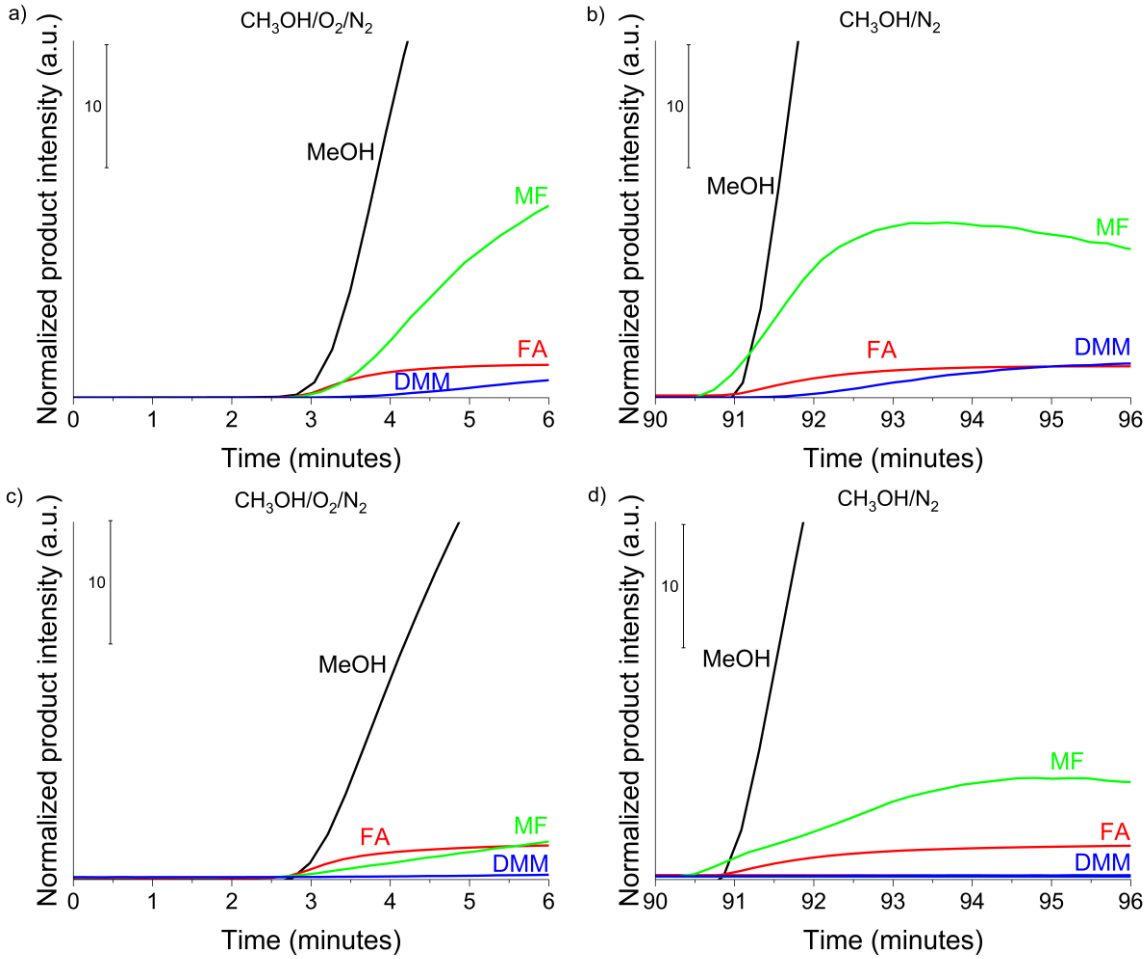

Figure II-13. Zoomed view of the initial transient response on 2.5 MoTi at 200 °C when a) switching from inert gas to $CH_3OH/O_2/Ar/N_2$ and b) when switching from N_2/Ar to $CH_3OH/N_2/Ar$ on a surface with high HCOO* coverage.

Figure II-14 compares the MS relative intensities for MF and DMM formation, normalized to the Mo content in the 2.5 MoTi and 15 MoTi samples. The 2.5 MoTi sample exhibits higher MF and DMM formation, consistent with the results obtained in the fixed-bed reactor tests (Figure II-3). Previously, it was suggested that the observed peak when switching from N_2/Ar to $CH_3OH/O_2/N_2/Ar$ in a formate-covered surface arises from the rapid consumption of surface formates. However, the slower decline of the peak in the 15 MoTi sample indicates a contribution to MF formation through the proposed parallel pathway in this sample.

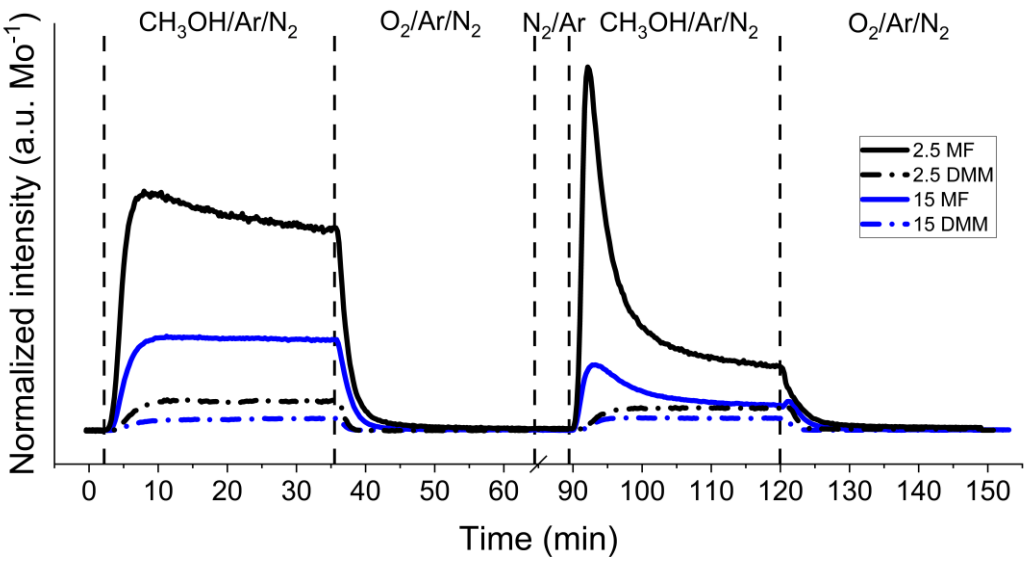

Figure II-14. Comparison of MF and DMM production normalized by Mo content (measured via MS) during operando-FTIR experiments for 2.5 MoTi and 15 MoTi catalysts.

The hypothesis of MF formation via surface formates can be further examined by calculating the rate of MF formation in the fixed bed reactor (extrapolating the kinetic data obtained in the experiments shown in Figure II-3 b) and Figure II-4 b) to the residence time in the FTIR cell reactor) and comparing it with the rate of HCOO* consumption, k_{HCOO*}, estimated from the initial rate of consumption when reactor feed is switched from Ar/N_2 to $CH_3OH/Ar/N_2$ (Figure II-9 b) and Figure II-11 b)).

The formate consumption rate is estimated according to equation II-5:

$$r_{HCOO^*} = k_{HCOO^*}\theta_{HCOO^*} \quad \text{(II-5)}$$

Since the formate coverage on our studied samples cannot be determined with our available data, the ratio $\theta_{HCOO^*}^{2.5MoTi}/\theta_{HCOO^*}^{15MoTi}$ was estimated by dividing the intensity of the HCOO* band for each catalyst, assuming similar extinction coefficients between the samples. Therefore, the $r_{HCOO^*}^{2.5MoTi}/r_{HCOO^*}^{15MoTi}$ can be calculated and compared with the $r_{MF}^{2.5MoTi}/r_{MF}^{15MoTi}$ obtained from the measurements in the fixed-bed reactor.

Table II-3. Formate coverage and consumption rate ratios derived from operando FTIR data after the N_2/Ar (90/10 %v/v) to $CH_3OH/N_2/Ar$ (1/89/10 %v/v) switch, and MF formation rate estimated from fixed-bed reactor measurements.

$k_{HCOO^*}^{2.5\ MoTi}/k_{HCOO^*}^{15\ MoTi}$ [a]	$\theta_{HCOO^*}^{2.5\ MoTi}/\theta_{HCOO^*}^{15\ MoTi}$ [a]	$r_{HCOO^*}^{2.5\ MoTi}/r_{HCOO^*}^{15\ MoTi}$ [a]	$r_{MF}^{2.5\ MoTi}/r_{MF}^{15\ MoTi}$ [b]
3.6	3.2	11.5	4.5

[a] W/F = 11 g_{cat} h m^3, T = 200 °C

[b] W/F = 11 g_{cat} h m^3, T = 225 °C, $CH_3OH/O_2/Ar/N_2$ (feed) = 4/9/87 %v/v

As both HCOO* consumption and MF formation rate ratios are of the same order of magnitude, despite the differences in temperature and methanol partial pressure, this provides quantitative evidence suggesting the possible involvement of surface formate in MF formation.

To finalize the comparison between HCOO* consumption and MF formation, an Arrhenius plot was constructed using the k_{HCOO*} values at different temperatures for the 2.5 and 15 MoTi samples (Figure II-15), estimated from IR measurements. The activation energies calculated from this plot were compared with those obtained from an Arrhenius plot for the MF formation (Figure II-16), obtained from MS measurements. The MF formation rates were estimated from the initial slope of the accumulated area of the total MF formed, as measured in the MS during the switch from Ar/N_2 to $CH_3OH/Ar/N_2$ (Figure II-9 b) and Figure II-11 b)). This step behaves as a batch reactor, given by the consumption of surface formates. The MF formation was corrected by subtracting the MS signals measured in P25 TiO_2 support sample at room temperature. Not all temperatures were used for the construction of the Arrhenius plots and the calculation of the activation energies. At higher temperatures, we approached the detection limit of the FTIR for the changes of HCOO* intensity with time lacking temporal resolution, while at lower temperatures, the low catalytic activity induced significant experimental error.

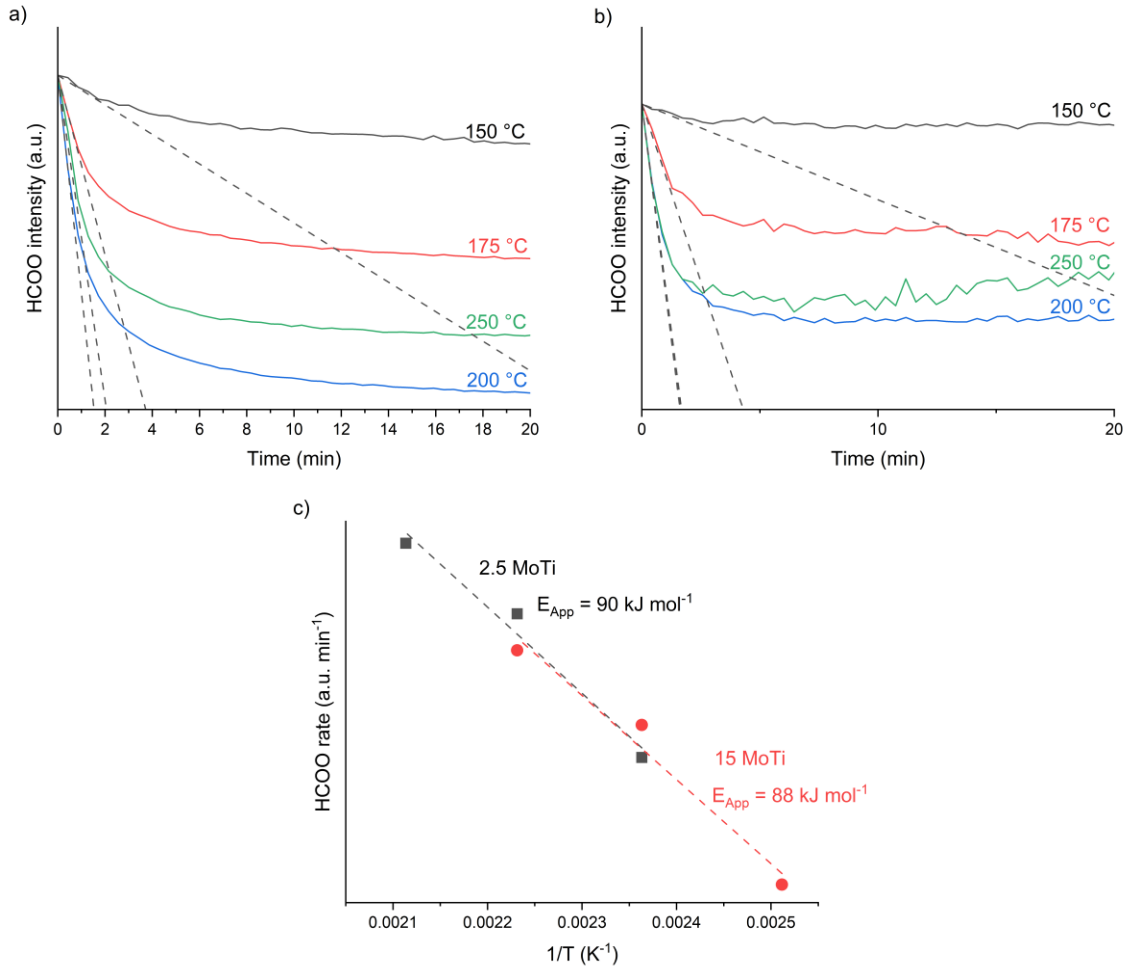

Figure II-15. HCOO* intensity obtained from IR measurements at 150-250 °C and their initial slopes when switching from Ar/N_2 to $CH_3OH/Ar/N_2$, for samples a) 2.5 MoTi and b) 15 MoTi. c) Arrhenius plot constructed with the HCOO* consumption rates.

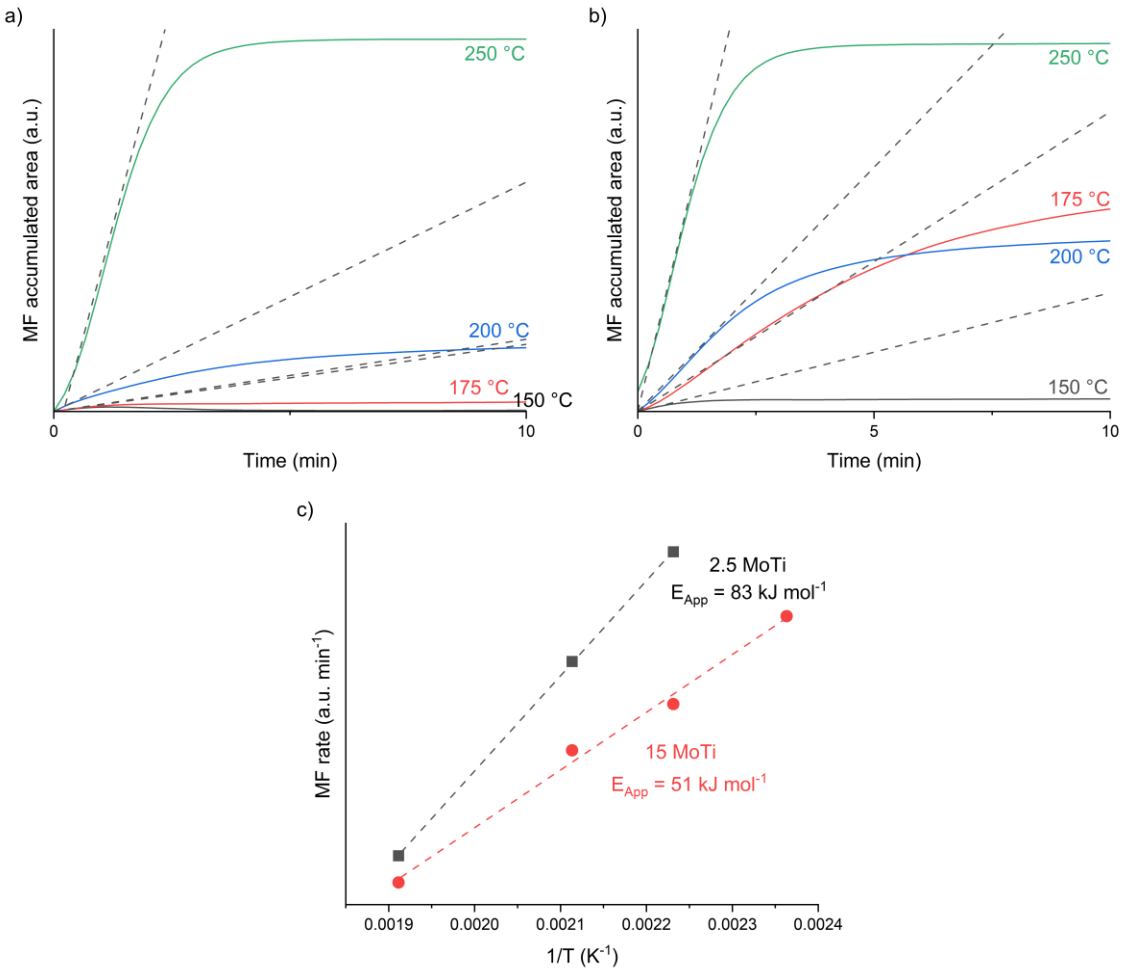

Figure II-16. MF accumulated areas obtained from MS measurements at 150-250 °C and their initial slopes when switching from Ar/N_2 to $CH_3OH/Ar/N_2$, for samples a) 2.5 MoTi and b) 15 MoTi. c) Arrhenius plot constructed with the MF formation rates.

Table II-4 shows the apparent activation energies values calculated from consumption of HCOO* species at the surface (IR) and MF formation rate (MS). The comparison between the activation energies for adsorbed formate consumption and MF formation allows us to compare the intrinsic activity of the reaction. The high activation energy values for HCOO* consumption (90 and 88 kJ mol^{-1} depending on Mo content) confirms that it is a chemical reaction and not a physical desorption. There are not stark differences between the activation energies for surface formate consumption across the supported samples suggesting that the HCOO* consumption is independent of the molybdenum oxide structure/domain size (oligomeric octahedral versus crystalline MoO_3 for 2.5 MoTi and 15 MoTi, respectively). On the contrary, the behavior of the MF formation shows a clear effect of metal content, as the activation energy decreases as the metal content increases (83 and 51 kJ mol^{-1} for 2.5 and 15 MoTi, respectively).

Table II-5. Calculated activation energies for MF formation and the HCOO consumption in Ti, 2.5 MoTi and 15 MoTi studied by operando-FTIR.

Sample	E_{App}MF ($kJ\ mol^{-1}$)	E_{App} HCOO ($kJ\ mol^{-1}$)
2.5 MoTi	83	90
15 MoTi	51	88

The similarity between the activation energies for HCOO* consumption and MF formation in the sample 2.5 MoTi indicates that adsorbed formates would be the intermediate in MF formation, consistent with all the previously shown evidence. Nevertheless, the difference in the activation energy of HCOO* consumption and MF formation for the 15 MoTi sample shows that, on this catalyst, the surface formates cannot explain the total MF formation. It was previously noted that this catalyst could not reach its maximum MF yield with a surface saturated with HCOO*, implying that this catalyst would form MF by two different pathways. The apparent activation energy for MF formation would be a ponderation of the apparent activation energy for these two pathways, one of which involves the activation energy of adsorbed formate consumption. The effect of the molybdenum oxide structure/domain size (oligomeric octahedral versus crystalline MoO_3 for 2.5 MoTi and 15 MoTi, respectively) on the reactivity of this new intermediate participating in a second pathway suggests that this pathway would occur on metal or interfacial metal/support sites, which are affected by metal content. This new pathway could be the hemiacetal intermediate, as was previously discussed.

3.3 Discussion

As shown on Chapter I, our catalyst characterization allows us to describe the structure of the supported molybdenum oxide as per the following findings. The MoTi catalysts are well dispersed on titania support, as indicated by the BET analysis. XRD and Raman spectroscopy show that crystalline bulk MoO_3 phases start to appear at a surface density of 8 at. Mo nm^{-2}, in line with the previously reported formation of a molybdenum monolayer at 4.6 at. Mo nm^{-2} [137]. Our catalysts have a higher dispersion than previously reported MoO_3/TiO_2 catalysts due to the preparation method using oxalic acid [173]. As per the Raman findings, in the 2.5 at. Mo nm^{-2} sample, the structure consists of octahedral oligomeric molybdenum oxide chains, while at 8 and 15 at. Mo nm^{-2}, these octahedral structures coexist with orthorhombic crystalline MoO_3, the latter being the predominant moiety. At 8 at. Mo nm^{-2}, the bulk MoO_3 crystals are small enough to produce weak diffraction peaks in the XRD patterns, due to the high molybdenum oxide dispersion achieved due to the addition of oxalic acid to the catalyst preparation. H_2-TPR results show that the sub-monolayer samples have a higher reducibility than the supported crystalline MoO_3 samples, the former reducing at lower temperatures attributed to the influence of titania support and its interaction with the molybdenum oxide.

The threshold of monolayer formation at 8 at. Mo nm^{-2} is noteworthy because it marks a shift on various physicochemical properties of the supported samples. At this metal content, the H_2 consumption per Mo atom, as measured by H_2-TPR, starts to decline as the molybdenum starts to form crystalline MoO_3 with inaccessible Mo atoms. It is also observed that the Mo oxidation state transitions from Mo^{5+} to Mo^{6+}, driven by the increase of the well-ordered crystalline structures on the catalyst surface, as observed by XPS and low-temperature CO adsorption. Additionally, at this metal content, the protonic acidity of the OH groups of the supported samples reach a plateau. NH_3-TPD results show that the total acidity decreases as the molybdenum surface density increases, likely related to the coverage of the Lewis sites of the titania, as was observed by FTIR of pyridine adsorption. The decrease in acidity stops at the monolayer formation due to the total utilization of OH groups sites on titania for Mo deposition, just before the formation of crystalline MoO_3.

The octahedral oligomeric sub-monolayer Mo catalyst (2.5 MoTi) presents stronger redox properties, due to the interaction between surface molybdenum oxide species and the titania support, as well as the presence of readily reducible Mo^{6+} sites. Similarly, it has been reported that V^{5+} has higher methanol ODH activity compared to V^{4+}/V^{3+}, in accordance with its higher oxidation state [205]. The presence of TiO_2 support and its low cation electronegativity enhances the catalytic activity of the Mo oxide for redox reactions [66,192,206,206–208]. The MoO_3 crystalline structure on the 15 MoTi catalyst lacks the above-mentioned characteristic while having a higher protonic acid strength due to the crystalline MoO_3 formation. Nevertheless, the total quantity of acid sites is lower in the crystalline structure than in the sub-monolayer samples due to less available surface titania Lewis acid sites.

Given the quantitative and qualitative evidence from operando-FTIR experiments, we propose the following reaction mechanism for MF formation on supported Mo catalysts. First, the lack of methanol conversion observed on unsupported titania catalysts demonstrates that methanol ODH occurs on Mo sites of the supported samples (Figure II-5). As the Mo content increases there is a shift at 8 at. Mo nm^{-2} of the primary oxidation states of Mo from Mo^{5+} in the octahedral oligomeric structures to predominantly Mo^{6+} in the crystalline samples. At the same time, the activity (methanol conversion) increases and reaches a plateau for the 8 MoTi sample, as shown on Figure II-5, likely due to this change in oxidation state and oxide structure, as related to the redox activity.

2.5 MoTi is active for MF and/or DMM formation, due to a mixed redox and acid properties of the support and the deposited metal [205,206]. When molybdenum oxide species are structured as oligomeric octahedra in a sub-monolayer configuration, we propose that MF formation follows the dioxymethylene-formate pathway, as evidenced by the quantitative and qualitative operando-FTIR data. It has been reported that MF production via this pathway requires dispersed supported oxides [205,206] with interfacial metal-support sites [48,89], as these catalysts must form and stabilize the dioxymethylene intermediate to prevent its

desorption as FA and promote its dehydrogenation to the adsorbed formate intermediate [197,205,206]. Molybdenum oxide has been previously identified as the active site for the methanol ODH reaction [42] with its initial oxidation state is regenerated by gaseous oxygen in a Mars-van Krevelen redox cycle [69,72,83–85]. Therefore, In the studied 2.5 MoTi sample, successive methanol dehydrogenation to form HCOO* intermediate should involve interfacial Mo-O-Ti sites instead of isolate surface Ti and/or Mo sites. The interaction between the observed Mo^{6+} and titania generates a highly active redox system that favors the reaction of FA on interfacial Mo-O-Ti sites, leading to MF formation rather than FA desorption. This is because titania as a support has an electrostatic effect on supported oxides enhancing the redox properties of the active specie, due to its amphoteric nature and redox capacity, facilitating nucleophilic metal-support interactions [66,192,206,206–208]. The HCOO* pathway has also been proposed for the methanol ODH to MF over V_2O_5/TiO_2 samples [42,50,51].

For 15 MoTi the catalyst mostly produce FA, as it is composed of supported crystalline MoO_3 species due to the interaction between neighboring Mo sites and the lack of support effect due to formation of crystalline MoO_3 oxide [64,75,190]. When dioxymethylene cannot be stabilized, such as on this sample, FA desorption dominates in accordance with previous reported data [64,75,190]. At the same time, at higher molybdenum loading samples, the crystalline MoO_3 bulk reduces the availability of the active sites involving titania, and as adsorbed formate formation requires Mo-O-Ti interfacial sites, MF formation occurs via a secondary, less dominant pathway, likely via the dehydrogenation of a hemiacetal intermediate on redox molybdenum oxide sites, as previously proposed for this reaction [86–92]. As Mo content increases, the hemiacetal pathway becomes more significant in total MF formation, explained by the loss of available interfacial sites, which reduces the contribution of the HCOO* pathway to zero. Nevertheless/Combined with the poor nucleophilic characteristics of the supported crystalline catalysts, the overall quantity of MF formed in this sample is much lower.

The hemiacetal intermediary has been reported to be form on Brønsted acid metal oxide sites [48,86–92]. However, as those acid sites are not abundant on the studied MoO_3 crystalline catalyst, as was observed by NH_3-TPD and FTIR of adsorbed pyridine, the catalyst is more selective to FA formation. In the 15 MoTi sample, with crystalline MoO3 structure, the adsorbed formaldehyde desorbs without further reaction due to the limited availability of interfacial Mo-O-Ti sites for MF formation and the lack of acid sites needed for DMM formation via the hemiacetal pathway [64,75,190]. DMM formation would follow the hemiacetal pathway on both low metal content and high metal content samples, with FA acidly dehydrating to form DMM on molybdenum acid sites. It is likely that the sub-monolayer molybdenum oxide samples are also forming MF via the hemiacetal pathway, in parallel with the adsorbed formate reaction. However, hemiacetal dehydrogenation is significantly slower than the HCOO* reaction due to the limited availability of acid molybdenum oxide sites and the abundance of interfacial Mo-O-Ti sites. This behavior is

evidenced by the differences observed between the 2.5 and 15 MoTi samples during operando-FTIR (Figure II-9 and Figure II-11, respectively) and in the fixed-bed reactor (Figure II-3 and Figure II-4, respectively). Therefore, the HCOO* pathway makes it the only significant route for MF formation on this sample.

Based on these observations, we propose that there are three key types of active sites in the methanol ODH reaction on MoO_3/TiO_2 samples, that explain why MF and DMM formation follow parallel formation routes: redox metal oxide sites responsible for dehydrogenating methanol to FA and dehydrogenating hemiacetal to form MF; Acid Mo oxide sites involved in the formation of hemiacetal intermediate and subsequent DMM formation and finally, redox interfacial sites which dehydrogenate formaldehyde to the adsorbed formate intermediate leading to MF formation as shown on Figure II-17.

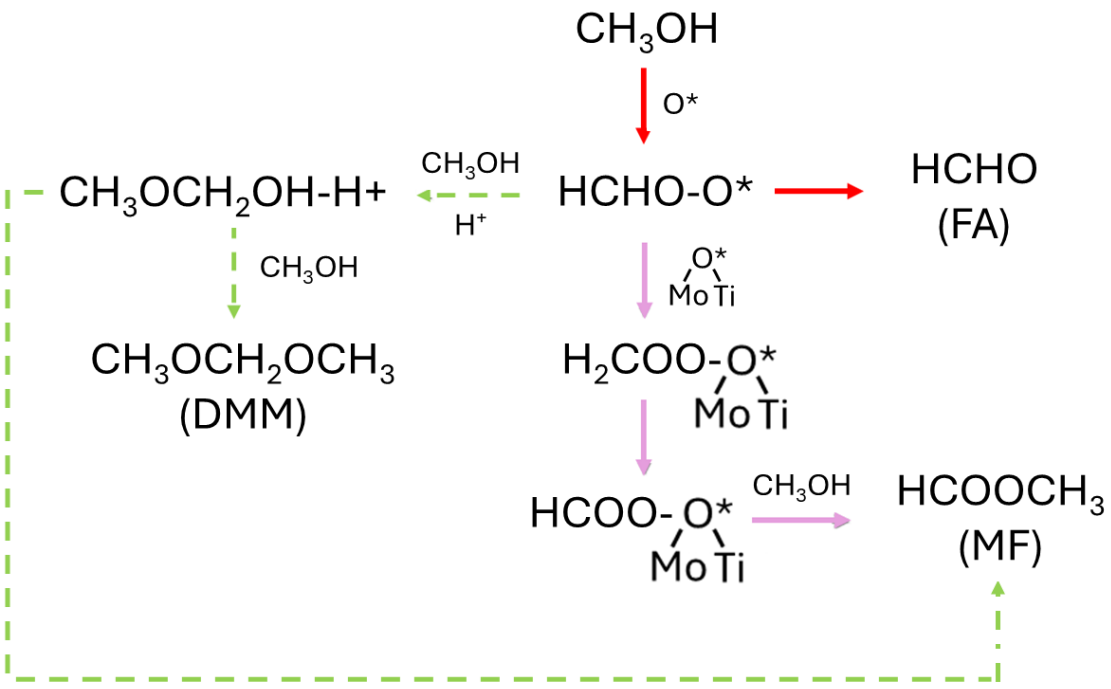

Figure II-17. Summary of the pathways proposed for the methanol ODH reaction considering the surface formate and hemiacetal intermediate on redox (O^*, red lines), acid (H^+, green lines) and interfacial (Mo-O-Ti^*, magenta lines) sites.

The various mechanisms proposed for methanol ODH can be reconciled through a unified explanation. When MoO_3 is dispersed on SiO_2, it rapidly forms a crystalline phase, favoring FA formation [64,189]. However, some dispersed/low content MoO_3/SiO_2 catalysts also produce MF, albeit with significantly lower TOF values [67], likely via the hemiacetal pathway due to the poor nucleophilic, redox, and amphoteric properties of the irreducible SiO_2, which hinder HCOO* pathway formation [64,75,190]. In contrast, DMM formation on sub-monolayer catalysts requires sufficient dispersion to prevent FA desorption and the presence of oxide acid sites to stabilize the hemiacetal intermediate. The studied MoO_3/TiO_2

samples lacked the necessary acidity, explaining the absence of DMM, whereas V_2O_5/TiO_2 catalysts, with Brønsted acid sites, effectively produce DMM in both sub-monolayer and crystalline configurations [42,48,188]. V_2O_5 catalysts have higher methanol conversion rate compared to MoO_3 catalysts, as demonstrated in a previous study on V_2O_5/TiO_2 catalysts with analogous preparation method and surface densities to those used in this work [188]. V_2O_5/TiO_2 catalysts achieved conversion values of 40–70% at 200 °C, compared to the 20–30% reported in this study, using similar catalyst mass (~0.2 g). This superior activity is attributed to the enhanced redox properties of V_2O_5 relative to MoO_3, as evidenced by its lower edge energy determined by UV-Vis DRS (2.3 eV [188] versus 2.8 eV [209], respectively). In terms of domain size and edge energy (or band gap), based on the structural and electronic properties of the samples in this work, the 2.5 MoTi catalyst, composed of oligomeric octahedral chains of MoO_x, should be more easily reduced than dispersed tetrahedral molybdenum oxide, as observed by H_2-TPR. This is attributed to its increasing domain size and band gap as the Mo content increases, with the oxidation state becoming predominantly Mo^{6+}. In the 15 MoTi sample, the monolayer threshold of MoO_3 on titania has already been exceeded, leading to inferior redox activity for oxidation reactions compared to the monolayer catalysts due to the limited accessibility of reactants to the crystalline structure. Nevertheless, both samples exhibit higher reducibility than bulk MoO_3 due to the influence of TiO_2. Among these catalysts, the sub-monolayer catalyst is particularly noteworthy as it combines both characteristics: it contains Mo^{6+} sites due to its larger domain size and lower band gap energy compared to dispersed samples, while maintaining full accessibility to metal sites and interfacial Mo–O–Ti sites in contrast to crystalline MoO_3 catalysts. The relationship between band gap and oxidation reactivity, as well as the maximum oxidation TOF values observed when the domain size ceases to increase as crystallinity is achieved in a crystalline oxide configuration, has been previously reported for oxidation reactions [48,210].

4. Conclusions

Methanol oxidative dehydrogenation was studied using MoO_3/TiO_2 supported samples with varying molybdenum content. As the Mo loading increased, the molybdenum oxide structure changed from oligomeric octahedral chains structures at sub-monolayer coverage to crystalline α-MoO_3. Qualitative and quantitative evidence obtained from fixed-bed reactor experiments and operando-FTIR measurements showed that samples with sub-monolayer octahedral oligomeric Mo oxide species produce MF via a HCOO* pathway, supported by similar rates and apparent activation energies observed for adsorbed formate consumption (83 kJ mol^{-1}) and MF formation (90 kJ mol^{-1}). On the contrary, supported crystalline MoO_3 oxide samples favored FA formation and the minimal MF produced follow a hemiacetal pathway, as indicated by the different apparent activation energies for HCOO* consumption (51 kJ mol^{-1}) and MF formation (88 kJ mol^{-1}).

Strong evidence indicates that methanol ODH activity on supported molybdenum oxide catalysts is governed by three types of active sites: redox metal sites, acid metal sites, and redox interfacial sites. Catalysts with oligomeric/octahedral structure form MF via the HCOO* pathway on redox Mo-O-Ti interfacial sites. In contrast, high-content crystalline catalysts, favor FA formation while MF forms at a lower rate via the hemiacetal pathway due to a lack of interfacial sites. DMM formation occurs at acid metal sites, though this pathway is less prominent due to the weak Brønsted acidity of these samples. The balance between these pathways explains the observed variations in product selectivity across the studied catalysts.

The proportion of the three significant active sites changes as metal content changes and the predominant structure of molybdenum oxide changes. The predominant pathway between the redox adsorbed formate mechanism and the acid hemiacetal mechanism is closely related to the redox properties of the catalysts. The reducibility of these oligomeric samples is higher than the crystalline MoO_3 oxide due to a combined effect of the readily reducible Mo^{6+} and the stronger interaction with the titania support in these sub-monolayer samples, which explains the observed activity and selectivity trends on the studied MoO_3/TiO_2 catalysts.

Chapter III: A detailed kinetic model for the methanol oxidative dehydrogenation on vanadia-based catalysts: aggregation state role and active site requirements

Summary

A kinetic model was derived for the methanol oxidative dehydrogenation to formaldehyde, methyl formate and dimethoxymethane on sub-monolayer and crystalline V_2O_5/TiO_2 catalysts. Considering a hemiacetal intermediate, the model combines Langmuir-Hinshelwood/Eley-Rideal/Mars-van Krevelen mechanisms, accounting for lattice oxygen redox sites and Brønsted acid sites. The fitted model depends on 4 thermodynamically consistent parameters, adequately simulating yield trends with temperature, residence time, and partial pressure of methanol, oxygen and added water. Oxidation steps follow a Mars-van Krevelen redox cycle, while the dimethoxymethane formation is reversible, as the water addition favored the hemiacetal intermediate. The catalyst with higher vanadia surface density was intrinsically more active (lower activation energy of the rate limiting step), attributed to its higher reducibility, while showing weaker methanol adsorption (lower enthalpy of chemisorption). The increase in reducibility correlates with the transition from monomers to polymers to crystalline vanadia when vanadium content increases, as observed by XRD, Raman spectroscopy and DRS-UV-vis.

1. Introduction

Vanadium oxide supported catalysts have been extensively studied for partial oxidation reactions [57,205,211–222], and more importantly, there are several studies for the methanol ODH reaction on these catalysts [45–54]. The Mars-van Krevelen redox cycle is unanimously accepted as the reaction mechanism on these catalysts, where the rate-determining step (RDS) is the dehydrogenation of a methanol molecule, leading to the formation of adsorbed FA[69,72,83–85]. Nevertheless, the mechanism that leads to the different products is still an open field. Kaichev and coworkers have shown that, during CH_3OH-O_2 turnovers on monolayer VO_x highly dispersed on TiO_2, the vanadia lattice oxygen participates in the oxidation of methanol via the classical Mars–van Krevelen mechanism, while the vanadium cations are reduced to the V^{4+} state[42]. A detailed mechanism involving dioxymethylene and formates as key intermediates was also proposed by these authors, as was initially postulated by Busca et al. [50]. In a later work, using Raman spectroscopy, they report an isolated monomeric vanadium oxide species (VO_x) with vanadium in a tetrahedral oxygen environment, while the increase of vanadium content leads to the formation of dimers and polymeric forms of $(VO_x)_n$ in an octahedral oxygen environment, detected only after the formation of 3D vanadium crystallites at the filling of the monolayer coverage. It was established that the crystalline V_2O_5 oxide is the least active structure in the selective oxidation of methanol, and that the polymeric forms of $(VO)_x$ are more active than the monomeric ones [51]. On the contrary, Liu and Iglesia have proposed an ODH mechanism with hemiacetal as the common intermediate for the formation of MF and DMM, with bifunctional pathways on the redox and acid sites of the catalyst [223]. This mechanism has

been confirmed by DFT calculations as the pathway with the lower energy barrier on V_2O_5/TiO_2 [90]. More recently, Broomhead and collaborators [48] also studied the ODH reaction on V_2O_5/TiO_2 and the effect of the surface density of the redox, Brønsted and Lewis sites on the catalytic pathways. The relative abundance of these three sites changes with the VO_x domain size and surface density, while, as the content of VO_x increases, its structure evolves from isolated monovanadates to two-dimensional planar polyvanadates followed by three-dimensional multi-layer polyvanadates. They suggested that FA is formed by CH_3OH dissociative adsorption and subsequent dehydrogenation on V-O redox site pairs at the VO_x-TiO_2 interface, while the DMM forms via methanol and hemiformal, derived from FA, on Brønsted sites at the VO_x-TiO_2 interface, meanwhile, the MF forms via Tishchenko reaction from FA molecules on exposed titania uncovered by VO_x. This different pathways for the MF and DMM formation is a consequence of the VO_x domain size: on highly dispersed, monomeric VO_x, as in the study by Broomhead et al., MF would follow the Tishchenko reaction on the Lewis sites of the titania, while on crystalline VO_x catalysts, MF would be formed by the formic or hemiacetal route, as the titania active sites are fully covered by VO_x. It can be seen that, even for the same active metal-support pairs, three mechanisms for MF and DMM formation have been proposed for the methanol ODH reaction: hemiacetal mechanism, formate/dioximethylene mechanism and Tishchenko reaction.

In light of the information given above, there is still a lack of understanding on specific reaction details, like nature of the intermediate species, type of active sites and reaction mechanisms. Moreover, although there is multiple evidence for the involvement of the hemiacetal intermediate in the formation of MF and DMM in V_2O_5/TiO_2 catalysts, a kinetic model specifically revolving around this intermediate has not yet been developed. In an effort to understand the complex parallel and series pathways of the methanol ODH reaction and the corresponding kinetics parameters that govern its reactivity, kinetic models for the formation of the main ODH reaction products (FA, MF and DMM), with only hemiacetal (HA) (CH_3OCH_2OH) as the MF and DMM intermediate, were rigorously derived on integral reaction conditions. V_2O_5/TiO_2 catalysts with variable vanadium content (0.5, 2.5, 8, 15 and 25 V atoms nm^{-2}) were used to understand the effect of the vanadia surface density on the kinetic parameters. The consideration of a hemiacetal intermediate parallel pathway allowed to adequately simulate the trends of FA, MF and DMM formation. The results indicate that there is an increase in the intrinsic ODH activity and a decrease of methanol heat of adsorption attributed to the growth of the vanadium domains with increasing vanadium content, which was confirmed through XRD, Raman, and UV-vis characterizations. A combined Langmuir-Hinshelwood/Eley-Rideal/Mars-van Krevelen kinetic model was successfully fitted for the methanol ODH reaction, considering hemiacetal as the intermediate for MF and DMM formation, with a mean average error of 20% and thermodynamically consistent kinetic parameters. The redox properties of the catalyst primarily determine the activity. The conclusions of this work are important for the

development of finely tuned supported VO_x catalysts in the pursuit of selective reaction products.

2. Experimental

2.1 Catalysts preparation

Supported catalysts containing vanadium oxide on titania were synthesized via wet impregnation with varying surface concentrations of vanadium (0.5, 2.5, 8, 15 and 25 atom V nm^{-2}) using ammonium metavanadate as the vanadium source (NH_4VO_3, Sigma-Aldrich), as was reported on a previous publication [215]. The procedure is analogous to the one described in Chapter 1, Section 2.2, using a ratio of 2 mol of oxalic acid per mol of NH_4VO. Bulk V_2O_5 was also prepared by calcination of NH_4VO_3 at 500 °C (heating rate of 10 °C min^{-1}) in static air for 1 h.

2.2 Catalysts characterization

X-ray diffraction (XRD) and BET surface area, pore volumes and pore size distributions were already described in Chapter 1, Section 2.2

Raman spectroscopy was performed in a high-resolution confocal LabRamHR Evolution Nano Horiba Jobin Yvon microscope, with a 633 nm Edge laser line excitation source with an output power of 13.3 mW at the source. The laser spot was focused on the sample using an optic Objective Olympus 100× VIS and NUV camera (B/S UV 50/50 + Lens F125 D25).

UV-vis diffuse reflectance spectroscopy (DRS) was performed in a Thermo Scientific Evolution 260 Bio spectrometer equipped with a Spectralon-coated integrating sphere ISA 220. The spectra were recorded in the range of 190 and 1100 nm using a Spectralon discs as a standard.

2.3 Catalytic activity measurements

Methanol ODH reaction was performed in a tubular fixed-bed stainless-steel reactor, in an analogous setup as the described in Chapter II, Section 2.1. The O_2/CH_3OH molar ratio was set to 1 (P_{CH3OH} = 4 kPa, P_{O2} = 4 kPa, P_{N2} = 92 kPa), and a total flow of 50 ml min^{-1} of the gas mixture was conducted through the catalytic bed. Each reaction condition was maintained for 3 h, and 7-8 measurements were made per condition. The steady state of the reaction was rapidly achieved, and the mean concentration of each reactant and product at steady state was calculated. An example of methanol concentration versus time on stream is shown in figure A-III.1 of Appendix: Chapter III.

CH_3OH conversion (X) and FA, MF and DMM yields (Y) were calculated according to equations II-1 to II-4 (Chapter II, section 2.1)

The effect of the reaction conditions on the reactions kinetics was studied, starting with the temperature (100-300 °C), followed by the variation of the total flow rate (20-70 ml min^{-1}), the partial pressure of reactants (1-20 kPa) and the addition of water to the reactor feed (0-3

kPa). These latter examinations were conducted at a temperature where FA, MF and DMM were formed, as to study the selectivity of the reaction.

Carbon balance was calculated as follows:

$$C_{bal} = \frac{CH_3OH_{in}}{CH_3OH_{OUT} + FA_{OUT} + 2\,MF_{OUT} + 3\,DMM_{OUT} + CO_{OUT} + CO_{2_{OUT}}} \times 100 \qquad \text{(III-1)}$$

2.4 Reactor modeling and kinetic parameter fitting

The reactor was modeled as an integral 1-D pseudo-homogeneous plug-flow reactor. Matlab was used to solve the integral form of the rate equations using the command *ode45*:

$$\frac{dP_i}{dW} = \frac{RT}{v}\, r_i \qquad \text{(III-2)}$$

Where P_i is the partial pressure for compound i (kPa), W is the mass of the catalyst bed (g), R is the universal gas constant (J mol^{-1} K^{-1}), T is temperature (K), v is the volumetric flow fed to the reactor and r_i is the net reaction rate for compound i (mol min^{-1} g_{cat}^{-1}). Transport and heat transfer limitations were ruled out in order to obtain parameters in strictly kinetic regime (Section A-III.2 to A-III.4, Appendix: Chapter III)

To estimate the numerical values of the kinetic parameters for the FA, MF and DMM formation models, an optimization problem was solved by minimizing the objective function given by the normalization of the squared errors of the prediction of the three partial oxidation products and the O_2 reaction consumption (equation III-3). This optimization problem is solved with Matlab using the function *lsqnonlin*, in order to obtain statistical parameters used for the computation of the confidence intervals of the kinetic parameters. The confidence interval of each parameter is obtained with the Matlab function *nlparci*, while the individual and total mean absolute percentage error (MAPE) values were calculated to evaluate the prediction accuracy (equations III-4 and III-5, respectively).

$$FO = \sum_{i=1}^{Nc} \frac{1}{N_i} \sum_{j=1}^{Ni} \left(\frac{P_j^{exp} - P_j^{calc}}{P_j^{exp}} \right)_i^2 \qquad \text{(III-3)}$$

$$MAPE_i = \frac{1}{N_i} \sum_{j=1}^{Ni} \left| \frac{P_j^{exp} - P_j^{calc}}{P_j^{exp}} \right|_i \times 100 \qquad \text{(III-4)}$$

$$MAPE_T = \sum_{i}^{N_c} \frac{1}{N_i} \sum_{j=1}^{Ni} \left| \frac{P_j^{exp} - P_j^{calc}}{P_j^{exp}} \right|_i \times 100 \qquad \text{(III-5)}$$

Where P^{exp} and P^{calc} are the experimental and calculated partial pressure of compound i, respectively, while Ni is the number of data points and Nc is the number of compounds considered in the objective function.

3. Results

3.1 Characterizations

Table III-1 shows vanadium surface density and its corresponding V_2O_5 loading (wt.%) of the synthesized catalysts, as well as the BET area and BJH pore volume and size. The surface area and pore size does not vary significantly with the increase in the vanadia loading until the catalyst 25VTi, indicating that the vanadium layer is not blocking the pores of TiO_2 for the catalysts with vanadium surface density lower than 25 at. V nm^{-2}. N_2 adsorption-desorption isotherms can be found on Figure A-III.5 (Appendix: Chapter III).

Table III-2. Vanadium surface density, surface BET area, mean pore volume and pore size in the supported V_2O_5 catalysts as a function of the nominal V_2O_5 content.

Sample	Loading (wt. %)	Surface density (V nm^{-2})	BET Area (m^2 g^{-1})	Pore volume (cm^3 g^{-1})	Pore Size (nm)
TiO_2	0	0	50	0.15	15
0.5 VTi	0.6	0.5	47	0.42	32
2.5 VTi	3.0	2.5	50	0.42	32
8 VTi	8.6	8	41	0.38	34
15 VTi	15	15	52	0.47	32
25 VTi	23	25	24	0.16	28

Figure III-1 shows the X-ray diffractograms of the VO_x/TiO_2 catalysts. All catalysts feature typical diffraction peaks of anatase and rutile for TiO_2, characteristic of P-25 TiO_2 support. At low vanadium content, there is an absence of diffraction peaks attributed to vanadium phases, indicating small size and/or amorphous phases. At vanadium surface density higher than 15 at. V nm^{-2}, peaks attributed to crystalline V_2O_5 start to appear. With the increase of vanadium content, dimers and polymeric forms of $(VO_x)_n$ are formed, being detected only after the filling of the monolayer coverage at 7.9 V nm^{-2}, as has been reported by Wachs [53,137]. These findings are in line with our Raman spectroscopy results on non-dehydrated samples, where at higher vanadium content (≥ 15 V nm^{-2}) a clear band appears at 994 cm^{-1}, corresponding to lattice vibrations of crystalline V_2O_5 (Figure III-2). This behavior is in agreement with Kaichev and co-workers findings based on Raman spectra, who report isolated monomeric vanadium oxide species VO_x and dimers and polymeric $(VO_x)_n$ at surface densities lower than 11.7 at. V nm^{-2} [51].

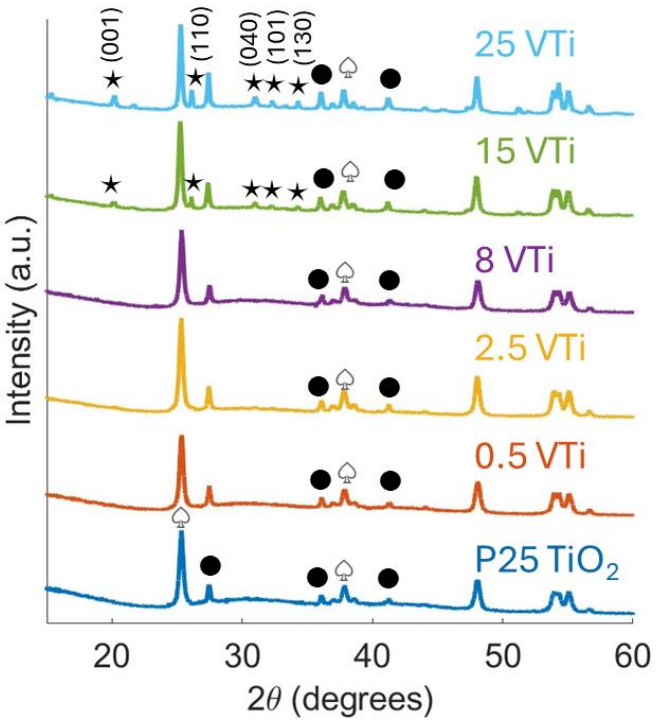

Figure III-1. X-ray diffraction patterns and V_2O_5 crystalline planes for all V_2O_5/TiO_2 supported catalysts and titania P25. ★: V_2O_5, ♤: anatase, ●: rutile.

Our Raman spectra only shows the region 1200-800 cm^{-2} because titania obscures Raman bands below 700 cm^{-1} [224]. Nevertheless, the information gathered studying this region permits to study the structure of vanadia on titania, because all the relevant species can be identified in this range: tetrahedral VO_x at low surface densities, then octahedral oligomeric $(VO_x)_n$ species in increasing proportion as we approach the monolayer coverage, and then crystalline V_2O_5 as the monolayer has been filled [225].

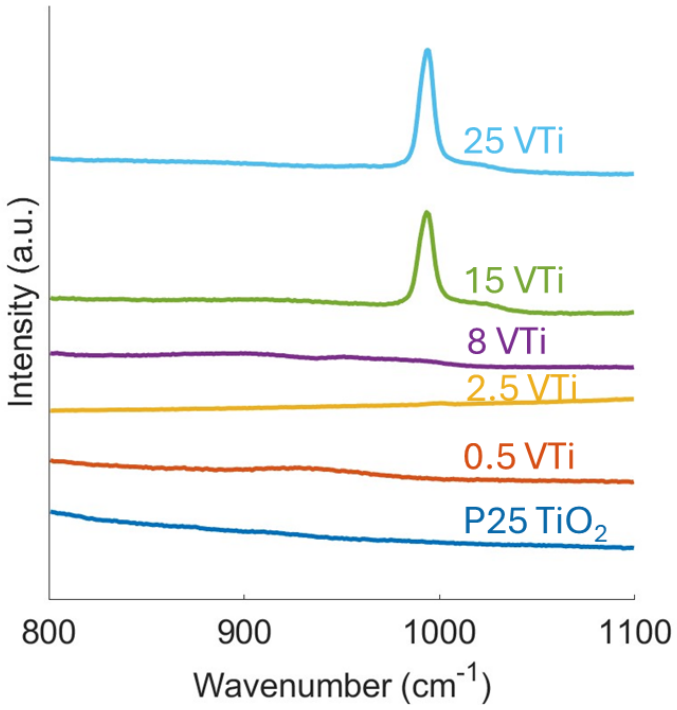

Figure III-2. Raman spectra of non-dehydrated V_2O_5/TiO_2 and TiO_2.

Based on previous works by multiple authors, our titania-supported vanadium catalysts can be identified as following. At 0.5 VTi, monomers of isolated tetrahedral mono-oxo VO_x species should be exclusively present, as has been previously reported for sub 2 at. V nm^{-2} surface densities [226,227]. At 2.5 and 8 VTi, as the surface coverage of vanadium increases, oligomeric chains of $(VO_x)_n$ start to appear, with increasing fraction until a monolayer of polymeric $(VO_x)_n$ is formed [205,207]. At 15 VTi and 25 VTi, as the monolayer has already been filled, the deposition of vanadium oxide forms a crystalline 3-D structure in a crystalline composition [225,228,229], as it was detected by XRD and Raman. These VO_x domains are of significance for ODH activity because they have different concentration of surface lattice oxygens with unique coordination spheres and neighboring atoms, depending on the three vanadium oxide aggregation states: terminal V=O pairs on all domains, bridging V-O-V moieties on polymeric and crystalline structures and binding V-O-Ti linkages on monomeric and polymeric vanadium phases. Given the differences on reactivity for these types of lattice oxygens, their concentration would be closely related to the redox Mars-van Krevelen reactivity, as it was discussed by Broomhead and collaborators [48].

The absorbance UV-vis spectra and the Kubelka-Munk function spectra, for all catalysts, are shown in Figure III-3.a and Figure III-3.b, respectively. The spectral bands in the 2-6 eV energy range can be attributed to the charge transfer transitions of the ligand O^{2-} to the metal V^{5+}, as was reported by Iglesia and coworkers[214]. Since these bands are broad, the edge energy (ε_0) is calculated using the Tauc law. ε_0 serves as a descriptor for the near-edge region

in amorphous semiconductors and the band gap transitions in crystalline semiconductors[230]. The energy is calculated by intercepting a straight line on the x-axis, given by the gradient of the function $[F(R\infty)h\nu]^2$ with respect to hv, after correcting by the subtraction of the overlap of the TiO_2 bands, as can be seen on Figure III-4.a. Figure III-4.b shows the effect of the vanadium surface density on the ε_0 parameter, with the V_2O_5 bulk adsorption energy value as a reference. As the vanadium surface density increases, the adsorption energy decreases towards the V_2O_5 bulk value, indicating the crystallization of the vanadium polymeric domains [214]. Therefore, the vanadium supported catalysts with lower surface density would have a high vanadia dispersion, since the bulk value is reached at 15 at. V nm^{-2} or higher, in agreement with the findings observed by XRD and Raman.

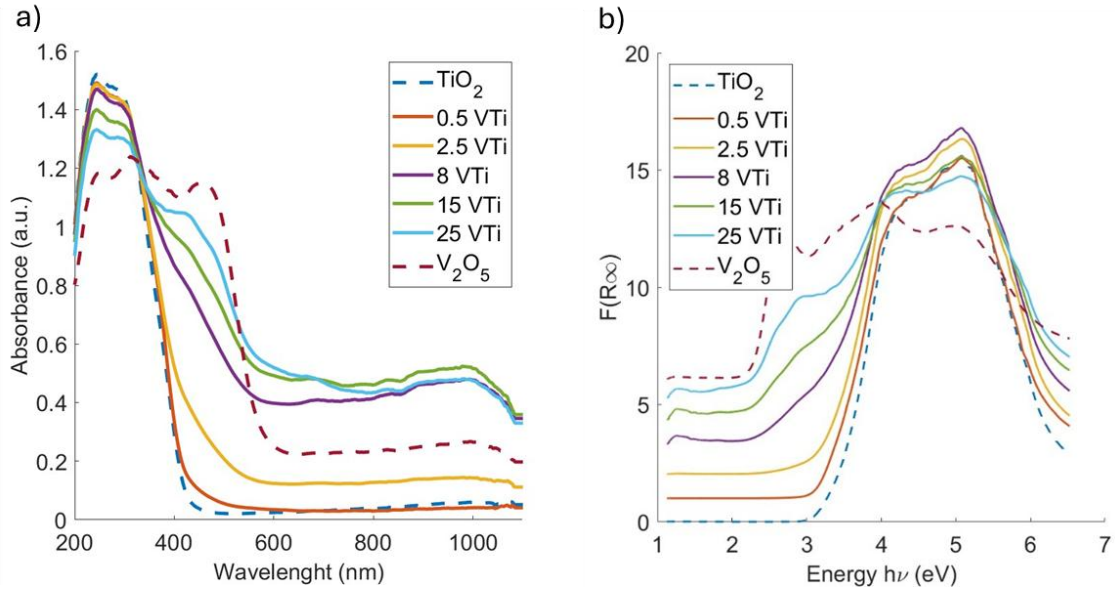

Figure III-3. DR UV-Vis spectra for all vanadia catalysts and TiO_2 a) Absorbance b) Kubelka Munk.

A decrease of the adsorption edge energy is related to a decrease of the band gap energy, which is also related to the reducibility of the metal oxides: Typical irreducible oxides such as MgO show a large band gap, while reducible oxides such as TiO_2 present small band gaps [231]. Reducibility of oxides is known to be linked to their redox activity, thus enhancing the ability to undergo reduction in the kinetically relevant steps for ODH reactions [66,69,89,232,233]. Therefore, the catalysts with higher vanadium surface density should be more active for the Mars-van Krevelen redox cycle in the methanol ODH reaction.

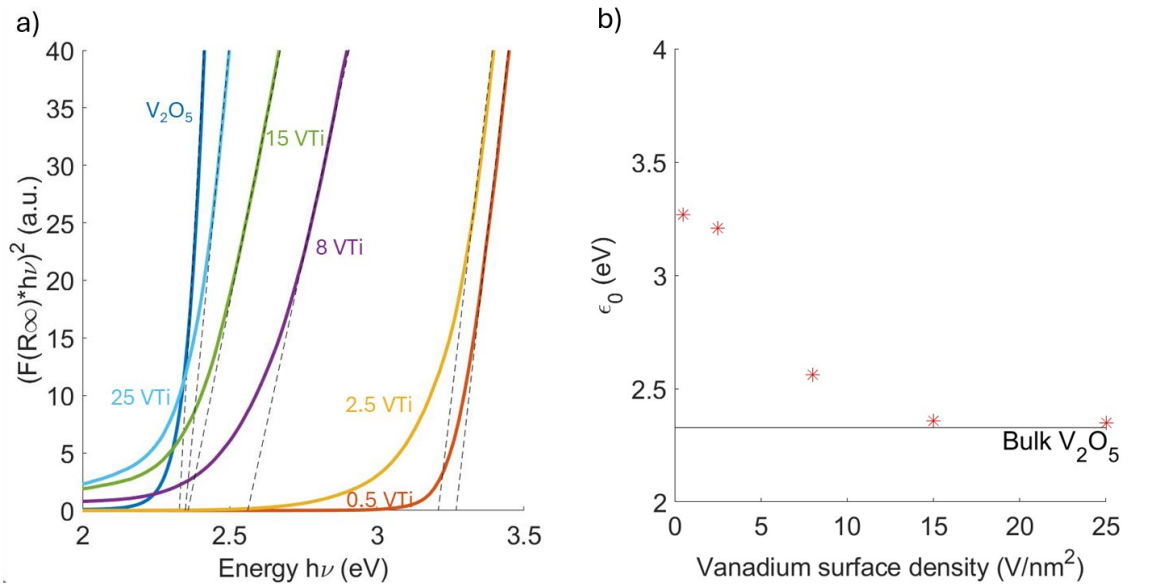

Figure III-4. a) Absorption edge energy (ε_0) calculated using the Tauc law from DR UV-vis spectra and b) absorption edge energy as a function of vanadium surface density. Bulk V_2O_5 is shown as a straight line.

3.2 Catalytic activity

To study the effect of the vanadium structure, specifically the effect of the vanadium phase (monomeric/polymeric versus crystalline) on the catalytic performance of the methanol ODH reaction, catalysts with surface density 2.5 at. V nm^{-2} and 15 at. V nm^{-2} were employed. These samples were selected due to their clear differences in structure and absorption edge energy, arising from the distinct characteristics of both sub-monolayer and crystalline vanadium configurations, as previously discussed. CH_3OH conversion for all catalysts as a function of temperature is shown in Figure III-5 while carbon balances for the data used in the kinetic modeling are shown in Figure A-III.6 (Appendix: Chapter III).

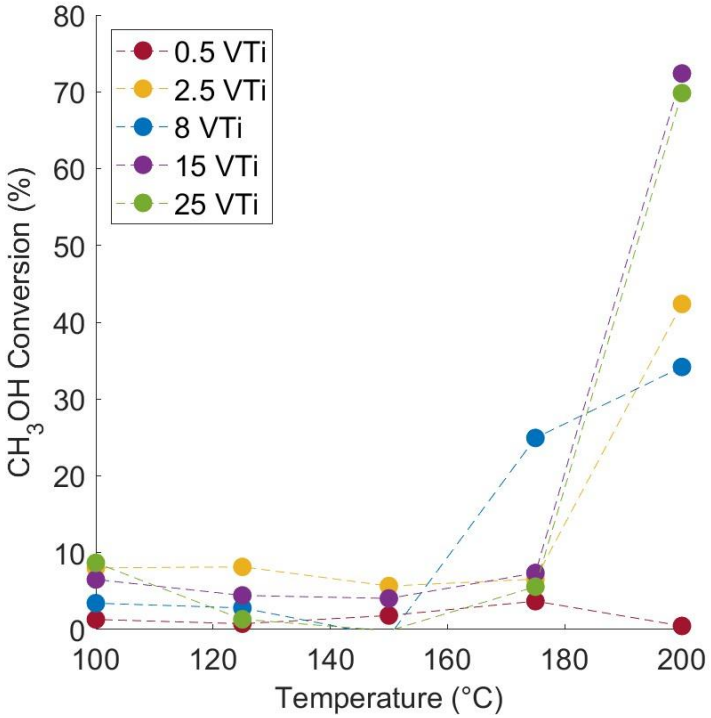

Figure III-5. Methanol conversion as a function of reaction temperature for all VTi catalysts (GHSV = 20 L h^{-1} g_{cat}^{-1}, $CH_3OH/O_2/N_2$ (feed) = 4/4/92 %v/v). S.10. Carbon balance for the data used in the kinetic modelling as a function of conversion.

Figure III-6.a and Figure III-6.b shows the FA, MF and DMM yield as function of the temperature, for the 2.5 at. V nm^{-2} and 15 at. V nm^{-2} catalysts, respectively. DMM is the main product at lower temperatures, with higher MF and FA yield as the temperature rises. In general, both catalysts have similar conversions (considering the differences in metal loading) at lower temperatures, while the 15 at. V nm^{-2} sample is more reactive at higher temperatures (Figure III-5 and Figure III-6). The 2.5 at. V nm^{-2} catalyst is more selective to partial oxidation products at higher temperatures. At higher temperatures, the total oxidation of CH_3OH yields CO and CO_2 as main reaction products.

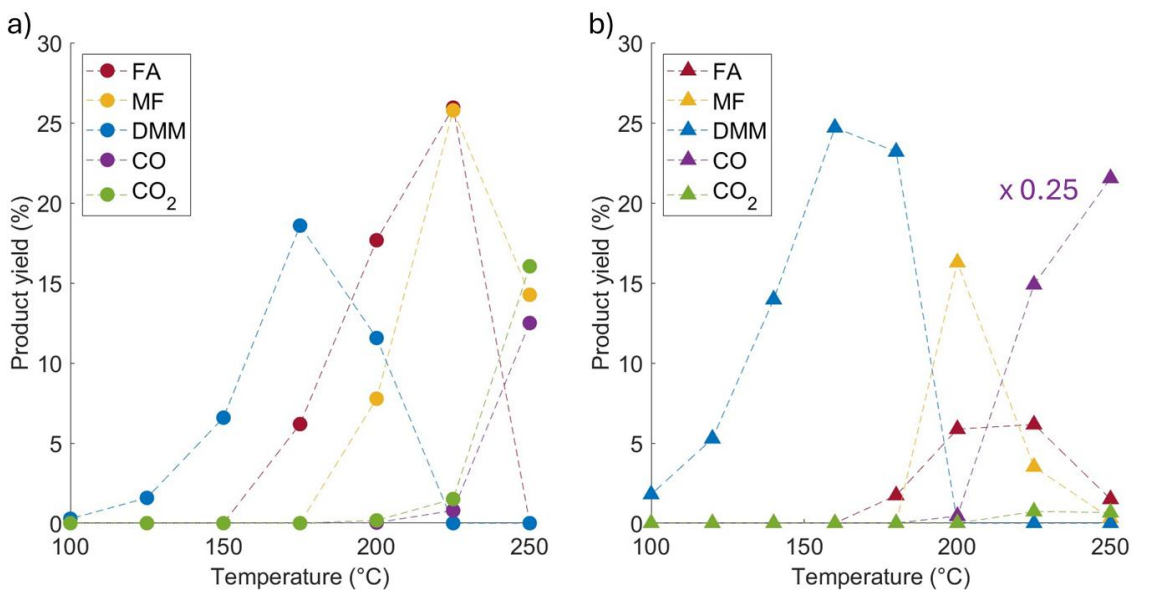

Figure III-6. Yield of FA, MF, DMM, CO and CO_2 as a function of reaction temperature for a) 2.5 VTi (GHSV = 20 L h^{-1} g_{cat}^{-1}, $CH_3OH/O_2/N_2$ (feed) = 4/4/92 %v/v) and b) 15 VTi (GHSV = 20 L h^{-1} g_{cat}^{-1}, $CH_3OH/O_2/N_2$ (feed) = 4/10/86 %v/v).

The differences observed on the catalytic behavior between both catalysts suggest that the VO_x surface structure influences the activity and the selectivity of the methanol ODH reaction, with higher VO_2 loading (or higher surface density of vanadium atoms) favoring the oxidation of methanol at higher temperatures.

It can also be seen that there is formation of DMM even if FA is not present, suggesting that the desorption and subsequent re-adsorption of FA is not a necessary step for the formation of DMM and MF, which will be later confirmed with the kinetic model fitting. It has been reported that FA would not adsorb on vanadium surfaces at room temperature [193]**.** It can also be seen that the maximum in the DMM formation is directly associated to the rise in MF yield, suggesting that the formation of both products depends on the same reaction intermediate. Hemiacetal (CH_3OCH_2OH) has been previously proposed in literature as the reaction intermediate for methanol ODH reaction [48,64,86,88,90,234–236], which is the reactive pathway backed by DFT calculations [90,91]. Figure III-7 shows a proposal of the reaction pathways considering this hemiacetal intermediate, where CH_3OH first oxidizes to form HCHO, which is subsequently converted to the hemiacetal reaction intermediate, which dehydrates to form DMM or oxidizes to form MF, in parallel pathways. Considering the hemiacetal parallel reactive pathways, the MF formation must have a higher apparent activation energy than the DMM formation, as the latter forms at lower temperatures (Figure III-6).

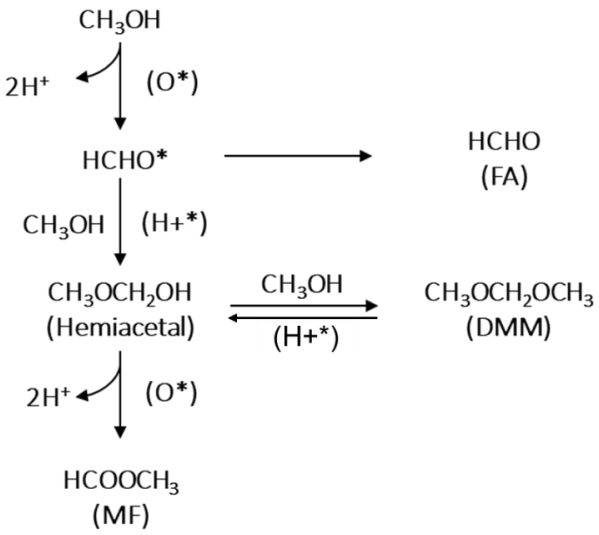

Figure III-7. Summary of the pathways for the methanol ODH reaction considering the hemiacetal intermediate.

Figure III-8.a and Figure III-8.b shows the FA, MF and DMM yield as function of the residence time for 2.5 and 15 at. V nm^{-2}, respectively. When the residence time increases, DMM formation decreases and MF proportionally increases, suggesting that the DMM formation can undergo its reverse reaction, as has been previously reported [48]. The MF formation from DMM is discarded, as previous DFT calculations or experimental evidence does not support this argument [42,90,91,234,237], in agreement with our findings. The DMM reverse reaction does not influence FA formation, suggesting that only the formation of DMM from the hemiacetal intermediate is reversible (Figure III-8).

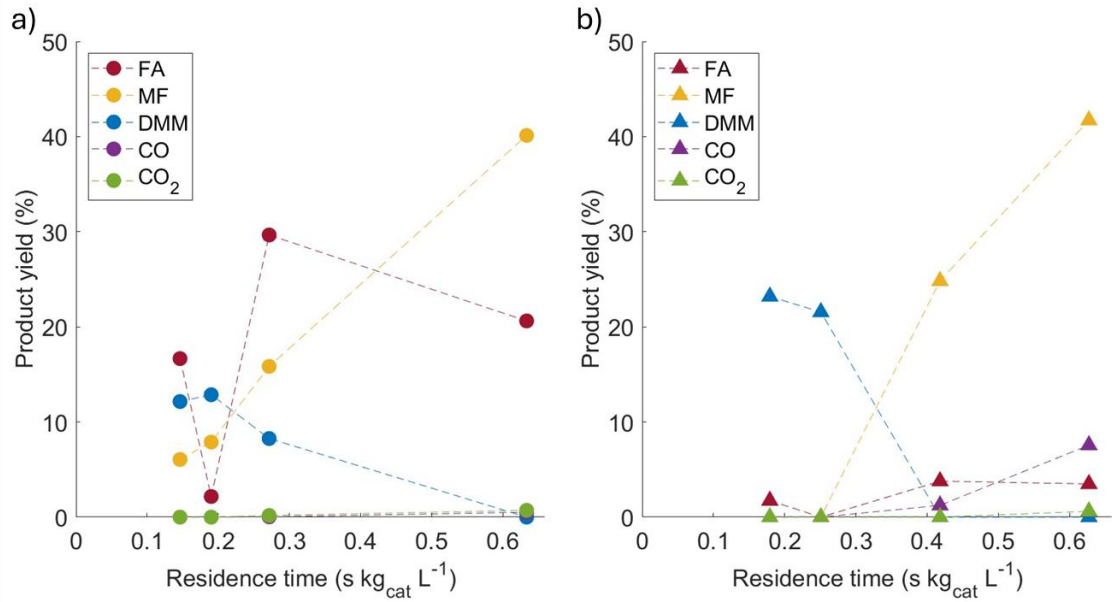

Figure III-8. Yield of FA, MF, DMM, CO and CO_2 as a function of the residence time for

a) 2.5 VTi (200 °C, $CH_3OH/O_2/N_2$ (feed) = 4/4/92 % v/v) and c) 15 VTi (180 °C, $CH_3OH/O_2/N_2$ (feed) = 4/10/86 % v/v).

Figure III-9 shows the effect of partial pressure of CH_3OH, O_2 and H_2O on the product yield for 2.5 and 15 V nm^{-2} catalysts. CH_3OH pressure can increase or decrease the formation of ODH products (Figure III-9.a and Figure III-9.b). The effect of CH_3OH pressure is hard to interpret, given the convoluted web of elemental steps consequence of the parallel and in series reactions, which in turn leads to complex L-H expressions, as will be shown later. The formation of ODH products is not significantly influenced by O_2 partial pressure (Figure III-9.c and Figure III-9.d), becoming negligible as the O_2 partial pressure is increased. This behavior is characteristic of Mars-van Krevelen redox reactions, suggesting that at higher O_2 pressures (when compared to CH_3OH pressure) the reoxidation steps are much faster than the ODH reaction, so the reduced center would be a minority species on the surface and the rate constant for this step can be disregarded, as has been reported [84,85,238,239]. Figure III-9.e shows that H_2O pressure influences the yield of the different product. It has been shown that the H_2O chemisorption and its competition with methanol for redox or acid sites can be disregarded, because its adsorption free energy is orders of magnitude lower than that of CH_3OH [48]. Thus, the effect of H_2O concentration on the yield of the ODH products would be consequence of the reversibility of the DMM formation, where the presence of water, a reaction product, would shift the chemical equilibrium and favor the DMM reverse reaction at higher H_2O pressures, to form the hemiacetal intermediary. H_2O would not affect the FA formation as this reaction is not in chemical equilibrium and/or is not affected by the DMM equilibrium, as was observed.

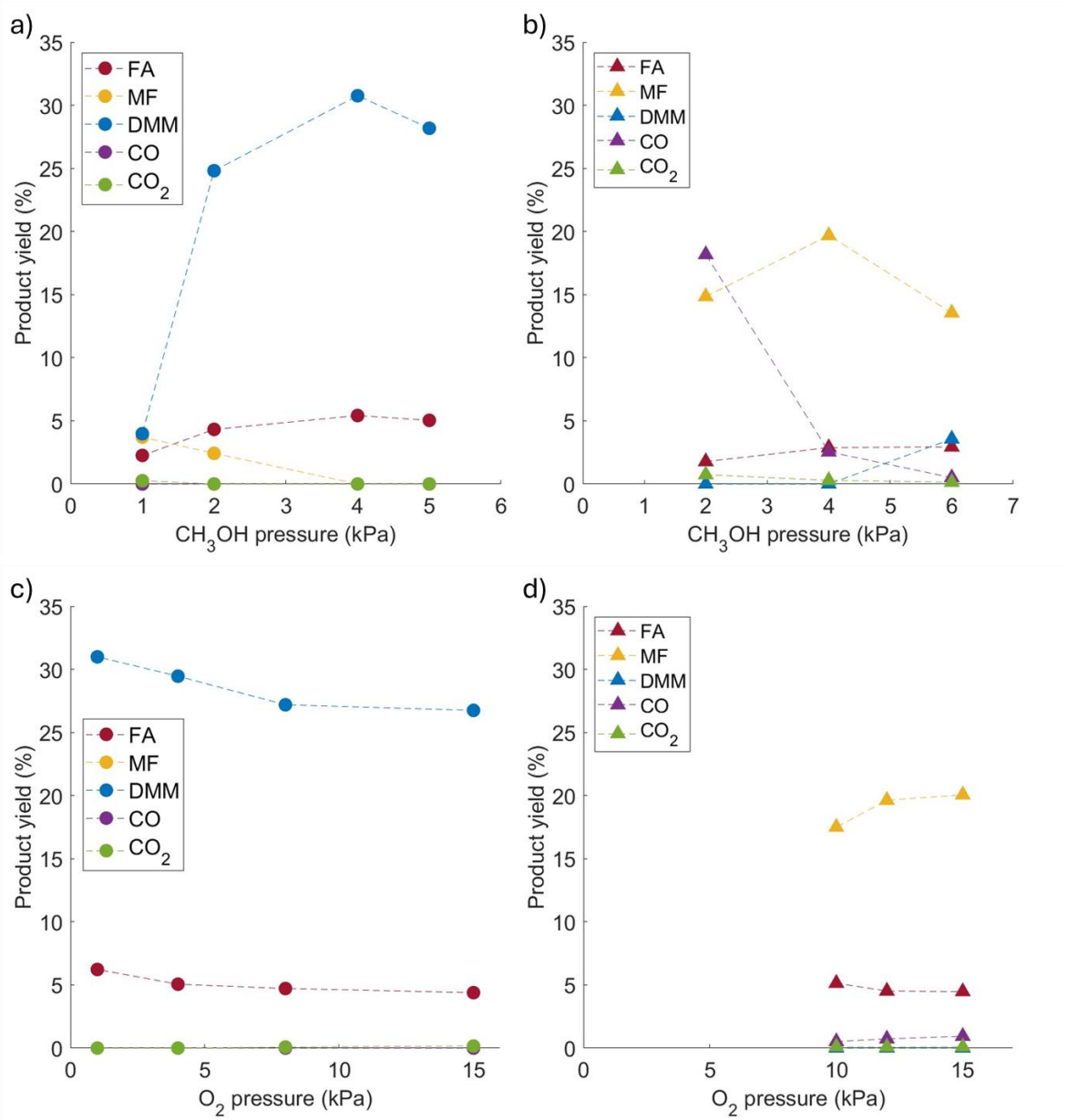
a)
b)
c)
d)
FA
MF
DMM
CO
CO2
Product yield (%)
CH3OH pressure (kPa)
O2 pressure (kPa)

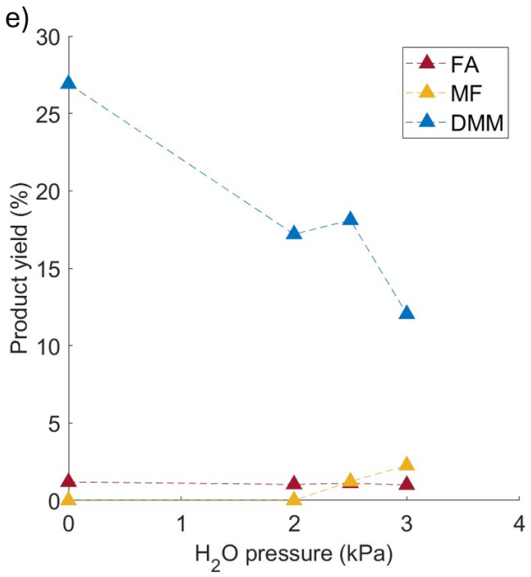

Figure III-9. Yield of FA, MF, DMM, CO and CO_2 as a function of: CH_3OH pressure on a) 2.5 VTi (GHSV = 20 L h^{-1} g_{cat}^{-1}, O_2/N_2 (feed) = 4/4/balance %v/v, 175 °C), b) 15 VTi (GHSV = 14 L h^{-1} g_{cat}^{-1}, O_2/N_2 (feed) = 4/10/balance %v/v, 190 °C); O_2 pressure on c) 2.5 VTi (GHSV = 20 L h^{-1} g_{cat}^{-1}, CH_3OH/N_2 (feed) = 4/balance %v/v, 175 °C), d) 15 VTi (GHSV = 14 L h^{-1} g_{cat}^{-1}, CH_3OH/N_2 (feed) = 4/balance %v/v, 190 °C; e) H_2O partial pressure on 15 VTi (GHSV = 14 L h^{-1} g_{cat}^{-1}, $CH_3OH/O_2/N_2$ (feed) = 4/10/balance %v/v).

3.3 Model derivation

A kinetic model for the methanol partial oxidation was proposed considering a hemiacetal intermediate [64,86], as shown on Figure III-7. The model consists of 14 net reactions steps and considers two different types of sites, a redox site for dehydrogenation reactions and an acid site for dehydration reactions, as has been proposed [84,191,223,238]. Each reaction product (FA, MF and DMM) has its own elementary steps which can be shared between them, and the net reaction rate is given by the sum of each step (e.g. $r_1 = r_1^{FA} + r_1^{MF} + r_1^{DMM}$). Table III-3 shows a plausible sequence of elementary steps for the methanol partial oxidation to FA, MF and DMM, considering previous DFT calculations and the experimental observations discussed on this work. For the sake of model simplicity, CO_x production from methanol data at high temperature (≈ 200-250 °C), was not considered on the model derivation. Besides, the data at low methanol partial pressure (1 kPa) was also not used for parameter fitting due to its high experimental error.

Table III-4. Summary of the net elementary steps for methanol ODH to form FA, MF and DMM, via hemiacetal intermediate.

Step	Description	Elemental Step
1	Molecular chemisorption of	$CH_3OH_{(g)} + O^* \overset{K_1}{\leftrightarrow} CH_3OH - O^*$

	methanol on a redox site	
2	Methanol dehydrogenation (rds):	$CH_3OH - O^* \xrightarrow{k_{ODH}} O_lH/HCHO - HO^*$
3	FA desorption:	$OH/HCHO - HO^* \xrightarrow{k_3} HCHO + O_lH/HO^*$
4	OH groups recombination:	$O_lH/HO^* \overset{K_4}{\leftrightarrow} * + H_2O$
5	First oxygen vacancy reoxidation:	$O_2 + * \xrightarrow{k_5} O^* + O_M$
6	Second oxygen vacancy reoxidation:	$O_M + * \xrightarrow{k_6} O^*$
7	Molecular chemisorption of methanol on an acid site:	$CH_3OH_{(g)} + H^+ \overset{K_7}{\leftrightarrow} CH_3OH - H^+$
8	Hemiacetal intermediate formation:	$CH_3OH - H^+ + O_lH/HCHO - HO^* \xrightarrow{k_8} HOCH_2OCH_3 - H^+ + O_lH/HO^*$
9	Hemiacetal interfacial spillover to a redox site	$HOCH_2OCH_3 - H^+ + O^* \overset{K_9}{\leftrightarrow} HOCH_2OCH_3 - O^* + H^+$
10	Hemiacetal dehydrogenation:	$HOCH_2OCH_3 - O^* \xrightarrow{k_{10}} OtH/HCOOCH_3 - HO^*$
11	MF desorption:	$OH/HCOOCH_3 - HO^* \xrightarrow{k_{11}} HCOOCH_3 + O_lH/HO^*$
12	Dehydration reaction:	$HOCH_2OCH_3 - H^+ + \underset{k_{12}^-}{\overset{k_{12}}{\rightleftarrows}} CH_2OCH_3 - H^+ + H_2O$
13	DMM reversible formation:	$CH_2OCH_3 - H^+ + CH3OH \overset{K_{13}}{\leftrightarrow} CH_2OCH_3OCH_3 - H^+$
14	DMM desorption:	$CH_2OCH_3OCH_3 - H^+ \overset{K_{14}}{\leftrightarrow} CH_2OCH_3OCH_3 + H^+$

O^*: redox lattice oxygen site.
H^+: Brønsted acid site.
O_M: unstable atomic oxygen species after the first oxygen vacancy regeneration with molecular O_2.
O_lH: O-H pair in a lattice oxygen next to the dehydrogenation site.

The first step of the reaction is the quasi-equilibrated methanol chemisorption on a redox site, a lattice O^* atom (step 1). This step can occur via molecular (CH_3OH) or dissociative (methoxy) chemisorption [84]. Kinetically, the distinction between both steps is irrelevant because both routes lead to the same rate equation. The second step is the irreversible abstraction of H atoms from an adsorbed methanol by action adjacent O^* species, to form the HCHO-HO^* pair (step 2). The H abstraction of the C-H bond is the indisputable kinetically relevant step [69,72,83–85]. FA can desorb (step 3) or react with a chemisorbed CH_3OH

molecule catalyzed by an acid site (step 8) to form the hemiacetal intermediate (CH_3OCH_2OH). There is evidence that the methanol ODH reaction is sensitive to the coverage of the active phase on the support [48,53,64,66,72,190], and previous works have proposed that the methanol reactions that require sites on both the metal and the support should occur on the interface between these two phases [48,240].

The hemiacetal intermediate formed on an acid site can undergo an acid-catalyzed nucleophilic addition and S_N1-condensation reaction. First, the hemiacetal undergoes a reversible and kinetically relevant dehydration (step 12). The dehydrated intermediate can react with gaseous methanol in an Eley-Rideal type mechanism, to form adsorbed DMM on an acid site (step 13), which can later desorb as gaseous DMM (step 14). This formation could be analogous to the formation of DME on acid sites from CH_3OH, which has been previously reported [238]. There exists the possibility that an analogous DMM formation occurs, with the reversible and kinetically relevant dehydration occurring after the CH_3OH substitution directly on the hemiacetal to form the hemiacetal-methanol dimer species (S_N2 pathway), but kinetically this is irrelevant as the net rate equation is the same. Given the low equilibrium constant, and the low concentration and spontaneous reaction of hemiacetal, these steps are considered in quasi equilibrium[48].

As the MF formation requires that the hemiacetal intermediate is dehydrogenated, this intermediate should spillover to a redox site (step 9). Here, hemiacetal can undergo a dehydration step analogous to that of methanol in the first part of the mechanism. The hemiacetal suffers a H abstraction using neighboring O^* atoms, to form the MF and OH pair (step 10), which can later desorb to form gaseous MF (step 11).

Finally, the proximate OH pairs can recombine to reversibly form gaseous H_2O and an O-vacancy. Gaseous O_2 can react with two vacancies on sequentially step and regenerate the vacancies via irreversible O_2 dissociation, completing a Mars-van Krevelen redox cycle, returning the V^{3+} to its initial electronic state (step 5 and 6). This reoxidation steps are much faster than the reduction steps, therefore their kinetics cannot be measured [84,85,238,239]. Consequently, these steps do not influence the rate equations.

Given the elementary steps on Table III-5, kinetic models for the formation of formation of FA, MF and DMM were derived. Details on the kinetic model derivation can be found on Appendix: Chapter III, Section A-IIII.7). The rate-determining step for each reaction path was the initial methanol dehydrogenation, as has been discussed by several authors [69,72,83–85]. That way, the mathematical expressions for the ODH products formation rates were derived, considering pseudo-steady-state treatments of the elementary steps and quasi-equilibrium approximations, expressed in terms of approach to equilibrium:

$$r_{FA} = \frac{K_1 k_{ODH} P_{CH_3OH} \theta_{O^*}}{1 + \frac{1}{k_{FA/HA}} K_7 P_{CH_3OH} \theta_{H^+}} \qquad \text{(III-6)}$$

$$r_{MF} = \frac{K_1 k_{ODH} P_{CH_3OH} \theta_{O^*}}{\left(1 + k_{FA/HA} \frac{1}{K_7 P_{CH_3OH} \theta_{H^+}}\right)\left(1 + \frac{1}{k_{MF/DMM}} \frac{\theta_{H^+}}{\theta_{O^*}}\right)} \left(1 + \eta \frac{1}{k_{MF/DMM}} \frac{\theta_{H^+}}{\theta_{O^*}}\right) \quad \text{(III-7)}$$

$$r_{DMM} = \frac{K_1 k_{ODH} P_{CH_3OH} \theta_{O*}}{\left(1 + k_{FA/HA} \frac{1}{K_7 P_{CH_3OH} \theta_{H^+}}\right)\left(1 + k_{MF/DMM} \frac{\theta_{O^*}}{\theta_{H^+}}\right)} (1 - \eta) \quad \text{(III-8)}$$

With:

$$k_{FA/HA} = \frac{k_3}{k_8} \quad \text{(III-9)}$$

$$k_{MF/DMM} = \frac{K_9 \, k_{10}}{k_{12}} \quad \text{(III-10)}$$

$$k_c = \frac{k_{12}^{-} \, K_{14}}{K_{13}} \quad \text{(III-11)}$$

And:

$$\eta = \frac{\frac{P_{DMM} P_{H2O}}{PCH3OH^3}}{K'_{DMM}} \frac{\left(1 + \frac{1}{k_{FA/HA}} K_7 \, P_{CH_3OH} \theta_{H^+}\right)}{K_7 \, \theta_{H^+}} \quad \text{(III-12)}$$

$$K'_{DMM} = \frac{K_1 \, k_{ODH}}{k_{FA/HA} \, k_{MF/DMM} \, k_C} \left(= \frac{K_1 \, k_2 \, k_8 \, k_{12} \, K_{13}}{k_3 \, k_9 \, K_{10} \, k_{12}^{-} \, K_{14}}\right) \quad \text{(III-13)}$$

$$\theta_{O_l} = \frac{1}{1 + K_1 \, P_{CH_3OH}} \quad \text{(III-14)}$$

$$\theta_{H^+} = \frac{1}{1 + \, K_7 \, P_{CH_3OH}} \quad \text{(III-15)}$$

From the integral kinetic data and the fitting of the kinetic parameters, the model can be simplified, reducing the number of kinetic parameters without abruptly increasing the fit error. The criteria for this simplification was the confidence interval, where a confidence interval that includes zero would mean that the parameter has a non-statistically significant effect on the proposed model. This was the case, as eliminating these parameters from the model did not increase significantly the MAPE.

First, methanol would chemisorb strongly on the acid site, or would dominate the acid site surface.

$$K_7 \, P_{CH_3OH} \theta_{H^+} \approx 1 \quad \text{(III-16)}$$

We also observed that for most of the points, DMM was the primary reaction product when comparing to MF, which then means that the ratio of DMM to MF forward formation rate, governed by the inverse of the $k_{MF/DMM}$ ratio, should be much greater than 1:

$$1 \ll \frac{1}{k_{MF/DMM}} \frac{\theta_{H^+}}{\theta_{O^*}} \tag{III-17}$$

Considering the above shown considerations, the kinetic expressions can be simplified to the following rate equations:

$$r_{FA} = \frac{K_1 k_{ODH} P_{CH_3OH} \theta_{O^*}}{1 + \frac{1}{k_{FA/HA}}} \tag{III-18}$$

$$r_{MF} = \frac{K_1 k_{ODH} P_{CH_3OH} \theta_{O^*}}{1 + k_{FA/HA}} (\eta) \tag{III-19}$$

$$r_{DMM} = \frac{K_1 k_{ODH} P_{CH_3OH} \theta_{O^*}}{1 + k_{FA/HA}} (1 - \eta) \tag{III-20}$$

While equation (III-12) turns to:

$$\eta = \frac{\frac{P_{DMM} P_{H2O}}{PCH3OH^2}}{K'_{DMM}} \left(1 + \frac{1}{k_{FA/HA}}\right) \tag{III-21}$$

This same expression can be obtained when considering the DMM formation in quasi-equilibrium in a pseudo-steady state Langmuir-Hinshelwood derivation ($r_{DMM} \approx 0$), which can be interpreted as that the DMM formation would be in quasi-equilibrium when compared to the rate of the kinetically relevant step: the methanol dehydrogenation. Given that the DMM formation is sufficiently fast to be considered in quasi-equilibrium, the MF formation rate goes from 0 (far away from DMM equilibrium) to the hemiacetal consumption rate (in the DMM equilibrium). It is worth to know that, after the simplifications, the steps that lead to DMM formation are not kinetically relevant, so DMM could be formed by S_N1 or S_N2 nucleophilic substitution.

In the proposed model, K_1 is the chemisorption constant of methanol on a redox site, while the k_{ODH} constant is the kinetic constant of the rate determing step C-H bond scission. The rate constant $k_{FA/HA}$ (eq. III-9) is a ratio of kinetics constants that determines the selectivity to the two different pathways that can undergo the HCHO: the desorption or its subsequent reaction to form hemiacetal. Parameter k_c lumps the different constants that define the net rate of DMM quasi-equilibrated formation. The rate of reoxidation of the oxygen vacancies was not considered on the model, given the observed weak effect of O_2 partial pressure, as was previously discussed. The kinetic equations are a function of two different site balances, the redox sites O^* and the Brønsted acid sites H^+ On the redox sites, only coverage of methanol was considered MARI, while on the acid sites the surface was completely

dominated by methanol. That way, we could develop a kinetic model for the formation of the three main products, FA, DMM and MF, that depends only on 4 parameters.

Given that the formation of each product (FA, MF and DMM) requires an initial methanol dehydrogenation step, the ODH net rate equals the sum of each rate of formation, consistent with a Mars-van Krevelen redox cycle involving V-O pairs.

$$r_{ODH} = r_{FA} + r_{MF} + r_{DMM} = K_1 k_2 P_{CH_3OH} \theta_{O^*} \quad \text{(III-22)}$$

The ODH reaction was considered irreversible, given the large equilibrium constants at the reaction temperatures [48].

3.4 Parameter fitting

A summary of the parameters of the kinetic models and the statistics are summarized on Table III-6. The preexponential factor is expressed as the value of the kinetic rate constant at 450 K, by the equation:

$$k_i = k_i^{450\ K} e^{-\frac{E_i}{R}\left(\frac{1}{T\ [K]} - \frac{1}{450\ [K]}\right)} \quad \text{(III-23)}$$

Table III-7. Parameter fitting for the FA, MF and DMM formation kinetic model, on 2.5 VTi and 15 VTi catalysts.

Kinetic parameter	**Sample**	
	2.5 at. V nm^{-2}	**15 at. V nm^{-2}**
$K_1^{450\ K}\ (kPa^{-1})$	1.37 ± 0.80	0.17 ± 0.06
$-\Delta H_1\ (kJ\ mol - 1)$	101.7 ± 36.7	83.7 ± 10.8
$k_{ODH}^{450\ K}\left(mol\ min^{-1}\ mol_{V_2O_5}^{-1}\right)$	3.46 ± 0.61	0.99 ± 0.24
$E_{a_{ODH}}\ (kJ\ mol^{-1})$	79.9 ± 5.1	61.1 ± 5.7
$k_{FA/HA}^{450\ K}$	0.82 ± 0.23	0.22 ± 0.02
$E_{a_{FA/HA}}\ (kJ\ mol^{-1})$	60.4 ± 22.5	88.3 ± 6.9
$K'^{450\ K}_{DMM}$	1.80 ± 1.41	0.10 ± 0.02
$-\Delta H'_{DMM}(kJ\ mol^{-1})$	276.7 ± 59.0	311.4 ± 25.0

The ODH kinetic constant is expressed as an apparent TOF normalized by total V_2O_5 content. This apparent TOF is not entirely appropriate for activity comparisons because it does not account for the surface vanadium oxide nor the particular active sites that actually participate in the ODH reaction, which may or may not be V-O-V pairs as has been contradictorily discussed for this reaction [48,51,205]. Instead, our discussion will be centered in the

energies of the contributing kinetic steps as a mean to compare the intrinsic activity of the reaction as its quantification is independent of the content of vanadium and the quantity of active sites.

The obtained kinetic parameters allow to quantitatively describe the differences observed between both catalysts. We observed an effect on the nature of the active with the increase of vanadium surface density, as reflected on the change on the value of the energies associated to the kinetic parameters. It can be seen that, at higher vanadium surface density, methanol has a lower heat of chemisorption $-\Delta H_1$ (101.7 versus 83.7 kJ mol^{-1}), which means that CH_3OH adsorbs more weakly on the redox sites on the 15 VTi catalyst; methanol ODH has a lower energy barrier $E_{a_{ODH}}$ (79.9 versus 61.1 kJ mol^{-1}), which means that the more coordinated VO_x surface of the 15 VTi catalyst dehydrogenates methanol more easily on the redox sites; the methanol transformation to MF and DMM, when compared to the desorption of FA, is favored on the 15 VTi catalyst, as the higher activation energy of the ratio $E_{a_{FA/HA}}$ shows (60.4 versus 88.3 kJ mol^{-1}); and the formation of MF is also favored, because the apparent enthalpy of the constant that defines the DMM equilibrium, $-\Delta H'_{DMM}$, obtained when lumping all the kinetic and adsorption/desorption constants of the elementary steps leading to the DMM formation, including the parallel pathways to FA and MF, is larger at higher surface densities (267.7 versus 311.4 kJ/mol). In this work, it has been previously shown that MF formation is affected by the DMM equilibrium (III-19), and the 2.5 VTi catalyst approaches the equilibrium at lower temperatures than the 15 VTi sample, which is a consequence of its lower $-\Delta H'_{DMM}$, as an exothermic reaction. When operating far away from the equilibrium, we would not observe MF formation, as is far slower than the DMM formation, which can be considered in quasi-equilibrium when compared to the rate-determining step.

The activation energy for methanol ODH reaction is in line with previously reported values on V_2O_5/TiO_2. Broomhead and collaborators report an activation energy for the *rds* of 76 kJ mol^{-1}, while Wachs reports values around 83 kJ mol^{-1} for monolayer and sub-monolayer vanadia catalysts[53]. On vanadium and chromium oxide, Cozzolino and coworkers report values of 40-80 kJ mol^{-1} for methanol ODH on supported and bulk catalysts [45], while Tatibouët reports, in general, values around 85 kJ mol^{-1}, no matter the catalyst/support duo [72].

Comparing the heat of CH_3OH adsorption values, our results are also in similar orders of magnitude compared to reported values of - 90 kJ mol^{-1} on monomeric VO_x supported on TiO_2, calculated by DFT [241], and values of -121 kJ mol^{-1} on a nano-structured vanadium oxide catalyst supported on TiO_2/SiO_2 [45].

Regarding the role of surface density of vanadia, by Raman, XRD and UV-vis we observed that at higher vanadium content, phases and bands attributed to crystalline V_2O_5 start to appear, accompanied by a decrease of the absorption edge energy calculated from the Tauc

law (also known as the energy of the band gap), approaching the bulk value at densities higher than 15 V nm^{-2}, evidencing the change from monomers and polymers of vanadium oxide to crystalline vanadium oxides. The link between the band gap energy and the reducibility of mixed oxides would mean that the crystalline catalyst is more reducible than the dispersed vanadium oxide catalyst, which then would explain the differences in the intrinsic ODH activity, specifically in the energies of the kinetic parameters. The 15 V nm^{-2} sample is the more active catalyst, with a lower energy barrier (or transition state energy) for the rate limiting step caused by its higher reducibility, as this step is the C-H bond dehydrogenation, and this property favors its capability to complete the redox cycles necessary for the dehydrogenation reactions of methanol in the rate limiting step.

The kinetic model reproduces the catalytic performance over the whole range of studied operation conditions (residence time, temperature, and partial pressure of reactants) and adequately predicts the methanol ODH products formation with MAPE values around the 20%.

In Figure III-10.a, parity plots of the models for catalyst 2.5 V nm^{-2} and 15 V nm^{-2} are shown, respectively, for the formation of FA, MF and DMM. Most of the points (60%) are inside the +-20 lines, with 80% of the points have less than 30% error. Some points are in a straight line parallel to the x-axis, due to neglecting the influence of O_2 pressure on the methanol ODH reaction. Nevertheless, the error introduced by this simplification is less than 20%. The parity plot of O_2 consumption rate, which was also fitted, can be found on Figure III-10.b.

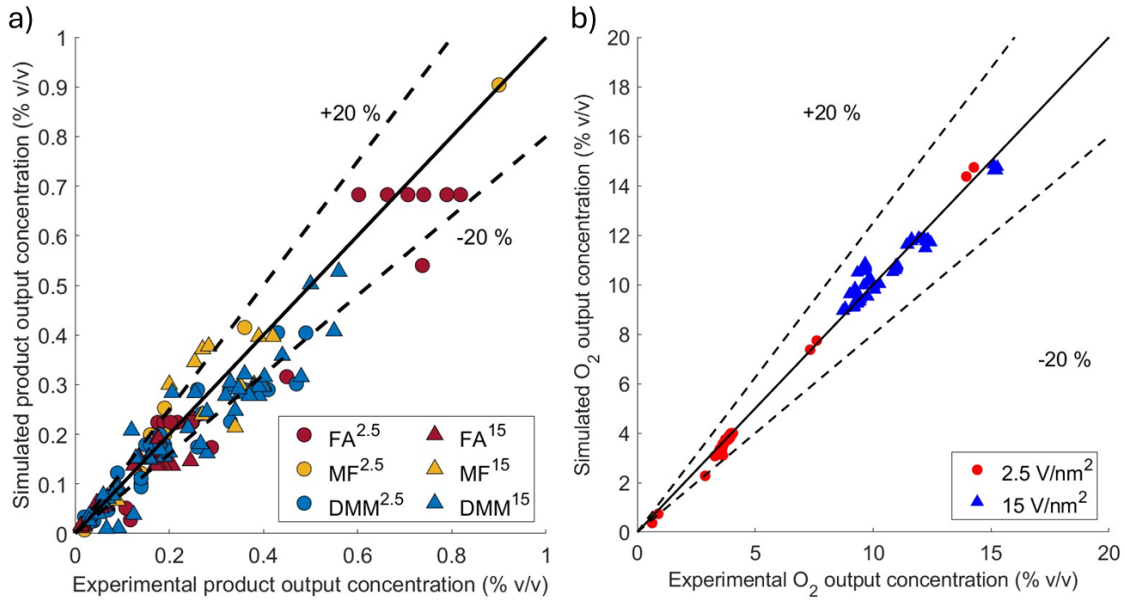

Figure III-10. Parity plot comparing experimental and predicted output concentrations on 2.5 VTi and 15 VTi catalysts for of a) FA, MF and DMM, b) O_2.

Figure III-11.a and Figure III-11.b shows experimental and simulated data for the 2.5 and 15 V nm^{-2} catalyst, respectively. The models adequately simulate the trends at temperatures

between 100 and 250 °C, correctly predicting the abrupt change of the yields with the temperature and the interchange of DMM and MF formation (Figures A-III.8 and A-III.9). The model also predicts the effect of residence time on the product yields (Figures A-III.10 and A-III.11), accurately simulating the decrease of DMM yield accompanied by the increase of MF yield as the residence time rises, given by the reverse reaction of DMM and the consequently MF formation. It can be seen that the model present discrepancies at low methanol partial pressures (≤ 1 kPa, Figures A-III.12 and A-III.13), most likely from the simplification presented on equation III-16, where methanol is presumed to dominate the acid surface. However, we should expect a lower coverage of methanol on the acid sites due to the lower methanol partial pressure. The model also predicts the change in the product distribution with the partial pressure of water and O_2 (Figures A-III.14 to A-III.17). Also, the model presents discrepancies when simulating the effect of O_2 pressure, due to the approximation for the rate of regeneration of the oxygen vacancies, which was considered to be much faster than the rate of methanol ODH. This simplification is only satisfied when the O_2 partial pressure is much greater than the CH_3OH partial pressure. Other discrepancies are due to the presence of CO_x on the reaction products, which were not considered in the derivation of the models.

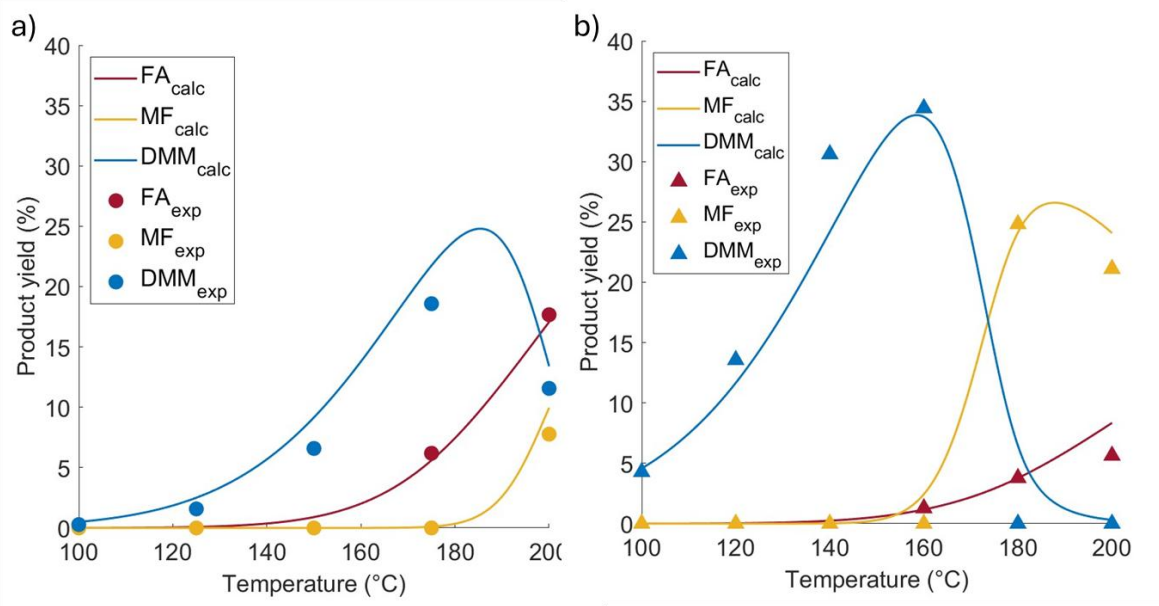

Figure III-11. Predicted (line) vs experimental (symbols) FA, MF and DMM yield on a) 2.5 VTi (GHSV = 20 L h^{-1} g_{cat}^{-1}, $CH_3OH/O_2/N_2$ (feed) = 4/4/balance %v/v) and b) 15 VTi (GHSV = 10 L h^{-1} g_{cat}^{-1}, $CH_3OH/O_2/N_2$ (feed) = 4/10/balance %v/v).

3.5 Selectivity descriptors

Given the proposed reaction mechanism and the kinetics expressions obtained, the selectivity of the different species can be analyzed to study the kinetic tuning for each different product,

towards the engineering of catalytic surfaces with finely tuned selectivity. In our complete model, the DMM to MF ratio is defined as:

$$\frac{r_{DMM}}{r_{MF}} = \frac{\frac{K_1 k_2 P_{CH_3OH} \theta_{O^*}}{\left(1 + k_{FA/HA} \frac{1}{K_7 P_{CH_3OH} \theta_{H^+}}\right)\left(1 + k_{MF/DMM} \frac{\theta_{O^*}}{\theta_{H^+}}\right)} (1 - \eta)}{\frac{K_1 k_2 P_{CH_3OH} \theta_O}{\left(1 + k_{FA/HA} \frac{1}{K_7 P_{CH_3OH} \theta_{H^+}}\right)\left(1 + \frac{1}{k_{MF/DMM}} \frac{\theta_{H^+}}{\theta_{O^*}}\right)} \left(1 + \eta \frac{1}{k_{MF/DMM}} \frac{\theta_{H^+}}{\theta_{O^*}}\right)} \quad \text{(III-24)}$$

If we are close to the DMM equilibrium, $\eta = 1$, and the net DMM formation is zero (therefore, the $\frac{r_{DMM}}{r_{MF}}$ ratio is zero). If we are far from equilibrium, $\eta = 0$, then:

$$\frac{r_{DMM}}{r_{MF}} = \frac{1}{k_{MF/DMM}} \frac{\theta_{H^+}}{\theta_{O^*}} \quad \text{(III-25)}$$

It can be seen that the $k_{MF/DMM}$ defines the DMM to MF forward rate. To maximize the selectivity to DMM, we would need to decrease the coverage of species on the acid sites, increase it on the redox sites and/or decrease the $k_{MF/DMM}$ rate constant.

The DMM to FA ratio is defined as:

$$\frac{r_{DMM}}{r_{FA}} = \frac{\frac{K_1 k_2 P_{CH_3OH} \theta_{O^*}}{\left(1 + k_{FA/HA} \frac{1}{K_7 P_{CH_3OH} \theta_{H^+}}\right)\left(1 + k_{MF/DMM} \frac{\theta_{O^*}}{\theta_{H^+}}\right)} (1 - \eta)}{\frac{K_1 k_2 P_{CH_3OH} \theta_{O^*}}{1 + \frac{1}{k_{FA/HA}} K_7 P_{CH_3OH} \theta_{H^+}}} \quad \text{(III-26)}$$

If we are close to the equilibrium, it can be seen that again the net DMM formation is zero. If we are far away from the equilibrium, the selectivity to DMM, when compared to FA, can be increased by decreasing the $k_{FA/HA}$ and $k_{MF/DMM}$ rate constant, as to maximize hemiacetal and DMM formation; increasing the methanol partial pressure and decreasing the coverage of species on the acid sites and increasing it on the redox sites.

The MF to FA ratio is defined as:

$$\frac{r_{MF}}{r_{FA}} = \frac{\frac{K_1 k_2 P_{CH_3OH} \theta_{O^*}}{\left(1 + k_{FA/HA} \frac{1}{K_7 P_{CH_3OH} \theta_{H^+}}\right)\left(1 + \frac{1}{k_{MF/DMM}} \frac{\theta_{H^+}}{\theta_{O^*}}\right)} \left(1 + \eta \frac{1}{k_{MF/DMM}} \frac{\theta_{H^+}}{\theta_{O^*}}\right)}{\frac{K_1 k_2 P_{CH_3OH} \theta_{O^*}}{1 + \frac{1}{k_{FA/HA}} K_7 P_{CH_3OH} \theta_{H^+}}} \quad \text{(III-27)}$$

The selectivity to MF when compared to FA depends on the DMM equilibrium. If we are close to the equilibrium, $\eta = 1$, the selectivity to MF can be increased by decreasing the $k_{FA/HA}$ rate constant, which in turn is maximizing the hemiacetal formation, increasing the methanol partial pressure, and decreasing the acid site coverage. In this case, the MF rate is equal to the hemiacetal net rate, as the DMM reaction is in equilibrium.

If we are far away from the DMM equilibrium, $\eta = 0$, we can increase the MF selectivity by increasing the $k_{MF/DMM}/k_{FA/HA}$ rate constant ratio, increasing the methanol pressure, and increasing the acid site coverage. It can be seen that the acid sites have an anti-synergistic effect, because they increase the hemiacetal formation but also increase the DMM formation, therefore, there should be an optimum in the concentration ratio of acid site to redox sites on the catalyst surface.

4. Conclusions

A Langmuir-Hinshelwood/Eley Rideal/Mars-van Krevelen kinetic model was successfully derived for the methanol ODH reaction products (FA, MF and DMM) considering hemiacetal as the intermediate for MF and DMM formation. The fitted model has a mean average error of 20% and depends on only 4 thermodynamically consistent kinetic parameters: the methanol chemisorption constant on the redox sites, the kinetic rate constant of the rate-limiting step (chemisorbed methanol C-H bond incision), the FA/HA kinetic rate constant ratio and the constant that groups the terms that define the DMM equilibrium. It was found that the redox properties primarily determine the activity of the catalysts, which in turn are closely related to the vanadium loading of the samples. When compared to the redox sites, the effect of coverage of the acid sites is non-statistically significant, as CH_3OH completely dominates the acid surface.

An increase in vanadium content leads to an increase in methanol ODH intrinsic activity (lower activation energy of the rate-determining step) and to a decrease in the coverage of adsorbed methanol species (lower enthalpy of CH_3OH chemisorption on the redox site). The lower activation energy of the rate limiting step as the surface density goes from 2.5 at. V nm^{-2} to 15 at. V nm^{-2} (61.1 kJ mol^{-1} versus 79.9 kJ mol^{-1}, respectively) correlates to the increase of the reducibility as the surface density of the catalysts rise, depicted as the decrease of adsorption edge energy from 3.2 eV to the bulk V_2O_5 value of 2.3 eV, as calculated from UV-vis results. Therefore, the crystalline VO_x domains enhance the capacity of the catalyst

to complete the necessary redox cycles for the methanol ODH reaction, while reducing the methanol chemisorption capacity.

The increased surface density of vanadium oxide influences the selectivity of the methanol ODH reaction by promoting the formation of hemiacetal and the approach to the DMM equilibrium, which can be considered in quasi-equilibrium when compared to the rate-determining step. Given that the DMM formation is sufficiently fast to be considered in quasi-equilibrium, the MF formation rate directly depends on the DMM equilibrium, going from 0 (far away from DMM equilibrium) to the hemiacetal consumption rate (in the DMM equilibrium). Further studies are necessary to quantify the effect of the redox and acid sites on the methanol ODH reaction mechanism.

Chapter IV: Effect of Si/Al Ratio on the activity and selectivity of V_2O_5/SiO_2-Al_2O_3 catalysts in methanol oxidative dehydrogenation

Summary

Methanol oxidative dehydrogenation was studied on low-loading, dispersed submonolayer V_2O_5/SiO_2-Al_2O_3 catalysts (0.7 V at nm-^{2}) with varying Si/Al ratio, in order to understand the effect of acid properties on the activity and selectivity of the reaction. H_2-TPR analysis showed similar redox properties across all samples, independent of the silica-alumina content. Similar methanol consumption TOF values (~10^{-4} s^{-1}) observed on all samples and also as compared with reported V_2O_5/Al_2O_3 catalysts indicates that the vanadium is uniformly interacting with alumina, regardless of silica conten. This findings confirm a common rate-determining step among the samples, exclusively governed by the redox properties of the supported catalysts. The deposition of vanadium on alumina reduced the alumina Lewis sites which form DME, resulting in selectivities similar to reported V_2O_5/SiO_2 catalysts. The similar redox properties and TOF values between samples confirmed that the acid properties of the support do not influence the methanol ODH redox activity. However, the composition of the support influences the selectivity, specifically the DMM/MF rate ratio. This is attributed to the change in Brønsted/Lewis ratio as the silica-alumina content changes. The catalysts should have stronger Brønsted acidity at support composition closer to pure alumina, as alumina has been reported to be necessary to activate the SiO_2 Brønsted acid sites. It was found that the Brønsted/Lewis acid ratio influences the DMM/MF formation rate ratio, with a maximum DMM/MF ratio of 3.8 observed at an Si mass fraction of 0.95. Nevertheless, the acidity of the metal oxide has a greater impact on ODH selectivity than that of the support.

1. Introduction

The acid properties of catalysts play a pivotal role in many reactions, influencing activity and/or selectivity toward different products, and the methanol oxidative dehydrogenation (ODH) reaction is not the exception. Brønsted (B) and Lewis (L) acid sites are usually associated with dehydration or acid condensation reactions, leading to products like dimethyl ether (DME), dimethoxymethane (DMM), and reaction intermediates such as hemiacetal. Therefore, the balance between these types of acid sites can significantly impact the product distribution in methanol ODH, making it critical for designing efficient catalysts tuned for specific reaction pathways.

In literature, the relationship between acidity and methanol ODH performance has been extensively studied. Single crystal studies have been employed to isolate the acid sites and avoid external influences from supports or oxide structure effects. For MoO_3 single crystals, the (100) surface contains Lewis acid site [131] which predominantly forms dimethoxymethane (DMM) [242–244]. In contrast, the MoO_3 (010) surface, lacking Lewis acid sites, only forms FA, indicating that FA formation does not require an acid site [245]. Similarly, in V_2O_5 single crystals, the (001) surface, analogous to the (100) surface of MoO_3,

is characterized by a dual site: a dehydrogenating redox site (for methoxy formation) and a Lewis acid site (for intermediate stabilization). This crystal selectively forms DMM, whereas FA formation requires only the dehydrogenating redox site [131].

Brønsted acid sites have also been proposed to play a significant role in methanol ODH by protonating methanol to form an intermediate for dehydration reactions. It was found that, as the number of Brønsted protons decreases, the coverage of protonated methanol intermediates diminishes, reducing DME formation more rapidly than redox ODH product formation (FA + MF + DMM) [246]. This leads to a higher selectivity toward oxidation pathways.

For more "real" catalysts, polyoxometalates (POMs) with Keggin type structures have been employed. These polyanionic clusters possess tunable redox and acidic sites [247], allowing researchers to investigate their effects on reaction kinetics [130,248,249]. It was shown that at high temperatures, surface crystallization[250,251] leads to Brønsted acidity loss[252], resulting in decreased DME selectivity and increased selectivity toward FA. The role of protons was further studied in POMs $H_{3+n}PV_nMo_{12-n}O_{40}$ supported on $K_3PMo_{12}O_4$[253]. It was found that the number of protons per Keggin unit directly correlates with the rate of total oxidation, while redox properties govern selectivity between dehydration and oxidation products. Additionally, substituting molybdenum with vanadium enhances both Brønsted acidity and redox properties, increasing methanol activity and redox selectivity.

The acid properties of the support can also impact catalytic activity. Lewis acidic supports, such as Nb_2O_5 and Al_2O_3, favor DME formation [254]. Similarly, in Keggin-type POMs supported on SiO_2, the acidic surface enhances dimethoxymethane (DMM) selectivity [249].

Recently, Lewis acid sites have been said to influence the MF formation via a Tischenko mechanism [48].

These findings highlight the importance of support selection in tuning both acidic and redox properties of supported catalysts. However, there is no general consensus on the effect of acid properties on the methanol ODH reaction, as the reaction activity has been said to be influenced by the acid properties and/or by the redox properties, DMM is formed on Lewis and/or Bronsted acid sites, and MF is formed on redox and/or Lewis acid sites. At the same time, comparisons between catalysts are challenging because conclusions are often drawn from experiments with different active phases and/or supports, each with its own redox properties and metal oxide structure. In this work, we synthetized SiO_2/Al_2O_3-supported molybdenum catalysts with varying silica percentage, and its effect on the methanol ODH activity and selectivity was evaluated. By changing the silica mass percentage in the aluminosilicate supports, we aimed to induce variations in the Brønsted/Lewis acid site ratio and examine their correlation with catalytic performance.

Our results demonstrate that the SiO_2/Al_2O_3 ratio influences the reaction pathways and product distribution in methanol ODH. Catalysts with higher Brønsted/Lewis acid site ratio

exhibited and increase in DMM/MF formation rate ratio, reaching a maximum near 100% Si, in accordance with the generation of Brønsted acid sites on the SiO_2 by its interaction with Al_2O_3. These findings provide valuable insights into the role of acid site balance in controlling methanol ODH selectivity and offer guidance for designing catalysts with tailored acidity for optimal performance.

2. Methodology

2.1 Catalyst preparation

SiO_2-Al_2O_3 mixed oxides were synthesized using the sol-gel method, varying the Si mass fraction (75, 85, 95, 99, and 100 %) following the methodology proposed by Agliullin et al. [255,256]. Tetraethyl orthosilicate (TEOS, $Si(OC_2H_5)_4$, Merck, CAS 78-10-4, ≥ 99%) was used as the silica precursor, while aluminum nitrate nonahydrate (ANN, $Al(NO_3)_3 \cdot 9H_2O$, Merck, CAS 7784-27-2, ≥ 98.5%) served as the alumina precursor. The samples were labelled χ Si, where χ stands for the silica mass fraction, expressed as wt.%. A representative preparation of the 75Si support is described as follows. Initially, 14 g of TEOS were dissolved in ethanol (EtOH, Merck, CAS 64-17-5, ≥ 99.9%) at a TEOS/EtOH molar ratio of 0.14. Simultaneously, 79 g of ANN was dissolved in distilled water, with the water amount determined by the quantity of TEOS used, at a TEOS/H_2O molar ratio of 0.1, under stirring at 300 rpm and room temperature. The TEOS solution was gradually added to the ANN solution, and the mixture was stirred for 30 min to homogenize. The resulting solution was then aged in a thermal bath at 60 °C for 20 h until gelation occurred. In the second step, the gel was removed from the bath, and ammonia (NH_4OH, Merck, CAS 105423, 28–30%) was added to the gel, at a TEOS/NH_4OH molar ratio of 1.26. The mixture was stirred in a rotary evaporator at room temperature for 1 h and aged overnight at 25 °C. The final gel was dried in an oven at 105 °C for 24 h and calcined in static air at 650 °C for 5 h, using a heating ramp of 10 °C/min. The calcined mixed oxides were subsequently employed as support for the synthesis of vanadia supported catalysts.

V_2O_5/SiO_2-Al_2O_3 supported catalysts were prepared by wet impregnation at a constant vanadium surface density (0.7 V at. nm^{-2}), in an analogous procedure as the described in Chapter III, section 2.1. The BET surface area of the synthesized SiO_2-Al_2O_3 was measured before the vanadium oxide impregnation.

2.2 Catalyst characterization

X-ray diffraction (XRD) and BET surface area, pore volumes and pore size distributions were determined as described in Chapter I, Section 2.2

H_2 Temperature programed reduction (H_2-TPR) was performed in a ChemBet Pulsar TPR/TPD (Quantachrome). Methodology details were described in Chapter I, Section 2.2

2.3 Catalytic activity measurements

The kinetic tests of the V_2O_5 /SiO_2-Al_2O_3 catalysts were performed in a stainless-steel tubular fixed-bed reactor in an analogous setup as described in Chapter II, Section 2.1.

The effect of the temperature (100-250 °C) and total flow rate (20-85 ml min^{-1}, constant length of catalyst bed) was studied. Due to the conversion values (> 10 %) necessary to obtain the 3 studied reaction products (FA, MF and DMM), the reaction was performed at integral reaction conditions. Deactivation of the catalyst was discarded by repeating the first reaction condition at the end of the experiments, observing the same activity. An example of methanol concentration versus time on stream is shown in figure A-IV.1 of Appendix: Chapter IV.

CH_3OH conversion (X) and FA, MF and DMM yields (Y) were calculated according to equations II-1 to II-4 (Chapter II, section 2.1).

3. Results

3.1 Characterization

Table IV-1 shows the properties of the synthesized silicoaluminates supports with varying silica content. The supports exhibit high surface areas, with pore sizes within the mesoporous range, confirming the effectiveness of the preparation method. Supports with silica content ranging from 75% to 99% (75Si to 99Si) display similar pore characteristics and BET surface areas. However, the 100Si sample differs, showing a lower BET area and larger pore size, likely due to the absence of ANN during preparation which should impact the correct sol-gel formation on this sample. The comparable BET surface areas among most supports indicate consistent structural properties, allowing the comparison of catalytic activity across the samples.

Table IV-1. Silica mass percent, surface BET area, mean pore volume and pore size in the mixed SiO_2 -Al_2O_3 supports synthesized by sol-gel.

Sample	Si (%)	BET Area (m^2 g^{-1})	Pore volume (cm^3 g^{-1})	Pore size (nm)
75Si	75	370	0.39	4.7
85Si	85	397	0.39	4.9
95Si	95	445	0.58	4.6
99Si	99	451	0.65	5.6
100Si	100	183	0.32	15.5

Table IV-2 presents the vanadia supported on aluminosilicates catalysts, with surface density of 0.7 at. V nm^{-2}. Due to the similar BET surface areas of the supports, the catalysts exhibit comparable nominal loadings, ranging from 3.8 to 4.6 wt.% V_2O_5. The exception is the 100Si

catalyst, which had a lower loading due to its reduced BET area. Additionally, no significant differences are observed in pore size or pore volume between the supports and the supported samples. This indicates good vanadia dispersion on the supports without evidence of pore blockage. N_2 adsorption-desorption isotherms of SiO_2-Al_2O_3 supports and V_2O_5/SiO_2-Al_2O_3 catalysts can be found on Figure A-IV.2 (Appendix: Chapter IV).

Table IV-2. Vanadium surface density, V_2O_5 weight percent, surface BET area, mean pore volume and pore size in the supported V_2O_5/SiO_2-Al_2O_3 catalysts as a function of the nominal V_2O_5 content.

Sample	Loading (V_2O_5 wt. %)	Surface density (at. V nm^{-2})	BET Area (m^2 g^{-1})	Pore Volume (cm^3 g^{-1})	Pore Size (nm)
V/75Si	3.8	0.7	291	0.39	4.97
V/85Si	4.1	0.7	351	0.31	4.73
V/95Si	4.5	0.7	445	0.52	5.09
V/99Si	4.6	0.7	402	0.63	6.83
V/100Si	1.9	0.7	175	0.32	14.21

Figure IV-1.a presents the XRD diffraction patterns of the SiO_2-Al_2O_3 mixed oxides. The synthesized silicoaluminates exhibit an amorphous structure, as indicated by the broad halo observed between 20° and 30° 2θ and the absence of characteristic peaks associated with the γ-Al_2O_3 phase. The contributions from amorphous silica and amorphous alumina cannot be distinguished, as both exhibits overlapping diffraction patterns in this range.

The XRD diffractogram of vanadium-supported SiO_2-Al_2O_3 catalysts (Figure IV-1.b) shows no detectable diffraction peaks corresponding to vanadium phases. This suggests sub-monolayer coverage on the mixed oxide surface and/or vanadium species with small crystallite sizes. Furthermore, no appreciable differences are observed between the XRD patterns of the SiAl supports and the supported V_2O_5 catalysts.

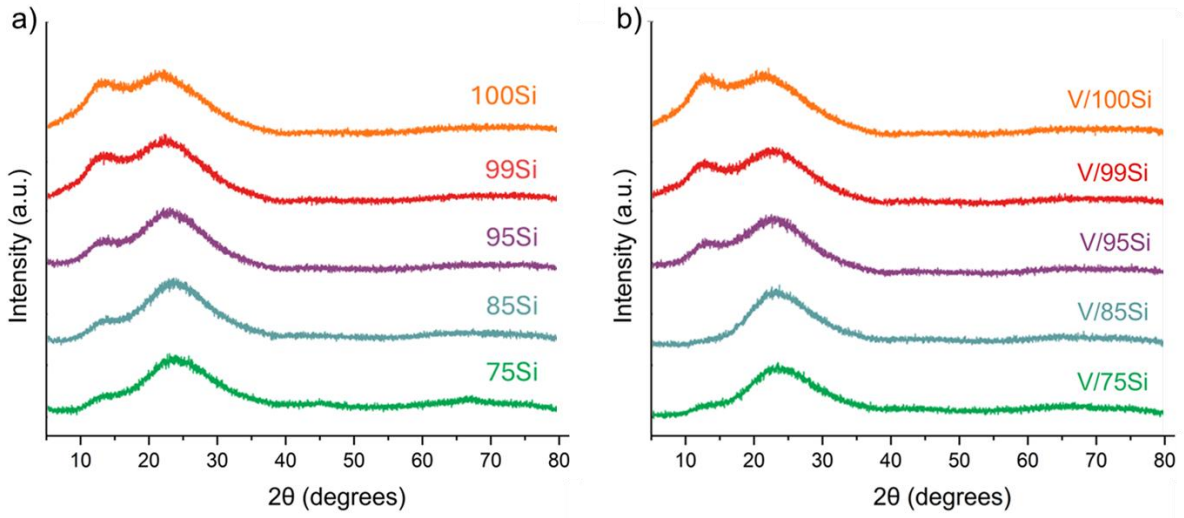

Figure IV-1. XRD diffraction patterns as a function of Si wt% of a) SiO_2-Al_2O_3 mixed oxides and b) supported V_2O_5 on SiO_2-Al_2O_3

Figure IV-2 displays the TPR profiles of the supported samples. The reduction peaks occur at similar temperatures across all samples, indicating that the alumina content does not significantly influence the reducibility of the catalysts. The peaks exhibit low intensity, consistent with the low vanadia loading. Highly dispersed VO_x on silica typically shows reduction peaks around 430 °C, while crystalline vanadia reduces at higher temperatures [257]. Similarly, vanadia supported on alumina exhibits reduction of polymeric surface VO_x near 450 °C, with crystalline phases reducing at higher temperatures [258].

These results suggest that neither silica nor alumina significantly affects the catalyst's reducibility, likely due to the lack of intrinsic redox properties as support. Instead, the silica-alumina serves primarily as a support to disperse the vanadia phase. The reduction temperatures confirm that vanadium is well-dispersed across the samples, forming polymeric surface VO_x rather than crystalline phases, as corroborated by the XRD results.

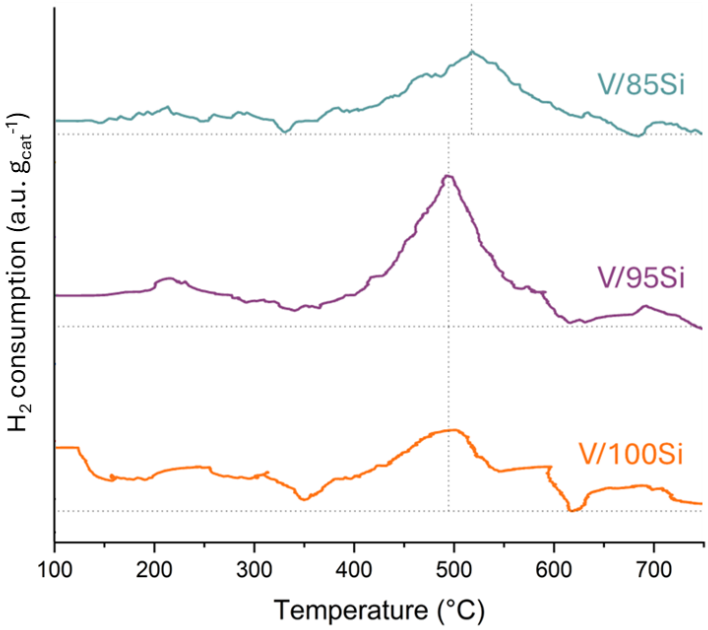

Figure IV-2. H_2 temperature programmed reduction for the V_2O_5/SiO_2-Al_2O_3 supported catalysts.

3.2 Catalytic activity

Figure IV-3 shows the effect of temperature on the product yields for all the prepared catalysts. The catalysts are selective for FA formation, achieving yields close to 50% at high temperatures (250 °C). In contrast, MF and DMM yields remain very low, with values below 2%. The V/100Si catalyst exhibits poor activity, as evidenced by product yields below 2% at temperatures as high as 250°C. These differences are attributed to its lower vanadium loading due to its significantly lower BET surface area, as well as the reported low activity of V_2O_5/SiO_2 catalysts for methanol ODH reaction [259]. Considering the above, this catalyst will be excluded from further analysis and discussion.

The observed trends for DMM and MF are consistent with previously reported catalysts. DMM forms predominantly at lower temperatures, gradually giving way to MF formation as the temperature increases. The catalysts were not active for CO and CO_2 formation at the temperatures studied, only producing traces (less than 2%) at 250°C.

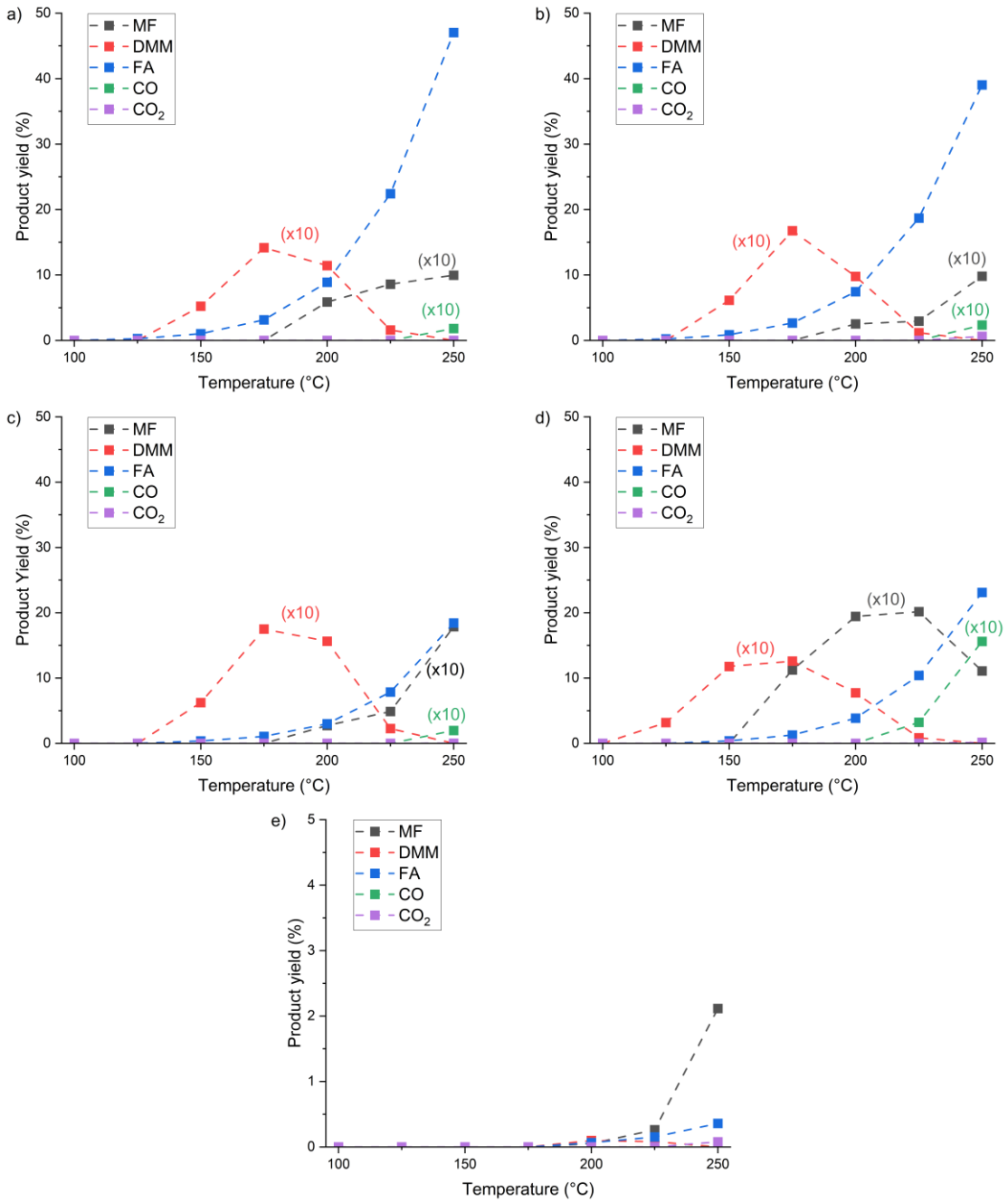

Figure IV-3. Yield of FA, MF, DMM, CO and CO_2 as a function of reaction temperature for a) V/75Si, b) V/85Si, c) V/95Si, d) V/99Si and e) V/100Si (GHSV = 15 L h^{-1} g_{cat}^{-1}, $CH_3OH/O_2/N_2$ (feed) = 4/9/87 %v/v)

Figure IV-4 depicts the effect of temperature on the conversion for all supported catalysts. The V/75Si, V/85Si, V/95Si, and V/99Si catalysts exhibit similar conversion values. Given their comparable vanadium loadings, it can be inferred that the SiO_2-Al_2O_3 ratio does not significantly influence methanol ODH activity (consistent with rds?). The observed

differences between these catalysts and the 100Si catalyst are likely attributed to the latter's lower vanadium loading, as was previously discussed.

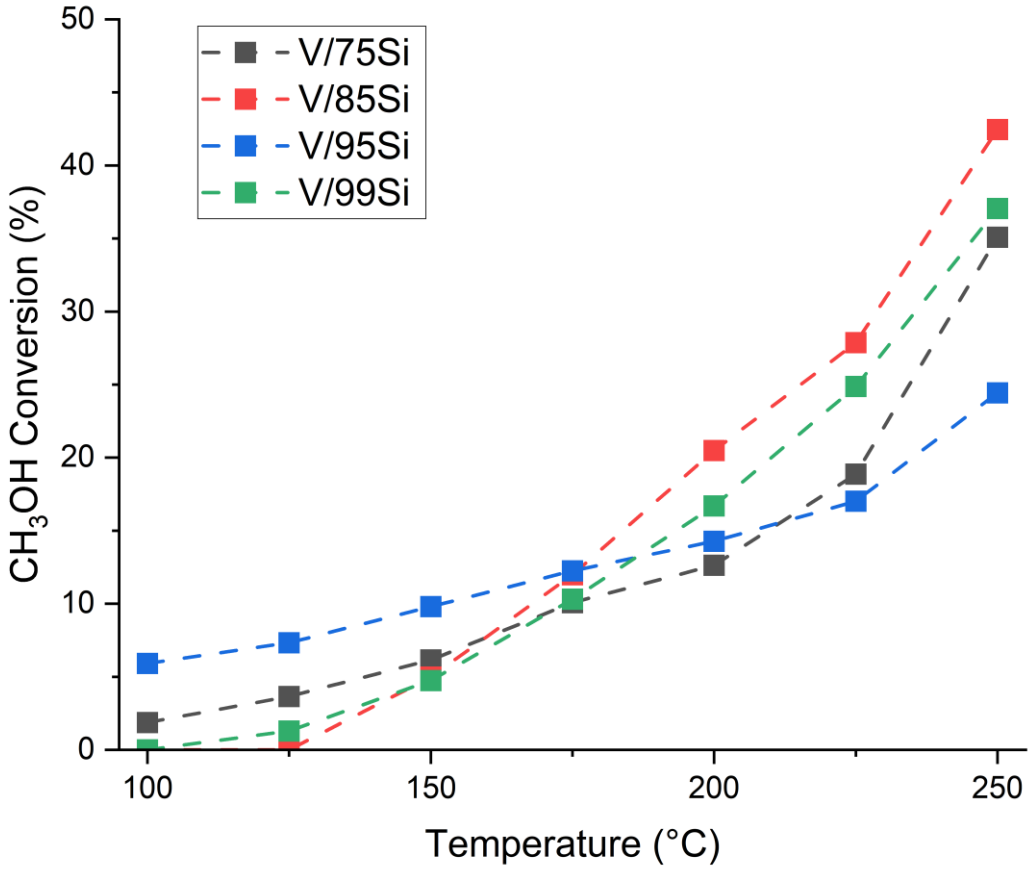

Figure IV-4. Conversion as a function of temperature for supported V_2O_5/SiO_2-Al_2O_3 (GHSV = 15 L h^{-1} g_{cat}^{-1}, $CH_3OH/O_2/N_2$ (feed) = 4/9/87 %v/v).

Figure IV-5 a) and Figure IV-5 b) show the effect of residence time on product yields at 225 °C for V/75Si and V/99Si, respectively. FA is the principal product across the entire flow range studied, with its yield increasing as residence time increases, consistent with the extended contact time of CH_3OH with the solid catalysts and confirming that FA is not an intermediary for MF and DMM formation. MF and DMM yields remain below 2%. The observed behavior is in accordance with previous reports, where DMM yield decreases with residence time while MF yield increases due to the equilibrium of DMM formation with its hemiacetal intermediate [48,188]. The slight decrease in methanol conversion in Figure IV-5 b) is attributed to the experimental error in its quantification, which is associated with the low methanol conversion (~10%).

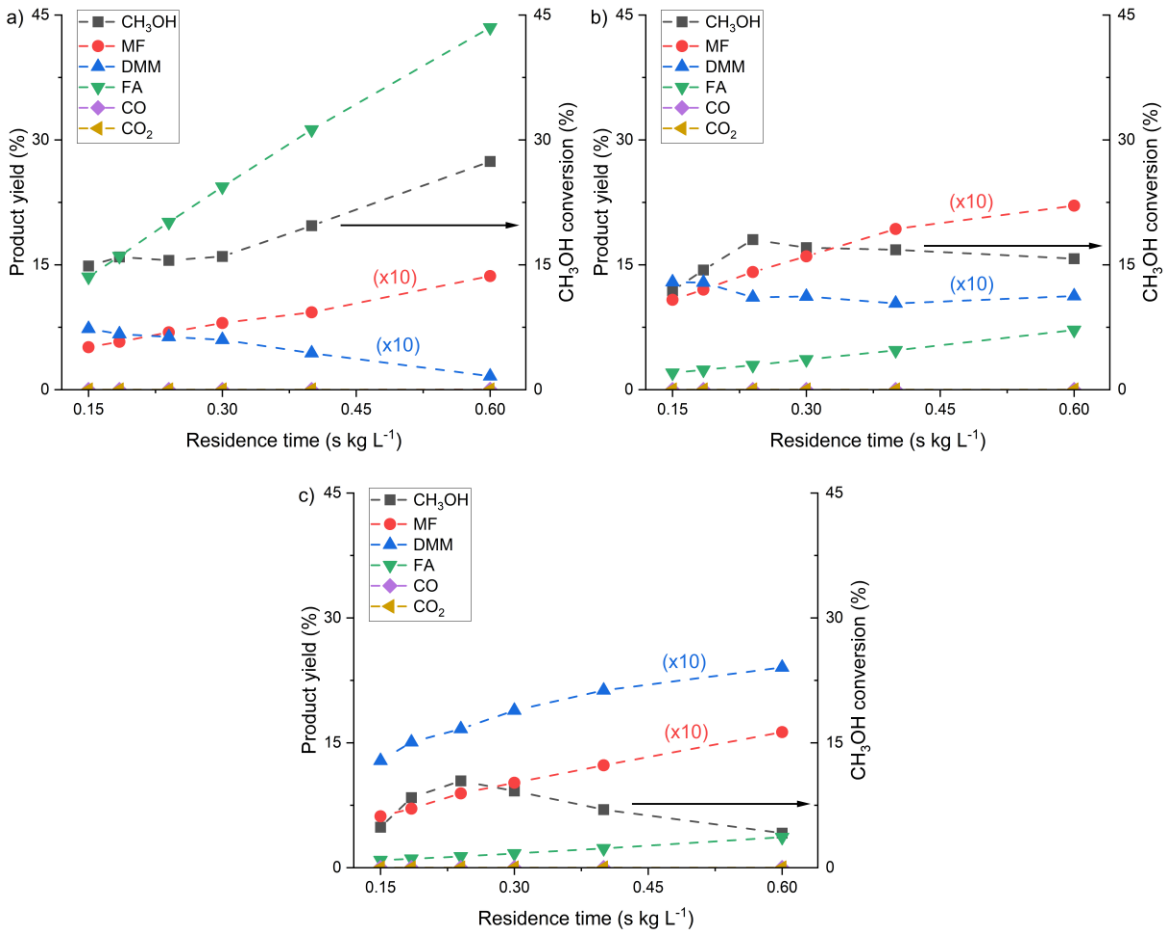

Figure IV-5. Yield of FA, MF, DMM, CO and CO_2 as a function of the residence time for a) V/75Si (225 °C, $CH_3OH/O_2/N_2$ (feed) = 4/9/87 % v/v) and b) V/99Si (225 °C, $CH_3OH/O_2/N_2$ (feed) = 4/9/87 % v/v),

Given that acidity and the SiO_2-Al_2O_3 ratio are expected to influence the DMM/MF product ratio, Figure IV-6 presents the rate ratio of DMM to MF. As residence time increases, the DMM/MF ratio decreases, aligning with the expected trend where DMM formation diminishes in favor of MF production. This effect of residence time is consistent across catalysts with varying SiO_2-Al_2O_3 ratios. However, temperature has the most significant influence on the DMM/MF ratio, highlighting its dominant role in determining product distribution.

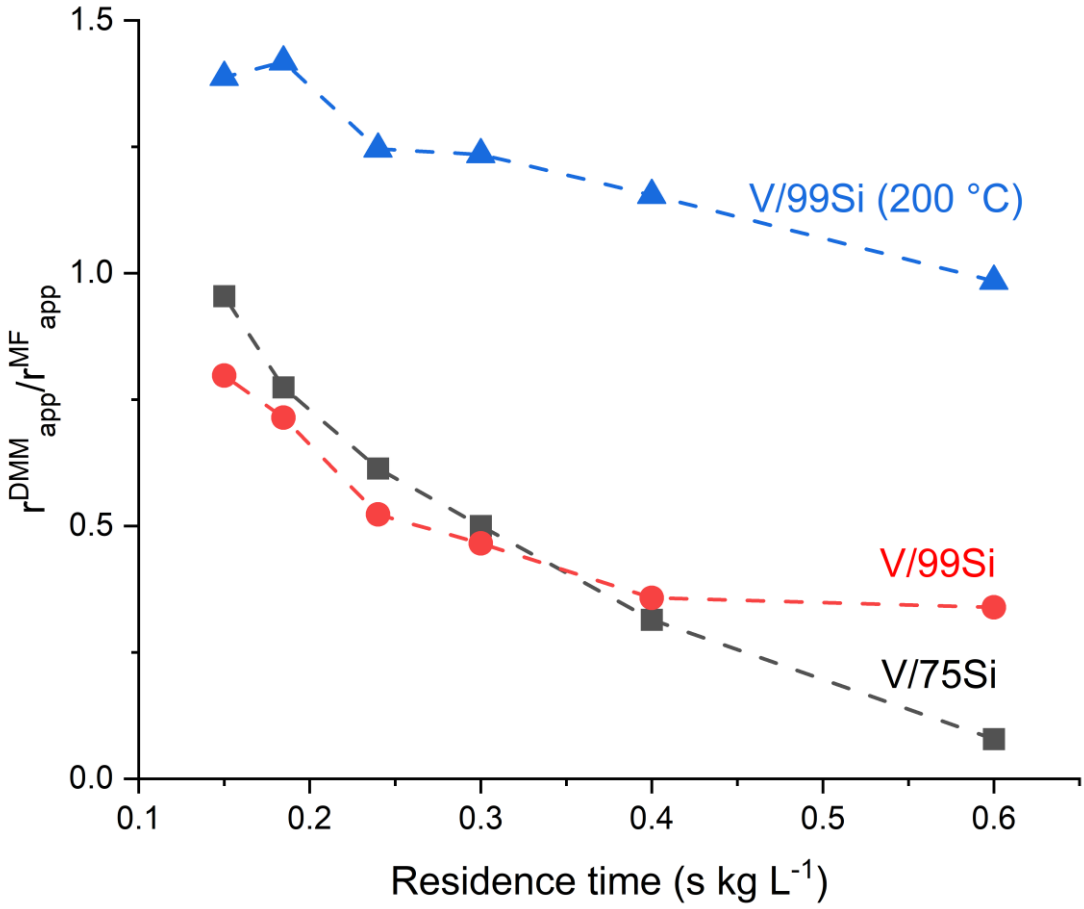

Figure IV-6. Effect of residence time on DMM/MF reaction rate ratio for V/75Si and V/99Si at 225 °C, and V/99Si at 200°C ($CH_3OH/O_2/N_2$ (feed) = 4/9/87 % v/v).

Figure IV-7 illustrates the effect of the SiO_2-Al_2O_3 ratio on methanol conversion. As previously discussed, the SiO_2-Al_2O_3 ratio does not significantly affect methanol conversion at isothermal conditions. Given the similar vanadium loading among the supported samples, the influence of support composition on methanol ODH activity can be ruled out.

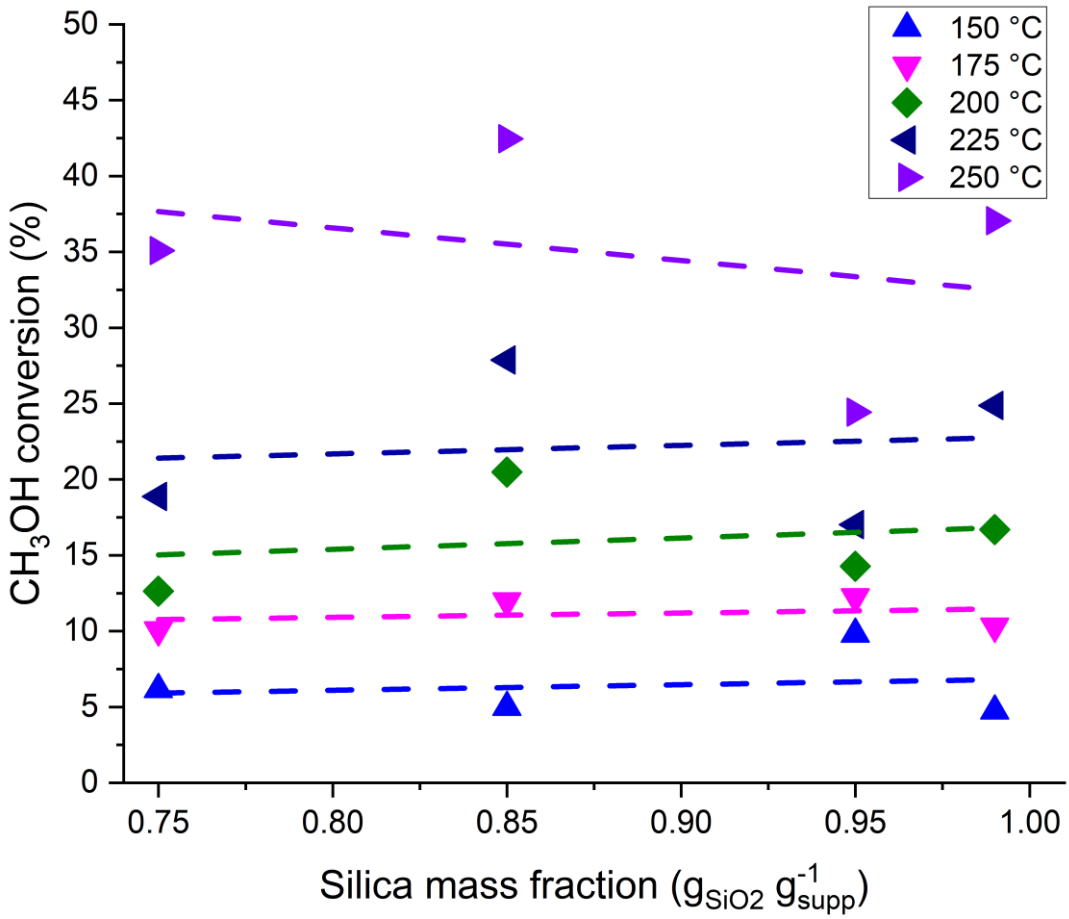

Figure IV-7. Conversion as a function of silica fraction for SiO_2-Al_2O_3-supported V_2O_5 catalysts at different reaction temperatures (GHSV = 15 L h^{-1} g_{cat}^{-1}, $CH_3OH/O_2/N_2$ (feed) = 4/9/87 %v/v)

Figure IV-8 shows the apparent TOF for methanol conversion and ODH products formation, obtained by normalizing the reaction rate (estimated assuming a differential reactor, which is not the case at higher temperatures due to the conversion values shown on Figure IV-7) by vanadium bulk content. The comparison is made at temperatures where both MF and DMM are present (200-225°C). The results indicate SiO_2-Al_2O_3 ratio does not significantly affect CH_3OH conversion, except at higher temperatures. This is consistent with the proposed mechanism for this reaction, where the initial activation of methanol during its oxidative dehydrogenation to formaldehyde restricts the overall turnovers since this reaction proceeds via CH_3OH dissociative adsorption followed by a kinetically relevant C−H bond scission of the CH_3O* intermediate on vanadia [48]. This suggests that other factors, such as temperature and vanadium loading, must be more influential in catalytic activity for the methanol ODH.

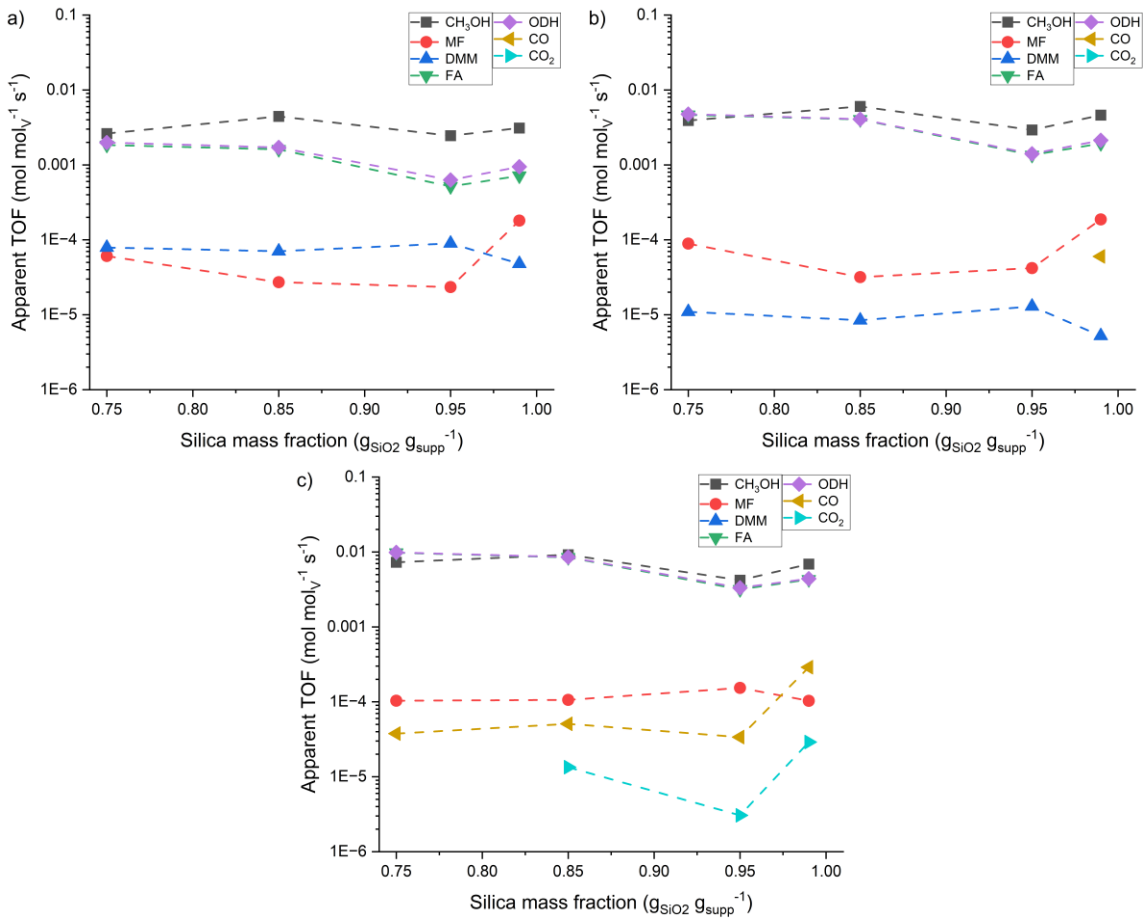

Figure IV-8. TOF of FA, MF, DMM, CO and CO_2 as a function of silica fraction at a) 200°C and b) 225 c) 250 °C; (GHSV = 15 L h^{-1} g_{cat}^{-1}, $CH_3OH/O_2/N_2$ (feed) = 4/9/87 %v/v).

Figure IV-9 a) shows the effect of the SiO_2-Al_2O_3 ratio on the DMM/MF ratio. It is evident that this ratio reaches a maximum near 95% silica, after which it decreases again on the V/100 Si catalyst. This trend can be compared with the reported the B/L acid site ratio of SiO_2-Al_2O_3 mixed oxides, where the interaction between SiO_2 and Al_2O_3 generates Brønsted acid sites, as neither SiO_2 nor Al_2O_3 possess Brønsted acidity on their own (Figure IV-9 b)) [155,260]. It can be concluded that an increase in the Brønsted/Lewis acidity ratio enhances DMM/MF formation. This can be interpreted as follows: Brønsted acidity promotes DMM formation and/or Lewis acidity favors MF formation, as has been previously reported [48]. However, it is important to note that the Lewis acidity discussed in the referenced work is associated with accessible titania support sites. We propose that the influence of titania on MF formation comes from interfacial metal-O-titania sites, as discussed previously in Chapter II, rather than from an acidity effect. Nevertheless, due to the redox differences between Al_2O_3 and TiO_2, it is possible that the V_2O_5/Al_2O_3-SiO_2 catalysts are forming MF via a less favorable pathway that involves Lewis acid sites, like the Tishchenko reaction.

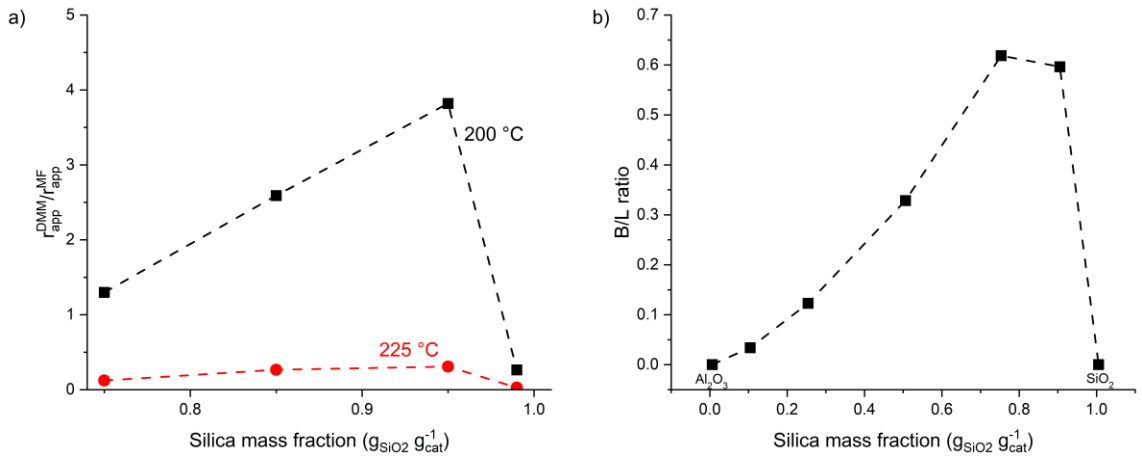

Figure IV-9. Effect of silica mass fraction on a) DMM/MF reaction rate ratio (GHSV = 15 L h^{-1} g_{cat}^{-1}, $CH_3OH/O_2/N_2$ (feed) = 4/9/87 %v/v), b) Brønsted/Lewis acid ratio (adapted from Rajagopal et al. [260]).

3.3 Discussion

The selectivity of V_2O_5/SiO_2-Al_2O_3 catalysts is consistent with prior studies on methanol ODH using V_2O_5/SiO_2 and V_2O_5/Al_2O_3 [259]. On this referenced work, V_2O_5/SiO_2 catalysts, primarily produce FA, with some DMM detected, while V_2O_5/Al_2O_3 catalysts are selective for FA and DME at higher vanadia loadings. This difference is attributed to the presence of Lewis acid sites on Al_2O_3, which are more active for methanol dehydration than for methanol ODH, leading to increased DME formation. Given that our studied supports are mostly silica, is to be expected that they behave like V_2O_5/SiO_2 in terms of selectivity.

The methanol oxidation TOF on supported mixed oxides has been shown to be significantly influenced by the support choice, often more than by the metal oxide content. Studies show a difference of an order of magnitude for the TOF between SiO_2 (~10^{-3} s^{-1}) and Al_2O_3 (~10^{-2} s^{-1}) [259]. In this work, at vanadium loadings where there are no apparent structure differences between silica and alumina, it was suggested that the differences in activity are due to different number of active sites for methanol oxidation. It was proposed that the strength of the V-O-support bond determines the number of active sites which could interact with methanol, and at the same time, it is related to the reducibility of the sample (weaker V-O-support bonds are easily reducible). Alumina is less electronegative than silica [48], therefore Al_2O_3 supported catalysts are more reactive for oxidation reactions [261].

One could expect that the TOF should diminish as the silica fraction increases, as the V_2O_5/SiO_2 catalysts are not active for methanol ODH. In our study, TPR profiles confirm similar reducibility across supports. It has been reported that the TOF on Al_2O_3-SiO_2-supported V_2O_5 catalysts is similar to V_2O_5/Al_2O_3 (and both one order of magnitude higher than SiO_2) [262]. This indicates an interaction exclusively between the vanadium and the alumina due to the low vanadium loading, as it prefers to be coordinated to alumina. On the

contrary, the selectivity of the catalysts studied in this thesis is similar to that of SiO_2, because they do not have significant alumina-free sites for DME formation.

The interplay between support acidity and vanadia structure plays a crucial role in selectivity. Selectivity depends on the vanadia structure [205] and the interplay of acid and redox properties [261]. Increasing vanadia loading increases the B/L ratio, as Brønsted acidity has been reported to increase linearly with vanadium content [172], and Brønsted acidity has been reported to enhance DMM formation [48]. Although the support enhances the acid properties of the catalysts, the acidity of the vanadia phase itself is more important, as the predominant FA selectivity of our samples could be explained by the lack of metal acid vanadia sites due to the low metal loadings.

Alumina-supported vanadia demonstrates lower selectivity towards DMM and MF compared to V_2O_5/TiO_2. We believe it is because alumina favors DME formation. On these samples, it should be easier for methanol to react with adsorbed methanol on acid support sites rather than on acid metal sites to form DMM. Therefore, the DME formation and methanol ODH reaction do not share adsorbed methanol/methoxy species, instead they require these species to be adsorbed on separate acid and redox sites, respectively. Silica, on the other hand, represents a special case due to its low reactivity, lack of acid sites and higher surface hydroxyl group acidity, which differently influences product selectivity compared to alumina [67]. FA selectivity is deeply related to the structure of the vanadia species. It has been reported that dispersed surface molybdenum species on silica agglomerate into MoO_3 under reaction conditions, which could explain why they produce FA instead of MF and/or DMM [67]. In contrast, for V_2O_5/TiO_2, surface oxide species exhibit dispersion rather than agglomeration [263]. The lability of vanadium surface species hinders the direct comparisons between vanadium and molybdenum systems.

4. Conclusions

The methanol oxidative dehydrogenation was studied on V_2O_5/SiO_2-Al_2O_3 catalysts with varying silica/alumina ratios. FA was identified as the main product consistent with the predominant silica composition of the mixed support. Product selectivity was influenced by silica/alumina ratio, which determines the Brønsted and Lewis acidity. Brønsted acid sites, associated with SiO_2, promoted DMM formation while Lewis acid sites, associated with Al_2O_3, favored methyl formate MF. However, the acidity of the vanadia phase itself is believed to play a more critical role in determining selectivity than the acidity of these supports.

The TOF values for methanol ODH and FA formation were independent of the Si/Al ratios, similar to the TOF values reported on V_2O_5/Al_2O_3, in accordance with the proposed methanol dehydrogenation mechanism, where the rate-determining step is governed by the redox properties of the catalyst. This behavior also suggests that vanadium preferentially interacts with alumina at low vanadium surface densities (0.7 at. V nm^{-2}). The deposition of vanadium on the alumina surface limits the availability of Al_2O_3 free sites, which limits DME formation

and results in selectivities similar to V_2O_5/SiO_2 catalysts. The similarity in H_2-TPR profiles between the samples indicates that the B/L ratio does not significantly alter the redox behavior of the active vanadium sites, in accordance with the similar TOF values for ODH activity and CH_3OH conversion.

Overall, the catalytic performance of V_2O_5/SiO_2-Al_2O_3 for methanol oxidative dehydrogenation is governed by the structure of vanadia and the interplay between redox and acid properties of vanadium and Si-Al support. These factors determine the balance between FA, DMM, and MF formation, highlighting the significance of support composition in the selectivity of the methanol ODH reaction.

General Conclusions

The work developed in this thesis demonstrates that the methanol oxidative dehydrogenation reaction is strongly influenced by the redox and acid properties of MoO_3/TiO_2, V_2O_5/TiO_2, and V_2O_5/SiO_2-Al_2O_3 catalysts. By varying metal-support pairs, metal loading, and support composition, this study identifies the key factors governing catalytic activity, product selectivity, active site availability and dominant reaction pathways.

The structural evolution of supported metal oxides with increasing metal content significantly impacts their redox and acid properties. At low loadings, metal oxides exist as dispersed oligomeric species, strongly interacting with the support. Upon reaching monolayer coverage, these species transform into crystalline oxide phases. This transformation threshold depends on both the metal oxide and the support composition, as highlighted in this thesis, and it has a high impact on the physicochemical properties of the supported catalysts.

For MoO_3/TiO_2 catalysts, octahedral oligomeric species transition to crystalline α-MoO_3 as the monolayer coverage is reached. This structural change is associated with a loss of the strong interaction between molybdenum oxide and the TiO_2 support, as evidenced by H_2-TPR analysis. The reducibility of Mo species changes with crystallization, and the oxidation state shifts from dispersed Mo^{5+} to more readily reducible Mo^{6+} species, as observed by XPS and low-temperature CO adsorption. Sub-monolayer catalysts, where MoO_3 strongly interacts with the electronegative TiO_2 support, exhibit particular redox properties due to a combined effect of titania and Mo^{6+}, enabling the successive dehydrogenation steps to produce methyl formate selectively from methanol, on interfacial Mo-O-Ti sites.

For V_2O_5/TiO_2 catalysts, likewise to the behavior observed in MoO_3/TiO_2 samples at sub-monolayer coverage, dispersed vanadium oxide species are selective for methyl formate and dimethoxymethane. Moreover, V_2O_5 is inherently more active than MoO_3, as demonstrated by the higher CH_3OH conversion. This superior activity is attributed to the enhanced redox properties of V_2O_5 compared to MoO_3, evidenced by its lower edge energy.

As the metal content increases and crystalline oxide phases form, significant differences between the catalysts supported on titania appear. While MoO_3/TiO_2 predominantly produces formaldehyde, V_2O_5/TiO_2 shows notable activity for dimethoxymethane formation. This difference is attributed to the higher acidity of V_2O_5/TiO_2, as Brønsted acidity has been reported to increase linearly with vanadium content, whereas the Brønsted acidity of MoO_3/TiO_2 changes minimally with Mo content, as observed by pyridine adsorption. The presence of acid sites in V_2O_5/TiO_2 facilitates DMM formation via the hemiacetal intermediate, while MoO_3/TiO_2 lacks sufficient acidity to sustain this pathway and desorbs formaldehyde instead.

A kinetic model was successfully derived for the V_2O_5/TiO_2 catalysts, incorporating the hemiacetal intermediate as the precursor to both MF and DMM. This model revealed that the

kinetic parameters differ between the sub-monolayer VO_x and the crystalline V_2O_5 species, attributed to the changes in redox and acid properties as the structure evolves. Crystalline V_2O_5/TiO_2 catalysts exhibited higher intrinsic activity with lower activation energy for the rate-limiting step, attributed to its enhanced reducibility, while compensating for weaker methanol adsorption (lower enthalpy of chemisorption). Notably, the estimated confidence intervales for the kinetic parameters of the sub-monolayer V_2O_5/TiO_2 catalyst were broader than its counterpart, which is now attributed to the absence of MF formation via the formate pathway in the proposed model, which worsens the statistical fit.

The acid properties of the support and the metal oxide phase were further examined using V_2O_5/SiO_2-Al_2O_3 catalysts. These systems provided insights into the differentiation between support acidity and active phase acidity. Brønsted/Lewis acid site ratio, influenced by the SiO_2 acid sites activation due to Al_2O_3, were found to favor the DMM/MF formation ratio. This aligns with the previously discussed DMM formation pathway via the hemiacetal intermediate, which requires Brønsted acid sites. However, the acid properties of the vanadia phase itself were shown to be more influential than the support acidity. This was evidenced by the absence of significant DMM or MF production in V_2O_5/SiO_2-Al_2O_3 samples due to their low vanadium loading and the resulting lack of vanadia acid sites, when compared to V_2O_5/TiO_2 catalysts. Importantly, support acidity had no impact on overall methanol activity, reaffirming that redox properties remain the primary determinant of methanol ODH reactivity.

Overall, this thesis highlights the complex interplay between redox and acid pathways in methanol ODH reactivity and selectivity. Acidity and redox properties are both influenced by the structure of the supported oxide, especially at the transformation threshold from dispersed oligomeric chains to crystalline oxide layers. Across all systems, DMM formation requires the availability of acid metal sites to stabilize hemiacetal intermediates, whereas MF formation depends on reducible redox interfacial sites, which facilitate the formate pathway. Hemiacetal intermediates can also produce MF through a parallel dehydrogenation reaction, but this pathway dominates only in the absence of readily reducible interfacial sites and in the presence of acid sites on the active oxide.

As a final remark, this work highlights the importance of balancing redox and acid site properties to control methanol ODH activity and specific product selectivity. The findings of this thesis provides useful insights into the relationships between catalyst structure, active site nature, and reaction mechanisms, offering valuable guidelines for designing tailored heterogeneous catalytic systems with optimized selectivity for the different products of methanol ODH.

References

[1] M.W. Jones, G.P. Peters, T. Gasser, R.M. Andrew, C. Schwingshackl, J. Gütschow, R.A. Houghton, P. Friedlingstein, J. Pongratz, C. Le Quéré, National contributions to climate change due to historical emissions of carbon dioxide, methane, and nitrous oxide since 1850, Sci Data 10 (2023) 155. https://doi.org/10.1038/s41597-023-02041-1.

[2] N. Abas, A. Kalair, N. Khan, Review of fossil fuels and future energy technologies, Futures 69 (2015) 31–49. https://doi.org/10.1016/j.futures.2015.03.003.

[3] A. Nemmour, A. Inayat, I. Janajreh, C. Ghenai, Green hydrogen-based E-fuels (E-methane, E-methanol, E-ammonia) to support clean energy transition: A literature review, Int J Hydrogen Energy 48 (2023) 29011–29033. https://doi.org/10.1016/j.ijhydene.2023.03.240.

[4] A. Nicita, G. Maggio, A.P.F. Andaloro, G. Squadrito, Green hydrogen as feedstock: Financial analysis of a photovoltaic-powered electrolysis plant, Int J Hydrogen Energy 45 (2020) 11395–11408. https://doi.org/10.1016/j.ijhydene.2020.02.062.

[5] A. Nemmour, C. Ghenai, A. Inayat, Parametric study and optimization of bio-hydrogen production using steam reforming of glycerol and biodiesel fuel mixtures, Biomass Convers Biorefin 13 (2023) 8713–8725. https://doi.org/10.1007/s13399-020-01230-x.

[6] A. Sonthalia, N. Kumar, M. Tomar, V. Edwin Geo, S. Thiyagarajan, A. Pugazhendhi, Moving ahead from hydrogen to methanol economy: scope and challenges, Clean Technol Environ Policy 25 (2021) 551–575. https://doi.org/10.1007/s10098-021-02193-x.

[7] D.D. Papadias, J.-K. Peng, R.K. Ahluwalia, Hydrogen carriers: Production, transmission, decomposition, and storage, Int J Hydrogen Energy 46 (2021) 24169–24189. https://doi.org/10.1016/j.ijhydene.2021.05.002.

[8] T. Umegaki, J.-M. Yan, X.-B. Zhang, H. Shioyama, N. Kuriyama, Q. Xu, Boron- and nitrogen-based chemical hydrogen storage materials, Int J Hydrogen Energy 34 (2009) 2303–2311. https://doi.org/10.1016/j.ijhydene.2009.01.002.

[9] G.A. Olah, Beyond Oil and Gas: The Methanol Economy, Angewandte Chemie International Edition 44 (2005) 2636–2639. https://doi.org/10.1002/anie.200462121.

[10] U. Mondal, G.D. Yadav, Methanol economy and net zero emissions: critical analysis of catalytic processes, reactors and technologies, Green Chemistry 23 (2021) 8361–8405. https://doi.org/10.1039/D1GC02078A.

[11] M. Behrens, Chemical hydrogen storage by methanol: Challenges for the catalytic methanol synthesis from CO2, Recyclable Catalysis 2 (2015). https://doi.org/10.1515/recat-2015-0009.

[12] S. Verhelst, J.W. Turner, L. Sileghem, J. Vancoillie, Methanol as a fuel for internal combustion engines, Prog Energy Combust Sci 70 (2019) 43–88. https://doi.org/10.1016/j.pecs.2018.10.001.

[13] N. de Fournas, M. Wei, Techno-economic assessment of renewable methanol from biomass gasification and PEM electrolysis for decarbonization of the maritime sector in California, Energy Convers Manag 257 (2022) 115440. https://doi.org/10.1016/j.enconman.2022.115440.

[14] L. Luo, H. Wang, C. Li, Y. Hu, Life cycle assessment of methanol vehicles from energy, environmental and economic perspectives, Energy Reports 8 (2022) 5487–5500. https://doi.org/10.1016/j.egyr.2022.04.009.

[15] G.A. Olah, Towards Oil Independence Through Renewable Methanol Chemistry, Angewandte Chemie International Edition 52 (2013) 104–107. https://doi.org/10.1002/anie.201204995.

[16] S. Ren, W.R. Shoemaker, X. Wang, Z. Shang, N. Klinghoffer, S. Li, M. Yu, X. He, T.A. White, X. Liang, Highly active and selective Cu-ZnO based catalyst for methanol and dimethyl ether synthesis via CO2 hydrogenation, Fuel 239 (2019) 1125–1133. https://doi.org/10.1016/j.fuel.2018.11.105.

[17] S.-W. Perng, H.-W. Wu, Effect of depth and diameter of cylindrical cavity in a plate-type methanol steam reformer on estimated net power of PEMFC, Energy Convers Manag 177 (2018) 190–209. https://doi.org/10.1016/j.enconman.2018.09.066.

[18] M. Fasihi, C. Breyer, Global production potential of green methanol based on variable renewable electricity, Energy Environ Sci 17 (2024) 3503–3522. https://doi.org/10.1039/D3EE02951D.

[19] J. Zhao, R. Shi, Z. Li, C. Zhou, T. Zhang, How to make use of methanol in green catalytic hydrogen production?, Nano Select 1 (2020) 12–29. https://doi.org/10.1002/nano.202000010.

[20] H. Valera, D. Kumar, A.K. Agarwal, Evaluating the effect of variable methanol injection timings in a novel co-axial fuel injection system equipped locomotive engine, J Clean Prod 349 (2022) 131452. https://doi.org/10.1016/j.jclepro.2022.131452.

[21] S. Chowdhury, Y. Kumar, S. Shrivastava, S.K. Patel, J.S. Sangwai, A Review on the Recent Scientific and Commercial Progress on the Direct Air Capture Technology to Manage Atmospheric CO_2 Concentrations and Future Perspectives, Energy & Fuels 37 (2023) 10733–10757. https://doi.org/10.1021/acs.energyfuels.2c03971.

[22] Carbon Recycling International (CRI): Projects, (n.d.). https://carbonrecycling.com/projects (accessed May 24, 2024).

[23] S. Sollai, A. Porcu, V. Tola, F. Ferrara, A. Pettinau, Renewable methanol production from green hydrogen and captured CO2: A techno-economic assessment, Journal of CO2 Utilization 68 (2023) 102345. https://doi.org/10.1016/j.jcou.2022.102345.

[24] C.F. Shih, T. Zhang, J. Li, C. Bai, Powering the Future with Liquid Sunshine, Joule 2 (2018) 1925–1949. https://doi.org/10.1016/j.joule.2018.08.016.

[25] G.A. Olah, A. Goeppert, G.K.S. Prakash, Beyond Oil and Gas: The Methanol Economy, Wiley, 2009. https://doi.org/10.1002/9783527627806.

[26] A. Goeppert, M. Czaun, J.-P. Jones, G.K. Surya Prakash, G.A. Olah, Recycling of carbon dioxide to methanol and derived products – closing the loop, Chem. Soc. Rev. 43 (2014) 7995–8048. https://doi.org/10.1039/C4CS00122B.

[27] Summary for Policymakers, in: Global Warming of 1.5°C, Cambridge University Press, 2022: pp. 1–24. https://doi.org/10.1017/9781009157940.001.

[28] L.E. Erickson, G. Brase, Paris Agreement on Climate Change, in: Reducing Greenhouse Gas Emissions and Improving Air Quality, CRC Press, Boca Raton, 2019: pp. 11–22. https://doi.org/10.1201/9781351116589-2.

[29] United Nations, Adoption of the Paris Agreement: Proposal by the President - Draft decision, n.d. https://unfccc.int/resource/docs/2015/cop21/eng/l09.pdf (accessed May 24, 2024).

[30] C. Wulf, P. Zapp, A. Schreiber, Review of Power-to-X Demonstration Projects in Europe, Front Energy Res 8 (2020). https://doi.org/10.3389/fenrg.2020.00191.

[31] C. Schnuelle, J. Thoeming, T. Wassermann, P. Thier, A. von Gleich, S. Goessling-Reisemann, Socio-technical-economic assessment of power-to-X: Potentials and limitations for an integration into the German energy system, Energy Res Soc Sci 51 (2019) 187–197. https://doi.org/10.1016/j.erss.2019.01.017.

[32] R. Daiyan, I. Macgill, R. Amal, Opportunities and Challenges for Renewable Power-to-X, ACS Energy Lett 5 (2020) 3843–3847. https://doi.org/10.1021/acsenergylett.0c02249.

[33] B.R. de Vasconcelos, J.M. Lavoie, Recent advances in power-to-X technology for the production of fuels and chemicals, Front Chem 7 (2019). https://doi.org/10.3389/fchem.2019.00392.

[34] J. Burre, D. Bongartz, L. Brée, K. Roh, A. Mitsos, Power-to-X: Between Electricity Storage, e-Production, and Demand Side Management, Chem Ing Tech 92 (2020) 74–84. https://doi.org/10.1002/cite.201900102.

[35] Z. Mi, V. Sick, Taking a Shortcut: Direct Power-to-X Conversion, Front Energy Res 8 (2020). https://doi.org/10.3389/fenrg.2020.00153.

[36] Siemens Energy, Power-to-X: The crucial business on the way to a carbon-free world., (2020). https://www.siemens-energy.com/global/en/home/products-services/product-offerings/hydrogen-solutions.html (accessed January 11, 2025).

[37] C. Arnaiz del Pozo, S. Cloete, Á. Jiménez Álvaro, Techno-economic assessment of long-term methanol production from natural gas and renewables, Energy Convers Manag 266 (2022) 115785. https://doi.org/10.1016/j.enconman.2022.115785.

[38] U. Olsbye, S. Svelle, M. Bjørgen, P. Beato, T.V.W. Janssens, F. Joensen, S. Bordiga, K.P. Lillerud, Conversion of Methanol to Hydrocarbons: How Zeolite Cavity and Pore Size Controls Product Selectivity, Angewandte Chemie International Edition 51 (2012) 5810–5831. https://doi.org/10.1002/anie.201103657.

[39] Y. Liu, F.M. Kirchberger, S. Müller, M. Eder, M. Tonigold, M. Sanchez-Sanchez, J.A. Lercher, Critical role of formaldehyde during methanol conversion to hydrocarbons, Nat Commun 10 (2019) 1462. https://doi.org/10.1038/s41467-019-09449-7.

[40] F. Dalena, A. Senatore, M. Basile, S. Knani, A. Basile, A. Iulianelli, Advances in Methanol Production and Utilization, with Particular Emphasis toward Hydrogen Generation via Membrane Reactor Technology, Membranes (Basel) 8 (2018) 98. https://doi.org/10.3390/membranes8040098.

[41] S.W. Kariuki, J. Wachira, M. Kawira, G. Murithi, Formaldehyde Use and Alternative Biobased Binders for Particleboard Formulation: A Review, J Chem 2019 (2019) 1–12. https://doi.org/10.1155/2019/5256897.

[42] V.V. Kaichev, G.Ya. Popova, Yu.A. Chesalov, A.A. Saraev, D.Y. Zemlyanov, S.A. Beloshapkin, A. Knop-Gericke, R. Schlögl, T.V. Andrushkevich, V.I. Bukhtiyarov, Selective oxidation of methanol to form dimethoxymethane and methyl formate over a monolayer V2O5/TiO2 catalyst, J Catal 311 (2014) 59–70. https://doi.org/10.1016/j.jcat.2013.10.026.

[43] J. Wu, R. Shi, Z. Qin, H. Liu, Z. Li, H. Zhu, Y. Zhao, J. Wang, Selective oxidation of methanol to methyl formate over bimetallic Au-Pd nanoparticles supported on SiO2, Journal of Fuel Chemistry and Technology 47 (2019) 780–790. https://doi.org/10.1016/S1872-5813(19)30034-9.

[44] A. Wittstock, V. Zielasek, J. Biener, C.M. Friend, M. Bäumer, Nanoporous Gold Catalysts for Selective Gas-Phase Oxidative Coupling of Methanol at Low Temperature, Science (1979) 327 (2010) 319–322. https://doi.org/10.1126/science.1183591.

[45] M. Cozzolino, R. Tesser, M. Diserio, P. Donofrio, E. Santacesaria, Kinetics of the oxidative dehydrogenation (ODH) of methanol to formaldehyde by supported vanadium-based nanocatalysts, Catal Today 128 (2007) 191–200. https://doi.org/10.1016/j.cattod.2007.06.072.

[46] T. Feng, J.M. Vohs, A TPD study of the partial oxidation of methanol to formaldehyde on CeO2-supported vanadium oxide, J Catal 221 (2004) 619–629. https://doi.org/10.1016/j.jcat.2003.10.002.

[47] T. Feng, J.M. Vohs, TPD–TGA and Calorimetric Study of the Partial Oxidation of Methanol on TiO2-Supported Vanadium Oxide, J Catal 208 (2002) 301–309. https://doi.org/10.1006/jcat.2002.3587.

[48] W.T. Broomhead, W. Tian, J.E. Herrera, Y.-H.C. Chin, Kinetic Coupling of Redox and Acid Chemistry in Methanol Partial Oxidation on Vanadium Oxide Catalysts, ACS Catal 12 (2022) 11801–11820. https://doi.org/10.1021/acscatal.2c01852.

[49] A.S. Elmi, E. Tronconi, C. Cristiani, J.P. Gomez Martin, P. Forzatti, G. Busca, Mechanism and active sites for methanol oxidation to methyl formate over coprecipitated vanadium-titanium oxide catalysts, Ind Eng Chem Res 28 (1989) 387–393. https://doi.org/10.1021/ie00088a002.

[50] Guido. Busca, A.S. Elmi, Pio. Forzatti, Mechanism of selective methanol oxidation over vanadium oxide-titanium oxide catalysts: a FT-IR and flow reactor study, J Phys Chem 91 (1987) 5263–5269. https://doi.org/10.1021/j100304a026.

[51] V. V. Kaichev, G.Ya. Popova, Yu.A. Chesalov, A.A. Saraev, T. V. Andrushkevich, V.I. Bukhtiyarov, Active component of supported vanadium catalysts in the selective oxidation of methanol, Kinetics and Catalysis 57 (2016) 82–94. https://doi.org/10.1134/S0023158416010043.

[52] G. Deo, A.M. Turek, I.E. Wachs, T. Machej, J. Haber, N. Das, H. Eckert, A.M. Hirt, Physical and chemical characterization of surface vanadium oxide supported on titania: influence of the titania phase (anatase, rutile, brookite and B), Appl Catal A Gen 91 (1992) 27–42. https://doi.org/10.1016/0926-860X(92)85176-C.

[53] G. Deo, I.E. Wachs, Reactivity of Supported Vanadium Oxide Catalysts: The Partial Oxidation of Methanol, J Catal 146 (1994) 323–334. https://doi.org/10.1006/jcat.1994.1071.

[54] D. Gasser, A. Baiker, Methanol oxidation on vanadium oxide catalyst prepared by in situ activation of amorphous vanadium pentoxide precursor, J Catal 113 (1988) 325–333. https://doi.org/10.1016/0021-9517(88)90261-8.

[55] K. Chen, S. Xie, A.T. Bell, E. Iglesia, Structure and Properties of Oxidative Dehydrogenation Catalysts Based on MoO3/Al2O3, J Catal 198 (2001) 232–242. https://doi.org/10.1006/jcat.2000.3125.

[56] K. Chen, A.T. Bell, E. Iglesia, The Relationship between the Electronic and Redox Properties of Dispersed Metal Oxides and Their Turnover Rates in Oxidative Dehydrogenation Reactions, J Catal 209 (2002) 35–42. https://doi.org/10.1006/jcat.2002.3620.

[57] M. Faraldos, M.A. Bañares, J.A. Anderson, H. Hu, I.E. Wachs, J.L.G. Fierro, Comparison of Silica-Supported MoO3and V2O5Catalysts in the Selective Partial Oxidation of Methane, J Catal 160 (1996) 214–221. https://doi.org/10.1006/jcat.1996.0140.

[58] P. Cheung, Liu, E. Iglesia, Kinetics and Mechanism of Dimethyl Ether Oxidation to Formaldehyde on Supported Molybdenum Oxide Domains, J Phys Chem B 108 (2004) 18650–18658. https://doi.org/10.1021/jp0477405.

[59] H. Liu, P. Cheung, E. Iglesia, Structure and support effects on the selective oxidation of dimethyl ether to formaldehyde catalyzed by MoOx domains, J Catal 217 (2003) 222–232. https://doi.org/10.1016/S0021-9517(03)00025-3.

[60] J.M. Tatibouet, J.E. Germain, J.C. Volta, Structure-sensitive catalytic oxidation: Alcohols on graphite-supported molybdenum trioxide, J Catal 82 (1983) 240–244. https://doi.org/10.1016/0021-9517(83)90136-7.

[61] F. Gonçalves, P.R.S. Medeiros, J.G. Eon, L.G. Appel, Active sites for ethanol oxidation over SnO2-supported molybdenum oxides, Appl Catal A Gen 193 (2000) 195–202. https://doi.org/10.1016/S0926-860X(99)00430-5.

[62] W.-H. Cheng, Methanol and Formaldehyde Oxidation Study over Molybdenum Oxide, J Catal 158 (1996) 477–485. https://doi.org/10.1006/jcat.1996.0047.

[63] D.S. Kim, I.E. Wachs, K. Segawa, Molecular Structures and Reactivity of Supported Molybdenum Oxide Catalysts, J Catal 149 (1994) 268–277. https://doi.org/10.1006/jcat.1994.1295.

[64] C. Louis, J.M. Tatibouët, M. Che, Catalytic properties of silica-supported molybdenum catalysts in methanol oxidation: The influence of molybdenum dispersion, J Catal 109 (1988) 354–366. https://doi.org/10.1016/0021-9517(88)90218-7.

[65] D. Kim, K. Segawa, T. Soeya, I. Wachs, Surface structures of supported molybdenum oxide catalysts under ambient conditions, J Catal 136 (1992) 539–553. https://doi.org/10.1016/0021-9517(92)90084-U.

[66] H. Hu, I.E. Wachs, Catalytic Properties of Supported Molybdenum Oxide Catalysts: In Situ Raman and Methanol Oxidation Studies, J Phys Chem 99 (1995) 10911–10922. https://doi.org/10.1021/j100027a035.

[67] M.A. Banares, H.C. Hu, I.E. Wachs, Molybdena on Silica Catalysts: Role of Preparation Methods on the Structure-Selectivity Properties for the Oxidation of Methanol, J Catal 150 (1994) 407–420. https://doi.org/10.1006/jcat.1994.1359.

[68] M. Seman, J.N. Kondo, K. Domen, R. Radhakrishnan, S.T. Oyama, Reactive and Inert Surface Species Observed during Methanol Oxidation over Silica-Supported

Molybdenum Oxide, J Phys Chem B 106 (2002) 12965–12977. https://doi.org/10.1021/jp0263828.

[69] S.T. Oyama, R. Radhakrishnan, M. Seman, J.N. Kondo, K. Domen, K. Asakura, Control of Reactivity in C−H Bond Breaking Reactions on Oxide Catalysts: Methanol Oxidation on Supported Molybdenum Oxide, J Phys Chem B 107 (2003) 1845–1852. https://doi.org/10.1021/jp0220276.

[70] T. Yang, J.H. Lunsford, Partial oxidation of methanol to formaldehyde over molybdenum oxide on silica, J Catal 103 (1987) 55–64. https://doi.org/10.1016/0021-9517(87)90092-3.

[71] J.M. Tatibouët, J.E. Germain, A structure-sensitive oxidation reaction: Methanol on molybdenum trioxide catalysts, J Catal 72 (1981) 375–378. https://doi.org/10.1016/0021-9517(81)90022-1.

[72] J.M. Tatibouët, Methanol oxidation as a catalytic surface probe, Appl Catal A Gen 148 (1997) 213–252. https://doi.org/10.1016/S0926-860X(96)00236-0.

[73] K. Brückman, B. Grzybowska, M. Che, J.M. Tatibouët, Methanol oxidation on MoO3/TiO2 catalysts, Appl Catal A Gen 96 (1993) 279–288. https://doi.org/10.1016/0926-860X(90)80016-8.

[74] K. Bruckman, J.M. Tatibouet, M. Che, E. Serwicka, J. Haber, Catalytic Behavior of Unsupported and Heteropolysalt-Supported H3+PV Mo12−O40 Heteropolyacids in the Test Reaction of CH3OH Oxidation, J Catal 139 (1993) 455–467. https://doi.org/10.1006/jcat.1993.1040.

[75] W.-H. Cheng, Selectivities in methanol oxidation over silica supported molybdena, Catal Letters 36 (1996) 87–93. https://doi.org/10.1007/BF00807210.

[76] M. Niwa, Role of the solid acidity on the MoO3 loaded on SnO2 in the methanol oxidation into formaldehyde, Catal Today 52 (1999) 71–81. https://doi.org/10.1016/S0920-5861(99)00064-4.

[77] L.J. Gregoriades, J. Döbler, J. Sauer, Oxidation of Methanol to Formaldehyde on Silica-Supported Molybdena: Density Functional Theory Study on Models of Mononuclear Sites, The Journal of Physical Chemistry C 114 (2010) 2967–2979. https://doi.org/10.1021/jp908609s.

[78] J.-M. Jehng, H. Hu, X. Gao, I.E. Wachs, The dynamic states of silica-supported metal oxide catalysts during methanol oxidation, Catal Today 28 (1996) 335–350. https://doi.org/10.1016/S0920-5861(96)00047-8.

[79] J.S. Chung, R. Miranda, C.O. Bennet, Mechanism of partial oxidation of methanol over MoO3, J Catal 114 (1988) 398–410. https://doi.org/10.1016/0021-9517(88)90043-7.

[80] C. La Fontaine, A. Yoboue, E. Berrier, A. Tougerti, F. Villain, E. Fonda, K. Hamraoui, J.-F. Paul, S. Cristol, Methanol conversion over TiO_2 -anatase supported oxomolybdate catalysts: an integrated *operando* – DFT modeling approach, Phase Transitions 84 (2011) 700–713. https://doi.org/10.1080/01411594.2011.578825.

[81] L.E. Briand, A.M. Hirt, I.E. Wachs, Quantitative Determination of the Number of Surface Active Sites and the Turnover Frequencies for Methanol Oxidation over Metal Oxide Catalysts: Application to Bulk Metal Molybdates and Pure Metal Oxide Catalysts, J Catal 202 (2001) 268–278. https://doi.org/10.1006/jcat.2001.3289.

[82] Y.C. Liu, G.L. Griffin, S.S. Chan, I.E. Wachs, Photo-oxidation of methanol using : Catalyst structure and reaction selectivity, J Catal 94 (1985) 108–119. https://doi.org/10.1016/0021-9517(85)90086-7.

[83] P. Forzatti, E. Tronconi, A.S. Elmi, G. Busca, Methanol oxidation over vanadia-based catalysts, Appl Catal A Gen 157 (1997) 387–408. https://doi.org/10.1016/S0926-860X(97)00026-4.

[84] P. Deshlahra, E. Iglesia, Methanol Oxidative Dehydrogenation on Oxide Catalysts: Molecular and Dissociative Routes and Hydrogen Addition Energies as Descriptors of Reactivity, The Journal of Physical Chemistry C 118 (2014) 26115–26129. https://doi.org/10.1021/jp507922u.

[85] P. Mars, D.W. van Krevelen, Oxidations carried out by means of vanadium oxide catalysts, Chem Eng Sci 3 (1954) 41–59. https://doi.org/10.1016/S0009-2509(54)80005-4.

[86] I.E. Wachs, R.J. Madix, The oxidation of methanol on a silver (110) catalyst, Surf Sci 76 (1978) 531–558. https://doi.org/10.1016/0039-6028(78)90113-9.

[87] J. Sambeth, L. Gambaro, H. Thomas, Study of the Adsorption/Oxidation of Methanol over Vanadium Pentoxide, Adsorption Science & Technology 12 (1995) 171–180. https://doi.org/10.1177/026361749501200301.

[88] H. Liu, E. Iglesia, Selective Oxidation of Methanol and Ethanol on Supported Ruthenium Oxide Clusters at Low Temperatures, J Phys Chem B 109 (2005) 2155–2163. https://doi.org/10.1021/jp0401980.

[89] W. Li, H. Liu, E. Iglesia, Structures and Properties of Zirconia-Supported Ruthenium Oxide Catalysts for the Selective Oxidation of Methanol to Methyl Formate, J Phys Chem B 110 (2006) 23337–23342. https://doi.org/10.1021/jp0648689.

[90] N. Li, S. Wang, Y. Sun, S. Li, First principles studies on the selectivity of dimethoxymethane and methyl formate in methanol oxidation over V_2O_5/TiO_2 -based catalysts, Physical Chemistry Chemical Physics 19 (2017) 19393–19406. https://doi.org/10.1039/C7CP02326J.

[91] N. Li, S. Wang, Q. Ren, S. Li, Y. Sun, Catalytic Mechanisms of Methanol Oxidation to Methyl Formate on Vanadia–Titania and Vanadia–Titania–Sulfate Catalysts, The Journal of Physical Chemistry C 120 (2016) 29290–29301. https://doi.org/10.1021/acs.jpcc.6b10289.

[92] J.-M. Tatibouët, H. Lauron-Pernot, Transient isotopic study of methanol oxidation on unsupported V2O5, J Mol Catal A Chem 171 (2001) 205–216. https://doi.org/10.1016/S1381-1169(01)00104-2.

[93] L. Cairati, F. Trifirò, SiO2 and Al2O3 as oxidation catalysts of methanol, J Catal 80 (1983) 25–30. https://doi.org/10.1016/0021-9517(83)90225-7.

[94] M. Ai, The production of methyl formate by the vapor-phase oxidation of methanol, J Catal 77 (1982) 279–288. https://doi.org/10.1016/0021-9517(82)90168-3.

[95] M. Ai, The reaction of formaldehyde on various metal oxide catalysts, J Catal 83 (1983) 141–150. https://doi.org/10.1016/0021-9517(83)90037-4.

[96] S. Jali, H.B. Friedrich, G.R. Julius, The effect of Mo(CO)6 as a co-catalyst in the carbonylation of methanol to methyl formate catalyzed by potassium methoxide under CO, syngas and H2 atmospheres. HP-IR observation of the methoxycarbonyl intermediate of Mo(CO)6, J Mol Catal A Chem 348 (2011) 63–69. https://doi.org/10.1016/j.molcata.2011.08.002.

[97] H. Hietala, Jukka, Vuori, Antti, Johnsson, Pekka, Pollari, Ilkka, Reutemann, Werner, Kieczka, Formic Acid, in: Ullmann's Encyclopedia of Industrial Chemistry, Wiley-VCH Verlag GmbH & Co. KGaA, 2016. https://doi.org/https://doi.org/10.1002/14356007.a12_013.pub3.

[98] L. Rong, Z. Xu, J. Sun, G. Guo, New methyl formate synthesis method: Coal to methyl formate, Journal of Energy Chemistry 27 (2018) 238–242. https://doi.org/10.1016/j.jechem.2017.07.015.

[99] J.J. Corral-Pérez, A. Bansode, C.S. Praveen, A. Kokalj, H. Reymond, A. Comas-Vives, J. Vandevondele, C. Copéret, P.R. Von Rohr, A. Urakawa, Decisive Role of Perimeter Sites in Silica-Supported Ag Nanoparticles in Selective Hydrogenation of CO2 to Methyl Formate in the Presence of Methanol, J Am Chem Soc 140 (2018) 13884–13891. https://doi.org/10.1021/jacs.8b08505.

[100] J.S. Lee, J.C. Kim, Y.G. Kim, Methyl formate as a new building block in C1 chemistry, Appl Catal 57 (1990) 1–30. https://doi.org/10.1016/S0166-9834(00)80720-4.

[101] D.J. Yuan, A.M. Hengne, Y. Saih, K.W. Huang, Nonoxidative Dehydrogenation of Methanol to Methyl Formate through Highly Stable and Reusable CuMgO-Based Catalysts, ACS Omega 4 (2019) 1854–1860. https://doi.org/10.1021/acsomega.8b03069.

[102] T. Sodesawa, Effect of support on dehydrogenation of methanol to methyl formate over Cu-containing catalysts prepared by ion exchange, Reaction Kinetics and Catalysis Letters 32 (1986) 63–69. https://doi.org/10.1007/BF02063451.

[103] S.P. Tonner, D.L. Trimm, M.S. Wainwright, N.W. Cant, Dehydrogenation of methanol to methyl formate over copper catalysts, Industrial & Engineering Chemistry Product Research and Development 23 (1984) 384–388. https://doi.org/10.1021/i300015a012.

[104] Y. Guo, G. Lu, X. Mo, Y. Wang, Vapor phase dehydrogenation of methanol to methyl formate in the catalytic membrane reactor with Cu/SiO2/ ceramic composite membrane, Catal Letters 99 (2005) 105–108. https://doi.org/10.1007/s10562-004-0783-3.

[105] G.A. Olah, Beyond oil and gas: The methanol economy, Angewandte Chemie - International Edition 44 (2005) 2636–2639. https://doi.org/10.1002/anie.200462121.

[106] R. Zhang, Y. Sun, S. Peng, In situ FTIR studies of methanol adsorption and dehydrogenation over Cu/SiO2 catalyst, Fuel 81 (2002) 1619–1624. https://doi.org/10.1016/S0016-2361(02)00085-6.

[107] A. Goosheneshin, R. Maleki, D. Iranshahi, M.R. Rahimpour, A. Jahanmiri, Simultaneous production and utilization of methanol for methyl formate synthesis in a looped heat exchanger reactor configuration, Journal of Natural Gas Chemistry 21 (2012) 661–672. https://doi.org/10.1016/S1003-9953(11)60417-9.

[108] F. Wang, C. Lu, Effect of coordinated ligands on catalytic properties of activated-carbon fibers-supported copper (II) complexes for the dehydrocoupling of methanol to methyl formate, Catal Commun 7 (2006) 709–712. https://doi.org/10.1016/j.catcom.2006.02.016.

[109] E.H. Shreiber, G.W. Roberts, Methanol dehydrogenation in a slurry reactor: evaluation of copper chromite and iron/titanium catalysts, Appl Catal B 26 (2000) 119–129. https://doi.org/10.1016/S0926-3373(00)00114-4.

[110] J. Chen, S. Qin, G. Song, T. Xiang, F. Xin, X. Yin, Shape-controlled solvothermal synthesis of Bi2S3 for photocatalytic reduction of CO2 to methyl formate in methanol, Dalton Transactions 42 (2013) 15133. https://doi.org/10.1039/c3dt51887f.

[111] J.J. Corral-Pérez, C. Copéret, A. Urakawa, Lewis acidic supports promote the selective hydrogenation of carbon dioxide to methyl formate in the presence of methanol over Ag catalysts, J Catal 380 (2019) 153–160. https://doi.org/10.1016/j.jcat.2019.10.013.

[112] C. Wu, Z. Zhang, Q. Zhu, H. Han, Y. Yang, B. Han, Highly efficient hydrogenation of carbon dioxide to methyl formate over supported gold catalysts, Green Chemistry 17 (2015) 1467–1472. https://doi.org/10.1039/c4gc01818d.

[113] K.M.K. Yu, C.M.Y. Yeung, C.T. Shik, Carbon dioxide fixation into chemicals (methyl formate) at high yields by surface coupling over a Pd/Cu/ZnO nanocatalyst, J Am Chem Soc 129 (2007) 6360–6361. https://doi.org/10.1021/ja0706302.

[114] K.M. Kerry Yu, S.C. Tsang, A Study of Methyl Formate Production from Carbon Dioxide Hydrogenation in Methanol over a Copper Zinc Oxide Catalyst, Catal Letters 141 (2011) 259–265. https://doi.org/10.1007/s10562-010-0500-3.

[115] G.O. Evans, C.J. Newell, Conversion of CO2, H2, and alcohols into formate esters using anionic iron carbonyl hydrides, Inorganica Chim Acta 31 (1978) L387–L389. https://doi.org/10.1016/S0020-1693(00)94933-8.

[116] Y. Zhao, Z. Qin, G. Wang, M. Dong, L. Huang, Z. Wu, W. Fan, J. Wang, Catalytic performance of V2O5/ZrO2-Al 2O3 for methanol oxidation, Fuel 104 (2013) 22–27. https://doi.org/10.1016/j.fuel.2010.03.008.

[117] C. La Fontaine, A. Yoboue, E. Berrier, A. Tougerti, F. Villain, E. Fonda, K. Hamraoui, J.F. Paul, S. Cristol, Methanol conversion over TiO2-anatase supported oxomolybdate catalysts: An integrated operando - DFT modeling approach, Phase Transitions 84 (2011) 700–713. https://doi.org/10.1080/01411594.2011.578825.

[118] J. Liu, E. Zhan, W. Cai, J. Li, W. Shen, Methanol selective oxidation to methyl formate over ReOx/ CeO2 catalysts, Catal Letters 120 (2008) 274–280. https://doi.org/10.1007/s10562-007-9280-9.

[119] H. Liu, E. Iglesia, Selective oxidation of methanol and ethanol on supported ruthenium oxide clusters at low temperatures, Journal of Physical Chemistry B 109 (2005) 2155–2163. https://doi.org/10.1021/jp0401980.

[120] L.E. Briand, A.M. Hirt, I.E. Wachs, Quantitative determination of the number of surface active sites and the turnover frequencies for methanol oxidation over metal oxide catalysts: Application to bulk metal molybdates and pure metal oxide catalysts, J Catal 202 (2001) 268–278. https://doi.org/10.1006/jcat.2001.3289.

[121] N.G. Valente, L.A. Arrúa, L.E. Cadús, Structure and activity of Sn-Mo-O catalysts: Partial oxidation of methanol, Appl Catal A Gen 205 (2001) 201–214. https://doi.org/10.1016/S0926-860X(00)00565-2.

[122] M. Niwa, Role of the solid acidity on the MoO3 loaded on SnO2 in the methanol oxidation into formaldehyde, Catal Today 52 (1999) 71–81. https://doi.org/10.1016/S0920-5861(99)00064-4.

[123] P. Forzatti, E. Tronconi, A.S. Elmi, G. Busca, Methanol oxidation over vanadia-based catalysts, Appl Catal A Gen 157 (1997) 387–408. https://doi.org/10.1016/S0926-860X(97)00026-4.

[124] J.B. Wu, R.P. Shi, Z.F. Qin, H. Liu, Z.K. Li, H.Q. Zhu, Y.X. Zhao, J.G. Wang, Selective oxidation of methanol to methyl formate over bimetallic Au-Pd nanoparticles supported on SiO2, Ranliao Huaxue Xuebao/Journal of Fuel Chemistry and Technology 47 (2019) 780–790. https://doi.org/10.1016/s1872-5813(19)30034-9.

[125] S. Yoon, K. Oh, F. Liu, J.H. Seo, G.A. Somorjai, J.H. Lee, K. An, Specific Metal-Support Interactions between Nanoparticle Layers for Catalysts with Enhanced Methanol Oxidation Activity, ACS Catal 8 (2018) 5391–5398. https://doi.org/10.1021/acscatal.8b00276.

[126] Y. Xiao, Y. Wang, A. Varma, Low-temperature selective oxidation of methanol over Pt-Bi bimetallic catalysts, J Catal 363 (2018) 144–153. https://doi.org/10.1016/j.jcat.2018.04.016.

[127] R. Wojcieszak, E.M. Gaigneaux, P. Ruiz, Direct Methyl Formate Formation from Methanol over Supported Palladium Nanoparticles at Low Temperature, ChemCatChem 5 (2013) 339–348. https://doi.org/10.1002/cctc.201200325.

[128] A. Wittstock, V. Zielasek, J. Biener, C.M. Friend, M. Bäumer, Nanoporous gold catalysts for selective gas-phase oxidative coupling of methanol at low temperature, Science (1979) 327 (2010) 319–322. https://doi.org/10.1126/science.1183591.

[129] J. Lichtenberger, D. Lee, E. Iglesia, Catalytic oxidation of methanol on Pd metal and oxide clusters at near-ambient temperatures, Physical Chemistry Chemical Physics 9 (2007) 4902–4906. https://doi.org/10.1039/b707465d.

[130] H. Liu, E. Iglesia, Selective one-step synthesis of dimethoxymethane via methanol or dimethyl ether oxidation on H3+nVnMo12-nPO40 Keggin structures, Journal of Physical Chemistry B 107 (2003) 10840–10847. https://doi.org/10.1021/jp0301554.

[131] J.M. Tatibouët, Methanol oxidation as a catalytic surface probe, 1997. https://doi.org/10.1016/S0926-860X(96)00236-0.

[132] M. Ai, The production of methyl formate by the vapor-phase oxidation of methanol, J Catal 77 (1982) 279–288. https://doi.org/10.1016/0021-9517(82)90168-3.

[133] M.A. Banares, H.C. Hu, I.E. Wachs, Molybdena on Silica Catalysts: Role of Preparation Methods on the Structure-Selectivity Properties for the Oxidation of Methanol, J Catal 150 (1994) 407–420. https://doi.org/10.1006/jcat.1994.1359.

[134] J. Lichtenberger, D. Lee, E. Iglesia, Catalytic oxidation of methanol on Pd metal and oxide clusters at near-ambient temperatures, Physical Chemistry Chemical Physics 9 (2007) 4902–4906. https://doi.org/10.1039/b707465d.

[135] V. V. Kaichev, G.Y. Popova, Y.A. Chesalov, A.A. Saraev, D.Y. Zemlyanov, S.A. Beloshapkin, A. Knop-Gericke, R. Schlögl, T. V. Andrushkevich, V.I. Bukhtiyarov, Selective oxidation of methanol to form dimethoxymethane and methyl formate over

a monolayer V2O5/TiO2 catalyst, J Catal 311 (2014) 59–70. https://doi.org/10.1016/j.jcat.2013.10.026.

[136] C.C. Zhang, L. Zheng, Z.M. Zhang, R.C. Dai, Z.P. Wang, J.W. Zhang, Z.J. Ding, Raman studies of hexagonal MoO_3 at high pressure, Physica Status Solidi (b) 248 (2011) 1119–1122. https://doi.org/10.1002/pssb.201000633.

[137] I.E. Wachs, Raman and IR studies of surface metal oxide species on oxide supports: Supported metal oxide catalysts, Catal Today 27 (1996) 437–455. https://doi.org/10.1016/0920-5861(95)00203-0.

[138] A.N. Desikan, L. Huang, S.T. Oyama, Structure and dispersion of molybdenum oxide supported on alumina and titania, Journal of the Chemical Society, Faraday Transactions 88 (1992) 3357. https://doi.org/10.1039/ft9928803357.

[139] R. Radhakrishnan, C. Reed, S.T. Oyama, M. Seman, J.N. Kondo, K. Domen, Y. Ohminami, K. Asakura, Variability in the Structure of Supported MoO_3 Catalysts: Studies Using Raman and X-ray Absorption Spectroscopy with ab Initio Calculations, J Phys Chem B 105 (2001) 8519–8530. https://doi.org/10.1021/jp0117361.

[140] B. Zhang, M.E. Ford, E. Ream, I.E. Wachs, Olefin metathesis over supported MoO_x catalysts: influence of the oxide support, Catal Sci Technol 13 (2023) 217–225. https://doi.org/10.1039/D2CY01612E.

[141] H. Hu, I.E. Wachs, S.R. Bare, Surface Structures of Supported Molybdenum Oxide Catalysts: Characterization by Raman and Mo L3-Edge XANES, J Phys Chem 99 (1995) 10897–10910. https://doi.org/10.1021/j100027a034.

[142] H. Shimada, N. Matsubayashi, T. Sato, Y. Yoshimura, A. Nishijima, N. Kosugi, H. Kuroda, XAFS study of molybdenum oxide catalysts on various supports, J Catal 138 (1992) 746–749. https://doi.org/10.1016/0021-9517(92)90321-8.

[143] A.L. Patterson, The Scherrer Formula for X-Ray Particle Size Determination, Physical Review 56 (1939) 978–982. https://doi.org/10.1103/PhysRev.56.978.

[144] A. Kubiak, W. Wojciechowska, B. Kurc, M. Pigłowska, K. Synoradzki, E. Gabała, D. Moszyński, M. Szybowicz, K. Siwińska-Ciesielczyk, T. Jesionowski, Highly Crystalline TiO2-MoO3 Composite Materials Synthesized via a Template-Assisted Microwave Method for Electrochemical Application, Crystals (Basel) 10 (2020) 493. https://doi.org/10.3390/cryst10060493.

[145] S. Guo, Z. Huang, L. Wang, X. Wu, H. Shen, G. Jing, MoO3/TiO2 catalyst with atomically dispersed O-Mo-O structures toward improving NH4HSO4 poisoning resistance for selective catalytic reduction of nitrogen oxides, J Hazard Mater 418 (2021) 126289. https://doi.org/10.1016/j.jhazmat.2021.126289.

[146] H. Yang, W. Yin, X. Zhu, P.J. Deuss, H.J. Heeres, Selective Demethoxylation of Guaiacols to Phenols using Supported MoO_3 Catalysts, ChemCatChem 14 (2022). https://doi.org/10.1002/cctc.202200297.

[147] V. Itthibenchapong, P. Chakthranont, C. Sattayanon, T. Butburee, K. Faungnawakij, S. Namuangruk, Understanding the promoter effect of bifunctional (Pt, Ni, Cu)-MoO3-x/TiO2 catalysts for the hydrodeoxygenation of p-cresol: A combined DFT and experimental study, Appl Surf Sci 547 (2021) 149170. https://doi.org/10.1016/j.apsusc.2021.149170.

[148] T. Toyao, S. Kayamori, Z. Maeno, S.M.A.H. Siddiki, K. Shimizu, Heterogeneous Pt and MoO_x Co-Loaded TiO_2 Catalysts for Low-Temperature CO_2 Hydrogenation To Form CH_3OH, ACS Catal 9 (2019) 8187–8196. https://doi.org/10.1021/acscatal.9b01225.

[149] K.V.R. Chary, K. Rajender Reddy, C. Praveen Kumar, Dispersion and reactivity of molybdenum oxide catalysts supported on titania, Catal Commun 2 (2001) 277–284. https://doi.org/10.1016/S1566-7367(01)00044-9.

[150] G.C. Bond, S. Flamerz, L. van Wijk, Structure and reactivity of titania-supported molybdenum and tungsten oxides, Catal Today 1 (1987) 229–243. https://doi.org/10.1016/0920-5861(87)80042-1.

[151] T. Malleswararao, E. Vicoruiz, M. Bañares, G. Deo, Obtaining the best composition of supported V2O5–MoO3/TiO2 catalyst for propane ODH reaction, J Catal 258 (2008) 324–333. https://doi.org/10.1016/j.jcat.2008.07.001.

[152] C. Martin, I. Martin, V. Rives, P. Malet, Alkaline-Metal Doped MoO3/TiO2Systems: Structure of Supported Molybdates, J Catal 161 (1996) 87–95. https://doi.org/10.1006/jcat.1996.0165.

[153] I.T. Ghampson, G. Pecchi, J.L.G. Fierro, A. Videla, N. Escalona, Catalytic hydrodeoxygenation of anisole over Re-MoO x /TiO 2 and Re-VO x /TiO 2 catalysts, Appl Catal B 208 (2017) 60–74. https://doi.org/10.1016/j.apcatb.2017.02.047.

[154] L. Feng, X. Li, D.B. Dadyburjor, E.L. Kugler, A Temperature-Programmed-Reduction Study on Alkali-Promoted, Carbon-Supported Molybdenum Catalysts, J Catal 190 (2000) 1–13. https://doi.org/10.1006/jcat.1999.2744.

[155] S. Rajagopal, H.J. Marini, J.A. Marzari, R. Miranda, Silica-Alumina-Supported Acidic Molybdenum Catalysts - TPR and XRD Characterization, J Catal 147 (1994) 417–428. https://doi.org/10.1006/jcat.1994.1159.

[156] A.M. de Jong, H.J. Borg, L.J. van IJzendoorn, V.G.F.M. Soudant, V.H.J. de Beer, J.A.R. van Veen, J.W. Niemantsverdriet, Sulfidation mechanism by molybdenum catalysts supported on silica/silicon(100) model support studied by surface

spectroscopy, J Phys Chem 97 (1993) 6477–6483. https://doi.org/10.1021/j100126a024.

[157] J. Chang, T. Danuthai, S. Dewiyanti, C. Wang, A. Borgna, Hydrodeoxygenation of Guaiacol over Carbon-Supported Metal Catalysts, ChemCatChem 5 (2013) 3041–3049. https://doi.org/10.1002/cctc.201300096.

[158] K. Bhattacharyya, J. Majeed, K.K. Dey, P. Ayyub, A.K. Tyagi, S.R. Bharadwaj, Effect of Mo-Incorporation in the TiO_2 Lattice: A Mechanistic Basis for Photocatalytic Dye Degradation, The Journal of Physical Chemistry C 118 (2014) 15946–15962. https://doi.org/10.1021/jp5054666.

[159] M.A. Bica de Moraes, B.C. Trasferetti, F.P. Rouxinol, R. Landers, S.F. Durrant, J. Scarmínio, A. Urbano, Molybdenum Oxide Thin Films Obtained by the Hot-Filament Metal Oxide Deposition Technique, Chemistry of Materials 16 (2004) 513–520. https://doi.org/10.1021/cm034551a.

[160] F. Xie, W.C.H. Choy, C. Wang, X. Li, S. Zhang, J. Hou, Low-temperature solution-processed hydrogen molybdenum and vanadium bronzes for an efficient hole-transport layer in organic electronics, Advanced Materials 25 (2013) 2051–2055. https://doi.org/10.1002/adma.201204425.

[161] N. Jada, K.J. Sankaran, R. Sakthivel, D. Sethi, P. Mohapatra, Synergistic effect of MoO3/TiO2 towards discrete and simultaneous photocatalytic degradation of E. coli and methylene blue in water, Bulletin of Materials Science 44 (2021) 167. https://doi.org/10.1007/s12034-021-02436-z.

[162] A.Q. Khan, S. Yuan, S. Niu, L. Zheng, W. Li, H. Zeng, Synthesis of molybdenum oxide-titanium dioxide nanocomposites with ultrashort laser ablation in water, Opt Express 25 (2017) A539. https://doi.org/10.1364/OE.25.00A539.

[163] A. Galtayries, S. Wisniewski, J. Grimblot, Formation of thin oxide and sulphide films on polycrystalline molybdenum foils: characterization by XPS and surface potential variations, J Electron Spectros Relat Phenomena 87 (1997) 31–44. https://doi.org/10.1016/S0368-2048(97)00071-6.

[164] E. McCafferty, J.P. Wightman, Determination of the concentration of surface hydroxyl groups on metal oxide films by a quantitative XPS method, Surface and Interface Analysis 26 (1998) 549–564. https://doi.org/10.1002/(SICI)1096-9918(199807)26:8<549::AID-SIA396>3.0.CO;2-Q.

[165] V.R. Sreelakshmi, A. Anu Kaliani, M. Jithin, Photochromic and hydrophilic self-cleaning nature of MoO3 thin films, Journal of Materials Science: Materials in Electronics 33 (2022) 9525–9537. https://doi.org/10.1007/s10854-021-07504-y.

[166] M.I. Zaki, B. Vielhaber, H. Knoezinger, Low-temperature carbon monoxide adsorption and state of molybdena supported on alumina, titania, ceria, and zirconia.

An infrared spectroscopic investigation, J Phys Chem 90 (1986) 3176–3183. https://doi.org/10.1021/j100405a026.

[167] K.I. Hadjiivanov, G.N. Vayssilov, Characterization of oxide surfaces and zeolites by carbon monoxide as an IR probe molecule, in: 2002: pp. 307–511. https://doi.org/10.1016/S0360-0564(02)47008-3.

[168] L.Yu. Novoselova, Mo and MoO 3 powders: Structure and resistance to CO, J Alloys Compd 615 (2014) 784–791. https://doi.org/10.1016/j.jallcom.2014.07.006.

[169] G. Ramis, G. Busca, V. Lorenzelli, FT-IR Study of the Dispersion of the Supported Phase on MoO $_3$ -TiO $_2$ Catalysts, Zeitschrift Für Physikalische Chemie 153 (1987) 189–200. https://doi.org/10.1524/zpch.1987.153.Part_1_2.189.

[170] K. Hadjiivanov, J. Lamotte, J.-C. Lavalley, FTIR Study of Low-Temperature CO Adsorption on Pure and Ammonia-Precovered TiO $_2$ (Anatase), Langmuir 13 (1997) 3374–3381. https://doi.org/10.1021/la962104m.

[171] K. Hadjiivanov, FTIR study of CO and NH3 co-adsorption on TiO2 (rutile), Appl Surf Sci 135 (1998) 331–338. https://doi.org/10.1016/S0169-4332(98)00298-0.

[172] M. Ai, The Oxidation Activity and Acid-base Properties of Mixed Oxide Catalysts Containing Titania. I. The TiO2–MoO3 and TiO2–V2O5 Systems, Bull Chem Soc Jpn 49 (1976) 1328–1334. https://doi.org/10.1246/bcsj.49.1328.

[173] M.A. Betiha, A.M. Rabie, A.M. Elfadly, F.Z. Yehia, Microwave assisted synthesis of a VO -modified disordered mesoporous silica for ethylbenzene dehydrogenation in presence of CO2, Microporous and Mesoporous Materials 222 (2016) 44–54. https://doi.org/10.1016/j.micromeso.2015.10.009.

[174] G. Mestl, T.K.K. Srinivasan, Raman Spectroscopy of Monolayer-Type Catalysts: Supported Molybdenum Oxides, Catalysis Reviews 40 (1998) 451–570. https://doi.org/10.1080/01614949808007114.

[175] T. Machej, J. Haber, A. M. Turek, I. E. Wachs, Monolayer V2O5/TiO2 and MoO3/TiO2 catalysts prepared by different methods, Appl Catal 70 (1991) 115–128. https://doi.org/10.1016/S0166-9834(00)84158-5.

[176] C. Andriopoulou, S. Boghosian, Heterogeneity of deposited phases in supported transition metal oxide catalysts: reversible temperature-dependent evolution of molecular structures and configurations, Physical Chemistry Chemical Physics 20 (2018) 1742–1751. https://doi.org/10.1039/C7CP07286D.

[177] F.F. Oloye, Raman spectroscopy and XRD study on molybdenum oxide supported titania, Results in Materials 5 (2020) 100064. https://doi.org/10.1016/j.rinma.2020.100064.

[178] K. Eda, Raman spectra of hydrogen molybdenum bronze, H0.30MoO3, J Solid State Chem 98 (1992) 350–357. https://doi.org/10.1016/S0022-4596(05)80245-2.

[179] M. Wen, X. Chen, Z. Zheng, S. Deng, Z. Li, W. Wang, H. Chen, In-Plane Anisotropic Raman Spectroscopy of van der Waals α-MoO $_3$, The Journal of Physical Chemistry C 125 (2021) 765–773. https://doi.org/10.1021/acs.jpcc.0c09178.

[180] J. Yan, G. Wu, N. Guan, L. Li, Z. Li, X. Cao, Understanding the effect of surface/bulk defects on the photocatalytic activity of TiO2: anatase versus rutile, Physical Chemistry Chemical Physics 15 (2013) 10978. https://doi.org/10.1039/c3cp50927c.

[181] J. Shi, J. Chen, Z. Feng, T. Chen, Y. Lian, X. Wang, C. Li, Photoluminescence Characteristics of TiO $_2$ and Their Relationship to the Photoassisted Reaction of Water/Methanol Mixture, The Journal of Physical Chemistry C 111 (2007) 693–699. https://doi.org/10.1021/jp065744z.

[182] A.M. Pennington, A.I. Okonmah, D.T. Munoz, G. Tsilomelekis, F.E. Celik, Changes in Polymorph Composition in P25-TiO $_2$ during Pretreatment Analyzed by Differential Diffuse Reflectance Spectral Analysis, The Journal of Physical Chemistry C 122 (2018) 5093–5104. https://doi.org/10.1021/acs.jpcc.7b10449.

[183] J. Song, S. Impeng, J. Zhang, J. Deng, D. Zhang, Elucidating the sensitivity of vanadyl species to water over V2O5/TiO2 catalysts for NOx abatement via operando Raman spectroscopy, J Catal 416 (2022) 198–208. https://doi.org/10.1016/j.jcat.2022.11.003.

[184] A.L. Godiksen, M.H. Funk, S.B. Rasmussen, S. Mossin, Assessing the Importance of V(IV) During NH3−SCR Using Operando EPR Spectroscopy, ChemCatChem 12 (2020) 4893–4903. https://doi.org/10.1002/cctc.202000802.

[185] Y. Zhu, J. Wang, H. Chu, Y.-C. Chu, H.M. Chen, *In Situ* / *Operando* Studies for Designing Next-Generation Electrocatalysts, ACS Energy Lett 5 (2020) 1281–1291. https://doi.org/10.1021/acsenergylett.0c00305.

[186] F. Zaera, In-situ and operando spectroscopies for the characterization of catalysts and of mechanisms of catalytic reactions, J Catal 404 (2021) 900–910. https://doi.org/10.1016/j.jcat.2021.08.013.

[187] L. Lukashuk, K. Foettinger, In Situ and Operando Spectroscopy: A Powerful Approach Towards Understanding Catalysts, Johnson Matthey Technology Review 62 (2018) 316–331. https://doi.org/10.1595/205651318X15234323420569.

[188] G. Galdames, P. Santander, R. Jiménez, A. Karelovic, A detailed kinetic model for the methanol oxidative dehydrogenation on vanadia-based catalysts: Aggregation state role and active site requirements, Appl Catal A Gen 682 (2024) 119807. https://doi.org/10.1016/j.apcata.2024.119807.

[189] C. LOUIS, Catalytic properties of silica-supported molybdenum catalysts in methanol oxidation: The influence of molybdenum dispersion, J Catal 109 (1988) 354–366. https://doi.org/10.1016/0021-9517(88)90218-7.

[190] J. Allison, W.A. Goddard III, Oxidative dehydrogenation of methanol to formaldehyde*1, J Catal 92 (1985) 127–135. https://doi.org/10.1016/0021-9517(85)90242-8.

[191] G. Cai, W.T. Broomhead, Y.-H.C. Chin, H. Cai, Advanced Kinetic and Titration Strategies for Assessing the Intrinsic Kinetics on Oxide and Sulfide Catalysts, Top Catal 66 (2023) 1102–1119. https://doi.org/10.1007/s11244-023-01849-w.

[192] L.J. Burcham, M. Badlani, I.E. Wachs, The Origin of the Ligand Effect in Metal Oxide Catalysts: Novel Fixed-Bed in Situ Infrared and Kinetic Studies during Methanol Oxidation, J Catal 203 (2001) 104–121. https://doi.org/10.1006/jcat.2001.3312.

[193] G. Busca, Infrared studies of the reactive adsorption of organic molecules over metal oxides and of the mechanisms of their heterogeneously-catalyzed oxidation, Catal Today 27 (1996) 457–496. https://doi.org/10.1016/0920-5861(95)00162-X.

[194] J.C. Lavalley, Infrared spectrometric studies of the surface basicity of metal oxides and zeolites using adsorbed probe molecules, Catal Today 27 (1996) 377–401. https://doi.org/10.1016/0920-5861(95)00161-1.

[195] G.Ya. Popova, Ya.A. Chesalov, T. V. Andrushkevich, E.S. Stoyanov, Heterogeneous selective oxidation of formaldehyde on oxide catalysts:In situ FTIR study of formaldehyde surface species on a V-Ti-O catalyst and oxygen effect, Kinetics and Catalysis 41 (2000) 546–552. https://doi.org/10.1007/BF02756073.

[196] G. Busca, J. Lamotte, J.C. Lavalley, V. Lorenzelli, FT-IR study of the adsorption and transformation of formaldehyde on oxide surfaces, J Am Chem Soc 109 (1987) 5197–5202. https://doi.org/10.1021/ja00251a025.

[197] G. Busca, On the mechanism of methanol oxidation over vanadia-based catalysts: a FT-IR study of the adsorption of methanol, formaldehyde and formic acid on vanad, Journal of Molecular Catalysis 50 (1989) 241–249. https://doi.org/10.1016/0304-5102(89)85067-9.

[198] V. Lochař, J. Machek, J. Tichý, Mechanism of selective oxidation of methanol over stannic oxide-molybdenum oxide catalyst, Appl Catal A Gen 228 (2002) 95–101. https://doi.org/10.1016/S0926-860X(01)00970-X.

[199] Y. Suda, T. Morimoto, Molecularly adsorbed water on the bare surface of titania (rutile), Langmuir 3 (1987) 786–788. https://doi.org/10.1021/la00077a037.

[200] K. Balakrishnan, J. Schwank, FTIR study of bimetallic Pt-Sn/Al2O3 catalysts, J Catal 138 (1992) 491–499. https://doi.org/10.1016/0021-9517(92)90301-W.

[201] C. Yang, C. Wöll, IR spectroscopy applied to metal oxide surfaces: adsorbate vibrations and beyond, Adv Phys X 2 (2017) 373–408. https://doi.org/10.1080/23746149.2017.1296372.

[202] J. Raskó, J. Kiss, Infrared study of the adsorption of CO and CH3 on silica-supported MoO3 and Mo2C catalysts, Appl Catal A Gen 253 (2003) 427–436. https://doi.org/10.1016/S0926-860X(03)00555-6.

[203] A.A. Tsyganenko, F. Can, A. Travert, F. Maugé, FTIR study of unsupported molybdenum sulfide?in situ synthesis and surface properties characterization, Appl Catal A Gen 268 (2004) 189–197. https://doi.org/10.1016/j.apcata.2004.03.038.

[204] R.H. Ellerbrock, H.H. Gerke, FTIR spectral band shifts explained by OM–cation interactions, Journal of Plant Nutrition and Soil Science 184 (2021) 388–397. https://doi.org/10.1002/jpln.202100056.

[205] I.E. Wachs, Catalysis science of supported vanadium oxide catalysts, Dalton Transactions 42 (2013) 11762. https://doi.org/10.1039/c3dt50692d.

[206] H. Liu, E. Iglesia, Selective Oxidation of Methanol and Ethanol on Supported Ruthenium Oxide Clusters at Low Temperatures, J Phys Chem B 109 (2005) 2155–2163. https://doi.org/10.1021/jp0401980.

[207] H. Tian, E.I. Ross, I.E. Wachs, Quantitative Determination of the Speciation of Surface Vanadium Oxides and Their Catalytic Activity, J Phys Chem B 110 (2006) 9593–9600. https://doi.org/10.1021/jp055767y.

[208] L.J. Burcham, I.E. Wachs, The origin of the support effect in supported metal oxide catalysts: in situ infrared and kinetic studies during methanol oxidation, Catal Today 49 (1999) 467–484. https://doi.org/10.1016/S0920-5861(98)00442-8.

[209] C. Caro, K. Thirunavukkarasu, M. Anilkumar, N.R. Shiju, G. Rothenberg, Selective autooxidation of ethanol over titania-supported molybdenum oxide catalysts: Structure and reactivity, Adv Synth Catal 354 (2012) 1327–1336. https://doi.org/10.1002/adsc.201000841.

[210] D.G. Barton, M. Shtein, R.D. Wilson, S.L. Soled, E. Iglesia, Structure and electronic properties of solid acids based on tungsten oxide nanostructures, Journal of Physical Chemistry B 103 (1999) 630–640. https://doi.org/10.1021/jp983555d.

[211] R.R. Langeslay, D.M. Kaphan, C.L. Marshall, P.C. Stair, A.P. Sattelberger, M. Delferro, Catalytic Applications of Vanadium: A Mechanistic Perspective, Chem Rev 119 (2019) 2128–2191. https://doi.org/10.1021/acs.chemrev.8b00245.

[212] B. Kilos, A.T. Bell, E. Iglesia, Mechanism and Site Requirements for Ethanol Oxidation on Vanadium Oxide Domains, The Journal of Physical Chemistry C 113 (2009) 2830–2836. https://doi.org/10.1021/jp8078056.

[213] O. Gómez-Cápiro, L. Bravo, P. Lagos, P. Santander, G. Pecchi, A. Karelovic, Kinetic and structural understanding of bulk and supported vanadium-based catalysts for furfural oxidation to maleic anhydride, Catal Sci Technol 11 (2021) 6477–6489. https://doi.org/10.1039/D1CY01060C.

[214] A. Khodakov, B. Olthof, A.T. Bell, E. Iglesia, Structure and Catalytic Properties of Supported Vanadium Oxides: Support Effects on Oxidative Dehydrogenation Reactions, J Catal 181 (1999) 205–216. https://doi.org/10.1006/jcat.1998.2295.

[215] P. Santander, L. Bravo, G. Pecchi, A. Karelovic, The consequences of support identity on the oxidative conversion of furfural to maleic anhydride on vanadia catalysts, Appl Catal A Gen 595 (2020) 117513. https://doi.org/10.1016/j.apcata.2020.117513.

[216] E. Papulovskiy, A.A. Shubin, O.B. Lapina, Investigation of vanadia-alumina catalysts with solid-state NMR spectroscopy and DFT, Physical Chemistry Chemical Physics 23 (2021) 19352–19363. https://doi.org/10.1039/d1cp03297f.

[217] L. Schumacher, J. Weyel, C. Hess, Unraveling the Active Vanadium Sites and Adsorbate Dynamics in VOx/CeO2Oxidation Catalysts Using Transient IR Spectroscopy, J Am Chem Soc 144 (2022) 14874–14887. https://doi.org/10.1021/jacs.2c06303.

[218] C.A. Carrero, R. Schloegl, I.E. Wachs, R. Schomaecker, Critical literature review of the kinetics for the oxidative dehydrogenation of propane over well-defined supported vanadium oxide catalysts, ACS Catal 4 (2014) 3357–3380. https://doi.org/10.1021/cs5003417.

[219] N. Hamilton, T. Wolfram, G. Tzolova Müller, M. Hävecker, J. Kröhnert, C. Carrero, R. Schomäcker, A. Trunschke, R. Schlögl, Topology of silica supported vanadium-titanium oxide catalysts for oxidative dehydrogenation of propane, Catal Sci Technol 2 (2012) 1346–1359. https://doi.org/10.1039/c2cy00541g.

[220] P. Kube, B. Frank, R. Schlögl, A. Trunschke, Isotope Studies in Oxidation of Propane over Vanadium Oxide, ChemCatChem 9 (2017) 3446–3455. https://doi.org/10.1002/cctc.201700847.

[221] A. Dinse, S. Khennache, B. Frank, C. Hess, R. Herbert, S. Wrabetz, R. Schlögl, R. Schomäcker, Oxidative dehydrogenation of propane on silica (SBA-15) supported vanadia catalysts: A kinetic investigation, J Mol Catal A Chem 307 (2009) 43–50. https://doi.org/10.1016/j.molcata.2009.03.008.

[222] C. Hess, Nanostructured vanadium oxide model catalysts for selective oxidation reactions, ChemPhysChem 10 (2009) 319–326. https://doi.org/10.1002/cphc.200800585.

[223] H. Liu, Effects of support on bifunctional methanol oxidation pathways catalyzed by polyoxometallate Keggin clusters, J Catal 223 (2004) 161–169. https://doi.org/10.1016/j.jcat.2004.01.012.

[224] I.R. Beattie, T.R. Gilson, Oxide phonon spectra, Journal of the Chemical Society A: Inorganic, Physical, Theoretical (1969) 2322. https://doi.org/10.1039/j19690002322.

[225] M.A. Vuurman, I.E. Wachs, A.M. Hirt, Structural determination of supported vanadium pentoxide-tungsten trioxide-titania catalysts by in situ Raman spectroscopy and x-ray photoelectron spectroscopy, J Phys Chem 95 (1991) 9928–9937. https://doi.org/10.1021/j100177a059.

[226] I.E. Wachs, The generality of surface vanadium oxide phases in mixed oxide catalysts, Appl Catal A Gen 391 (2011) 36–42. https://doi.org/10.1016/j.apcata.2010.08.048.

[227] J.L. Bronkema, D.C. Leo, A.T. Bell, Mechanistic studies of methanol oxidation to formaldehyde on isolated vanadate sites supported on high surface area anatase, Journal of Physical Chemistry C 111 (2007) 14530–14540. https://doi.org/10.1021/jp073826x.

[228] G. Centi, Nature of active layer in vanadium oxide supported on titanium oxide and control of its reactivity in the selective oxidation and ammoxidation of alkylaromatics, Appl Catal A Gen 147 (1996) 267–298. https://doi.org/10.1016/S0926-860X(96)00179-2.

[229] G.T. Went, L.-J. Leu, A.T. Bell, Quantitative Structural Analysis of Dispersed Vanadia Species in TiO2(Anatase)-Supported V205, 1992.

[230] J. Tauc, Optical properties and electronic structure of amorphous Ge and Si, Mater Res Bull 3 (1968) 37–46. https://doi.org/10.1016/0025-5408(68)90023-8.

[231] Z. Helali, A. Jedidi, O.A. Syzgantseva, M. Calatayud, C. Minot, Scaling reducibility of metal oxides, Theor Chem Acc 136 (2017) 100. https://doi.org/10.1007/s00214-017-2130-y.

[232] Y. Zhao, Z. Qin, G. Wang, M. Dong, L. Huang, Z. Wu, W. Fan, J. Wang, Catalytic performance of V2O5/ZrO2–Al2O3 for methanol oxidation, Fuel 104 (2013) 22–27. https://doi.org/10.1016/j.fuel.2010.03.008.

[233] T. Sodesawa, Effect of support on dehydrogenation of methanol to methyl formate over Cu-containing catalysts prepared by ion exchange, Reaction Kinetics and Catalysis Letters 32 (1986) 63–69. https://doi.org/10.1007/BF02063451.

[234] Z. Liu, R. Zhang, S. Wang, N. Li, R. Sima, G. Liu, P. Wu, G. Zeng, S. Li, Y. Sun, Highly Efficient and Stable Vanadia–Titania–Sulfate Catalysts for Methanol Oxidation to Methyl Formate: Synthesis and Mechanistic Study, The Journal of

Physical Chemistry C 120 (2016) 6591–6600. https://doi.org/10.1021/acs.jpcc.5b12621.

[235] H. Liu, E. Iglesia, Selective One-Step Synthesis of Dimethoxymethane via Methanol or Dimethyl Ether Oxidation on $H_{3+n}V_nMo_{12-n}PO_{40}$ Keggin Structures, J Phys Chem B 107 (2003) 10840–10847. https://doi.org/10.1021/jp0301554.

[236] K. Takahashi, N. Takezawa, H. Kobayashi, MECHANISM OF FORMATION OF METHYL FORMATE FROM FORMALDEHYDE OVER COPPER CATALYSTS, Chem Lett 12 (1983) 1061–1064. https://doi.org/10.1246/cl.1983.1061.

[237] J.-M. Tatibouët, H. Lauron-Pernot, Transient isotopic study of methanol oxidation on unsupported V2O5, J Mol Catal A Chem 171 (2001) 205–216. https://doi.org/10.1016/S1381-1169(01)00104-2.

[238] P. Deshlahra, R.T. Carr, S.-H. Chai, E. Iglesia, Mechanistic Details and Reactivity Descriptors in Oxidation and Acid Catalysis of Methanol, ACS Catal 5 (2015) 666–682. https://doi.org/10.1021/cs501599y.

[239] S. Kwon, P. Deshlahra, E. Iglesia, Dioxygen activation routes in Mars-van Krevelen redox cycles catalyzed by metal oxides, J Catal 364 (2018) 228–247. https://doi.org/10.1016/j.jcat.2018.05.016.

[240] J.J. Corral-Pérez, A. Bansode, C.S. Praveen, A. Kokalj, H. Reymond, A. Comas-Vives, J. VandeVondele, C. Copéret, P.R. von Rohr, A. Urakawa, Decisive Role of Perimeter Sites in Silica-Supported Ag Nanoparticles in Selective Hydrogenation of CO_2 to Methyl Formate in the Presence of Methanol, J Am Chem Soc 140 (2018) 13884–13891. https://doi.org/10.1021/jacs.8b08505.

[241] A. Goodrow, A.T. Bell, A Theoretical Investigation of the Selective Oxidation of Methanol to Formaldehyde on Isolated Vanadate Species Supported on Silica, The Journal of Physical Chemistry C 111 (2007) 14753–14761. https://doi.org/10.1021/jp072627a.

[242] J. TATIBOUET, A structure-sensitive oxidation reaction: Methanol on molybdenum trioxide catalysts, J Catal 72 (1981) 375–378. https://doi.org/10.1016/0021-9517(81)90022-1.

[243] J. TATIBOUET, Structure-sensitive catalytic oxidation: Alcohols on graphite-supported molybdenum trioxide, J Catal 82 (1983) 240–244. https://doi.org/10.1016/0021-9517(83)90136-7.

[244] J. ZIOKOWSKI, Crystallochemical model of active sites on oxide catalysts, J Catal 100 (1986) 45–58. https://doi.org/10.1016/0021-9517(86)90070-9.

[245] Z. Sojka, M. Che, EPR Study of the Interaction of O- Ions with CH3OH within the Coordination Sphere of Mo Ions Grafted on Silica: A New Approach for the Study of

the Mechanism of Catalytic Reactions, J Phys Chem 99 (1995) 5418–5430. https://doi.org/10.1021/j100015a027.

[246] J.-M. Tatibouët, M. Che, M. Amirouche, M. Fournier, C. Rocchiccioli-Deltcheff, Catalytic oxidation of methanol by 12-molybdosilicic acid supported on silica: dispersion effect, J. Chem. Soc., Chem. Commun. (1988) 1260–1261. https://doi.org/10.1039/C39880001260.

[247] S.S. Wang, G.Y. Yang, Recent Advances in Polyoxometalate-Catalyzed Reactions, Chem Rev 115 (2015) 4893–4962. https://doi.org/10.1021/cr500390v.

[248] P. Deshlahra, E. Iglesia, Methanol Oxidative Dehydrogenation on Oxide Catalysts: Molecular and Dissociative Routes and Hydrogen Addition Energies as Descriptors of Reactivity, Journal of Physical Chemistry C 118 (2014) 26115–26129. https://doi.org/10.1021/jp507922u.

[249] H. Liu, E. Iglesia, Effects of support on bifunctional methanol oxidation pathways catalyzed by polyoxometallate Keggin clusters, J Catal 223 (2004) 161–169. https://doi.org/10.1016/j.jcat.2004.01.012.

[250] A. Bielański, A. Małecka, L. Kybelkova, Infrared study of the thermal decomposition of heteropolyacids of the series H3+xPMo12–xVxO40, Journal of the Chemical Society, Faraday Transactions 1: Physical Chemistry in Condensed Phases 85 (1989) 2847. https://doi.org/10.1039/f19898502847.

[251] A. Bielański, A. Malecka, J. Poźniczek, DTA and TG analysis of heteropolyacids of the series H(3+x)PMo(12−x)VxO40·nH2O, Journal of Thermal Analysis 35 (1989) 1699–1707. https://doi.org/10.1007/BF01912944.

[252] C. ROCCHICCIOLIDELTCHEFF, Structure and catalytic properties of silica-supported polyoxomolybdates II. Thermal Behavior of Unsupported and Silica-Supported 12-Molybdosilicic Acid catalysts from IR and Catalytic Reactivity Studies, J Catal 126 (1990) 591–599. https://doi.org/10.1016/0021-9517(90)90022-C.

[253] K. Bruckman, J.M. Tatibouet, M. Che, E. Serwicka, J. Haber, Catalytic Behavior of Unsupported and Heteropolysalt-Supported H3+PV Mo12−O40 Heteropolyacids in the Test Reaction of CH3OH Oxidation, J Catal 139 (1993) 455–467. https://doi.org/10.1006/jcat.1993.1040.

[254] H. Hu, I.E. Wachs, Catalytic properties of supported molybdenum oxide catalysts: In situ Raman and methanol oxidation studies, Journal of Physical Chemistry 99 (1995) 10911–10922. https://doi.org/10.1021/j100027a035.

[255] M.R. Agliullin, V.P. Talzi, N.A. Filippova, V.R. Bikbaeva, S. V. Bubennov, T.R. Prosochkina, N.G. Grigorieva, N. Narender, B.I. Kutepov, Two-step sol–gel synthesis of mesoporous aluminosilicates: highly efficient catalysts for the preparation of 3,5-

dialkylpyridines, Appl Petrochem Res 8 (2018) 141–151. https://doi.org/10.1007/s13203-018-0202-0.

[256] M.R. Agliullin, I.G. Danilova, A. V. Faizullin, S. V. Amarantov, S. V. Bubennov, T.R. Prosochkina, N.G. Grigor'Eva, E.A. Paukshtis, B.I. Kutepov, Sol-gel synthesis of mesoporous aluminosilicates with a narrow pore size distribution and catalytic activity thereof in the oligomerization of dec-1-ene, Microporous and Mesoporous Materials 230 (2016) 118–127. https://doi.org/10.1016/j.micromeso.2016.05.007.

[257] J. Song, X. Fan, X. Yu, L. Kong, X. Xiao, Z. Xie, Z. Zhao, One-pot synthesis of V doped mesoporous SiO2 catalysts for selective oxidation of ethane and propane, ChemistrySelect 8 (2023). https://doi.org/10.1002/slct.202301510.

[258] M. V. Martínez-Huerta, X. Gao, H. Tian, I.E. Wachs, J.L.G. Fierro, M.A. Bañares, Oxidative dehydrogenation of ethane to ethylene over alumina-supported vanadium oxide catalysts: Relationship between molecular structures and chemical reactivity, Catal Today 118 (2006) 279–287. https://doi.org/10.1016/j.cattod.2006.07.034.

[259] G. Deo, I.E. Wachs, Reactivity of Supported Vanadium Oxide Catalysts: The Partial Oxidation of Methanol, 1994.

[260] S. Rajagopal, J.A. Marzari, R. Miranda, Silica-Alumina-Supported Mo Oxide Catalysts: Genesis and Demise of Brønsted-Lewis Acidity, J Catal 151 (1995) 192–203. https://doi.org/10.1006/jcat.1995.1021.

[261] I.E. Wachs, B.M. Weckhuysen, Structure and reactivity of surface vanadium oxide species on oxide supports, 1997.

[262] X. Gao, I.E. Wachs, Structural Characteristics and Reactivity Properties of Highly Dispersed Al2O3/SiO2 and V2O5/Al2O3/SiO2 Catalysts, J Catal 192 (2000) 18–28. https://doi.org/10.1006/jcat.2000.2822.

[263] I.E. Wachs, In situ Raman spectroscopy studies of catalysts, 1999.

.

Appendix: Chapter I

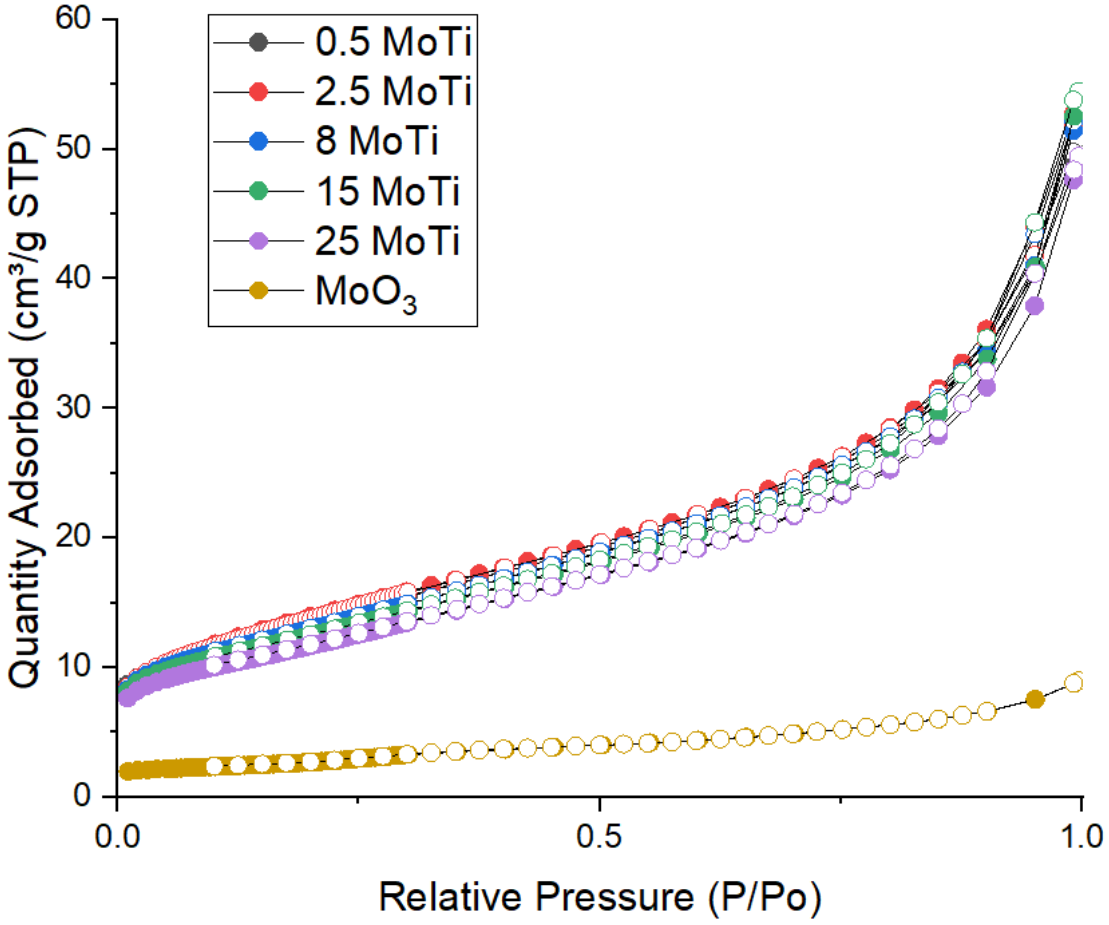

Figure A-I.1. Adsorption-desorption isotherms for all 5 molybdenum supported catalysts and bulk MoO_3.

Appendix: Chapter II

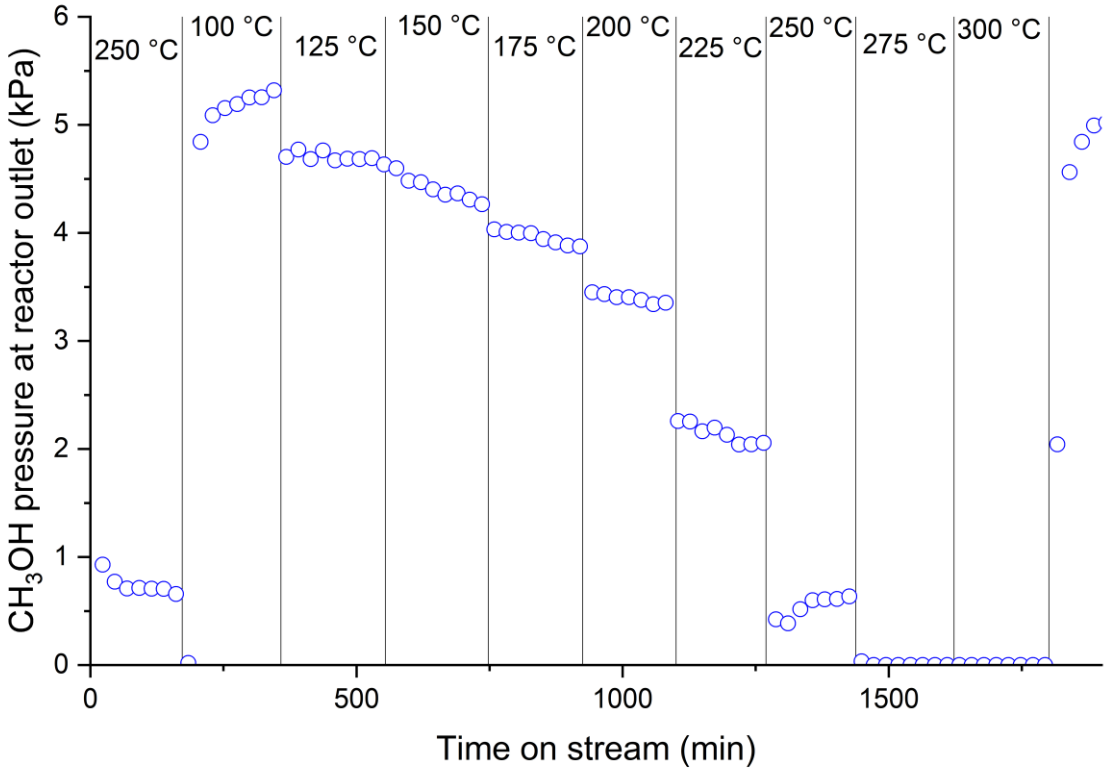

Figure A-II.1. CH_3OH partial pressure as a function of time on stream on 15 MoTi catalyst (GHSV = 19 L h^{-1} g_{cat}^{-1}, $CH_3OH/O_2/N_2$ (feed) = 4/9/87 %v/v).

Appendix: Chapter III

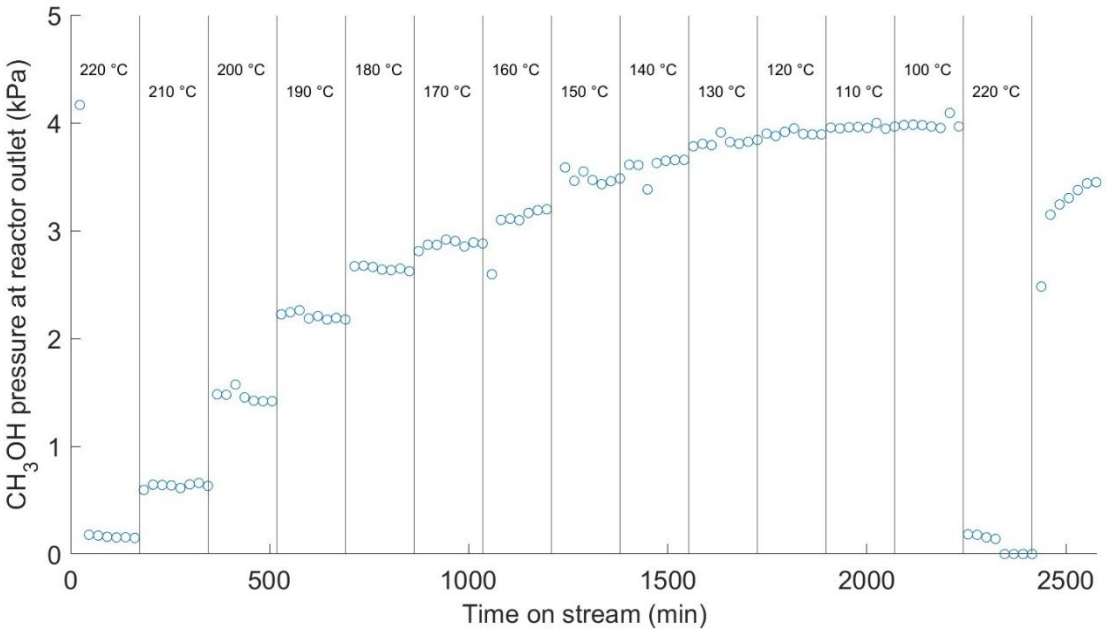

Figure A-III.1. CH_3OH partial pressure as a function of time on stream on 15 VTi catalyst (GHSV = 20 L h^{-1} g_{cat}^{-1}, $CH_3OH/O_2/N_2$ (feed) = 4/10/86 %v/v).

A-III.2. Internal diffusion limitations:

The presence of internal diffusion limitations was studied by the Weisz-Prater Criterion [264]:

$$N_{W-P} = \frac{r_{obs} R_P^2}{C_s D_{eff}} \leq 0.3$$

Where N_{W-P} is the Weisz – Prater Number, r_{obs} is the observed reaction rate (mol cm^{-3} s^{-1}), R_p is the catalyst particle radius (cm), C_s is the reactant concentration on the catalyst surface (mol cm^{-3}) and D_{eff} is the effective diffusivity (cm^2 s^{-1}).

The effective diffusivity is defined as:

$$D_{eff} = \frac{1}{\frac{1}{D_b} + \frac{1}{D_{KN}}}$$

Where D_b is the diffusion coefficient on the bulk fluid and D_{KN} is the Knudsen diffusivity. In small pores, Knudsen diffusion dominates [265], then:

$$D_{eff} \approx D_{KN}$$

Knudsen diffusion is defined as:

$$D_{KN} = \bar{v} \frac{d_p}{3}$$

Where $\bar{v}$ is the mean velocity (cm s^{-1}) and d_p is the is the pore diameter (cm).

The mean velocity is determined by the equation:

$$\bar{v} = \sqrt{\frac{8 k_b T N_A}{\pi M M_g}}$$

Where k_b is the Boltzmann constant (1.38 x 10^{-16} erg K-1), T is the temperature (K), N_A is the Avogadro number (6.022 x 10^{23} mol^{-1}) and MM_g is the molar mass of the gas reactant (g mol^{-1}).

The bulk concentration is estimated supposing ideal gas:

$$C_S = \frac{P}{RT}$$

Where P is the partial pressure of the gas that diffuses (kPa), T is the temperature (K) and R is the ideal gas constant (8.31447 x 10^{-3} kPa cm^3 K^{-1} mol^{-1}).

The observed reaction rate was estimated supposing differential reactor:

$$r_{obs} \approx \frac{v_0 \, (C_{A0} - C_{Ae})}{W}$$

Where v_0 is the gas bulk flow rate ($cm^3\ s^{-1}$), C_{A0} is the concentration of reactant on the reactor feed (mol cm^{-3}), C_{Ae} is the concentration of reactant on the exit of the reactor (mol cm^{-3}) and W is the mass of catalyst (g).

Two extreme reaction conditions were studied: high reaction rate and high concentration of methanol, and low reaction rate and low concentration of methanol, for each catalyst sample.

Sample	Temperature (°C)	Pore size (nm)	r_{obs} (x 10^6 mol $cm^{-3}\ s^{-1}$)	C_s (x 10^7 mol cm^{-3})	D_{eff} (cm^2 s)	N_{W-P}
2.5 VTi	200	32	5.3	2.5	0.061	0.12
2.5 VTi	200	32	11	13	0.061	0.05
15 VTi	225	32	9.6	2.4	0.060	0.22
15 VTi	225	32	19	12	0.060	0.09

We are far away from the diffusion regime at high methanol concentration ($N_{W-P} < 0.1$), but we cannot disregard diffusion limitations at lower methanol pressures ($N_{W-P} \approx 0.3$).

A-III.3. External diffusion limitations:

The presence of external diffusion limitations was studied by the Mears Criterion [266],

$$MR = \frac{r_{obs} \rho_b R_p n}{k_c C_{Ab}} \leq 0.15$$

Where r_{obs} is the observed reaction rate (mol $kg^{-1}\ s^{-1}$), ρ_b is the bulk density of the catalyst bed (kg m_{-3}), R_p is the catalyst particle radius (cm), n is the reaction order and C_{Ab} is the bulk reactant concentration (mol m^{-3}).

Bulk density of the catalyst is calculated:

$$\rho_b = (1 - \Phi)\rho_c$$

Where ρ_c is the solid density of the catalyst (kg m^{-3}) and Φ is the porosity.

The porosity of the catalyst bed is estimated as [267]:

$$\Phi = \frac{1}{\left(D/d_p\right)^2} + 0.375$$

Where D is reactor diameter (m) and d_p is catalyst particle diameter (m).

The external mass transfer coefficient is calculated according to the Thoenes-Kramers correlation [268]:

$$k_c = \left(\frac{U\, d_p\, \rho}{\mu\,(1-\Phi)}\right)^{1/2} \left(\frac{\mu}{\rho\, D_{AB}}\right)^{1/3} \left(\frac{D_{AB}\,(1-\Phi)}{d_p\,\Phi}\right)$$

Where U is the superficial gas velocity through the bed (m s^{-1}), ρ is the fluid density (kg m^{-3}), μ is the fluid viscosity (kg m^{-1} s^{-1}) and D_{AB} is the gas phase diffusivity (m^2 s^{-1}). The gas properties were approximated to those of N_2, as it has the highest concentration (92 %).

Because we are in the presence of a ternary mixture, the gas phase diffusivity is calculated according to Blanc's law [269]:

$$D_{AB} = \left(\sum_{\substack{j=1 \\ j\neq i}}^{n} \frac{x_j}{D_{ij}}\right)^{-1}$$

The gas phase diffusivity of methanol in oxygen and in nitrogen is calculated using the Hirschfelder et al. expression [270]:

$$D_{AB} = \frac{0.00266\, T^{3/2}}{P\, M_{AB}^{1/2} \sigma_{AB}^2 \Omega_D}$$

Where T is the temperature (K), P is pressure (bar), σ_{AB} is the characteristic length of the intermolecular force law (A°) and Ω_D is the diffusion collision integral.

M_{AB} is defined as:

$$M_{AB} = 2\left(\frac{1}{M_A} + \frac{1}{M_B}\right)^{-1}$$

Where M_A and M_B are the molecular weight of species A and B, respectively.

σ_{AB} is estimated as:

$$\sigma_{AB} = (\sigma_A \sigma_B)^{1/2}$$

Where the characteristic Lennard-Jones length for each species is calculated using the Brokaw method [271]:

$$\sigma = \left(\frac{1.585\, V_b}{1 + 1.3\, \delta^2}\right)^{1/3}$$

while δ is estimated from:

$$\delta = \frac{1.94 \times 10^3\, \mu_p^2}{V_b\, T_b}$$

Where μ_p is the dipole moment (debyes), T_b is the normal boiling point (K) and V_b is the liquid molar volume at normal boiling point (cm^3 mol^{-1}), calculated from the Tyn and Calus method [272]:

$$V_b = 0.285\, V_c^{1.048}$$

Where V_c is the critical volume ($cm^3\ mol^{-1}$).

Ω_D is evaluated according to Neufield equation [273]:

$$\Omega_D = \frac{A}{(T^*)^B} + \frac{C}{\exp(DT^*)} + \frac{E}{\exp(FT^*)} + \frac{G}{\exp(HT^*)} + \frac{0.19\delta_{AB}^2}{T^*}$$

Where A = 1.06036, B = 0.15610, C = 0.19300, D = 0.47635, E = 1.03587, F = 1.52996, G = 1.76474, H = 3.89411.

T* is defined as:

$$T^* = \frac{KT}{\varepsilon_{AB}}$$

$\frac{\varepsilon_{AB}}{K}$ is defined as:

$$\frac{\varepsilon_{AB}}{K} = \left(\frac{\varepsilon_A}{K}\frac{\varepsilon_B}{K}\right)^{1/2}$$

Where $\frac{\varepsilon}{K}$ is calculated as follows:

$$\frac{\varepsilon}{K} = 1.18\,(1 + 1.3\delta^2)\,T_b$$

Two extreme reaction conditions were studied: high reaction rate and high concentration of methanol, and low reaction rate and low concentration of methanol on 15 VTi, sample which has a faster reaction rate.

Sample	Temperature (°C)	D_{AB} (x 10^5 m^2 s^{-1})	r_{obs} (x 10^3 mol kg^{-1} s^{-1})	C_s (mol m^{-3})	k_c (m s^{-1})	MR (x 10^7)
15 VTi	225	3.6	2.6	0.44	5.2	1.5
15 VTi	225	3.9	5.2	2.20	5.5	0.56

Given the low values of the Mears number, the external mass transfer effects can be neglected.

A-III.4. External heat transfer effects limitations

External heat transfer effects were studied by the Mears criterion [266]:

$$\left|\frac{-\Delta H_{Rx}\, r_{obs}\, \rho_b R_p\, E_{app}}{h\, T^2\, R_g}\right| < 0.15$$

Where h is the heat transfer coefficient between gas and pellet (kJ m^{-2} s^{-1} K^{-1}), R_g is the gas constant (8.314 J mol^{-1} K^{-1}), ΔH_{Rx} is the heat of reaction (kJ mol^{-1}) and E_{app} is the apparent activation energy (kJ mol^{-1}).

The heat transfer coefficient is calculated from:

$$h = \frac{Nu\, k_f}{d_p}$$

Where Nu is the Nusselt number, k_f is the thermal conductivity (W m^{-1} K^{-1}) and d_p is the catalyst particle diameter (m).

The Nusselt number is estimated from [274]:

$$Nu = 2 + 0.6 \cdot\ Re^{0.5} \cdot Pr^{0.33}$$

Where Re is the Reynolds number and Pr is the Prandt number. The gas properties were approximated to those of N_2, as it has the highest concentration (92 %).

ΔH_{Rx} of MF formation was considered as the heat of reaction of methanol oxidation, as is the most exothermic reaction.

One extreme reaction condition was studied on 15 VTi, which showed the fastest reaction rate.

Sample	T (°C)	ΔH_{Rx} (kJ mol^{-1})	r_{obs} (mol m^{-3} s^{-1})	E_{app} (kJ mol^{-1})	Re (x 10^{-2})	Pr	Un (x 10^{-1})	H (x 10^{-3} W K^{-1})	MR (x 10^{5})
15 VTi	225	418.1	19	179	8.5	0.71	2.2	1.19	2.1

Given the low values of the Mears number, the external heat transfer effects can be neglected.

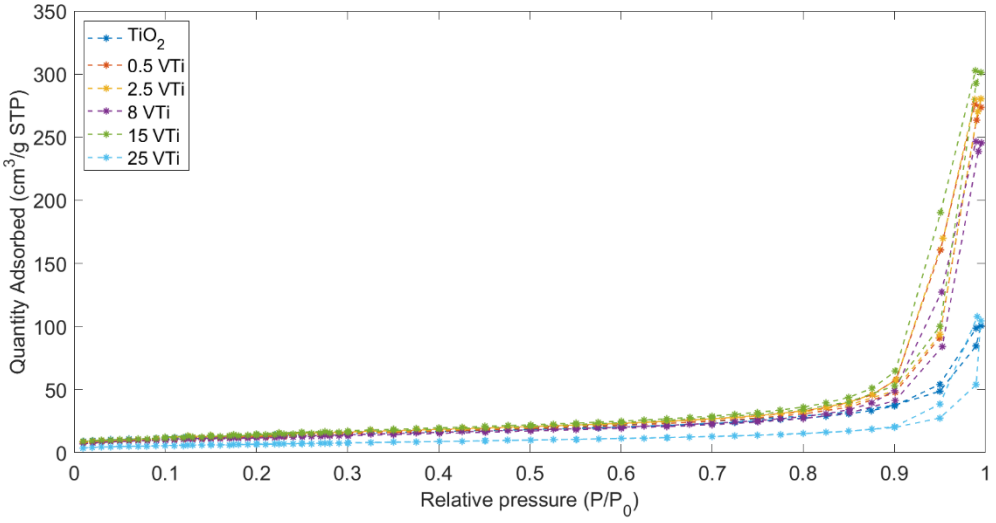

Figure A-III.5. Adsorption-desorption isotherms for all 5 vanadia supported catalysts and TiO_2.

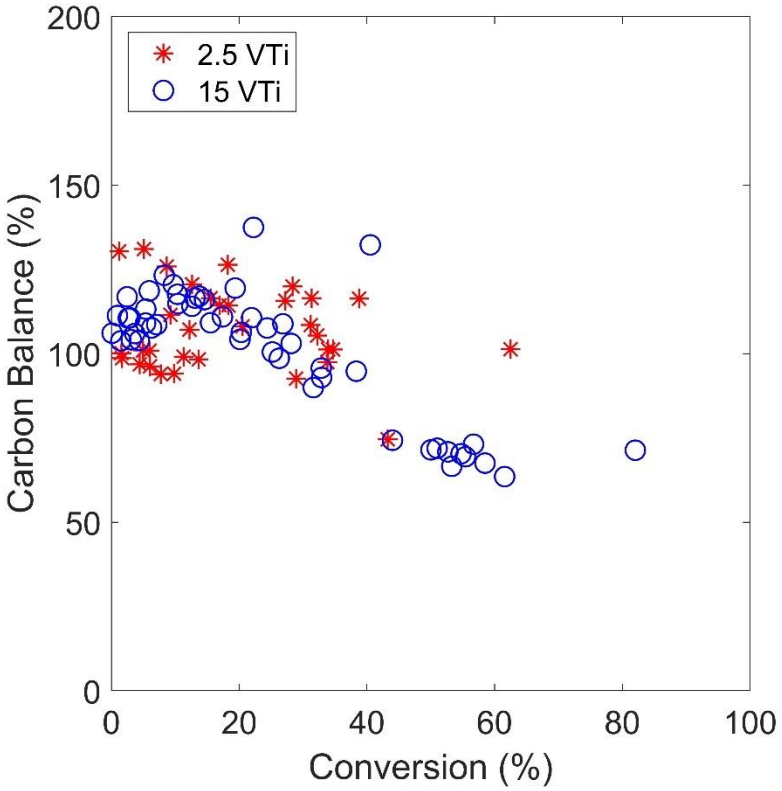

Figure A-III-6. Carbon balance for the data used in the kinetic modelling as a function of conversion.

A-III.7. Langmuir-Hinshelwood kinetic model derivation for methanol ODH reaction:

Given the elementary steps on Table III.2, the corresponding net rate expressions are:

1	Molecular chemisorption of methanol on a redox site	$r_1 = k_1^+ P_{CH_3OH} \theta_{O^*} - k_1^- \theta_{CH_3OH-O^*}$
2	Methanol dehydrogenation (rds):	$r_{ODH} = k_{ODH} \theta_{CH_3OH-O^*}$
3	FA desorption:	$r_3 = k_3 \theta_{O_lH/HCHO-HO^*}$
4	OH groups recombination:	$r_4 = k_4 \theta_{O_lH/HO^*} - k_4^- P_{H_2O} \theta$
5	First oxygen vacancy reoxidation:	$r_5 = k_5 P_{O_2} \theta$
6	Second oxygen vacancy reoxidation:	$r_6 = k_6 \theta_{O_M} \theta$
7	Molecular chemisorption of methanol on an acid site:	$r_7 = k_7^+ P_{CH_3OH} \theta_{H^+} - k_7^- \theta_{CH_3OH-H^+}$
8	Hemiacetal intermediate formation:	$r_8 = k_8 \theta_{CH_3OH-H^+} \theta_{O_lH/HCHO-HO^*}$
9	Hemiacetal spillover to a redox site:	$r_9 = k_9 \theta_{HOCH_2OCH_3-H^+} \theta_{O^*} - k_9^- \theta_{HOCH_2OCH_3-O^*} \theta_{H^+}$
10	Hemiacetal dehydrogenation:	$r_{10} = k_{10} \theta_{HOCH_2OCH_3-O^*}$
11	MF desorption:	$r_{11} = k_{11} \theta_{O_lH/HCOOCH_3-HO^*}$
12	Dehydration reaction:	$r_{12} = k_{12}\theta_{HOCH_2OCH_3-H^+} - k_{12}^-\theta_{CH_2OCH_3-H^+}P_{H_2O}$
13	DMM reversible formation:	$r_{13} = k_{13} \theta_{CH_2OCH_3-H^+} P_{CH_3OH} - k_{13}^-\theta_{CH_2OCH_3OCH_3-H^+}$
14	DMM desorption:	$r_{14} = k_{14}\theta_{CH_2OCH_3OCH_3-H^+} - k_{14}^-P_{CH_2OCH_3OCH_3}\theta_{H^+}$

Each methanol ODH product reaction rate was derived separately, and the net reaction for each elementary step was calculated as the sum of the respective rate for each product (e.g. $r_1 = r_1^{FA} + r_1^{MF} + r_1^{DMM}$), as to not predeterminate the selectivity of FA, MF and DMM .

Steps 1, 4, 7, 9, 13 and 14 are considered in quasi-equilibrium:

$$K_1 = \frac{k_1}{k_1^-} = \frac{\theta_{CH_3OH-O^*}}{P_{CH_3OH}\,\theta_{O^*}}$$

$$K_4 = \frac{k_4^-}{k_4} = \frac{\theta_{OH/HO^*}}{P_{H_2O}\,\theta}$$

$$K_7 = \frac{k_7}{k_7^-} = \frac{\theta_{CH_3OH-H^+}}{P_{CH_3OH}\,\theta_{H^+}}$$

$$K_9 = \frac{k_9}{k_9^-} = \frac{\theta_{HOCH_2OCH_3-O^*}\,\theta_{H^+}}{\theta_{HOCH_2OCH_3-H^+}\,\theta_{O^*}}$$

$$K_{13} = \frac{k_{13}}{k_{13}^-} = \frac{\theta_{CH_2OCH_3OCH_3-H^+}}{\theta_{CH_2OCH_3-H^+}\,P_{CH_3OH}}$$

$$K_{14} = \frac{k_{14}^{-}}{k_{14}} = \frac{\theta_{CH_2OCH_3OCH_3-H^+}}{P_{CH_2OCH_3OCH_3}\theta_{H^+}}$$

The net coverage of all intermediate species are given for the next set of differential equations:

$$\frac{d\theta_{CH_3OH-O^*}}{dt} = r_1 - r_2$$

$$\frac{d\theta_{O_lH/HCHO-HO^*}}{dt} = r_2 - r_3 - r_8$$

$$\frac{d\theta_{O_lH/HO^*}}{dt} = r_3 + r_8 - r_4$$

$$\frac{d\theta_*}{dt} = r_4 - r_5 - r_6$$

$$\frac{d\theta_{O_M}}{dt} = r_5 - r_6$$

$$\frac{d\theta_{CH_3OH-H^+}}{dt} = r_7 - r_8$$

$$\frac{d\theta_{HOCH_2OCH_3-H^+}}{dt} = r_8 - r_9 - r_{12}$$

$$\frac{d\theta_{HOCH_2OCH_3-O^*}}{dt} = r_9 - r_{10}$$

$$\frac{d\theta_{O_lH/HCOOCH_3-HO^*}}{dt} = r_{10} - r_{11}$$

$$\frac{d\theta_{CH_2OCH_3-H^+}}{dt} = r_{12} - r_{13}$$

$$\frac{d\theta_{CH_2OCH_3OCH_3-H^+}}{dt} = r_{13} - r_{14}$$

Considering pseudo steady state approximation, the differential equations that describe the coverage of the species are equal to zero:

$$\frac{d\theta}{dt} = 0$$

There are a total of 13 species and 11 independent equations. The last two equations that round up the degrees of freedom are the site balances of redox and acid sites:

$$1 = \theta_* + \theta_{CH_3OH-O^*} + \theta_{O^*} + \theta_{O_lH/HO^*}$$

$$1 = 1 + \theta_{H^+} + \theta_{CH_3OH-H^+}$$

The system of 13 lineal equations was solved with "Mathematica" software, using the command "Solve". The coverages of the intermediate species are expressed as a function of the coverage of the active sites, θ_{O_l} and θ_{H^+}. Then:

$$\theta_{O_lH/HCHO-HO^*} = \frac{K_1 k_2\, P_{CH_3OH}\, \theta_{O^*}}{1 + \frac{K_7 k_8}{k_3} P_{CH_3OH}\, \theta_{H^+}}$$

$$\theta_{O_lH/HCOOCH_3-HO^*} = \frac{K_1 k_2 P_{CH_3OH} \theta_{O^*}}{k_{11}\left(1 + \frac{k_3}{K_8}\frac{1}{K_7 P_{CH_3OH}\theta_{H^+}}\right)\left(1 + \frac{k_{12}}{k_{10}\, K_9}\frac{\theta_{H^+}}{\theta_{O^*}}\right)} + \frac{i_{12} K_{14}\, P_{DMM}\, P_{H_2O}\theta_{H^+}}{k_{11} K_{13}\, P_{CH_3OH}\left(1 + \frac{k_{12}}{k_{10}\, K_9}\frac{\theta_{H^+}}{\theta_{O^*}}\right)}$$

$$\theta_{HOCH_2OCH_3-H^+} = \frac{K_1 k_2 P_{CH_3OH} \theta_{O^*}}{k_{12}\left(1 + \frac{k_3}{K8}\frac{1}{K_7 P_{CH_3OH}\theta_{H^+}}\right)\left(1 + \frac{k_{10}\, K_9}{k_{12}}\frac{\theta_{O^*}}{\theta_{H^+}}\right)} - \frac{i_{12}\, K_{14}\, P_{DMM}\, P_{H_2O}\theta_{H^+}}{k_{12}\, P_{CH_3OH}\, K_{13}\left(1 + \frac{k_{10}\, K_9}{k_{12}}\frac{\theta_{O^*}}{\theta_{H^+}}\right)}$$

$$\theta_{CH_2OCH_3-H^+} = \frac{K_{14}\, PDMM\, \theta_{H^+}}{K_{13}\, P_{CH_3OH}}$$

$$\theta_{CH_3OH-O^*} = K_1\, P_{CH_3OH}\, \theta_{O^*}$$

$$\theta_* = \frac{K_1\, k_2\, P_{CH_3OH}\, \theta_{O^*}}{k_5\, P_{O_2}}$$

$$\theta_{O_lH/HO^*} = \frac{K_1\, k_2\, K_4\, P_{CH_3OH}\, P_{H_2O}\, \theta_{O^*}}{k_5\, P_{O_2}}$$

$$\theta_{CH_3OH-H^+} = K_7\, P_{CH_3OH}\, \theta_{H^+}$$

With:

$$\theta_{O^*} = \frac{1}{1 + K_1\, P_{CH_3OH} + \frac{K_1\, k_{ODH}\, P_{CH_3OH}}{2\, k_5 P_{O_2}}\left(K_4\, P_{H_2O} + 1\right)}$$

$$\theta_{H^+} = \frac{1}{1 + K_7\, P_{CH_3OH}}$$

If the reoxidation step is much faster than the oxidation of methanol ($2\, k_5 P_{O_2} \gg K_1\, k_{ODH}\, P_{CH_3OH}$), then:

$$\theta_{O^*} \approx \frac{1}{1 + K_1\, P_{CH_3OH}}$$

Finally, the rates of FA, MF and DMM formation are given by the equations:

$$r_{FA} = r_3 = k_3 \theta_{O_1H/HCHO-HO^*}$$

$$r_{MF} = r_{10} = k_{10} \theta_{HOCH_2OCH_3-O^*}$$

$$r_{DMM} = r_{12} = k_{12} \theta_{HOCH_2OCH_3-H^+} - k_{12}^{-} \theta_{CH_2OCH_3-H^+} P_{H_2O}$$

In order to find the elementary steps that fit the data with the better fitting, some other possible models were tried.

a) DMM formation by L-H mechanism and S_N2 substitution:

$r_{FA} = \dfrac{K_1 k_2 P_{CH_3OH} \theta_O}{1 + \dfrac{1}{k_{FA/HA}} K_7 P_{CH_3OH} \theta_{H^+}}$
$r_{MF} = \dfrac{K_1 k_2 P_{CH_3OH} \theta_O}{\left(1 + k_{FA/HA} \dfrac{1}{K_7 P_{CH_3OH} \theta_{H^+}}\right)\left(1 + \dfrac{1}{k_{MF/DMM}} \dfrac{K_7\, P_{CH3OH} \theta_{H^+}^2}{\theta_O}\right)} \left(1 + \eta \dfrac{1}{k_{MF/DMM}} \dfrac{K_7\, P_{CH3OH} \theta_{H^+}^2}{\theta_O}\right)$
$r_{DMM} = \dfrac{K_1 k_2 P_{CH_3OH} \theta_O}{\left(1 + k_{FA/HA} \dfrac{1}{K_7 P_{CH_3OH} \theta_{H^+}}\right)\left(1 + k_{MF/DMM} \dfrac{\theta_O}{K_7\, P_{CH3OH} \theta_{H^+}^2}\right)} (1 - \eta)$

b) DMM formation by E-R mechanism (as in this publication) and S_N2 substitution:

$r_{FA} = \dfrac{K_1 k_2 P_{CH_3OH} \theta_O}{1 + \dfrac{1}{k_{FA/HA}} K_7 P_{CH_3OH} \theta_{H^+}}$
$r_{MF} = \dfrac{K_1 k_2 P_{CH_3OH} \theta_O}{\left(1 + k_{FA/HA} \dfrac{1}{K_7 P_{CH_3OH} \theta_{H^+}}\right)\left(1 + \dfrac{1}{k_{MF/DMM}} \dfrac{P_{CH3OH} \theta_{H^+}}{\theta_O}\right)} \left(1 + \eta \dfrac{1}{k_{MF/DMM}} \dfrac{P_{CH3OH} \theta_{H^+}}{\theta_O}\right)$
$r_{DMM} = \dfrac{K_1 k_2 P_{CH_3OH} \theta_O}{\left(1 + k_{FA/HA} \dfrac{1}{K_7 P_{CH_3OH} \theta_{H^+}}\right)\left(1 + k_{MF/DMM} \dfrac{\theta_O}{P_{CH3OH} \theta_{H^+}}\right)} (1 - \eta)$

c) DMM formation by L-H mechanism and S_N1 substitution (as in this publication):

$r_{FA} = \dfrac{K_1 k_2 P_{CH_3OH} \theta_O}{1 + \dfrac{1}{k_{FA/HA}} K_7 P_{CH_3OH} \theta_{H^+}}$
$r_{MF} = \dfrac{K_1 k_2 P_{CH_3OH} \theta_O}{\left(1 + k_{FA/HA} \dfrac{1}{K_7 P_{CH_3OH} \theta_{H^+}}\right)\left(1 + \dfrac{1}{k_{MF/DMM}} \dfrac{K_7\, \theta_{H^+}^2}{\theta_O}\right)} \left(1 + \eta \dfrac{1}{k_{MF/DMM}} \dfrac{K_7\, \theta_{H^+}^2}{\theta_O}\right)$
$r_{DMM} = \dfrac{K_1 k_2 P_{CH_3OH} \theta_O}{\left(1 + k_{FA/HA} \dfrac{1}{K_7 P_{CH_3OH} \theta_{H^+}}\right)\left(1 + k_{MF/DMM} \dfrac{\theta_O}{K_7\, \theta_{H^+}^2}\right)} (1 - \eta)$

d) Irreversible hemiacetal spillover (step 9), DMM formation by E-R mechanism (as in this publication) and S_N1 substitution (as in this publication):

$r_{FA} = \dfrac{K_1 k_2 P_{CH_3OH} \theta_O}{1 + \dfrac{1}{k_{FA/HA}} K_7 P_{CH_3OH} \theta_{H^+}}$
$r_{MF} = \dfrac{K_1 k_2 P_{CH_3OH} \theta_O}{\left(1 + k_{FA/HA} \dfrac{1}{K_7 P_{CH_3OH} \theta_{H^+}}\right)\left(1 + \dfrac{1}{k_{MF/DMM}} \dfrac{1}{\theta_O}\right)} \left(1 + \eta \dfrac{1}{k_{MF/DMM}} \dfrac{1}{\theta_O}\right)$
$r_{DMM} = \dfrac{K_1 k_2 P_{CH_3OH} \theta_O}{\left(1 + k_{FA/HA} \dfrac{1}{K_7 P_{CH_3OH} \theta_{H^+}}\right)\left(1 + k_{MF/DMM} \dfrac{\theta_O}{1}\right)} (1 - \eta)$

e) Irreversible hemiacetal spillover (step 9), DMM formation by L-H mechanism and S_N1 substitution (as in this publication):

$r_{FA} = \dfrac{K_1 k_2 P_{CH_3OH} \theta_O}{1 + \dfrac{1}{k_{FA/HA}} K_7 P_{CH_3OH} \theta_{H^+}}$
$r_{MF} = \dfrac{K_1 k_2 P_{CH_3OH} \theta_O}{\left(1 + k_{FA/HA} \dfrac{1}{K_7 P_{CH_3OH} \theta_{H^+}}\right)\left(1 + \dfrac{1}{k_{MF/DMM}} \dfrac{K_7\, \theta_{H^+}}{\theta_O}\right)} \left(1 + \eta \dfrac{1}{k_{MF/DMM}} \dfrac{K_7\, \theta_{H^+}}{\theta_O}\right)$
$r_{DMM} = \dfrac{K_1 k_2 P_{CH_3OH} \theta_O}{\left(1 + k_{FA/HA} \dfrac{1}{K_7 P_{CH_3OH} \theta_{H^+}}\right)\left(1 + k_{MF/DMM} \dfrac{\theta_O}{K_7\, \theta_{H^+}}\right)} (1 - \eta)$

In general, the models only change the order of the terms that define the ratio of MF/DMM formation, in particular the exponents, from values of zero to 2. These exponents were optimized, and the E-R, S_N1, reversible spillover model was selected.

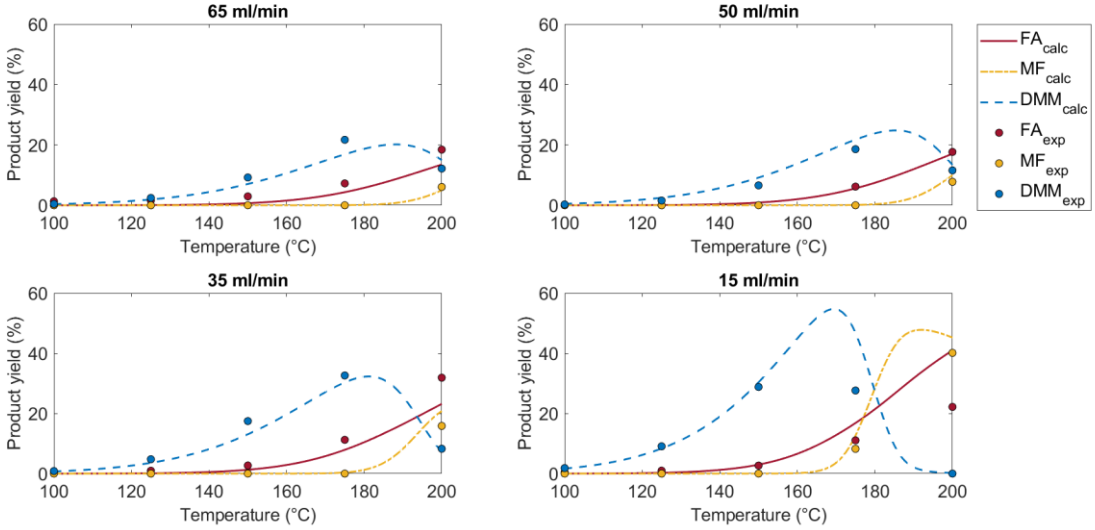

Figure A-III.8. Predicted vs experimental FA, MF and DMM yield as a function of temperature on 2.5 VTi (m_{cat} = 0.15, $CH_3OH/O_2/N_2$ (feed) = 4/4/balance %v/v).

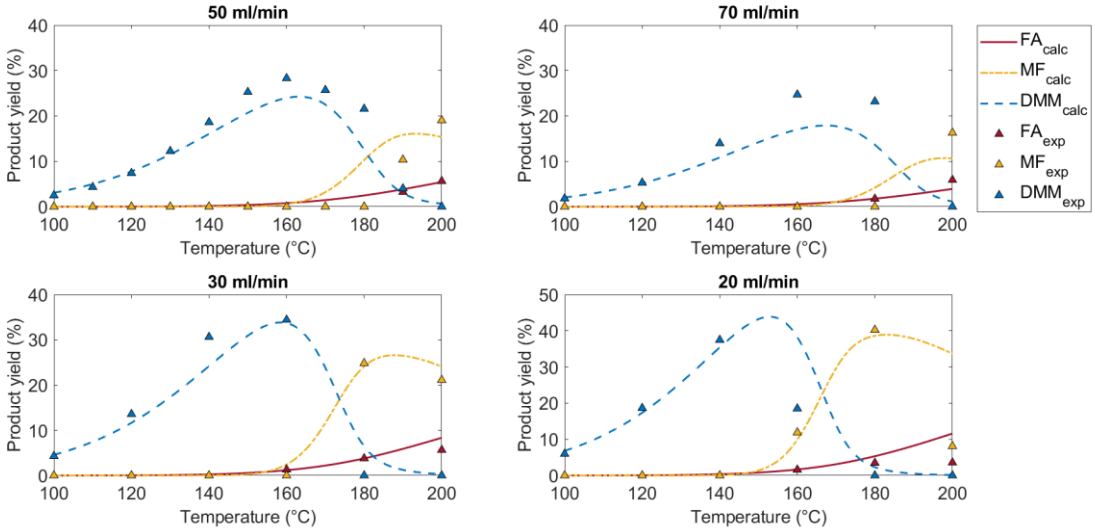

Figure A-III.9. Predicted vs experimental FA, MF and DMM yield as a function of temperature on 15 VTi catalyst (m_{cat} = 0.2 g, $CH_3OH/O_2/N_2$ (feed) = 4/10/balance %v/v).

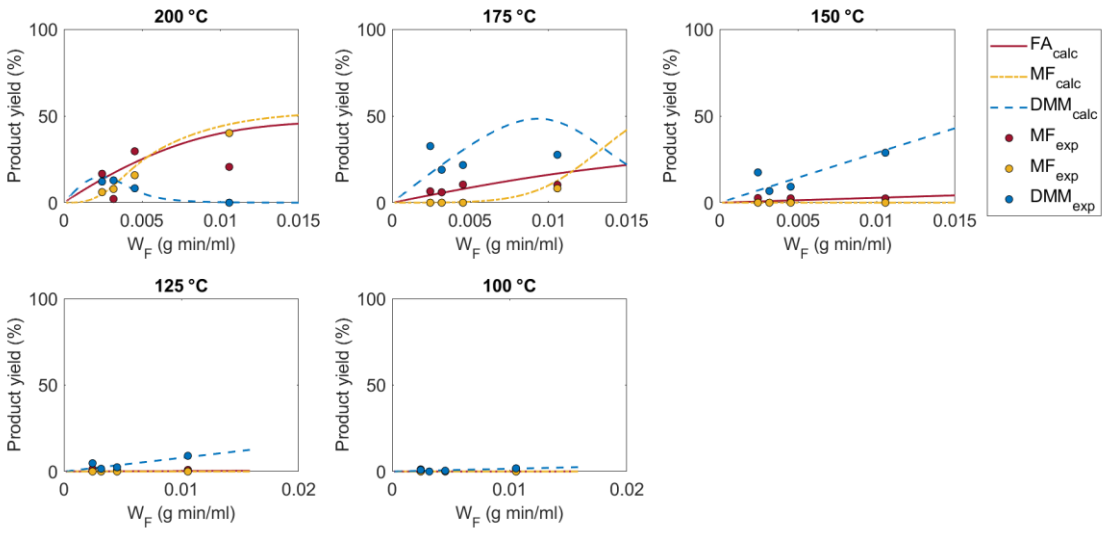

Figure A-III.10. Predicted vs experimental FA, MF and DMM yield as a function of residence time on 2.5 VTi ($CH_3OH/O_2/N_2$ (feed) = 4/4/balance %v/v)

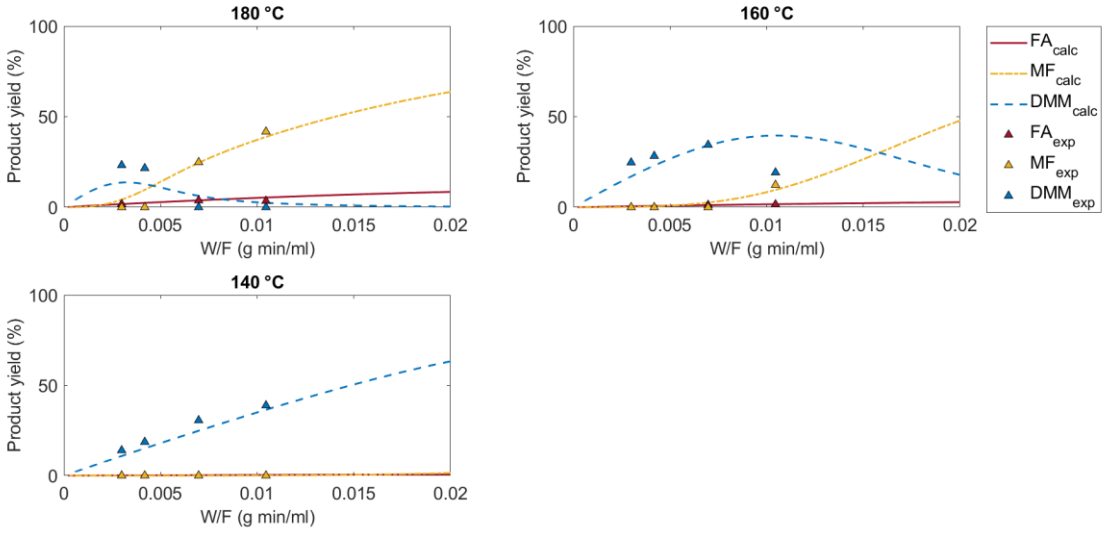

Figure A-III.11. Predicted vs experimental FA, MF and DMM yield as a function of residence time on 15 VTi catalyst ($CH_3OH/O_2/N_2$ (feed) = 4/10/balance %v/v, T = 175 °C).

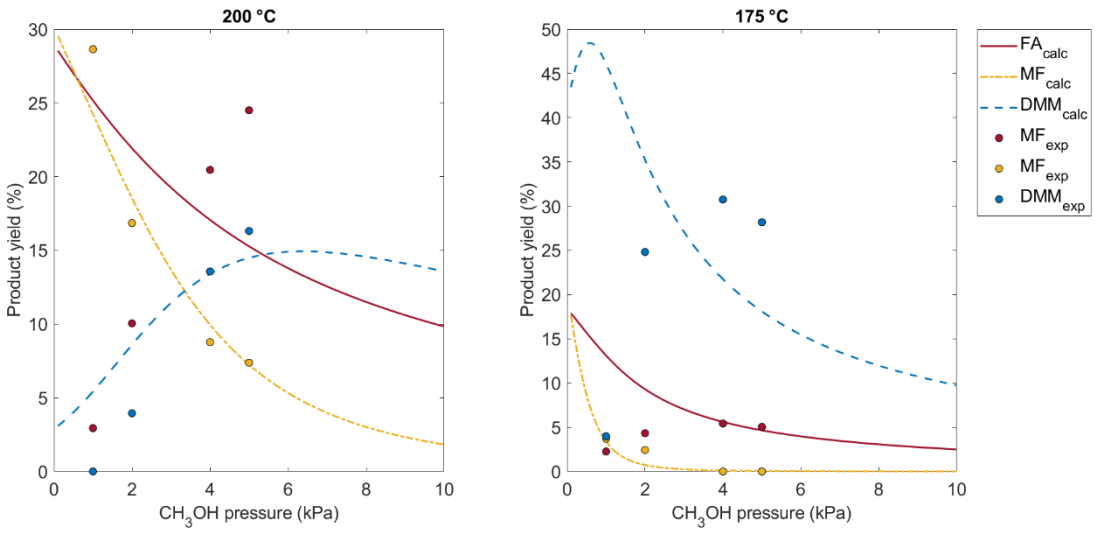

Figure A-III.12. Predicted vs experimental FA, MF and DMM yield as a function of CH_3OH pressure on 15 VTi (GHSV = 15 L h^{-1} g_{cat}^{-1}, $CH_3OH/O_2/N_2$ (feed) = -/10/balance %v/v).

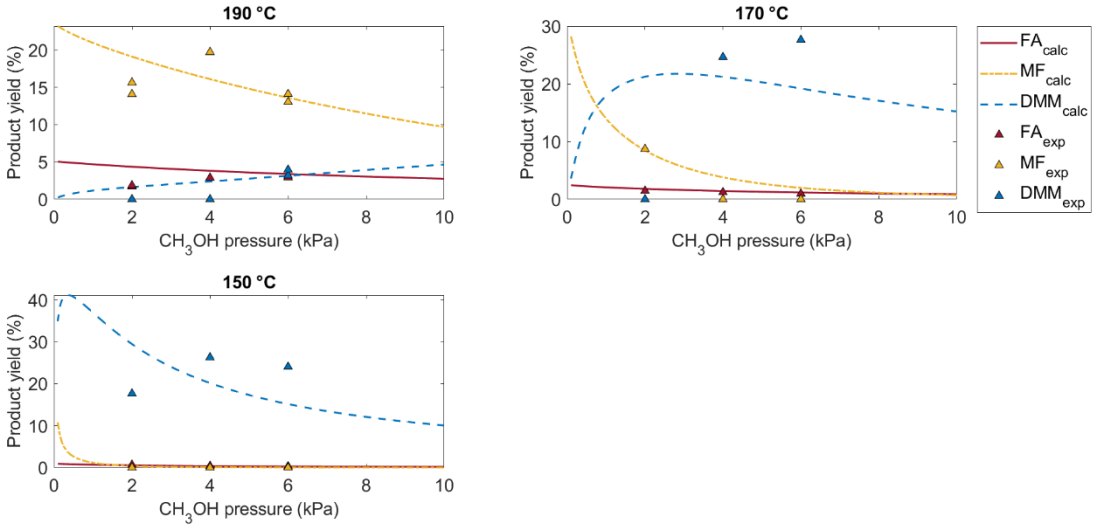

Figure A-III.13. Predicted vs experimental FA, MF and DMM yield as a function of CH_3OH pressure on 15 VTi (GHSV = 15 L h^{-1} g_{cat}^{-1}, $CH_3OH/O_2/N_2$ (feed) = 4/10/balance %v/v).

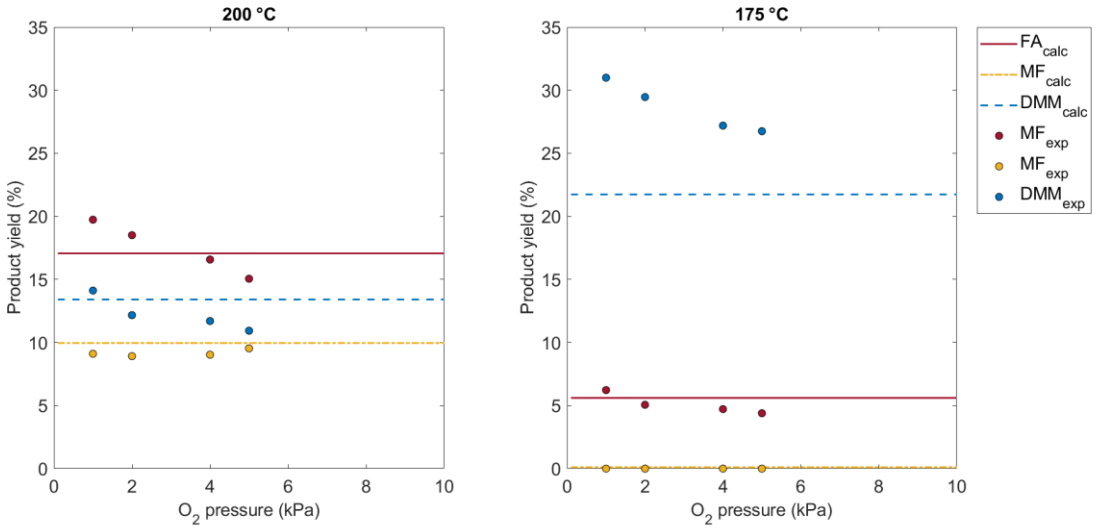

Figure A-III.14. Predicted vs experimental FA, MF and DMM yield as a function of O_2 pressure on 2.5 VTi (GHSV = 20 L h^{-1} g_{cat}^{-1}, $CH_3OH/O_2/N_2$ (feed) = 4/-/balance %v/v)

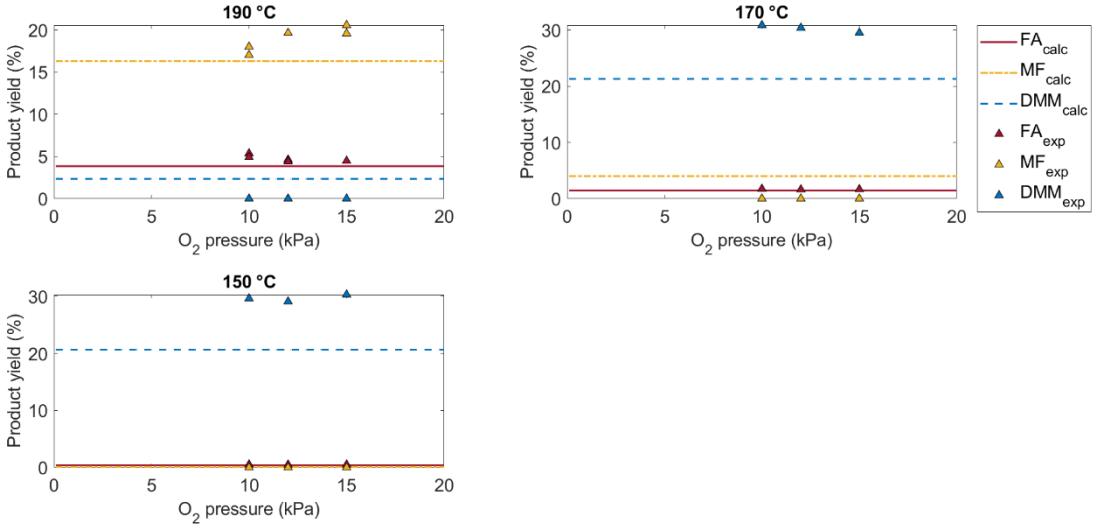

Figure A-III.15. Predicted vs experimental FA, MF and DMM yield as a function of O_2 pressure on 15 VTi (GHSV = 15 L h^{-1} g_{cat}^{-1}, $CH_3OH/O_2/N_2$ (feed) = 4/-/balance %v/v).

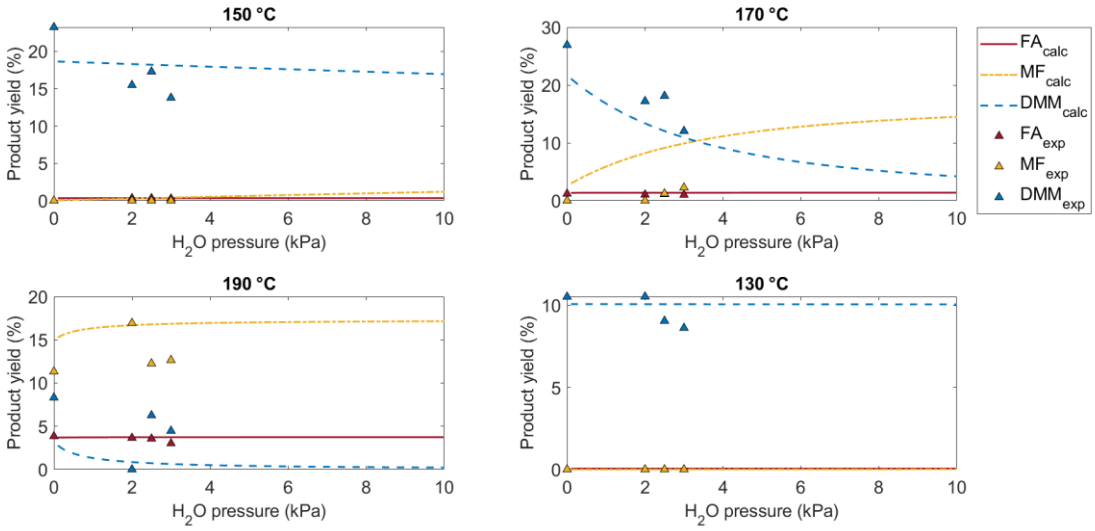

Figure A-III.16. Predicted vs experimental FA, MF and DMM yield as a function of H_2O pressure the feed, on 15 VTi (GHSV = 15 L h^{-1} g_{cat}^{-1}, $CH_3OH/O_2/H_2O/N_2$ (feed) = 4/10/-/balance %v/v).

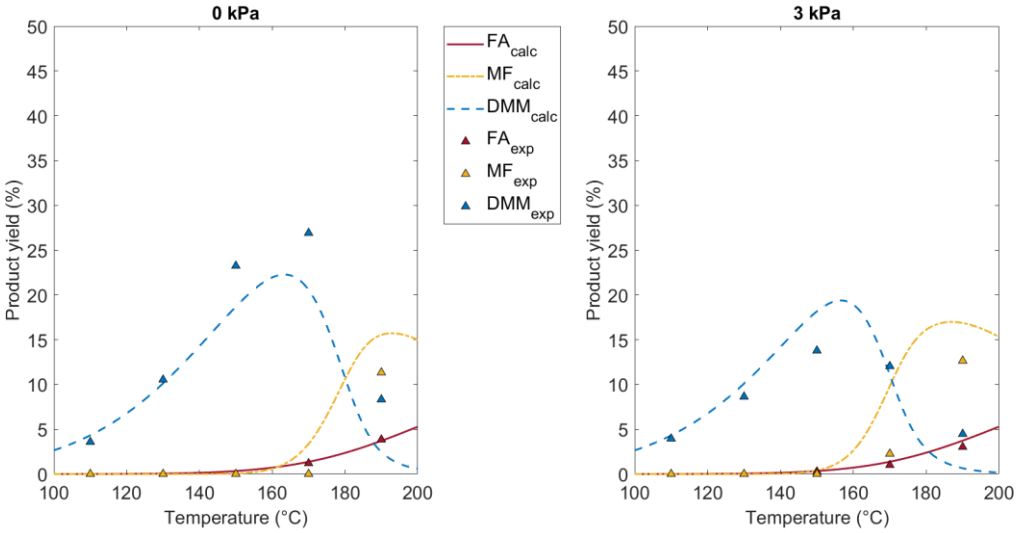

Figure A-III.17. Predicted vs experimental FA, MF and DMM yield as a function of temperature on 15 VTi catalyst, with water on the feed (GHSV = 15 L h^{-1} g_{cat}^{-1}, $CH_3OH/O_2/H_2O/N_2$ (feed) = 4/10/-/balance %v/v).

Appendix: Chapter IV

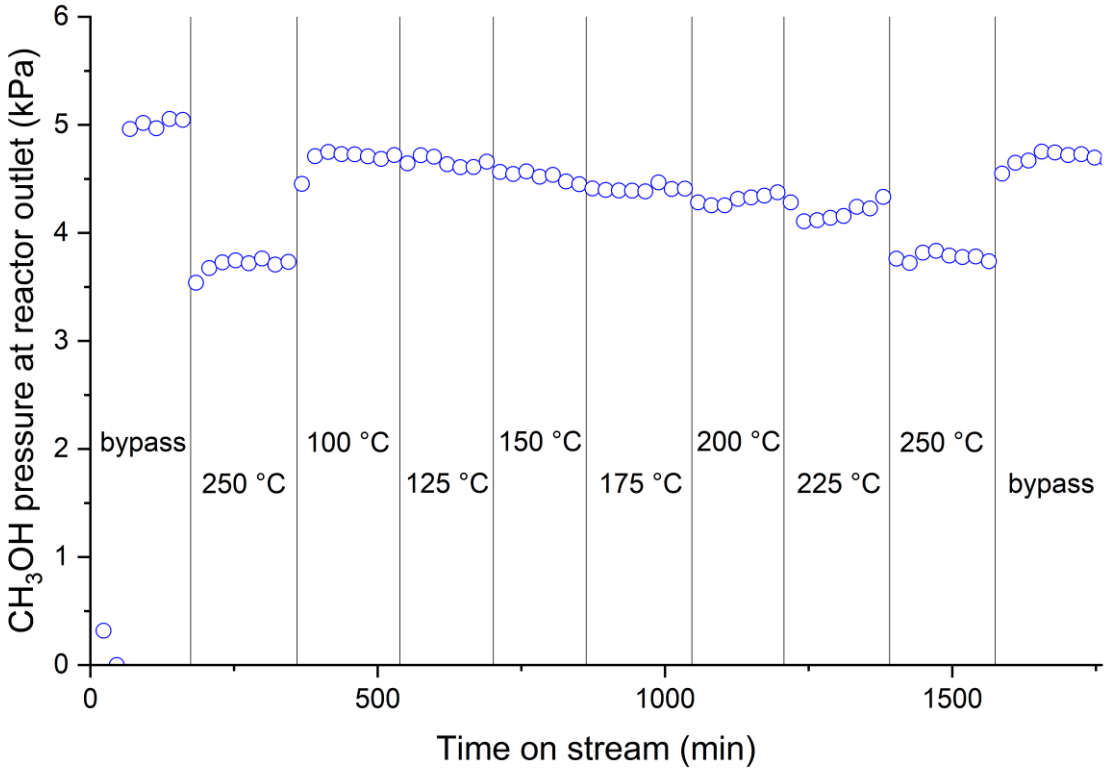

Figure A-IV.1. CH_3OH partial pressure as a function of time on stream on V/99Si catalyst (GHSV = 15 L h^{-1} g_{cat}^{-1}, $CH_3OH/O_2/N_2$ (feed) = 4/9/87 %v/v).

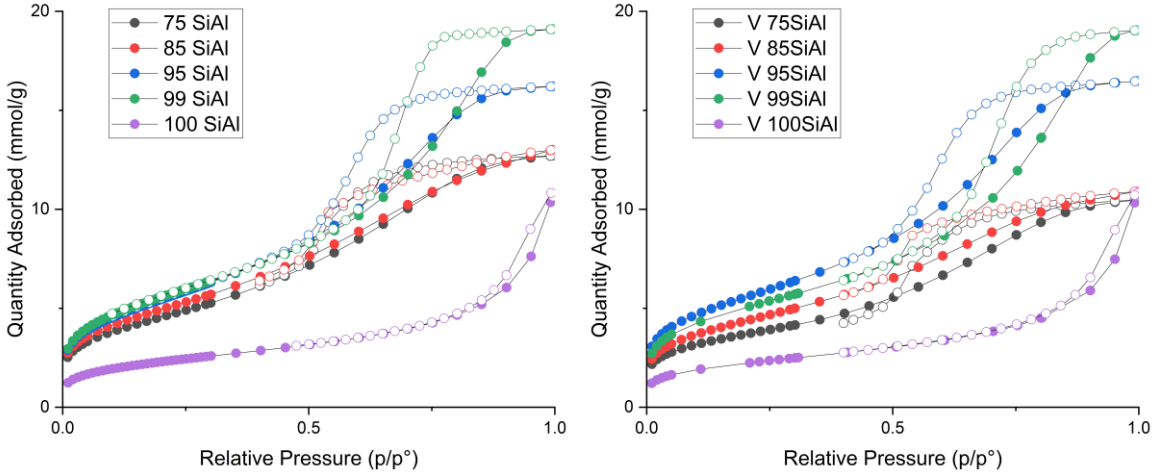

Figure A-IV.2. Adsorption-desorption isotherms for all 5 SiO_2-Al_2O_3 supports, and 5 V_2O_5/SiO_2-Al_2O_3 supported catalysts.

Appendix References

[264] P.B. Weisz, C.D. Prater, Interpretation of Measurements in Experimental Catalysis, in: Advances in Catalysis, 1954: pp. 143–196. https://doi.org/10.1016/S0360-0564(08)60390-9.

[265] M.Albert. Vannice, Kinetics of catalytic reactions, Springer, 2005.

[266] D.E. Mears, Tests for Transport Limitations in Experimental Catalytic Reactors, Industrial & Engineering Chemistry Process Design and Development 10 (1971) 541–547. https://doi.org/10.1021/i260040a020.

[267] A.S. Pushnov, Calculation of average bed porosity, Chemical and Petroleum Engineering 42 (2006) 14–17. https://doi.org/10.1007/s10556-006-0045-x.

[268] D. Thoenes, H. Kramers, Mass transfer from spheres in various regular packings to a flowing fluid, Chem Eng Sci 8 (1958) 271–283. https://doi.org/10.1016/0009-2509(58)85034-4.

[269] A. Blanc, Mobility of ions in gases, Journal de Physique Théorique et Appliquée 7 (1908) 825–839.

[270] J.O. Hirschfelder, R.Byron. Bird, E.L. Spotz, The Transport Properties of Gases and Gaseous Mixtures. II., Chem Rev 44 (1949) 205–231. https://doi.org/10.1021/cr60137a012.

[271] R.S. Brokaw, Predicting Transport Properties of Dilute Gases, Industrial & Engineering Chemistry Process Design and Development 8 (1969) 240–253. https://doi.org/10.1021/i260030a015.

[272] Jaime Benitez, Principles and modern applications of mass transfer operations., Third Edition, Wiley, 2016.

[273] P.D. Neufeld, A.R. Janzen, R.A. Aziz, Empirical Equations to Calculate 16 of the Transport Collision Integrals Ω(l, s)* for the Lennard-Jones (12–6) Potential, J Chem Phys 57 (1972) 1100–1102. https://doi.org/10.1063/1.1678363.

[274] W.E., M.W.R. Ranz, EVAPORATION OF DROPS, in: A-to-Z Guide to Thermodynamics, Heat and Mass Transfer, and Fluids Engineering, Begellhouse, 1952: pp. 141–146. https://doi.org/10.1615/AtoZ.e.evaporation_of_drops.